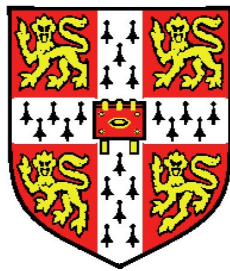


Dynamic Properties of Materials: Phonons from Neutron Scattering



Elizabeth Ruth Cope
Christ's College
University of Cambridge

This dissertation is submitted for the degree of

Doctor of Philosophy

May 2010

Abstract

A detailed understanding of fundamental material properties can be obtained through the study of atomic vibrations, performed experimentally with neutron scattering techniques and coupled with the two powerful new computational methodologies I have developed. The first approach involves phonon-based simulations of the pair distribution function – a histogram of localised atomic positions generated experimentally from total scattering data. This is used to reveal ordering behaviour, to validate interatomic models and localised structure, and to give insights into how far dynamic behaviour can be studied using total scattering techniques. Most importantly, the long-standing controversy over dynamic disorder in β -cristobalite is resolved using this technique.

Inelastic neutron spectroscopy (INS) allows *direct* study of vibrational modes through their interaction with the neutron beam, and is the experimental basis for the second strand of the new methodology. I have developed new simulation and refinement tools based on the next generation of spectrometers currently being commissioned at the ISIS pulsed neutron source. This allows a detailed powder spectroscopy study of cristobalite and vitreous silica demonstrating that the Bose peak and so-called ‘fast sound’ features can be derived from standard lattice dynamics in both the crystal and the amorphous counterpart, and allowing discussion of their origins. Given the controversy in the literature, this is a key result.

The new methodology also encompasses refinement of interatomic models against powder INS data, with aluminium providing a successful test-case. A more complex example is seen in calcite, with experimental data collected during the commissioning of the new MERLIN spectrometer. Simulated one-phonon coherent INS spectra for the single crystal and powder (the latter including approximations to multi-phonon and multiple scatter) are fully convolved with experimental resolution functions. These are used in the analysis of the experimental data, yielding previously unpublished dispersion curves and soft mode information, as well as allowing the effectiveness of powder refinement of more complex materials to be assessed.

Finally, I present further applications with technologically important materials – relaxor ferroelectrics and high temperature pnictide superconductors. The conclusions draw together the different strands of the work, discussing the importance of these new advances together with future developments and scientific applications.

Declaration

This dissertation is the result of my own work and includes nothing which is the outcome of work done in collaboration except where specifically indicated in the text.

This dissertation has not been submitted in whole or in part for a degree at this or any other institution.

The limit on length prescribed by the Department of Earth Sciences Degree Committee, University of Cambridge, is not exceeded by this dissertation.

Elizabeth Ruth Cope

21st May, 2010

Acknowledgements

I am indebted to my supervisors, Martin Dove in Cambridge and Stephen Bennington at ISIS, who have provided invaluable support, encouragement and direction. I would like to thank Julian Gale for letting me use GULP as the cornerstone to my work, and for adding the force constant capabilities. From ISIS, I am grateful to Toby Perring for helpful discussions and use of TOBYFIT; to the instrument scientists on my experiments: Rob Bewley, Tatiana Guidi, Chris Frost and Chris Stock; to Russel Ewings for help and discussions on HORACE; and to Matt Tucker and Dave Keen for helpful discussions on PDFs. From Cambridge, I would like to thank Richard Bruin, Toby White, Andrew Walker, Mark Calleja and Ian Frame, for giving freely and generously of their time to help, particularly in the early years, with various levels of computing issues. I have also benefited from many helpful discussions and general encouragement from Andrew Goodwin, for which I am most grateful. The PDF work could not have been completed without Andrew Goodwin, Matt Tucker and Jade Hui providing experimental RMC data; and Erika Palin, Lars Peters, Matt Tucker, and Wenduo Zhou kindly testing the PDF code and documentation. It has been a pleasure to work with Frank Weber on the pnictide study and with Chris Stock on PMN. I am grateful to Masa Arai for allowing me to reproduce his INS data.

I have been supported financially by the Natural Environment Research Council (UK), who were also generous enough to provide me with two periods of funded maternity leave. The Science and Technology Facilities Council also provided funding as my CASE sponsor, for which I am grateful.

I cannot begin to express my gratitude to my friends and family for their emotional and practical support, allowing me to perform experiments and juggle deadlines around my two small children. My parents, Mike & Helen Shand, my in-laws, David & Liz Cope, and the children's god-parents, Andrew & Catherine Shimmin and Tiffer & Amy Robinson have all been amazing, and are much loved by all of us. Finally, thanks must go to my wonderful and patient husband, Peter, and my children, Matty and Rachel. I could not have done this without their support.

For Matthew and Rachel

*This 'book' may not be suitable for bedtime,
but it is dedicated to you.*

Contents

| | | |
|----------|--|----------|
| 1 | Introduction and General Theory | 1 |
| 1.1 | General introduction | 1 |
| 1.1.1 | Using neutrons to probe dynamics | 1 |
| 1.1.2 | Interatomic models | 3 |
| 1.1.3 | Model validation and refinement | 4 |
| 1.2 | Lattice dynamics | 4 |
| 1.2.1 | Modes of vibration | 4 |
| 1.2.2 | The Bose-Einstein distribution | 6 |
| 1.2.3 | Interatomic forces and the dynamical matrix | 7 |
| 1.2.4 | Dispersion curves | 8 |
| 1.2.5 | Formalism for neutron spectroscopy | 9 |
| 1.2.6 | Thermal motion | 11 |
| 1.3 | Interatomic computational models | 12 |
| 1.3.1 | Computing resources | 13 |
| 1.4 | Neutron scattering | 14 |
| 1.4.1 | Experimental geometry | 14 |
| 1.4.2 | The scattering function | 15 |
| 1.4.3 | Coherent and incoherent spectroscopy | 16 |
| 1.4.4 | Inelastic neutron spectroscopy (INS) | 17 |
| 1.4.5 | Time of flight spectrometers at ISIS | 19 |
| 1.4.6 | MERLIN: the new spectrometer | 21 |
| 1.4.7 | Total scattering and pair distribution functions | 23 |
| 1.4.8 | Phonons-from-diffraction | 26 |
| 1.5 | Objectives of this thesis | 27 |

| | | |
|----------|--|-----------|
| 2 | Pair Distribution Functions: Theory, Implementation and Examples | 28 |
| 2.1 | Introduction | 28 |
| 2.2 | Theory | 29 |
| 2.3 | The GULP PDF module | 32 |
| 2.3.1 | Main purpose | 32 |
| 2.3.2 | Implementation | 32 |
| 2.3.3 | Input | 32 |
| 2.3.4 | Output | 33 |
| 2.4 | Agreement factors | 34 |
| 2.5 | Examples | 35 |
| 2.5.1 | MgO | 36 |
| 2.5.2 | Calcium/strontium titanates | 36 |
| 2.5.3 | Phonons-from-diffraction | 40 |
| 2.5.4 | α -Cristobalite (SiO_2): interatomic models and the PDF | 42 |
| 2.5.4.1 | Experiment and simulated PDFs | 43 |
| 2.5.4.2 | Energy cut-offs | 45 |
| 2.5.4.3 | Refinement using PDFs | 49 |
| 2.5.4.4 | Choice of model | 49 |
| 2.6 | Conclusions | 50 |
| 3 | Evaluation of domain models for β-cristobalite from the Pair Distribution Function | 52 |
| 3.1 | Introduction | 52 |
| 3.2 | Historical survey of models of disorder in β -cristobalite | 54 |
| 3.2.1 | Multi-site models | 54 |
| 3.2.2 | Domain models | 55 |
| 3.2.2.1 | The WL model | 56 |
| 3.2.2.2 | The HG model | 56 |
| 3.2.3 | The Rigid Unit Mode model | 56 |
| 3.2.4 | A new domain model: the HP model | 58 |
| 3.2.5 | Is there a way to reconcile the models? | 58 |
| 3.3 | Experiment | 60 |
| 3.4 | Simulation | 60 |
| 3.4.1 | Agreement factors | 61 |
| 3.5 | Results, discussion and conclusions | 61 |
| 3.5.1 | A benchmark from analysis of α -cristobalite | 61 |

| | | |
|----------|--|-----------|
| 3.5.2 | Evaluation of domain models for β -cristobalite | 61 |
| 3.5.3 | Discussion and conclusions | 63 |
| 4 | New Methodologies for Inelastic Neutron Scattering | 66 |
| 4.1 | Introduction | 66 |
| 4.2 | Existing software and file-types | 69 |
| 4.3 | The new GULP SQW module | 71 |
| 4.3.1 | Main purpose | 71 |
| 4.3.2 | Implementation | 72 |
| 4.3.2.1 | Background: multi-phonon and multiple scattering | 74 |
| 4.3.2.2 | Density of states | 76 |
| 4.3.3 | Input | 77 |
| 4.3.4 | Output | 77 |
| 4.4 | TOBYFIT: new developments | 78 |
| 4.4.1 | Main purpose | 78 |
| 4.4.2 | Implementation and program design | 79 |
| 4.4.2.1 | Programming details | 81 |
| 4.4.3 | Input | 82 |
| 4.4.4 | Output | 82 |
| 4.5 | Aluminium | 83 |
| 4.5.1 | Experiment | 83 |
| 4.5.2 | Models | 83 |
| 4.5.2.1 | General TOBYFIT setup | 83 |
| 4.5.2.2 | Force constant (FC) model | 85 |
| 4.5.2.3 | Lennard-Jones (LJ) potential model | 85 |
| 4.5.2.4 | Comparison to experiment | 87 |
| 4.6 | Conclusions | 87 |
| 5 | α-Cristobalite and v-SiO₂: a powder INS study of the Bose peak and related phonon modes | 90 |
| 5.1 | Introduction | 90 |
| 5.2 | Model structures, pair distribution functions, and specific heat calculations | 94 |
| 5.3 | Experiment | 98 |
| 5.4 | Simulations | 98 |
| 5.5 | Results and discussion: $E_i = 35$ meV data | 102 |
| 5.6 | Dispersion curves | 104 |
| 5.7 | Results and discussion: higher energy features | 106 |

| | | |
|----------|--|------------|
| 5.8 | Contributions from selected atoms | 109 |
| 5.9 | Conclusions | 111 |
| 6 | Calcite: a powder and single crystal INS study | 113 |
| 6.1 | Introduction | 113 |
| 6.2 | The interatomic models | 116 |
| 6.2.1 | The Archer potential model | 116 |
| 6.2.2 | Developing the force constant (FC) model | 116 |
| 6.3 | Powder INS experiments, simulations and refinements | 119 |
| 6.3.1 | Experiment | 119 |
| 6.3.2 | Powder simulations and refinement | 119 |
| 6.3.3 | INS results and discussion | 120 |
| 6.3.4 | Comparison with experimental phonon properties | 125 |
| 6.3.5 | Conclusions | 126 |
| 6.4 | Single crystal | 127 |
| 6.4.1 | Experiment | 128 |
| 6.4.2 | Simulations | 128 |
| 6.4.3 | Results and discussion | 129 |
| 6.4.3.1 | INS spectra | 129 |
| 6.4.3.2 | Dispersion curves | 133 |
| 6.4.4 | Conclusions | 139 |
| 7 | Further Applications | 140 |
| 7.1 | PMN: a single crystal INS study | 140 |
| 7.1.1 | Introduction | 140 |
| 7.1.2 | Experiment | 142 |
| 7.1.3 | Simulations | 142 |
| 7.1.4 | Results | 143 |
| 7.1.4.1 | PDF simulations | 143 |
| 7.1.4.2 | INS simulations | 145 |
| 7.1.5 | Conclusions | 147 |
| 7.2 | Ba _{1-x} K _x Fe ₂ As ₂ : powder simulations and refinement | 147 |
| 7.2.1 | Experiment | 149 |
| 7.2.2 | Simulations and refinement | 149 |
| 7.2.3 | Preliminary results | 150 |
| 7.2.4 | Conclusions | 152 |

| | | |
|----------|---|------------|
| 8 | Summary and Conclusions | 153 |
| A | Additional Details for the new GULP SQW Module | 158 |
| A.1 | Neutron scattering lengths | 158 |
| A.2 | Energy binning | 159 |
| A.3 | Q binning | 159 |
| A.4 | Setting the Q binning for single crystals in the <code>neutron</code> block | 160 |
| A.5 | Additional powder options set in the <code>neutron</code> block | 161 |
| A.6 | Output | 161 |
| A.6.1 | <code>.sqw</code> files | 161 |
| A.6.2 | <code>.sqwt</code> files | 162 |
| A.6.3 | <code>.bose</code> files | 162 |
| A.6.4 | <code>.dos</code> files | 164 |
| B | Using TOBYFIT with the new GULP SQW Module | 166 |
| B.1 | The <code>run</code> menu | 166 |
| B.2 | Cross section models | 167 |
| B.2.1 | ‘External parameters’ $P1-5$ | 168 |
| B.2.2 | Potential parameters | 168 |
| B.2.3 | Single crystals cross section models | 168 |
| B.2.4 | Powder cross section models | 169 |
| B.3 | Integration Methods | 170 |
| B.4 | Background Models | 170 |
| B.5 | Fitting in TOBYFIT: MULTIFRILLS | 170 |
| B.6 | GULP input files for use with TOBYFIT | 172 |
| B.6.1 | The <code>gulpinput.gin</code> file | 172 |
| B.6.2 | The <code>parameter.gin</code> file | 173 |
| C | Additional Scripts | 175 |
| C.1 | MATLAB functions for tidying <code>.spe</code> files prior to a fit | 175 |
| C.2 | Perl scripts for the manual parallelisation of SQW simulations | 177 |
| | References | 192 |

List of Figures

| | | |
|------|---|----|
| 1.1 | Dispersion curves for aluminium | 9 |
| 1.2 | Experimental scattering geometry | 15 |
| 1.3 | An engineering diagram of MERLIN | 20 |
| 1.4 | The accessible region of \mathbf{Q}, ω space for time of flight spectroscopy | 20 |
| 1.5 | $\rho^{\text{PDF}}(r)$ and weighted partials of SrTiO ₃ | 24 |
| | | |
| 2.1 | Fourier ripples and the RMC dataset for α -cristobalite | 35 |
| 2.2 | $D(r)$ for MgO | 37 |
| 2.3 | $D(r)$ SrTiO ₃ | 37 |
| 2.4 | Unit cells for calcium/strontium titanates | 38 |
| 2.5 | $T(r)$ of Ca _{<i>x</i>} Sr _{1-<i>x</i>} TiO ₃ at $x = 0.5$ | 39 |
| 2.6 | Role of energy cut-offs in $D(r)$ of MgO | 41 |
| 2.7 | Role of energy cut-offs in PDF peak widths of MgO | 41 |
| 2.8 | Role of energy cut-offs in PDF peak widths of SrTiO ₃ | 42 |
| 2.9 | The unit cell of α -cristobalite | 43 |
| 2.10 | α -Cristobalite PDFs | 44 |
| 2.11 | α -Cristobalite density of states | 46 |
| 2.12 | The effect of cut-offs on α -cristobalite PDFs | 47 |
| 2.13 | The effect of cut-offs on selected α -cristobalite PDF peak widths | 48 |
| | | |
| 3.1 | Crystal structural refinement of β -cristobalite with a single-site model | 53 |
| 3.2 | Crystal structural refinement of β -cristobalite with a six-site model | 55 |
| 3.3 | Crystal structures of β -cristobalite models | 57 |
| 3.4 | Experimental and RMC $D(r)$ of β -cristobalite including partial $d'(r)$ | 59 |
| 3.5 | $D(r)$ of α - and β -cristobalite | 62 |
| | | |
| 4.1 | TOBYFIT and GULP: the fitting cycle | 79 |
| 4.2 | Experiment and simulated INS spectra for aluminium | 84 |

| | |
|--|-----|
| 4.3 Cuts through aluminium data and simulations | 86 |
| 5.1 ‘Fast sound’ INS spectra in v -SiO ₂ | 93 |
| 5.2 Silica model structures | 95 |
| 5.3 The PDF of v -SiO ₂ and α -cristobalite | 96 |
| 5.4 Specific heat for v -SiO ₂ and α -cristobalite | 97 |
| 5.5 Simulations and experimental INS spectra | 99 |
| 5.6 One phonon scattering functions simulations | 100 |
| 5.7 Cuts at constant Q and ω | 103 |
| 5.8 Dispersion curves calculated from the Sanders model for α -cristobalite | 105 |
| 5.9 One-phonon spectra weighted by ω/Q in the first Brillouin zone | 105 |
| 5.10 Higher energy simulated spectra with experimental resolution, weighted by ω/Q | 107 |
| 5.11 Higher energy modes in the simulations | 108 |
| 5.12 Scattering from selected atoms | 110 |
| 6.1 The calcite unit cell | 114 |
| 6.2 Force constant interactions in calcite | 117 |
| 6.3 Calcite powder data at $E_i = 15$ and 45 meV | 121 |
| 6.4 Constant- Q cuts through $E_i = 15$ and 45 meV for calcite powder | 122 |
| 6.5 One-phonon model simulations of calcite powder scattering | 122 |
| 6.6 Calcite powder data at $E_i = 250$ meV | 123 |
| 6.7 Constant- Q cut through $E_i = 250$ meV powder calcite data | 123 |
| 6.8 Experimental sweep for 45 meV single crystals of calcite | 128 |
| 6.9 Calcite data along the \mathbf{c}^* axis at $h = k = 0$ and $h = 1, k = 0$ | 130 |
| 6.10 Calcite data along the \mathbf{a}^* axis at $k = 0, l = -10$ and $k = 0, l = -12$ | 131 |
| 6.11 Calcite data towards F at $\mathbf{v} = -3$ and $\mathbf{v} = 0$ | 132 |
| 6.12 Single crystal slices showing dispersion curves along \mathbf{c}^* | 134 |
| 6.13 Single crystal slice showing dispersion curves along \mathbf{a}^* | 135 |
| 6.14 Single crystal slice showing dispersion curves towards F | 135 |
| 6.15 Experimental and Archer model dispersion curves for calcite | 137 |
| 6.16 Experimental and FC model dispersion curves for calcite | 138 |
| 7.1 Polyhedral model of ideal PMN, and experimental sweep | 141 |
| 7.2 Comparison of PDFs from experiment and models | 144 |
| 7.3 Partial PDFs of PMN | 144 |
| 7.4 INS single crystal slices from experiment and models | 146 |
| 7.5 Phonon modes at higher energies for PMN | 147 |

| | | |
|-----|--|-----|
| 7.6 | Structure of $\text{Ba}_{1-x}\text{K}_x\text{Fe}_2\text{As}_2$ | 148 |
| 7.7 | Experimental and simulated INS spectra | 150 |
| 7.8 | One phonon INS simulations | 152 |

Chapter 1

Introduction and General Theory

The importance of the dynamic properties of materials is introduced, together with the general formalism of lattice dynamics and the computational approaches used to calculate the atomic vibrations from interatomic models. Neutron scattering provides an excellent experimental probe of atomic vibrations, so a formalism and description of experimental technique is presented. In the light of this, the aims of the current work can be given.

1.1 General introduction

1.1.1 Using neutrons to probe dynamics

Understanding the properties of many mineralogical systems as well as complex new classes of technologically important materials makes it necessary to consider more than just atomic arrangements. The study of atomic scale motion (quantised as *phonon modes*) is essential to predict which phases will be stable and where the transitions occur, as well as explaining phenomena such as thermal expansion and thermal conductivity. Therefore, this thesis combines computer modelling of atomic displacements with experimental neutron scattering techniques to probe local structure and dynamics for a wide range of materials.

The study of dynamics through inelastic scattering techniques is referred to as *spectroscopy*. Most familiar are the Raman and IR light scattering techniques, which are widely available, highly sensitive, cheap to use, and give accurate finger-prints of vibrational modes. However, they are limited to studying vibrations at a specific point in reciprocal space – the Brillouin zone centre – and have restrictive selection rules as to which modes are ‘active’ or visible. Spectroscopy using beams of x-rays or neutrons allows the study of modes across the entire Brillouin zone. But these are no longer lab-based techniques. Inelastic X-ray or Neutron Spectroscopy (IXS or INS), requires the greater flux and specialist machines of a centralised facility such as the European Synchrotron Radiation Facility (ESRF) providing IXS in France (URL - A), or the

ISIS neutron spallation source in Oxfordshire (URL - B). The two techniques are complementary due to the different scattering mechanisms: X-rays are scattered by the atom's electron cloud whereas neutrons are scattered by the atomic nuclei. Ongoing development of more sophisticated spectrometers continues to push the experimental boundaries: it is the development of new neutron spectrometers at ISIS that has provided the impetus for the work contained in this thesis.

Neutrons are highly suited to studying atomic scale structure and dynamics for four main reasons: thermal neutrons have a de Broglie wavelength that is comparable to interatomic distances and an energy that is comparable to phonon modes; they interact strongly with atomic nuclei via short range nuclear forces so there is no systematic dependence on scattering amplitude across the periodic table; neutron scattering only weakly perturbs the scattering system, preventing complications due to surfaces, charges or core electron states; and neutrons are highly penetrating, allowing the non-destructive investigation of the bulk of materials. Moreover, neutron scattering intensities provide crucial information (and can be measured in absolute units, unlike standard IR and Raman spectroscopy), allowing detailed comparisons to be made between theory (computer simulations) and experimental results. As neutrons have a magnetic moment they also interact with unpaired electrons in magnetic atoms via electromagnetic dipole-dipole interactions making them an ideal probe of magnetic properties.

My work has focused on using and developing interatomic models and computer simulations to aid interpretation of the conventional inelastic neutron spectroscopy (INS) approach to the study of dynamics, and also looking at the dynamical information contained in neutron total scattering data. Of the two, total scattering experiments are relatively inexpensive, time efficient and versatile. As with standard laboratory diffraction techniques, a beam of particles – in this case neutrons – are diffracted by the sample giving information on the long range average structure (Bragg scattering). Total scattering also takes account of the diffuse component, which arises due to instantaneous fluctuations in the atomic density giving information on localised disorder. Total scattering data can be analysed through the Pair Distribution Function (PDF), obtained by Fourier transform. The PDF shows the local and mid-range structure and demonstrates the effect of atomic scale motion. I have developed new analytical tools based on the simulation of the PDF using phonon information from an interatomic model, which are powerfully used to resolve the on-going controversy over the dynamically disordered β -cristobalite structure. This technique also allows 'computational experiments' with the structure, for example, visualising the effects of different cation ordering schemes.

Recent developments have allowed dynamical information to be successfully extracted from the total scattering data (Goodwin *et al.*, 2005, 2006) giving 'phonons-from-diffraction' using the

information embodied in the Pair Distribution Function (PDF). However, the more conventional approach to the study of phonons is through inelastic spectroscopy. As in diffraction experiments (which conventionally focus on the elastic scattering), the change in direction of the particle beam arises from the position of atoms within the sample. The main emphasis of inelastic experiments is the study of the change in energy, which gives information concerning the atomic motion.

Historically, triple axis spectrometers (TAS) at reactor sources have dominated INS, allowing point-by-point exploration of reciprocal space (\mathbf{Q} -space). Spallation sources will soon exceed the effective flux of reactor sources, and permit spatially simultaneous data collection, so there is currently great interest in new time-of-flight direct geometry spectrometers such as those being developed at ISIS, providing the incentive for the new analytical tools developed for this thesis.

INS with time-of-flight spectrometers is nothing new, but the recent (2008) commissioning of MERLIN (Bewley, 2002; Bewley *et al.*, 2009; Dove *et al.*, 2002a), together with the current installation¹ and development of LET (URL - C), mark the start of a new paradigm. These machines have rapid data collection rates (over an order of magnitude faster than pre-existing spectrometers), simultaneous data collection over large solid angles, highly pixelated position-sensitive detectors (crucial for accurate single crystal work), and the capability to use advanced sample environments such as pressure cells, cryostats, and large magnets. This exceeds previous possibilities for powder work and is making single crystal work sufficiently rapid, over a suitable range of environments, to become routine. By revealing phonons from many Brillouin zones simultaneously, it is now possible to ‘see the unexpected’, rather than just looking for features theoretically predicted. The wealth of phonon information contained in these results needs new analytical tools such as the suite of software I have developed.

1.1.2 Interatomic models

Science today is no longer clearly divided into ‘theory’ and ‘experiment’, but often exists in the cross-over between the two disciplines. Computer modelling has enabled mathematically complex theories to be implemented to aid the design and interpretation of experimental data, feeding back into more accurate theoretical models.

In seeking to understand atomic vibrations, it is helpful to build interatomic models to study the different interactions within a sample. Phenomenologically, this can most simply be visualised as springs linking the different atoms, with different spring constants for different species and between nearest- and next-nearest-neighbours. This is the basis for force constant models.

¹At the time of submission, LET has only a limited range of detector banks installed, but has recently seen its first neutrons.

The actual interactions are carefully balanced interatomic potential energies, for which many models have been developed (see standard texts such as Dove, 1993). These are related to the phenomenological force constants by taking the first derivative.

Using standard lattice dynamical calculations it is possible to extract dynamical information about the exact nature of each atomic vibration from these interatomic models. This thesis demonstrates how I am able to use this to simulate experimental data and track phonon contributions, explaining the origins of key features seen through neutron total scattering and INS. This ranges from PDF analysis, using the phonon model to give information on the spread of interatomic distances to help elucidate local structure and dynamics, through powder and single crystal INS simulations tracking contributions of specific modes. With the addition of experimental resolution functions, the INS simulations can be directly compared to experiment.

1.1.3 Model validation and refinement

The key challenge in this field today is the development of accurate interatomic models. I am now able to provide comparison of simulations with powder INS spectra to validate of a model. The full single crystal INS spectrum provides a highly rigorous test as this encapsulates all the dynamical information. What is also needed is a means of refining the underlying model against experimental results, making full use of the vast array of detectors on the new generation of spectrometers. Powder samples are often readily available; indeed there are materials for which there are no suitable single crystals. Powder diffraction is now routinely used for structural refinement, so I pose the question, ‘How far can powder INS be used for refinement of interatomic models?’.

1.2 Lattice dynamics

In order to understand the relationship between neutron scattering and atomic scale motion, a formal description of the classical mechanics is required. The Newtonian physics that govern this movement is well described in a number of texts (e.g. Willis & Pryor, 1975), so this introduction will simply give an overview, showing the key equations with particular emphasis on those needed for spectroscopy and encoded in the new analysis software.

1.2.1 Modes of vibration

Atoms within a solid are constantly in motion. These vibrations are travelling waves comprised of correlated displacements of atoms from their equilibrium positions. Each mode is described

by an angular frequency ω and wavevector \mathbf{k} , giving both the direction and periodicity of the displacements.

Crystalline structures can be reduced to a basic *unit cell* which contains the set of atoms that allows the entire crystal to be reproduced by symmetry. In this work, I define the position of the j th atom in the l th unit cell to have average position \mathbf{r}_{jl} with respect to a given origin such that:

$$\mathbf{r}_{jl} = \mathbf{R}_j + \mathbf{l} \quad (1.1)$$

where \mathbf{R}_j is the position of atom j within the cell and \mathbf{l} is the position of the cell from the given origin.

Each of the Z atoms in every unit cell posses three degrees of freedom, giving $3Z$ independent modes ν at each wavevector (with index k). Within Born-von-Kármán theory (stipulating periodic boundary conditions), the displacement of a single atom can be seen as the sum of each component vibrational mode ν :

$$\mathbf{u}_{jl}(t) = \sum_{\mathbf{k}, \nu} \mathbf{A}_j(\mathbf{k}, \nu) \exp(i[\mathbf{k} \cdot \mathbf{r}_{jl} - \omega_j(\mathbf{k}, \nu)t]) \quad (1.2)$$

where \mathbf{k} is the wave vector of the travelling wave ν ($\mathbf{k} = 2\pi/\lambda$), and $\omega_j(\mathbf{k}, \nu)$ is the angular frequency as a function of \mathbf{k} . The amplitude vector, $\mathbf{A}_j(\mathbf{k}, \nu)$, is proportional to the mass weighted *polarisation vector*, $\mathbf{e}_j(\mathbf{k}, \nu)$:

$$\mathbf{A}_j(\mathbf{k}, \nu) = \frac{A(\mathbf{k}, \nu)}{\sqrt{Nm_j}} \mathbf{e}_j(\mathbf{k}, \nu) \quad (1.3)$$

with N as the number of unit cells, m_j the atomic mass of atom j . The normalised mode amplitude $A(\mathbf{k}, \nu)$ is now independent of atom type. The polarisation vectors are orthonormal to each other, and each gives the direction of atomic motion for the particular atom in the cell. Thus knowledge of the atomic positions, mode frequency and polarisation vector gives the crucial information on atomic motion.

It is common practice to express the displacement in terms of the *normal mode coordinate*¹, $Q(\mathbf{k}, \nu, t)$, which subsumes both the amplitude and time-dependence through:

$$Q(\mathbf{k}, \nu, t) = A(\mathbf{k}, \nu) \exp[-i\omega_j(\mathbf{k}, \nu)t] \quad (1.4)$$

¹The notation for the normal mode coordinate, $Q(\mathbf{k}, \nu, t)$, should not be confused with \mathbf{Q} , which I will use to denote the momentum transfer for a single crystal, or Q ($= |\mathbf{Q}|$) for a powdered sample.

to give the *normal mode equation*:

$$\mathbf{u}_{jl} = \frac{1}{\sqrt{Nm_j}} \sum_{\mathbf{k}, \nu} \mathbf{e}_j(\mathbf{k}, \nu) \exp(i\mathbf{k} \cdot \mathbf{r}_{jl}) Q(\mathbf{k}, \nu, t) \quad (1.5)$$

This is the key equation for describing atomic motion, and the basis for interpreting the dynamical information contained in neutron scattering data.

Before making use of the equations governing these normal modes, it should be noted that the literature is inconsistent in the phasing of the polarisation, often without explicit definitions. There are two commonly used settings depending on whether the atomic position in the unit cell is included in the equations as a separate phase factor, or included in the eigenvector. The first, written as \mathbf{e} , is that introduced above and found in standard texts such as Willis & Pryor (1975) and Dove (1993). Lovesey (1984) uses the alternative setting, expressing it as σ , but I use \mathbf{e}^{sig} here to avoid confusion with PDF peak widths. The default setting¹ in the lattice dynamical software used in this thesis is also \mathbf{e}^{sig} .

In the alternative setting the displacement is expressed in terms of the average position of the cell, \mathbf{l} , not the average absolute position of the atom, \mathbf{r}_{jl} , as in Eqn. 1.5, giving:

$$\mathbf{u}_{jl} = \frac{1}{\sqrt{Nm_j}} \sum_{\mathbf{k}, \nu} \mathbf{e}^{\text{sig}}_j(\nu, \mathbf{k}) \exp(i\mathbf{k} \cdot \mathbf{l}) Q(\mathbf{k}, \nu, t) \quad (1.6)$$

This is because the position of the atom within the cell is here subsumed into the polarisation vector. The settings are related by this phase factor:

$$\mathbf{e}^{\text{sig}}_j(\mathbf{k}, \nu) = \mathbf{e}_j(\mathbf{k}, \nu) \cdot \exp[i\mathbf{k} \cdot \mathbf{R}_j] \quad (1.7)$$

1.2.2 Population of normal modes: the Bose-Einstein distribution

The quantisation of normal modes into *phonons* arises from a quantum dynamical exploration analogous to the quantisation of light into *photons*. This is described in detail in many solid-state texts (e.g. Lovesey, 1984), but can be combined with the classical results already introduced here. Importantly, the energy of each normal mode is limited to:

$$E(\mathbf{k}, \nu) = \left(n(\omega) + \frac{1}{2}\right) \hbar\omega_j(\mathbf{k}, \nu) \quad (1.8)$$

¹I convert to \mathbf{e} for the inelastic neutron scattering (SQW) code where the phasing is crucial. The phasing cancels out in calculations of the PDF (see Chapter 2) so the eigenvectors remain in the \mathbf{e}^{sig} format to optimise the code.

Each n relates to a single phonon mode. Averaging over time, the *occupation of states*, $n(\omega)$, is a temperature dependent property given by the Bose-Einstein distribution:

$$n(\omega) = \left(\exp \left[\frac{\hbar\omega_j(\mathbf{k}, \nu)}{k_B T} \right] - 1 \right)^{-1} \quad (1.9)$$

where $k_B T > \hbar\omega$, this reduces to $n(\omega) \approx k_B T (\hbar\omega_j(\mathbf{k}, \nu))^{-1}$. For many situations it is possible to work within the ‘high temperature approximation’ where these equations yield the same result for the time averaged energy of each mode as the classical equipartition result: the average energy of each degree of motion is $E = k_B T$.

1.2.3 Interatomic forces and the dynamical matrix

Within a crystal, the behaviour of each atom is dependent upon those surrounding it. This is most simply visualised by forces acting between atoms as if they were connected by springs. There is a linear relationship between force and displacement, with the force on atom j due to atom j' described through Newton’s equation of motion for atom j , with mass m_j , summing over all atoms including $j = j'$:

$$m_j \ddot{\mathbf{u}}_{jl}(t) = \sum_{j'l'} \Phi \begin{pmatrix} j & j' \\ l & l' \end{pmatrix} \mathbf{u}_{j'l'}(t) \quad (1.10)$$

Φ is the *force-constant matrix*, or *self-matrix*. A force constant model is an interatomic model describing this set of interactions (or just the longitudinal and transverse components) which can be used in the calculation of dynamic properties. However, such a model is purely phenomenological, giving no explanation of the physical origin of the interaction.

Explaining the underlying physics requires a description of the interatomic potential energy. There are many different models, and the appropriate potential model for each group of atoms is used depending on the type of material, structure, bonding and atomic species.

Φ is derived from the potential energy, V , between pairs of axes α and α' , where $\alpha = 1, 2, 3$:

$$\Phi \begin{pmatrix} j & j' \\ l & l' \end{pmatrix} = \left(\frac{d^2 V}{du_{\alpha,jl} du_{\alpha',j'l'}} \right) \quad (1.11)$$

which yields the full equation:

$$m_j \omega_j^2(\mathbf{k}, \nu) \hat{\mathbf{u}}_j(\mathbf{k}, \nu) = \sum_{j'l'} \Phi \begin{pmatrix} j & j' \\ 0 & l' \end{pmatrix} \cdot \hat{\mathbf{u}}_{j'l'}(\mathbf{k}, \nu) \exp[i\mathbf{k} \cdot (\mathbf{r}_{j'l'} - \mathbf{r}_{j0})] \quad (1.12)$$

By expressing the displacements of each atom j along each of the Cartesian axes and collecting the relevant terms, a $3Z$ mass weighted column vector is obtained for each mode and

wavenumber which is the *polarisation vector* of Eqn. 1.3:

$$\mathbf{e}(\mathbf{k}, \nu) = \begin{pmatrix} \sqrt{m_1} \hat{u}_{x,1}(\mathbf{k}, \nu) \\ \sqrt{m_1} \hat{u}_{y,1}(\mathbf{k}, \nu) \\ \sqrt{m_1} \hat{u}_{z,1}(\mathbf{k}, \nu) \\ \sqrt{m_2} \hat{u}_{x,2}(\mathbf{k}, \nu) \\ \cdot \\ \cdot \\ \cdot \\ \sqrt{m_Z} \hat{u}_{z,Z}(\mathbf{k}, \nu) \end{pmatrix} \quad (1.13)$$

Expressing Eqn. 1.12 in this form gives the matrix equation that introduces $\mathbf{D}(\mathbf{k})$, the $3Z \times 3Z$ Hermitian *dynamical matrix*:

$$\omega^2(\mathbf{k}, \nu) \mathbf{e}(\mathbf{k}, \nu) = \mathbf{D}(\mathbf{k}) \cdot \mathbf{e}(\mathbf{k}, \nu) \quad (1.14)$$

defining the dynamical matrix as:

$$\mathbf{D}_{\alpha j, \alpha' j'}(\mathbf{k}) = \frac{1}{\sqrt{m_j m_{j'}}} \sum_{\nu} \Phi_{\alpha \alpha'} \begin{pmatrix} j & j' \\ 0 & l' \end{pmatrix} \exp[i\mathbf{k} \cdot (\mathbf{r}_{j\nu} - \mathbf{r}_{j'0})] \quad (1.15)$$

This equation has $3Z$ solutions yielding the dynamical information about each of the $3Z$ normal modes through the diagonalisation of the dynamical matrix. The eigenvalues are the squares of the frequencies, and the eigenvectors give the (possibly complex¹) orthogonal polarisation vectors. As it is a Hermitian matrix, the eigenvalues are always real. The frequencies can be negative, which implies instability.

Thus it has been shown that any model that can describe the interatomic forces (either directly or as the derivatives of a potential model) can be used to construct a dynamical matrix for any wavevector. This, in turn, gives the key dynamical information for each individual phonon mode in the form of the frequency and polarisation vector (eigenvector). This is the crucial information that we seek to extract from neutron scattering experiments.

1.2.4 Dispersion curves

Given that a crystal with Z atoms in the unit cell and periodic boundary conditions will have $3Z$ phonon modes for each \mathbf{k} -point, it is helpful to be able to describe the different modes in more detail. The three lowest energy modes are known as *acoustic modes*, so called because dispersion starts with the characteristic $\omega = c \mathbf{k}$ relationship seen in sound waves. These tend to zero at Γ (located at the Brillouin zone centre). At this point they represent pure translations of the crystal. Where there are more than two atoms in the unit cell, *optic modes* are also present,

¹Complex eigenvectors allow the relative phasing of displacements to be represented.

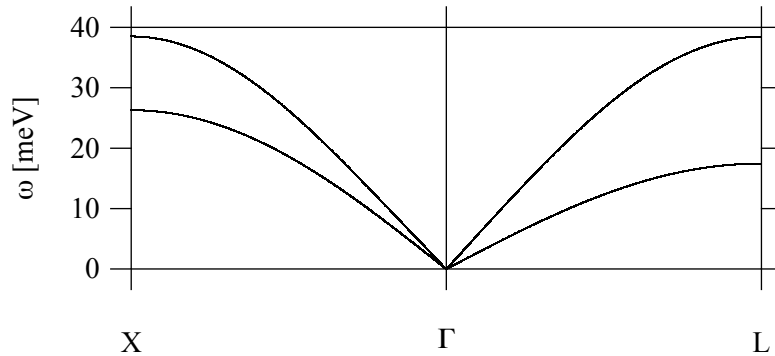


Figure 1.1: Dispersion curves for aluminium, calculated in GULP from the Lennard-Jones model produced in Section 4.5.2.3, between $X = [0.5 \ 0 \ 0.5]$, $\Gamma = [0 \ 0 \ 0]$, and $L = [0.5 \ 0.5 \ 0.5]$.

so called because in ionic crystals the long wavelength modes can interact with electromagnetic radiation, giving rise to characteristic optical properties. These modes always have a non-zero minimum frequency of vibration.

A plot of frequency of these vibrational modes along \mathbf{k} is known as the *phonon dispersion curve* and has the periodicity of the reciprocal lattice. These are usually produced along the high symmetry directions, allowing phonon behaviour of a crystal to be summarised in one diagram. This is the information that has traditionally been extracted from IXS and INS experiments, although it ignores the effects of the eigenvectors and the different intensities in different Brillouin zones.

Branches in the phonon dispersion curves are characterised as either longitudinal or transverse, depending on the direction of the polarisation vector with regard to the direction of propagation, \mathbf{k} . The *longitudinal branches* are polarised parallel to \mathbf{k} at the zone centre. *Transverse branches* are polarised perpendicular to the direction of propagation. Fig. 1.1 shows the dispersion curves for the simple aluminium $Fm\bar{3}m$ structure between $X = [0.5 \ 0 \ 0.5]$, $\Gamma = [0 \ 0 \ 0]$, and $L = [0.5 \ 0.5 \ 0.5]$ derived from the empirical potential model used in Chapter 4.

1.2.5 Formalism for neutron spectroscopy: defining the scattering conditions

Neutron scattering provides a direct probe of lattice dynamics through the interaction of a beam of neutrons with the atomic nuclei. Experimentally, the incoming neutron beam is characterised by having an incident energy E and wave-vector \mathbf{k} . It will be scattered by the sample, whereupon it has a final energy E' and wave-vector \mathbf{k}' .

Neutron scattering is expressed in terms of the change in momentum, \mathbf{Q} , known as the *scattering vector*:

$$\mathbf{Q} = \mathbf{k} - \mathbf{k}' \quad (1.16)$$

and energy transfer:

$$\hbar\omega_j(\mathbf{k}, \nu) = E - E' \quad (1.17)$$

Neutrons are scattered by the sample in two distinct processes: elastic scattering (diffraction), where there is no change in the energy of the neutron beam, and inelastic scattering, where the beam interacts with the system in two ways:

- phonon creation (neutron energy loss): change is described as positive,
- phonon annihilation (neutron energy gain): change is described as negative.

The energy of thermal neutrons, such as those used in neutron scattering experiments, is comparable to that of atomic vibrations, and so we can observe appreciable changes in the neutron energy following an inelastic scattering event.

The law for the *conservation of energy*, showing that the energy is conserved regardless of whether a phonon is created (+) or destroyed (-), and holding for both coherent and incoherent scattering, can be expressed using the de Broglie wavelength for the neutrons:

$$\lambda = \frac{\hbar}{m_j \nu} \quad (1.18)$$

as:

$$\hbar\omega_j(\mathbf{k}, \nu) = \frac{1}{2}m_j v^2 - \frac{1}{2}m_j v'^2 = \frac{\hbar^2}{2m_j} (k^2 - k'^2) \quad (1.19)$$

The other condition for inelastic neutron scattering is the *conservation of crystal momentum*. This is defined in terms of the reciprocal scattering vector, \mathbf{Q} , which is related to the change in the wavevector due to the scattering event as described in Eqn. 1.16.

Conservation of crystal momentum holds for coherent scattering, and means that the one-phonon intensity is only permitted when the *scattering vector* is:

$$\mathbf{Q} = \mathbf{H} + \mathbf{k} \quad (1.20)$$

defining reciprocal lattice vector, \mathbf{H} :

$$\mathbf{H} \equiv h_1 \mathbf{b}_1 + h_2 \mathbf{b}_2 + h_3 \mathbf{b}_3 \quad (1.21)$$

and \mathbf{k} as the wave vector of the lattice mode of vibration.

While defining the scattering vector, it is helpful to introduce the convention which I adopt throughout this thesis of using \mathbf{Q} in the context of the scattering function (defined below) for single crystal experiments, where each \mathbf{Q} is well defined, and Q ($= |\mathbf{Q}|$) for use with powder experiments¹, where the orientational average makes the component \mathbf{Q} vectors inaccessible.

1.2.6 Thermal motion

Before considering the details of neutron scattering, it is important to understand the displacement of atoms due to thermal effects, so the matrix equations used in the implementation of the neutron scattering code are given here in full.

The most useful measure of thermal motion is the *mean square displacement*, which in a full model must be assumed to be anisotropic. It is found from the time averaged vector dot product (normally expressed with angle brackets) of momentum transfer and instantaneous displacement. Using matrix notation, this is:

$$\langle (\mathbf{Q} \cdot \mathbf{u})^2 \rangle = \mathbf{Q}^T \langle \mathbf{u}\mathbf{u}^T \rangle \mathbf{Q} \quad (1.22)$$

The matrix $\langle \mathbf{u}\mathbf{u}^T \rangle$ is known as the *mean square displacement matrix*, \mathbf{B} . There is such a matrix for every atom j (j subscripts are assumed to improve clarity):

$$\mathbf{B} = \langle \mathbf{u}\mathbf{u}^T \rangle = \begin{pmatrix} \langle u_1^2 \rangle & \langle u_1 u_2 \rangle & \langle u_1 u_3 \rangle \\ \langle u_1 u_2 \rangle & \langle u_2^2 \rangle & \langle u_2 u_3 \rangle \\ \langle u_1 u_3 \rangle & \langle u_2 u_3 \rangle & \langle u_3^2 \rangle \end{pmatrix} \quad (1.23)$$

As the phases of the modes are independent, when substituting \mathbf{u}_j from Eqn. 1.2, the cross terms in the average cancel, giving:

$$\mathbf{B}_j = \frac{\hbar}{Nm_j} \sum_{\nu \mathbf{k}} \frac{1}{\omega_j(\mathbf{k}, \nu)} \left(\frac{1}{2} + (\exp\left(\frac{\hbar\omega_j(\mathbf{k}, \nu)}{k_B T}\right) - 1)^{-1} \right) \times [\mathbf{e}_j(\mathbf{k}, \nu)(\mathbf{e}_j^*(\mathbf{k}, \nu))^T] \quad (1.24)$$

This mean squared displacement matrix can be calculated for each atom in the unit cell, allowing the accurate calculation of the harmonic *atomic temperature factor* for use in the *phonon structure factor* introduced below. The atomic temperature factor can be expressed, for any atom j , as:

$$\begin{aligned} T_j(\mathbf{Q}) &= \exp(-W_j) \\ &= \exp\left(-\frac{1}{2} \langle (\mathbf{Q} \cdot \mathbf{u}_j)^2 \rangle\right) \\ T_j(\mathbf{Q}) &= \exp\left(-\frac{1}{2} \mathbf{Q}^T \mathbf{B}_j \mathbf{Q}\right) \end{aligned} \quad (1.25)$$

¹This should not be confused with the normal mode coordinate, $Q(\mathbf{k}, \nu, t)$.

Thus the full anisotropic *temperature factor* can be extracted from a lattice dynamical model and used in the calculation of the neutron scattering intensity.

1.3 Interatomic computational models

The lattice dynamical formalism introduced in this chapter enables atomic models to be used to produce phonon information, namely the full set of dispersion curves together with the eigenvectors of each vibration. Such calculations are computationally demanding, involving the diagonalisation of many dynamical matrixes. There exist a number of academic software tools designed to perform these calculations: I make use of GULP, the General Utility Lattice Program (Gale & Rohl, 2003)¹.

The new analysis techniques I have developed are based on new modules for this code, taking full advantage of the power of GULP to produce phonon information from an interatomic model with the calculations optimised according to crystal symmetry. Conventionally, the energy is calculated from a Coulomb matrix (refineable atomic charges) and a set of potential models: the dynamical matrix is found through (local) energy minimisation with the hessian calculated at the stationary points.

To assist with the current work, the main author of this code, Julian Gale, has added the ability to enter a force constant model directly, rather than taking the derivative of the energy. Whereas a full interatomic potential model is ‘optimised’² by the code to ensure that the system is at an energy minimum, this is not appropriate for force constants³. However, force constants should be tuned against experimental ‘observables’ for a given temperature and pressure. For fitting phonon models against the large experimental datasets, this simpler approach has many advantages as the geometry remains constant and the relationship between phonon modes and force constants is less complex. More details on the interatomic models and the software development necessary to generate the pair distribution functions and inelastic scattering simulations based on these phonon calculations are given in the subsequent chapters.

The dynamical matrix returned by GULP is the mass-weighted Cartesian second derivative of the energy, which can be diagonalised to extract the vibrational information as described above. GULP also allows the use of a ‘shell model’ where the dynamical matrix is modified to take better account of the polarisability of atoms using ‘mass-less shells’ representing the outer electron cloud, coupled to a ‘massive core’ through a spring constant. The charge is split

¹GULP is written in FORTRAN 95, and currently available for Mac OS X, Linux, and Windows. The source code (on academic licence for those with university email addresses) is available from URL - D.

²This is a process of geometry optimisation using the NR or BFGS minimiser as described in the GULP manual.

³I make extensive use of force constant models for phonon calculations, but the energy and gradient output from GULP should be ignored as they are likely to be inconsistent.

between the core and shell, and can be refined. Diagonalisation is performed using the standard EISPACK (URL - E) diagonaliser, and the resulting eigenvalues are the square of the vibrational frequencies. In a stable system, these should always be positive: the standard way of expressing unstable frequencies is to denote them as negative. The new GULP modules still function with unstable frequencies but issue warnings.

It should be noted that at the Γ point the standard evaluation of the dynamical matrix fails to describe the degeneracy of transverse and longitudinal optic modes for charged particles because it does not account for the electric field these vibrations produce. The precise splitting is governed by the direction of approach, and recent versions of GULP make a non-analytical correction to the dynamical matrix to account for this. The new modules avoid evaluation of the dynamical matrix at the Γ point where possible.

The main advantage of using GULP has been that many pre-existing empirical and *ab initio* models can be easily implemented to give the necessary phonon information to produce simulations that are directly comparable to the key experimental probes of atomic motion described in the next section. GULP also allows these models to be refined against experimental ‘observables’ such as vibrational frequencies, elastic and dielectric constants. This was important in the initial development of the calcite force constant model in Chapter 6. The main challenge of this thesis, however, was to refine interatomic models against more detailed phonon information to accurately reproduce the eigenvectors as well as frequencies. To do this, I have linked GULP to another least squared refinement package (TOBYFIT, designed for simulation and refinement of magnetic neutron scattering experiments¹).

The development of the new simulation modules for GULP has provided the central core to the new techniques of experiment design and data analysis described in this thesis. Together with the commissioning of the next generation of spectrometers, this is providing new ways to look at the dynamical properties of materials.

1.3.1 Computing resources

I have made extensive use of the computing resources both at ISIS and in Cambridge for performing simulations and manipulating the resulting datasets. All simulations have been performed on Linux machines. Within Cambridge, I use the CamGrid²: a distributed computing resource based on the Condor middleware which makes use of dedicated machines federated from across the university, together with ‘spare’ computing power on desktops. Computing requirements are matched against available machines, and ‘jobs’ run remotely. This gives access to high memory

¹Source code and documentation for the latest version are available from URL - F.

²Complete documentation is provided at URL - G.

machines where necessary, as well as allowing for (manual) parallelisation of my simulations, splitting components over many machines.

The system requirements – both filespace, processor power and memory – for manipulating the four-dimensional single crystal MERLIN experimental and simulated datasets were so large that all such analysis was performed on a dedicated Linux machine for MERLIN at ISIS.

1.4 Neutron scattering

The derivation of scattering theory is well known (Dove, 2002; Lovesey, 1984; Squires, 1978), so it is sufficient here to simply state the key results in order to define the terminology used in this work and demonstrate the link between the different types of neutron scattering together with their relationship to the scattering function, $S(\mathbf{Q}, \omega)$. It is worth noting that ‘energy’ and ‘frequency’ are often used interchangeably to refer to the characteristic vibration of a certain mode (as $E = \pm\hbar\omega$, with the sign depending on phonon creation or annihilation): the formalism contains ω but the experimental results from machines such as MERLIN are expressed in the energy units of meV.

1.4.1 Experimental geometry

In a neutron spectroscopy experiment, a well characterised neutron beam passes through a sample before colliding with detectors. In the new generation of instruments like MERLIN, these banks of detectors cover a huge solid angle around the sample. The formalism that follows, however, is equally applicable to triple axis spectrometers, where a single detector is moved through the scattering plane to seek out phonon modes, or to diffractometers, which collect data at the elastic line.

The nomenclature varies within the literature, and the way the number of neutrons detected are quantified can be defined in several different ways. For the purpose of this work, we need only consider the number of neutrons with initial energy E scattered per second in a particular direction (θ, ϕ) (into the small solid angle $d\Omega$ subtended by the detector and the sample) with post-scatter energy between E' and $E' + dE'$ (see Fig. 1.2 for the experimental geometry). Such a measurement is known as the *partial differential cross section* (Squires, 1978, and this work) or the *double differential cross section* (Lovesey, 1984) and defined here as:

$$\frac{d^2\sigma}{d\Omega dE'} = \frac{n_n}{\Phi d\Omega dE'} \quad (1.26)$$

where n_n is the number of neutrons scattered per second into $d\Omega_{\theta,\phi}$ with final energy between E and $E + dE'$, and Φ is the flux of incident neutrons. The partial differential cross-section has

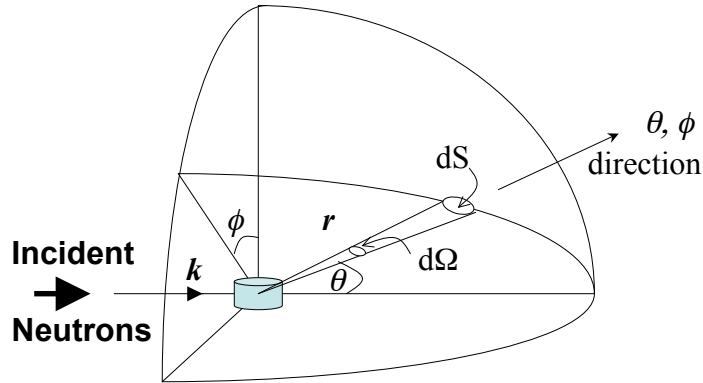


Figure 1.2: The experimental geometry for scattering of beam of thermal neutrons with incident energy E , detected at a distance of r and angle θ, ϕ . The incident neutrons have wavevector \mathbf{k} , and a final scattered wavevector of \mathbf{k}' . After Squires (1978).

dimensions of area/energy. It is related to the theoretical response function $S(\mathbf{Q}, \omega)$, which is variously defined in different texts to include different constant factors. This function is known as the *dynamic structure factor* (Lovesey, 1984), *scattering factor* (Dove, 2002), or *scattering function* (Dove, 1993, and this work) and is always proportional to the partial differential cross-section. I define the relationship here as:

$$\frac{d^2\sigma}{d\Omega dE'} = \frac{k'}{k} S(\mathbf{Q}, \omega) \quad (1.27)$$

where \mathbf{k} is the incident wavevector and \mathbf{k}' the final wavevector. This factor is removed during the data normalisation process (the conversion from raw counts of neutrons to the scattering function). The experimental data collected on spectrometers such as MERLIN are expressed as this scattering function in units of mbarn/meV, following normalisation.

1.4.2 The scattering function

The *scattering function* is proportional to the experimentally measured *partial differential cross section* (Eqn. 1.26). It is defined as:

$$S(\mathbf{Q}, \omega) = \int F(\mathbf{Q}, t) \exp(-i\omega t) dt \quad (1.28)$$

$F(\mathbf{Q}, t)$ is the *intermediate scattering function* which is dependent on the *density operator* $\rho(\mathbf{Q}, t)$: the Fourier transform of the instantaneous nuclear density weighted by the *scatter-*

ing length, b_j .

$$F(\mathbf{Q}, t) = \langle \rho(\mathbf{Q}, t) \rho(-\mathbf{Q}, 0) \rangle \quad (1.29)$$

$$\rho(\mathbf{Q}, t) = \sum_j b_j \exp(i\mathbf{Q} \cdot \mathbf{r}_j(t)) \quad (1.30)$$

Thus the full equation for the *scattering function*, applicable to diffraction as well as spectroscopy, is:

$$S(\mathbf{Q}, \omega) = \sum_{i,j} \left(b_i b_j \exp(i\mathbf{Q} \cdot [r_i - r_j]) \times \int \langle \exp(i\mathbf{Q} \cdot [\mathbf{u}_i(t) - \mathbf{u}_j(0)]) \rangle \exp(-i\omega t) dt \right) \quad (1.31)$$

1.4.3 Coherent and incoherent spectroscopy

Neutrons are scattered from the atomic nuclei, and the relative amplitude of scattering from different atoms is weighted by the *scattering length*, b , (equivalent to the x-ray *form factor*, f). For neutrons, this is independent of wavelength, depending on nuclear spin state as well as the nuclear isotope number. Many nuclei have no spin, or weak spin effects, or else the relative abundance is such that we can justifiably assume a constant *scattering length* for all atoms of that element. However when there is considerable variation between the scattering lengths of different isotopes or spin states, two different types of scattering length can be distinguished.

The classic example (Dove, 2002) is for ^1H , where the spin dependence of the proton-neutron interaction means that there are four possible scattering lengths. Three are parallel, giving spin totals of +1, 0 and -1. The fourth has anti-parallel spins, and a total spin of 0.

| | |
|----------------------|------------------------|
| $\uparrow\uparrow$ | $b = 10.7 \text{ fm}$ |
| $\uparrow\downarrow$ | $b = -47.7 \text{ fm}$ |

In order to take account of this averaging, the intermediate scattering function should be considered in two parts:

$$F(\mathbf{Q}, t) = F_{\text{coh}}(\mathbf{Q}, t) + F_{\text{inc}}(\mathbf{Q}, t) \quad (1.32)$$

The coherent scattering function uses the average scattering length, and so pertains to the correlated processes – elastic Bragg scattering and the coherent phonon scattering that elucidate the phonon dispersion curves. This can be expanded as:

$$F_{\text{coh}}(\mathbf{Q}, t) = \frac{1}{Z} \int \sum_{i,j} \bar{b}_i \bar{b}_j \langle \rho_i(\mathbf{Q}, t) \rho_j(-\mathbf{Q}, 0) \rangle \quad (1.33)$$

where Z is the number of atoms, with interactions between atoms i and j .

The *incoherent* term is similarly defined as:

$$F_{\text{inc}}(\mathbf{Q}, t) = \frac{1}{Z} \sum_{i,j} \overline{b_i b_j} - \bar{b}_i \bar{b}_j \langle \rho_i(\mathbf{Q}, t) \rho_j(-\mathbf{Q}, 0) \rangle \quad (1.34)$$

However, there is no correlation between the incoherent scattering length and a particular atomic site, leading to the result that:

$$\overline{b_i b_j} = \bar{b}_i \bar{b}_j \quad \text{for } i \neq j \quad (1.35)$$

Thus these terms then subtract out of Eqn. 1.34 leaving the $i = j$ terms.

The coherent scattering depends on the time-dependent correlation in the position of the same type and different types of atom, giving interference effects. The incoherent scattering, however, depends only on the position of the same atom at different times, so does not give interference effects.

It is also useful at this stage to relate the *scattering length* to the *cross section*:

$$\sigma_{\text{inc}} = 4\pi \left[\overline{b^2} - (\bar{b})^2 \right] \quad (1.36)$$

$$\sigma_{\text{coh}} = 4\pi (\bar{b})^2 \quad (1.37)$$

1.4.4 Inelastic neutron spectroscopy (INS)

By expanding the *coherent* term as instantaneous atomic displacements from the mean position, it is possible to extract information about phonon dispersion curves and other dynamic processes.

Consider an atom j , with position $\mathbf{r}_j(t)$. If \mathbf{r}_j is the average position, and $\mathbf{u}_j(t)$ the displacement such that $\mathbf{r}_j(t) = \mathbf{r}_j + \mathbf{u}_j(t)$. The *coherent intermediate scattering function* is:

$$F_{\text{coh}}(\mathbf{Q}, t) = \sum_{i,j} \bar{b}_i \bar{b}_j \exp(i\mathbf{Q} \cdot (\mathbf{r}_i - \mathbf{r}_j)) \langle \exp(i\mathbf{Q} \cdot [\mathbf{u}_i(t) - \mathbf{u}_j(0)]) \rangle \quad (1.38)$$

The time correlation function is the last term in this equation, and contains the dynamical information. Assuming the atoms move with harmonic motion, this (time averaged) term can be rearranged as shown (a rigorous proof of this can be seen in Ziman (1979)):

$$\begin{aligned} \langle \exp(i\mathbf{Q} \cdot [\mathbf{u}_i(t) - \mathbf{u}_j(0)]) \rangle &= \exp\left(-\frac{1}{2} \langle [\mathbf{Q} \cdot (\mathbf{u}_i(t) - \mathbf{u}_j(0))]^2 \rangle\right) \\ &= \exp\left(-\frac{1}{2} \langle [\mathbf{Q} \cdot \mathbf{u}_i(t)]^2 \rangle - \frac{1}{2} \langle [\mathbf{Q} \cdot \mathbf{u}_j(0)]^2 \rangle + \langle [\mathbf{Q} \cdot \mathbf{u}_i(t)] [\mathbf{Q} \cdot \mathbf{u}_j(0)] \rangle\right) \end{aligned} \quad (1.39)$$

The first two terms in the final expression of Eqn. 1.39 correspond to normal Debye-Waller temperatures factors (see Section 1.2.6).

The third term can be expanded as a power series:

$$\exp(\langle [\mathbf{Q} \cdot \mathbf{u}_i(t)] [\mathbf{Q} \cdot \mathbf{u}_j(0)] \rangle) = \sum_{m=0}^{\infty} \frac{1}{m!} \langle [\mathbf{Q} \cdot \mathbf{u}_i(t)] [\mathbf{Q} \cdot \mathbf{u}_j(0)] \rangle^m \quad (1.40)$$

Substituting this back into the scattering equation gives:

$$\begin{aligned} S_m^{\text{coh}}(\mathbf{Q}, \omega) &= \frac{1}{m!} \sum_{i,j} \bar{b}_i \bar{b}_j \exp(i\mathbf{Q} \cdot (\mathbf{r}_i - \mathbf{r}_j)) \exp(-W_i(\mathbf{Q}) - W_j(\mathbf{Q})) \\ &\quad \times \int \langle [\mathbf{Q} \cdot \mathbf{u}_i(t)] [\mathbf{Q} \cdot \mathbf{u}_j(0)] \rangle^m \exp(-i\omega t) dt \end{aligned} \quad (1.41)$$

The first term in the series, $m = 0$, corresponds to elastic scattering (Bragg), as used in diffraction experiments. The second term, $m = 1$, corresponds to single phonon scattering. Higher terms refer to multi-phonon scattering.

Taking $m = 1$, substituting in the equations for the instantaneous displacement (Eqn. 1.2), and ensuring that the sum runs over all reciprocal lattice vectors \mathbf{H} , and all atomic modes (using the ν subscript to indicate all j, \mathbf{k}, ν), the *one-phonon coherent dynamical scattering function* can be shown to be:

$$\begin{aligned} S_1^{\text{coh}}(\mathbf{Q}, \omega) &= \sum_{i,j} \bar{b}_i \bar{b}_j \exp(i\mathbf{Q} \cdot (\mathbf{r}_i - \mathbf{r}_j)) \exp(-W_i(\mathbf{Q}) - W_j(\mathbf{Q})) \\ &\quad \times \int \langle [\mathbf{Q} \cdot \mathbf{u}_i(t)] [\mathbf{Q} \cdot \mathbf{u}_j(0)] \rangle \exp(-i\omega t) dt \\ &= \frac{(2\pi)^3}{V} \sum_{\mathbf{H}} \sum_{\nu} \frac{1}{2\omega(\mathbf{k}, \nu)} |F_{\nu}^{\text{coh}}(\mathbf{Q})|^2 \\ &\quad \times ([1 + n(\omega)] \delta(\omega + \omega(\mathbf{k}, \nu)) + n(\omega)) \\ &\quad \times \delta(\omega - \omega(\mathbf{k}, \nu)) \delta(\mathbf{Q} + \mathbf{k} - \mathbf{H}) \end{aligned} \quad (1.42)$$

where i and j are neighbouring atoms, \mathbf{r}_i and \mathbf{r}_j are the average atomic position. $F_{\nu}(\mathbf{Q})$ is the *phonon structure factor* (distinct from the *intermediate scattering function*). It can be expressed as:

$$F_{\nu}(\mathbf{Q}) = \sum_j \frac{\bar{b}_j}{\sqrt{m_j}} \exp(-W_j) \exp(i\mathbf{Q} \cdot \mathbf{r}_j) (\mathbf{Q} \cdot \mathbf{e}_j(\mathbf{k}, \nu)) \quad (1.43)$$

This equation gives the full four-dimensional scattering pattern, as would be observed from the coherent scattering from a single crystal. Frequently, experiments are performed using powder samples, where the resulting pattern is the average over all orientations. The notation $S(Q, \omega)$ will be used for powder-averaged scatter, while $S(\mathbf{Q}, \omega)$ will refer to the full single crystal dataset.

The key results to be taken from this section are the *one phonon coherent scattering function* (Eqn. 1.42) and the component *phonon structure factor* (Eqn. 1.43). The main aim of this work is to calculate these $S_1(\mathbf{Q}, \omega)$ intensities using interatomic models. In so doing, the incoherent scattering is ignored – for many of the systems studied here the incoherent scattering is negligible. The elastic scattering (Bragg peaks) are also not included in the simulations. For powders, simple approximations are made for one multi-phonon and multiple scattering backgrounds, as described in detail in Chapter 4. Notwithstanding the problems of these additional scattering events, convolution of the one phonon coherent scattering with instrument-specific resolution functions gives simulations directly comparable to experimental data.

1.4.5 Time of flight spectrometers at ISIS

All the experimental work in this thesis was performed at the ISIS pulsed spallation source. ISIS is an accelerator-driven neutron source, where pulses of 800 MeV protons collide at 160 kW with a water-cooled tungsten target 50 times a second with a typical current of 200 μA . The resulting neutrons pass through a small moderator (with a volume of ~ 0.5 l) which slows the fast neutrons to the energies required for the various experimental techniques used at the facility. The moderators are surrounded by a water-cooled beryllium reflector which scatters neutrons back into the moderators and doubles the useful flux. The temperature of each moderator effects the resulting energy: the symmetrically poisoned¹ ambient water moderator on MERLIN offers maximum flux at ~ 45 meV.

The engineering diagram of MERLIN in Fig. 1.3 gives a typical example of the progress of the neutrons. They are directed into the instrument – in the case of MERLIN using new supermirror guides – and pass through a series of choppers made of neutron blocking materials with a narrow slit (collimator) to allow neutrons through for limited phased periods of time. First, a background-suppressing ‘ T_0 ’ chopper rotates with the same frequency as the ISIS pulse, blocking the beam as the protons strike the target (at time zero). This prevents high-energy neutrons causing a large time-dependent background. The beam is now suitable for use in crystal alignment as a white beam, or can be monochromated to produce small packets of neutrons at a desired velocity. On MERLIN, this is done with a Fermi-chopper suspended magnetically in a vacuum, and able to rotate about a vertical axis at up to 12 times the ISIS pulse frequency (50 Hz). This type of chopper is well suited to high-energy neutrons, making fast time-cuts and giving excellent energy resolution. However, for slow neutrons, as used with the new LET machine, a rotating disk spinning about a horizontal axis is more appropriate. The effective open

¹‘Symmetrically poisoned’ means that a thin sheet of neutron absorbing material (Gd) is put into the centre of the moderator. This effectively reduces the size of the moderator, sharpening the time structure of the neutrons but at a cost to the flux.

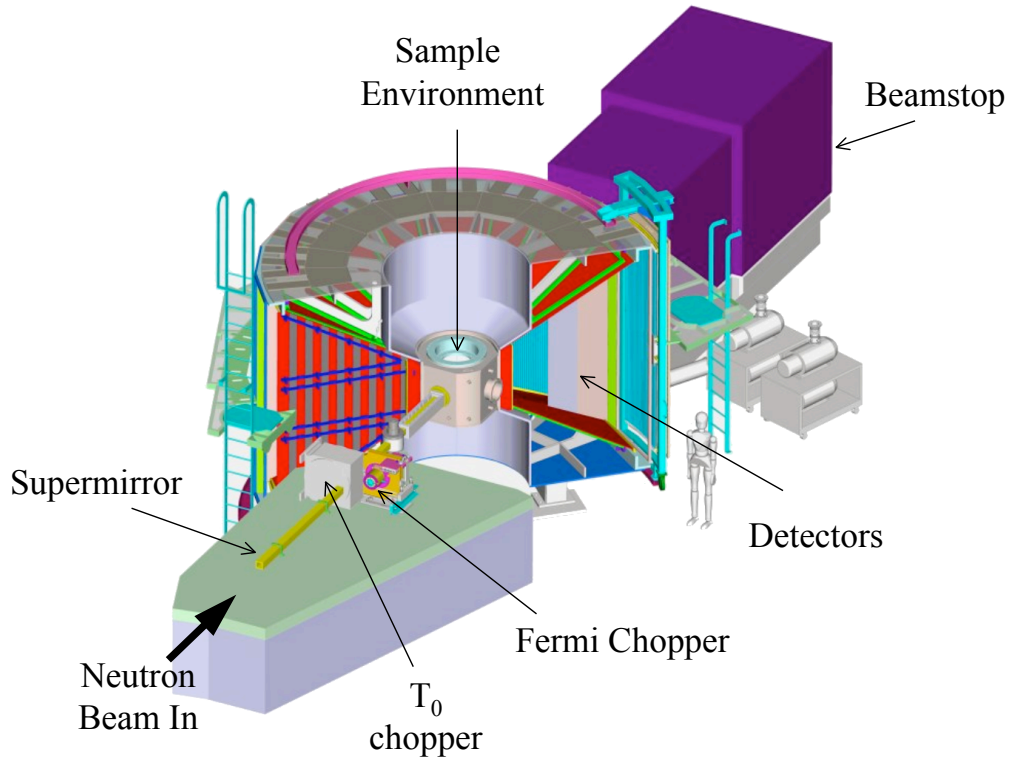


Figure 1.3: Engineering diagram of MERLIN with cutaway tank to show the details. Man shown for scale. Image courtesy of ISIS.

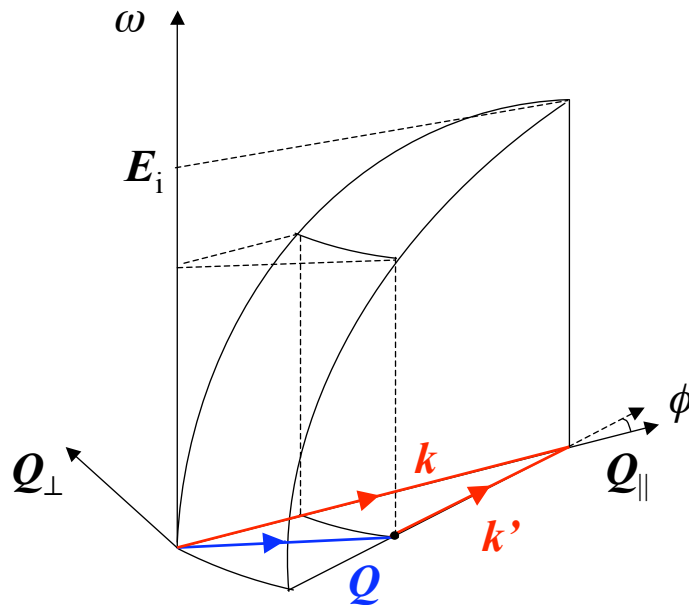


Figure 1.4: The accessible region of \mathbf{Q}, ω space in a time-of-flight spectrometer at incident energy E_i . The line at angle ϕ to the incident wavevectors gives all the scattered wavevectors \mathbf{k}' intercepted by the detector at that scattering angle. For a given \mathbf{Q} the energy transfer is obtained by dropping a line from the paraboloid to meet the end of the vector \mathbf{Q} .

time is dependent on the type of chopper, the frequency and chosen incident energy. Typical energy resolution on MERLIN at the elastic line, for maximum flux, is $\sim 5\%$.

To minimise background scattering the entire flight path is kept under vacuum, and the sample environment is carefully designed to minimise the amount of material in the beamline: the top loading CCR used in many of the experiments described in this thesis has thinned windows of aluminium such that only 0.4 mm total thickness is in the direct beam.

Monochromated neutrons pass through the sample chamber and are scattered by the sample. Raw data are collected in the form of number of neutrons detected over time-of-flight. The precise incident energy is extracted from the time peaks in monitors¹ positioned beyond the sample with a specific spatial separation. This allows the time at which the neutrons arrived at the sample to be calculated (from E_i , the monitor time-peaks and spatial positions). Knowing both the distance between sample and detectors and time of post-scatter-flight allows the time peaks at each detector to be converted to final energies, giving the energy transfer. This process, together with the removal of the k'/k factor, is known as ‘normalisation’. With appropriate additional parameters, this can be expressed in absolute units of mbarn/meV, or relative units based on flux normalisation from the monitors.

In time-of-flight experiments, the accessible region of \mathbf{Q}, ω is restricted to the surface of a paraboloid for each incident energy (Fig. 1.4) due to the quadratic relations between energy and wavevector seen in Eqn. 1.19. The sample orientation gives the direction of the vector \mathbf{Q} with respect to the crystal reciprocal lattice. The energy transfer for a given \mathbf{Q} is obtained by dropping a line from the paraboloid to meet the end of the vector \mathbf{Q} . This configuration arises from the components of the scattering vectors parallel and perpendicular to the incident beam for a given detector at angle ϕ :

$$\mathbf{Q}_{\parallel} = \mathbf{k} - \mathbf{k}' \cos \phi \quad (1.44)$$

$$\mathbf{Q}_{\perp} = -\mathbf{k}' \sin \phi \quad (1.45)$$

1.4.6 MERLIN: the new spectrometer

The motivation for the work contained in this thesis arose from the development of a new generation of spectrometers requiring new methods of data analysis. MERLIN (Bewley, 2002; Bewley *et al.*, 2009) is the new high count rate, medium energy resolution, direct geometry chopper spectrometer at ISIS, with a position sensitive detector bank covering over π steradians of

¹These are often low efficiency scintillation detectors, or, in the case of MERLIN, novel He³ gas detectors which surround a very thin vanadium foil, sampling the whole beam without detecting gamma radiation. The monitors give a measure of the amount of beam seen by the sample, which is used to assess the run-length in terms of the number of counts. This offsets temporal variations of beam which are beyond the control of the experimentalists.

solid angle. MERLIN (Fig. 1.3) complements the high resolution MAPS spectrometer URL - M, used for the PMN experiments in Chapter 7). MAPS has been described (Bewley *et al.*, 2009) as creating a new paradigm in INS, as the first spectrometer to allow large volumes of reciprocal space to be studied simultaneously, but the flux restrictions mean it is ideally suited to low-dimensional magnetic studies and not exploring phonon dispersion curves across the entire Brillouin zone. MERLIN, however, is ideally suited to the study of phonons (as well as general single crystal and powder work, extreme sample environments, magnetism, etc.). Technological developments, such as the latest super-mirror technologies, instrument design, and the use of a dedicated moderator have improved the flux possibilities¹. However, the flux gains come at the expense of increased beam divergence (dependent on incident energy).

When first commissioned, MERLIN had the largest detector range of any spectrometer at ISIS², using newly designed position sensitive detectors with a resolution of 20 mm at the centre of the tubes (increasing slightly to 23 mm). The sample to detector distance is 2.5 m. The detectors form a cylindrical array with an angular range of -45° to $+135^\circ$ degrees in the horizontal plane and $\pm 30^\circ$ degrees in the vertical plane, each 25 mm wide and 3 m long. These are mounted *within* the vacuum tank (requiring advances in electronics), reducing the gaps in detector coverage³. There are nine doors, with a two tube-width gap between each. To help eliminate suprisons due to scattering across the tank, a sheet of neutron absorbing material emerges into the tank towards the centre of the sample forming a ‘vane’ between all the high angle banks. Each 3 m tube is split into 256 ‘detector pixels’ ~ 11 mm in size, giving ~ 69000 detector pixels. Each of these has 2500 time channels giving a total of 172 million bins. For powders, the detector pixels are grouped into rings (defined in the instrument parameter files). The instrument has been designed to limit the background neutron scattering, achieving backgrounds of approximately 28 neutrons/hour/metre of detector tube, comparable to other ISIS machines.

MERLIN was commissioned in 2008: the calcite experiments reported in Chapter 6 formed part of the initial scientific commissioning. The challenge of working with the huge MERLIN datasets provided the impetus for the **SQW** software development described in this thesis, so all methodologies are given for the specific example of the new MERLIN spectrometer at ISIS, but are equally applicable to other ISIS spectrometers such as MAPS, MARI and LET, and in principle to any direct chopper spectrometer.

¹MERLIN has flux gains of up to 20 times those seen on the instrument it replaces, at an incident energy of 10 meV.

²LET, the new cold neutron multi-chopper spectrometer on target station two, has recently seen its first neutrons, and will eventually have an even wider detector range coupled with excellent energy resolution. The new techniques developed in this thesis are equally applicable to LET.

³Door edges and vanes still give missing regions.

1.4.7 Total scattering and pair distribution functions

Study of the effects of dynamics is not limited to spectrometers, but can be seen using diffractometers, such as GEM at ISIS (Williams *et al.*, 1997), through total scattering experiments. As the name suggests, this involves collecting the complete diffraction pattern; diffuse scattering as well as Bragg peaks. Initially developed for liquids, this technique is now routinely used with powdered crystalline samples to study local disorder. The observed scattering is integrated over all orientations and energies to obtain the $S(Q)$ total scattering function (following Keen, 2001):

$$S(Q) = \frac{1}{Z} \sum_{i,j} b_i b_j \frac{\sin(Q|\mathbf{r}_i - \mathbf{r}_j|)}{Q|\mathbf{r}_i - \mathbf{r}_j|} \quad (1.46)$$

$$= i(Q) + \sum_m c_m \langle b_m^2 \rangle \quad (1.47)$$

where Q is the modulus of the scattering vector, Z is the number of atoms, i and j label different atoms, b_j is the scattering length of atom j , \mathbf{r}_j is the instantaneous position of atom j , m represents an atom type, and c_m is the number concentration of atom type m .

A Fourier transform of the experimental data is proportional to a function known as the Pair Distribution Function (PDF). This gives the relative probability of finding a pair of atoms of type m and n separated by a distance between r and $r + \delta r$. The atomic positions that contribute to the Bragg peaks in the elastic scattering give the peak positions in the PDF, the crystal arrangement (number of neighbours) gives the area under each peak, while the dynamic properties of the material are responsible for the width of the peak.

Chung & Thorpe (1997, 1999) developed a phonon-based model of the PDF, which I have incorporated into the new GULP PDF module to allow the calculation of PDFs for crystalline and amorphous materials through the use of empirical models and lattice dynamics. There are many different expressions of the PDF in the literature, each used in different situations. Chung and Thorpe use ρ^{PDF} as it is zero below the minimum inter-pair spacing, and best suited to sum-of-residual type agreement factor calculations. For harmonic phonons, each component partial (pair-specific) peak has a Gaussian shape with area proportional to the number of neighbours – making it effectively a histogram of interatomic distances – and temperature-dependent widths that are obtained by summing over all phonons. This real space correlation function tends to the number density (ρ_0) at high r as can be seen for SrTiO₃ (described in Chapter 2) in Fig. 1.5, together with the weighted partial PDFs for each constituent pair.

The function $i(Q)$ in Eqn. 1.47 is related to the experimentally accessible *differential correlation function*, $D(r)$ (with units of 1/length) by:

$$Qi(Q) = \rho_0 \int D(r) \sin(Qr) dr \quad (1.48)$$

$$D(r) = \frac{2}{\pi} \int Qi(Q) \sin(Qr) dQ \quad (1.49)$$

where $\rho_0 = n/(V_{\text{unit cell}})$, the average number density (units of 1/volume). In the same way, the *total radial distribution function*¹, $G(r)$ (with units of 1/area) which is related to $D(r)$ by:

$$D(r) = 4\pi r \rho_0 G(r) \quad (1.50)$$

and is found through this pair of Fourier transforms:

$$i(Q) = \rho_0 \int 4\pi r^2 G(r) \frac{\sin(Qr)}{Qr} dr \quad (1.51)$$

$$G(r) = \frac{1}{2\pi^3 \rho_0} \int 4\pi Q^2 i(Q) \frac{\sin(Qr)}{Qr} dQ \quad (1.52)$$

It is often helpful to consider the underlying pair-wise contributions to the total PDF through the partials. $D(r)$ is related to the familiar $g(r)$ and weighted $d'(r)$ partial PDFs through:

$$D(r) = 4\pi r \rho_0 \sum_{m,n} c_m c_n \bar{b}_m \bar{b}_n (g_{m,n}(r) - 1) \quad (1.53)$$

$$= \sum_{m,n} d'_{m,n}(r) \quad (1.54)$$

with \bar{b}_m as the coherent scattering length of atom-type m .

The new GULP module also gives results in the form of $T(r)$, the *total correlation function*², with units of 1/length, and the PDF described by Chung & Thorpe (1997) and in the PDFFIT program (Proffen & Billinge, 1999) as the *radial distribution function*, (also referred to as the *pair distribution function* in Chung & Thorpe, 1999) and written as $G^{\text{PDF}}(r)$ by Keen (2001), with units of 1/area.

¹ $G(r)$ is often expressed in units of Barns ($1 \times 10^{-28} \text{ m}^2 = 1 \times 10^{-8} \text{ \AA}^2$), but in the GULP output \AA^2 is used to be consistent with the other correlation functions.

² $T(r)$, like $G(r)$ and $D(r)$, is calculated as part of the ATLAS suit of programs (Soper *et al.*, 1989), as used at ISIS.

The relationship between these main correlation functions are:

$$G(r) = \frac{G^{\text{PDF}}(r) \left(\sum_{m=1}^Z c_m \bar{b}_m \right)^2}{4\pi r \rho_0} \quad (1.55)$$

$$D(r) = 4\pi r \left[\rho^{\text{PDF}}(r) - \rho_0 \right] \left(\sum_{m=1}^Z c_j \bar{b}_m \right)^2 \quad (1.56)$$

$$D(r) = G^{\text{PDF}}(r) \left(\sum_{m=1}^Z c_m \bar{b}_m \right)^2 \quad (1.57)$$

$$T(r) = D(r) + 4\pi r \rho_0 \left(\sum_{m=1}^Z c_m \bar{b}_m \right)^2 \quad (1.58)$$

$$= \left(G^{\text{PDF}}(r) + 4\pi r \rho_0 \right) \left(\sum_{m=1}^Z c_m \bar{b}_m \right)^2 \quad (1.59)$$

1.4.8 Phonons-from-diffraction

The traditional approach for extracting phonon dispersion curves has been from inelastic neutron scattering data (INS). However, there are situations where there are no suitable single crystals, so there is a desire to be able to extract phonon information from other approaches. While the link between dynamics and the peak widths in the PDF has been known since the 1960s (e.g. Kaplow *et al.*, 1964, 1965) it was not until the 1990s that the full collection of total scattering data was technologically possible, prompting the question of whether the dynamical properties of materials can be extracted from this relatively simple and quick experimental technique¹.

In recent years, there have been several attempts to extract dynamical information from neutron powder diffraction studies (e.g. Dimitrov *et al.*, 1999; Goodwin *et al.*, 2004; Graf *et al.*, 2003), although this approach was opposed by Reichardt & Pintschovius (2001). Graf *et al.* (2003) successfully refined the parameters of a model PDF against an experimental PDF, for some simple systems, but in more complex cases observed a strong dependence upon the choice of starting model. These are usually generated through a refinement against other experimental data, such as inelastic neutron results, so are not truly phonons-from-diffraction alone. However, recent work by our group in Cambridge (Goodwin *et al.*, 2005, 2006) has focussed on the use of a *Reverse Monte Carlo* (RMC, Tucker *et al.*, 2001c) approach, to directly probe the dynamical information available within the PDF. This model-independent approach, which takes account

¹While a typical single crystal experiment on MERLIN may take several days to collect a full set of data at a single temperature, a GEM total scattering experiment takes a matter of hours.

of crystal symmetry, has been very successful in extracting dispersion curves in a number of model systems.

A major part of this thesis has been concerned with producing and utilising PDF simulation software based on empirical interatomic models. The impetus for this arose from discussions with Andrew Goodwin about the limitations of extracting phonon information from neutron total scattering experiments. While the low frequency dynamical information extracted from RMC analysis of total scattering experiments provides excellent agreement to that seen from INS data, the PDF is insensitive to high frequency modes, such as zone-centre LO/TO splitting in MgO. By performing simulations with the new GULP PDF module, it has been possible to track the contributions of different mode energies to the overall PDF, as seen in Chapter 2.

1.5 Objectives of this thesis

The main objectives of my work have been to develop new methodologies to assist in the design and analysis of neutron scattering experiments, advancing understanding of atomic-scale motion (phonon behaviour) in a wide range of materials. The various strands will be developed and combined in the examples given throughout the thesis, with the following specific aims:

1. development of new methodologies allowing the phonon-based simulation of PDFs, together with detailed analysis of the relative contributions of different modes and atoms to this behaviour,
2. simulation of the one-phonon coherent inelastic neutron scattering from general interatomic models, and application of this approach to a wide range of materials,
3. convolution of the simulated INS spectra with appropriate resolution functions, allowing direct comparison to experiment for both powders and single crystals,
4. refinement of interatomic models with experimental powder INS data, allowing the viability of this much-needed approach to be assessed,
5. the ability to manipulate the INS simulations to help elucidate the origins of observed phonon behaviour,
6. application of these new methodologies in the study of the structure and dynamics of a number of mineralogical and technologically important materials.

Chapter 2

Pair Distribution Functions: Theory, Implementation and Examples

A new module has been developed for the widely used General Utility Lattice Program (GULP). The phonon-based theory developed by Chung & Thorpe (1997) to calculate pair distribution function (PDF) peak-widths has been utilised to give a selection of commonly used correlation functions. A numerical library of neutron scattering information is now available within GULP, and is used to produce results that can be compared to neutron scattering experimental data. The influence of different phonon modes on the PDF can be assessed by excluding modes above or below a cut-off frequency. Results¹ are presented for sample crystallographic systems MgO, SrTiO₃ and α -cristobalite as well as Ca_xSr_{1-x}TiO₃ at $x = 0.5$, which makes use of the capability to handle partial occupancies to compare different Ca/Sr ordering arrangements with a disordered model in which every Ca/Sr site has 50% occupancy of both species. The implications of the relative contribution of modes of different energies to the PDF peak width is discussed both for ‘phonons-from-diffraction’ and the selection and refinement of interatomic potential models.

2.1 Introduction

The Pair Distribution Function (PDF) has been used (under various names) for many years to provide an understanding of both structure and dynamics on the atomic scale. It was initially

¹The majority of the work presented in this chapter has already been published (Cope & Dove, 2007; Goodwin *et al.*, 2005, 2006).

developed for liquids (Zernike & Prins, 1927), and has continued to be useful with amorphous materials (Warren, 1978). As early as the 1960's, workers were making use of the dynamic contributions to the PDF (Kaplow *et al.*, 1964). More recently it has become an important tool for use with crystalline materials (Toby *et al.*, 1990). As the PDF allows visualisation of local displacements in the diffraction data, rather than just average atomic structure, Dimitrov *et al.* (1999) suggested that it might be possible to extract phonon dispersion curves from diffraction data, making use of iterative techniques such as the Reverse Monte Carlo (RMC) algorithm. Our group in Cambridge have used a model-independent approach to extract dynamic information from atomistic configurations such as those generated using RMC with a number of materials, but find the high-frequency regions to be irretrievable (Goodwin *et al.*, 2005, 2006). Therefore, I propose combining the phonons-from-diffraction techniques with a model-dependent approach, such as that given here, for the study of systems for which established spectroscopic techniques are prohibitive or inappropriate.

The PDF is found experimentally through a Fourier transform of the observed total scattering function $S(Q)$ from neutron or X-ray diffraction experiments. Working within harmonic lattice dynamics, the PDF can be modelled using Gaussians. Recently, Chung & Thorpe (1999) proposed a method for calculating these Gaussian peak widths from phonon calculations, thus providing a phonon-based model of PDFs.

Chung & Thorpe (1999) used their theory specifically with semiconductor alloys, and it seemed appropriate to implement the theory such that PDFs for other crystalline materials could be easily produced. GULP is widely used within the community to generate phonon information from interatomic models. Thus, with the addition of neutron scattering data, is ideally suited to this purpose.

There are two main applications for this new modelling approach. First, to assist in the design of experiments, giving a theoretical model of experimental outcome. Second, to 'experiment' on the model, for example changing cation distribution, or investigating different phonon contributions.

2.2 Theory

The PDF, as introduced in Section 1.4.7, is derived experimentally by Fourier transform of the observed total scattering function from neutron or X-ray diffraction experiments (Keen, 2001). The crystal structure gives peak positions and integrated areas, while the phonons give the temperature-dependent widths.

Chung & Thorpe (1999) proposed a formalism¹ for the computation of ρ^{PDF} which I have implemented for interatomic potential models (Cope & Dove, 2007), and is to be released in the next version of GULP. They give the probability of finding a pair of atoms i and j , with position \mathbf{r}_i and \mathbf{r}_j respectively, at position \mathbf{r} by:

$$\rho_{ij}(\mathbf{r}) = \langle \delta(\mathbf{r} - (\mathbf{r}_j - \mathbf{r}_i)) \rangle \quad (2.1)$$

where $\langle \dots \rangle$ is the statistical average implying both configurational and thermal averages. Summing over all such pairs gives the *density function* $\rho(\mathbf{r})$, which is averaged by using each atom in turn as the starting point. Working with a crystal lattice, the complexity of such calculations is reduced because only atoms in the first unit cell are used as starting points. Moreover, GULP reduces the crystal symmetry to a primitive cell, minimising the required number of calculations.

Consider a lattice of unit cells each containing Z atoms. Denote the position of atom i in the original unit cell as \mathbf{r}_{i_0} and similarly atom j in the ℓ th unit cell as \mathbf{r}_{j_ℓ} . Define the pair separation vector between two atoms i_0 (in the original unit cell) and j_ℓ (in the ℓ th unit cell) as $\mathbf{r}_{i_0 j_\ell} = \mathbf{r}_{j_\ell} - \mathbf{r}_{i_0}$.

The density function (with units of 1/volume) is the weighted sum over all pairs between atom i_0 and atom j in all unit cells, averaged over the number of atoms in the unit cell. The spherical average is taken, dividing by $4\pi r^2$:

$$\rho^{\text{PDF}}(r) = \frac{1}{4\pi r^2 Z} \sum_{\ell} \left(\sum_{i_0} \sum_{j'} w_{ij} \rho_{i_0 j_\ell}(\mathbf{r}) \right) \quad (2.2)$$

where the prime indicates $i_0 \neq j_0$ (i.e. $\mathbf{r}_{i_0 j_\ell} \neq 0$). The weighting is dependent on the concentration, c_i (fraction of atoms i in the primitive cell), and coherent bound scattering length, \bar{b}_i , and is expressed as:

$$w_{ij} = \frac{\bar{b}_i \bar{b}_j}{\left(\sum_{i=1}^Z c_i \bar{b}_i \right)^2} \quad (2.3)$$

$\rho^{\text{PDF}}(r)$ is related to the more familiar and experimentally derived $D(r)$ as:

$$D(r) = 4\pi r \left[\rho^{\text{PDF}}(r) - \rho_0 \right] \left(\sum_{i=1}^Z c_i \bar{b}_i \right)^2 \quad (2.4)$$

¹I make use of the notation of Keen (2001) to describe this form of PDF. It is chosen for computer modelling as it is zero below the minimum inter-pair spacing, tending to the number density at high r , thus well suited to sum-of-residual type agreement factor calculations. This is also the form used in the PDFFIT program (Proffen & Billinge, 1999) as well as by several current workers in this field, e.g. Billinge & Egami (1993); Proffen *et al.* (2003).

As suggested by Eqn. 2.1, if the atoms were completely stationary, the density function would be a series of delta functions located at the interatomic spacings. To account for thermal motion, Chung & Thorpe (1997) demonstrated that, within the harmonic approximation, the Debye-Waller theorem can be used to justify the use of a series of weighted Gaussian peaks $\rho_{ij}(r)$, centred at the inter-pair spacing, r_{ij} , with width σ_{ij} .

The width is used in a normal Gaussian to give the pair-specific density function:

$$\rho_{i_0j_\ell}(\mathbf{r}) = \frac{1}{\sqrt{2\pi\sigma_{i_0j_\ell}^2}} \exp\left[-\frac{|\mathbf{r}_{i_0j_\ell}| - r}{2\sigma_{i_0j_\ell}^2}\right] \quad (2.5)$$

These are then summed as in Eqn. 2.2 to give the $\rho^{\text{PDF}}(r)$ density function. The partial density function for atomic pair ij is made by summing only $\rho_{i_0j_\ell}(\mathbf{r})$ for that pair. The weighted sum of all the partials is the total density function, as was illustrated for SrTiO₃ in the General Introduction (Chapter 1, Fig. 1.5).

Taking $\hat{\mathbf{r}}_{ij}$ to be the unit vector between atoms i and j , and $\mathbf{u}_{ij} = \mathbf{u}_j - \mathbf{u}_i$ to be the difference in displacement, where \mathbf{u}_i is the displacement of atom i , then the width is given by:

$$\sigma_{ij} = \left\langle [\mathbf{u}_{ij} \cdot \hat{\mathbf{r}}_{ij}]^2 \right\rangle^{\frac{1}{2}} \quad (2.6)$$

This can be expressed in terms of phonon modes as:

$$\sigma_{i_0j_\ell}^2 = \frac{\hbar}{2N} \sum_{\mathbf{k}, \nu} \frac{2 n(\omega(\mathbf{k}, \nu)) + 1}{\omega(\mathbf{k}, \nu) |\mathbf{r}_{i_0j_\ell}|^2} |[\mathbf{u}_{j_\ell}(\mathbf{k}, \nu) - \mathbf{u}_{i_0}(\mathbf{k}, \nu)] \cdot \mathbf{r}_{i_0j_\ell}|^2 \quad (2.7)$$

where the displacements $\mathbf{u}_{i\ell}$ are as given in Eqn. 2.8. It should be noted that this corrects a typographical error in Reichardt & Pintschovius (2001) Eqn. 3, where the numerator is multiplied by a factor of $\sqrt{m_i}$ rather than divided by it.

$$\mathbf{u}_{i\ell} = \frac{\mathbf{e}_i(\mathbf{k}, \nu) \exp[i\mathbf{k} \cdot \mathbf{r}_{i\ell}]}{\sqrt{m_i}} \quad (2.8)$$

N is the number of \mathbf{k} -points, ν is the mode index, $n(\omega(\mathbf{k}, \nu))$ is the Bose occupation number (Eqn. 1.9). $\omega(\mathbf{k}, \nu)$ is the frequency from the eigenvalues of the dynamical matrix, and $\mathbf{e}_i(\mathbf{k}, \nu)$ is the eigenvector for atom i (either setting may be used here, as the phase factor cancels, see Section 1.2.1). GULP generates \mathbf{e}^{sig} , so this setting is used to minimise computation error and optimise the code. The mass of atom i is m_i . This is implemented within GULP with the \mathbf{k} -point sampling of the first Brillouin zone performed with a Monkhorst-Pack grid (Monkhorst & Pack, 1976) to give an even spread of \mathbf{k} -points. The more dense the grid, the more accurate the results will be at the expense of longer processing times and memory requirements. The density of

the grid required depends on the system under study, and must be established by means of a convergence test.

2.3 Program description for the GULP PDF module

2.3.1 Main purpose

For a given interatomic potential model, this module uses the phonon information (eigenvectors and frequencies) generated within GULP to calculate the PDF peak widths for every atomic pair up to a given radius. This is then used to produce several commonly used correlation functions including both total and partial (pair-specific) pair distribution functions.

2.3.2 Implementation

Every atomic pair, up to a given radius (`rmax`), is considered in turn. Phonon information for every \mathbf{k} -point within a sufficiently dense Monkhorst-Pack grid is used to calculate the contribution to the width of the PDF peak from that pair. These are summed and suitably averaged to give the total $\rho^{\text{PDF}}(r)$ function, which is converted into each of the total correlation functions listed in Section 1.4.7. The contributions from all pairs of each type are also used to output the partial PDFs. The user can control how much of this is written to file (see Section 2.3.4). Other useful data and statistics are included in the standard output.

It should be noted that the GULP eigenvectors, produced with the EISPACK diagonaliser, are always returned with the bottom right-hand element set to zero. This introduces an arbitrary phase factor between different Brillouin zones. Crucially, it destroys the relationship that the conjugate of an eigenvector is the same as the eigenvector of the negative \mathbf{k} -point [$\mathbf{e}^{\text{sig}}(-\mathbf{k}) = \mathbf{e}^{\text{sig}*}(\mathbf{k})$], which the PDF calculations rely upon. However, this can be avoided by ensuring that all calculations were performed by extrapolation¹ from a single Γ -centred Brillouin zone.

2.3.3 Input

The conventional input for GULP is a simple text file with keywords at the top, controlling the general behaviour, followed by options which set up the specific cell and other parameters. New keywords and options are available for use with normal GULP input files, listed in Table 2.1; some of these, such as `PDF` or `PDFcut`, change the behaviour of the program whereas others, such as `nowidth` or `coreinfo` merely affect the output behaviour. The PDF options are entered within

¹The default setting for the first Brillouin zone in GULP is an unconventional one in order to avoid the problem of evaluating the dynamical matrix at Γ as noted in Section 1.3: instead of being Γ -centred, GULP uses the Γ -point as the origin in a cell extending to (111) in fractional reciprocal lattice coordinates, so the actual \mathbf{k} -points evaluated approach but do not reach Γ . For PDF calculations, the Monkhorst-Pack grid is shifted back to be Γ centred.

| | |
|------------------|---|
| PDF | calculate peak widths and PDFs |
| PDFcut | as PDF but ‘cut off’ all phonon contributions $\omega > \mathbf{wmax}$ or $\omega < \mathbf{wmin}$ |
| PDFkeep | with PDFcut, set all $\omega > \mathbf{wmax}$ to \mathbf{wmax} (or $\omega < \mathbf{wmin}$ to \mathbf{wmin}) |
| Coreinfo | Output atomic information (for cores not shells) used in phonon calculations. |
| Nopartial | Suppress output of partial PDFs. |
| Nofreq | Suppress eigenvector output after phonon calculation. (<i>modified</i> GULP keyword, previously <i>suppress generation</i>) |
| Nowidth | Suppress output of peak widths for PDF calculations |
| Makeeigenarrays | Store all eigenvectors and frequencies after calculation |
| Converteigen | Convert eigenvectors to alternative setting before storing |
| ArrayFrequencies | Output phonon details from internal arrays |
| Shift | Shift the centre of the BZ generated using shrink to Γ |

Table 2.1: Summary of new PDF module keywords

the **neutron**¹ block, and allow users to specify the maximum radius (using **rmax**, default = 5 Å) and the number of bins (using **rbins**, default 100), and set the output filenames.

The ‘experimental’ keywords are **PDFcut**, and **PDFkeep**, which limit the range of phonon frequencies used either by ignoring anything above/below the given frequency limit, or by replacing anything above/below the given limit with the limiting value itself. In these cases, **wmax** or **wmin** are used to specify the frequency limits².

Other standard GULP input options should be used: of particular importance here are **temperature** and **shrink** (used for adjusting the density of the Monkhorst-Pack grid generating an even distribution of **k**-points). When using **shrink**, it is essential that the user checks that convergence of phonon properties (e.g. peak width) with number of **k**-points has been achieved. A new GULP keyword has been added to force a Γ -centred Brillouin zone: **shift**. All PDF calculations are performed in this manner, but the keyword can be used manually to obtain the same range of **k**-points without performing the PDF calculation.

2.3.4 Output

In addition to normal GULP output, three simple text file-types can be produced. First, a **.wid** file lists the width contribution from every atomic pair (unless the keyword **nowidth** is given); second, a **.pdfs** file containing the PDF correlation functions up to the maximum radius

¹This is a section of the input file normally headed by **neutron**, containing a selection of commands, and closed with the work **end**. However, the block is headed with **PDF** instead of **neutron** in forthcoming release in GULP

²The default units are THz, but this can be changed by adding **unit freq [rad/THz/cm/wav/meV]**. The same units will be used for output.

| | |
|-------------------------|--|
| <code>neutron</code> | Start of neutron input block used for PDF input options. Closed with <code>end</code> . |
| <code>rmax</code> | Sets maximum radius (Å) for PDF calculation |
| <code>rbins</code> | Sets number of bins to be used in PDF output |
| <code>wmax</code> | Sets maximum phonon frequency to be considered |
| <code>wmin</code> | Sets minimum phonon frequency to be considered |
| <code>units</code> | When followed by the <code>freq</code> and <code>[rad/THz/cm/wav/meV]</code> (radians, THz, cm^{-1} = wavenumbers, meV) sets the input/output frequency units overruling default of THz |
| <code>output pdf</code> | Specifies the filename for <code>.wid</code> and <code>.pdfs</code> output files |

Table 2.2: Summary of new PDF module options for use in the neutron block

using the `rbins` specified at input; and finally a set of numbered `.pdfs` files for the partial pdfs (unless suppressed by `nopartial`). The PDF correlation functions given are (in the Keen, 2001 formalism) $\rho^{\text{PDF}}(r)$, $G^{\text{PDF}}(r)$, $G(r)$, $D(r)$, and $T(r)$. In addition the PDF module contributes to the general Chemical Markup Language (CMLTM) output generated using FoX (White *et al.*, 2006).

2.4 Agreement factors

To provide a quantitative means of comparison of the quality of the fit, two numerical measures have been used. As $D(r)$ oscillates around zero at high r , it is not appropriate for use in a ‘sum-of-residuals’ type agreement factor, so $\rho^{\text{PDF}}(r)$ is used. Toby & Egami (1992) produced a standard PDF agreement factor, A^2 , which directly parallels the R -factor used in crystal structure refinement. When both model and observed functions have been evaluated at n equally spaced points in r , the agreement factor is defined as:

$$A^2 = \frac{1}{n\rho_0^2} \sum_{l=1}^n [\rho_{\text{obs}}^{\text{PDF}}(r_l) - \rho_{\text{model}}^{\text{PDF}}(r_l)]^2 \quad (2.9)$$

This function will emphasise the fit to low- r structural detail. As I also frequently use r -weighted data in the form of $D(r)$, which is the form directly accessible through the Fourier transform of total scattering data, it is appropriate to define a further agreement factor based on $r\rho^{\text{PDF}}(r)$ to take account of the higher r features when focusing on the mid-range detail:

$$A_r^2 = \frac{1}{n\rho_0^2} \sum_{l=1}^n [r\rho_{\text{obs}}^{\text{PDF}}(r_l) - r\rho_{\text{model}}^{\text{PDF}}(r_l)]^2 \quad (2.10)$$

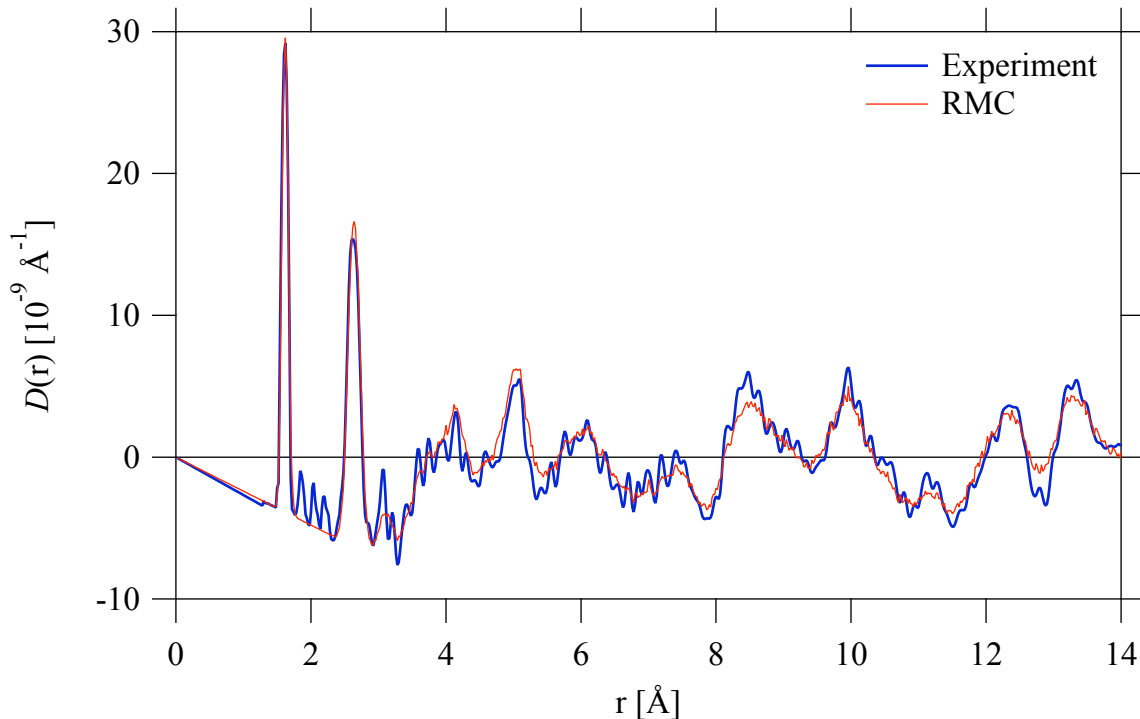


Figure 2.1: A comparison of the experimental data, showing the large truncation ripples, and the RMC dataset for α -cristobalite. The fit is excellent, giving agreement factors of $A^2 = 0.015$ and $A_r^2 = 0.2$.

2.5 Examples

The new module for GULP was tested against several crystallographic systems. Comparison is made between GULP output and PDFs extracted from experimental neutron total scattering experiments. Theoretically, to obtain a true PDF from diffraction data, the Fourier integration should be carried out to infinite Q . In reality, it has to be terminated at a finite value of Q determined by the experimental setup. This can result in truncation ripples from the Fourier transform, as clearly seen in Fig. 2.1. One way to avoid this is to use the Reverse Monte Carlo (RMC) approach, discussed in detail elsewhere (Tucker *et al.*, 2001a), to generate an atomistic configuration consistent with the diffraction pattern. These configurations give excellent agreement to experimental data, with typical A^2 and A_r^2 agreement factors of 0.015 and 0.2 respectively – the small discrepancies arise where the RMC does not reproduce the truncation ripples. Standard procedures (see, for example, Howe *et al.*, 1989) were followed to correct the data for background scattering, instrument resolution etc., before generating the ‘experimental RMC’ dataset. I present the model PDFs in this chapter alongside ‘experimental RMC’ data instead of the raw experimental PDFs to avoid these truncation ripples.

2.5.1 MgO

MgO was chosen for initial testing because it has well understood lattice dynamics (Sangster *et al.*, 1970) and a small number of atoms in the unit cell. The interatomic potential model of Baram & Parker (1996) was used, and the GULP calculation performed using 27000 \mathbf{k} -points.

Simulations were compared to the ‘experimental RMC’ PDF extracted from experimental neutron total scattering data collected at room temperature on the GEM instrument at the ISIS pulsed spallation neutron source (Williams *et al.*, 1997) over a range of momentum transfers $0 \leq Q \leq 42 \text{ \AA}^{-1}$. RMC is used to avoid the truncation ripples that arise from the Fourier transform of the experimental data. Further details on this experiment and the RMC analysis performed by others in our group, showing the validity of the RMC dataset, are published in Goodwin *et al.* (2005).

Comparing the experimental RMC data and model in Fig. 2.2, it can be seen that the peaks appear in the same places (i.e. the model optimises to have the same unit cell) and there is consistently close agreement to peak width over the full range of radii. However, the phonon model here gives peaks that are uniformly narrow. This is reflected in the agreement factors $A^2 = 0.136$ and $A_r^2 = 1.96$, obtained over the entire range of r shown in the graph.

2.5.2 Calcium/strontium titanates

The calcium/strontium titanates were studied as they have reasonably well understood lattice dynamics, yet are much more complicated than MgO, and illustrate several features of the methodology. This solid solution has the ideal cubic perovskite structure (Fig. 2.4(a)) at room temperature for the pure $x = 0$ SrTiO₃ end-member, while the $x = 1$ CaSrTiO₃ end-member has an orthorhombic structure with space group $Pnma$, due to rotations of the TiO₆ tetrahedra about the three crystallographic axes. What is particularly interesting about these perovskites is the cation ordering (between A = Sr or Ca) observed on the 12-fold coordinated perovskite A-sites at intermediate x : at $x = 5$ the structure is $P2_1nm$, as shown in Fig. 2.4(b). The Rietveld refinements of Hui *et al.* (2007) have shown that standard powder diffraction techniques cannot unambiguously reveal the ordering pattern, so Hui *et al.* used a new RMC approach of ‘atom-swapping’ (Tucker *et al.*, 2007), adjusting the cation ordering in a configuration of 14000 atoms to bring about agreement with experimental total scattering data. It is interesting to perform a similar investigation from a computational perspective, to see the effects of adjusting the cation ordering in the model on the PDF.

Experimental neutron total scattering data for these perovskites had been collected as described by Goodwin *et al.* (2005) on the GEM instrument at ISIS over a large range of momentum transfers ($2.2 \leq Q \leq 46 \text{ \AA}^{-1}$) and used as input to the Reverse Monte Carlo (RMC)

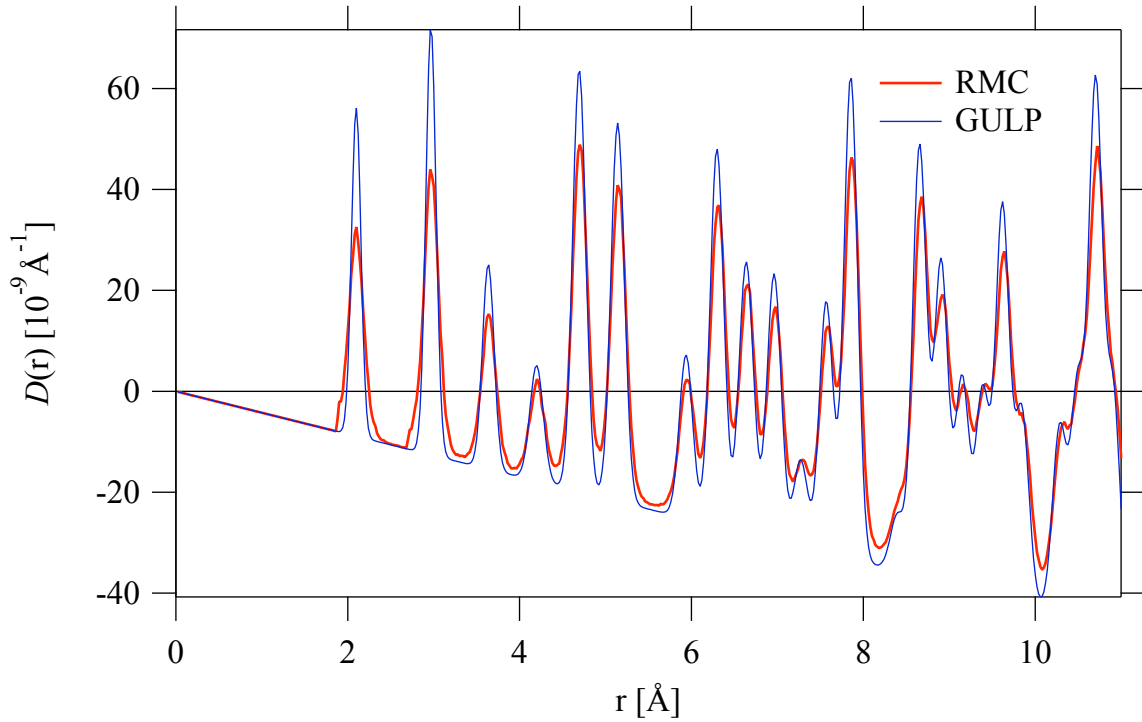


Figure 2.2: $D(r)$ for MgO at room temperature comparing GULP calculations (blue line) to RMC results derived from experimental data (red line). Agreement factors are $A^2 = 0.136$, $A_r^2 = 1.96$

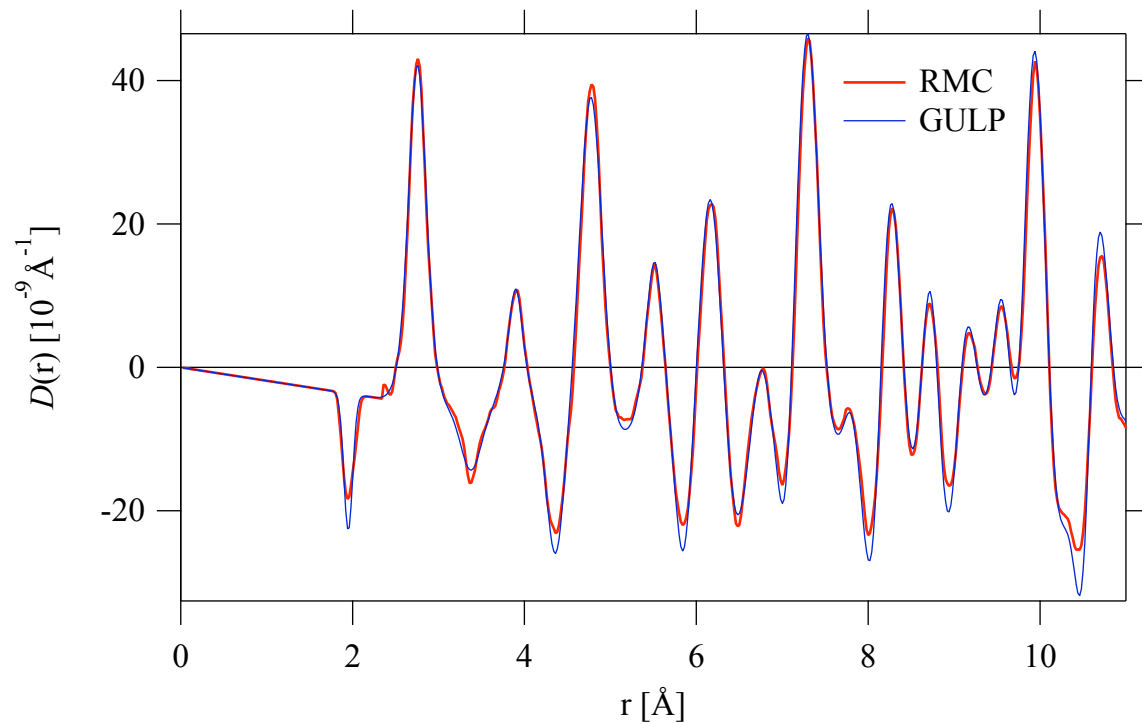


Figure 2.3: $D(r)$ for SrTiO₃ at room temperature comparing GULP calculations (blue line) to RMC results derived from experimental data (red line). Agreement factors are $A^2 = 0.029$, $A_r^2 = 0.778$.

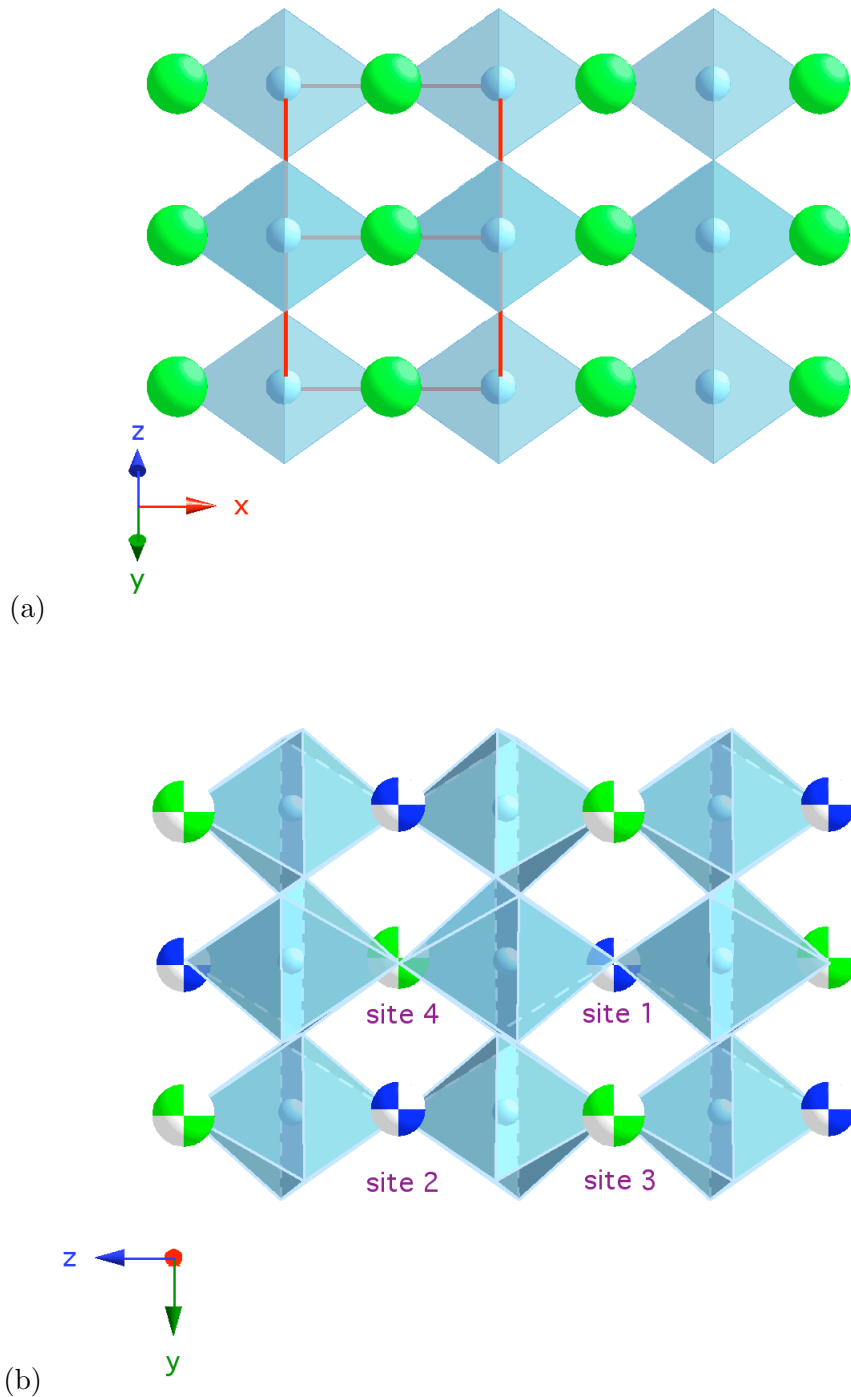


Figure 2.4: The unit cells for (a) the pure SrTiO_3 end-member and (b) the $x = 0.5$ intermediate $\text{Ca}_x\text{Sr}_{1-x}\text{TiO}_3$, shown to scale. The tetrahedrally coordinated Ti are shown in pale blue coordination polyhedra. Sr is shown in green, and Ca in blue, with the possible A-site cation ordering in the intermediate structure represented by segmented spheres. The sites labels are used in Fig. 2.5 to distinguish the three possible ordering patterns. The colour of the cations in this figure shows the ordering observed experimentally.

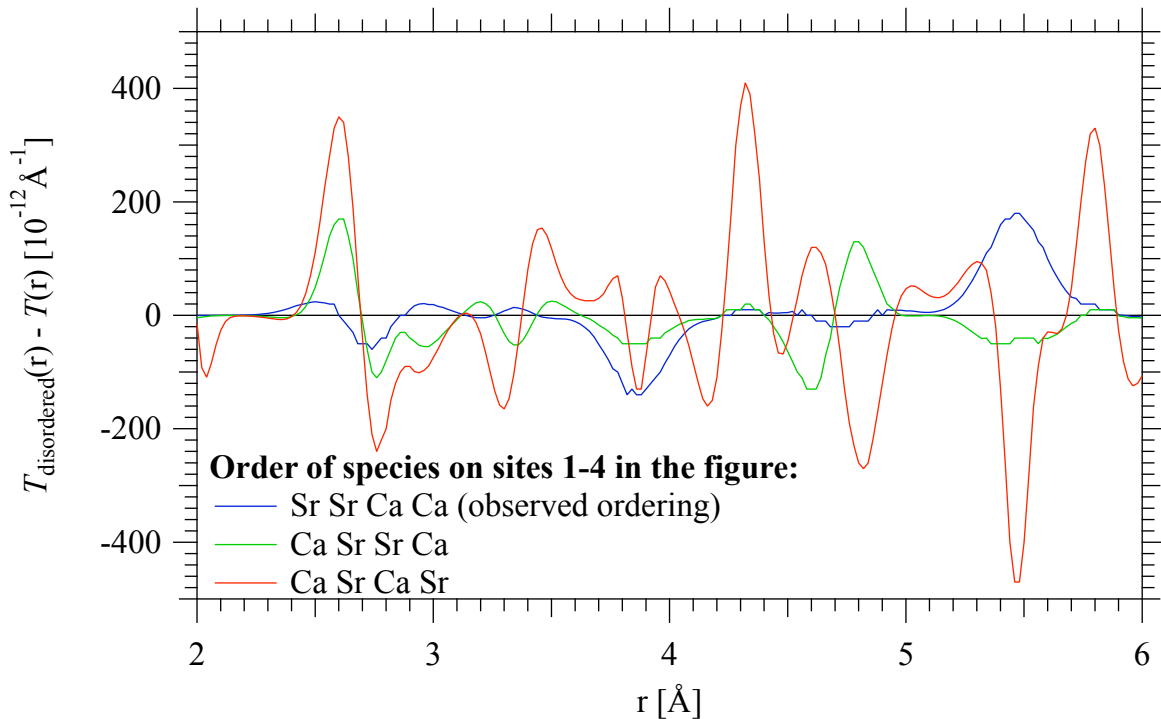


Figure 2.5: $\text{Ca}_x\text{Sr}_{1-x}\text{TiO}_3$ at $x = 0.5$, showing the difference between the $T(r)$ (the most appropriate choice of PDF for peak-fitting) for the disordered structure and the three possible ordered structures, all calculated using GULP. The structure seen experimentally is the ‘observed ordering’, giving rock-salt like coordination of the two cations. What has been demonstrated here is that there are real differences in the PDF that can be probed experimentally to establish ordering. The possible sites are shown in Fig. 2.4(b).

procedure to generate PDFs from approximately 2000 configurations, as described in the primary reference. Using the RMC ‘experimental’ dataset avoids truncation ripples while giving an excellent match to experimental data, as demonstrated by Goodwin *et al.* (2005); Hui *et al.* (2007).

An empirical potential model capable of studying the lattice dynamics across the entire solid solution was refined in GULP against a range of experimental ‘observables’: unit cell, elastic constants, and IR modes for both end-members, and an ordered intermediate $\text{Ca}_x\text{Sr}_{1-x}\text{TiO}_3$ with $x = 0.5$. The PDF and total scattering data were *not* included in the GULP refinement of the potential model. The potential model was first tested against the PDF for the SrTiO_3 end-member: SrTiO_3 results were produced by optimising the energy at constant volume with a unit cell fixed¹ at $a = 3.9 \text{ \AA}$. Convergence of phonon properties was achieved with 3375 \mathbf{k} -points.

¹to be the same as that found experimentally by Hui *et al.* (2005).

Fig. 2.3 shows the excellent agreement ($A^2 = 0.029$, $A_r^2 = 0.778$) of the GULP model and experimental RMC dataset. The peak shapes are well reproduced, demonstrating both the validity of the method and the use of this refined empirical potential model for further investigations.

The effects of ordering on intermediate $\text{Ca}_x\text{Sr}_{1-x}\text{TiO}_3$ with $x = 0.5$ were studied. 50% partial occupancies were set with ‘mean-field’ atoms with the physical properties of the combined species for each occupancy. The three possible ordered structures were also implemented: the rock-salt type ordering provided the best fit to the experimental PDF. The effects of the different ordering patterns are best seen by comparing the difference plots between the disordered (mean field) model and the three possible ordered arrangements. It is clear that each ordering gives rise to an observably different PDF (Fig. 2.5). This provides an additional validation for the approach taken by Hui *et al.*, who observed the rock-salt like ordering pattern on average over the RMC configurations derived from experimental total scattering spectra. The most noticeable differences here are in the width of the peaks, although it was differences in integrated peak areas that allowed Hui *et al.* to determine the natural ordering of $\text{Ca}_{0.5}\text{Sr}_{0.5}\text{TiO}_3$ through RMC ‘atom swapping’.

This study on calcite/strontium titanates has both demonstrated the ability of the new analytical tool to reproduce experimental PDFs when combined with a good interatomic model, as well as showing how computational experiments on cation ordering can reveal the subtle changes to the PDF that are to be expected in experimental data, confirming the results of RMC ‘atom swapping’ analysis.

2.5.3 Phonons-from-diffraction: limiting the energy range in MgO and SrTiO₃

The challenge of extracting phonon dispersion curves from diffraction data has been discussed in Section 1.4.8. It was in order to establish the appropriate energy range over which this technique might be possible that this simulation tool was initially developed.

The new GULP module was used with both MgO and SrTiO₃ to study the role of different phonon modes on the overall width of the PDF peaks. GULP simulations with the PDFcut keyword over a range of cut-off frequencies show low frequency modes dominate the PDF. Room temperature results of the dependence of various peak widths on ω_{max} demonstrate that the peak widths in the PDF are relatively insensitive to most of the high energy modes. For MgO (Fig. 2.7), most of the peak widths have stopped changing by ~ 15 THz; for SrTiO₃ (Fig. 2.8), this occurs at ~ 10 THz. Each individual line on the graph comes from a distinct pair at a particular r -spacing; the distinct shapes of the curves are due to the independent information

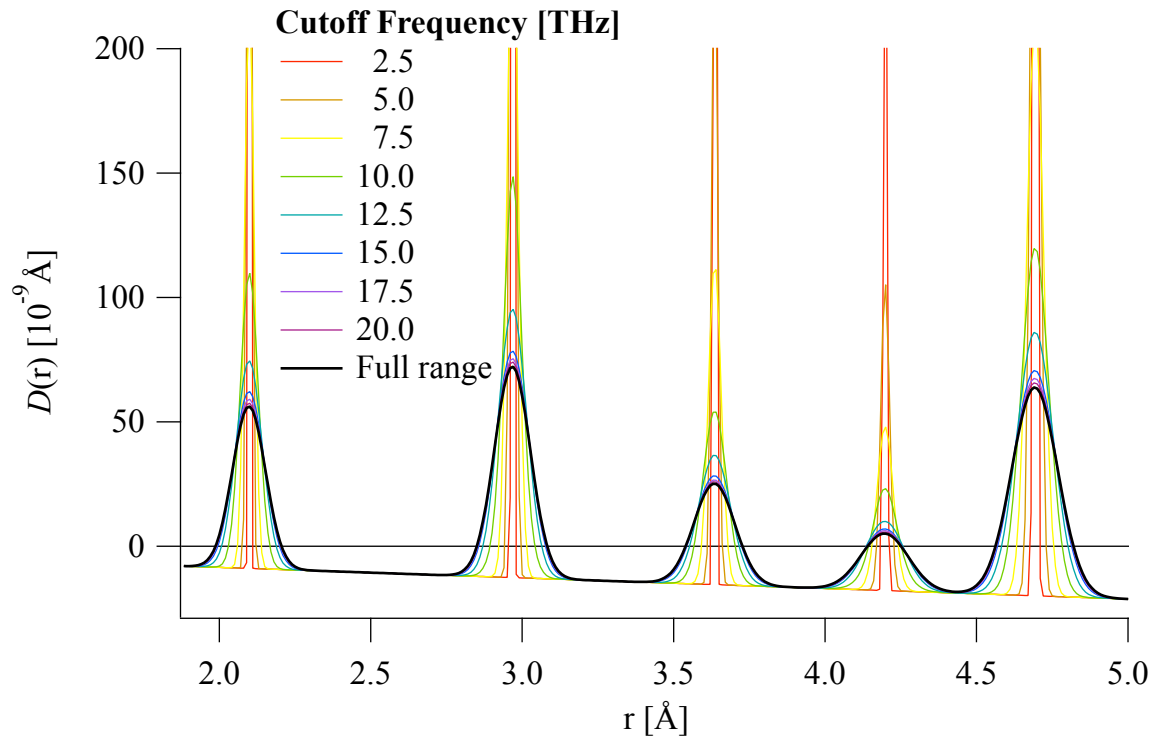


Figure 2.6: The effect of the cut-offs on the $D(r)$ peak widths for MgO, showing how the low energy modes dominate: by ~ 15 THz the peak shapes show very little difference to the full energy model.

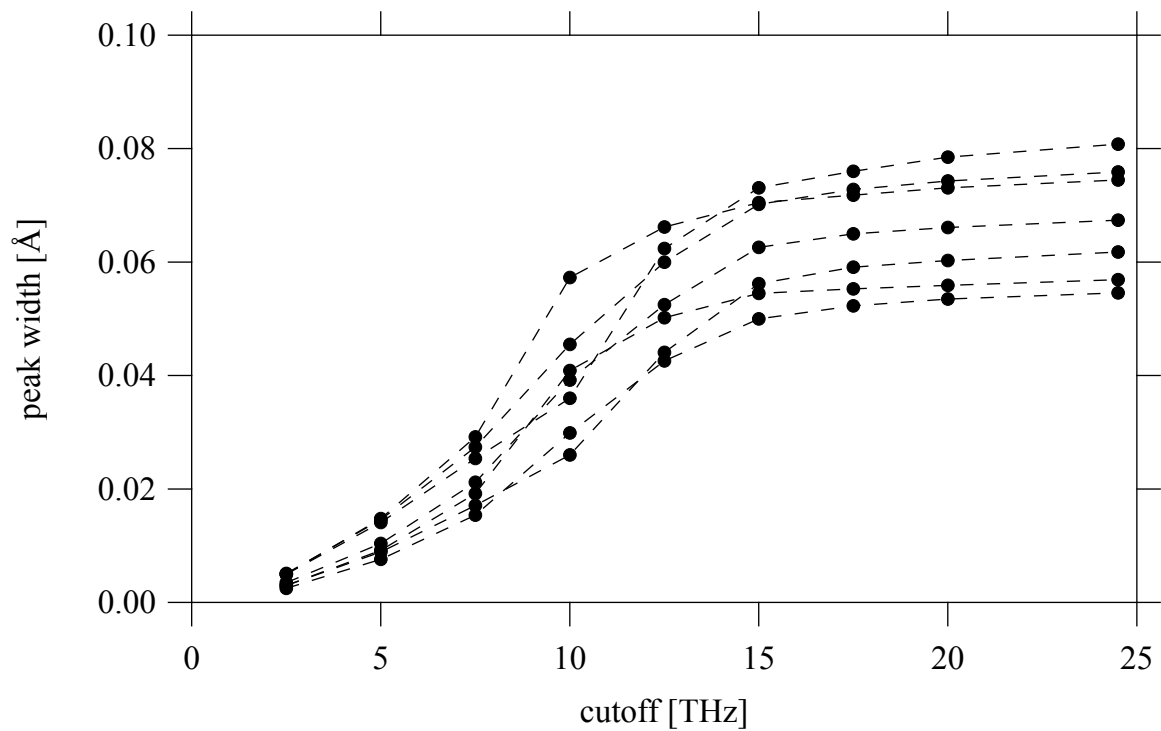


Figure 2.7: PDF peak widths for a selection of peaks for MgO, against the maximum cut-off frequency used in the new GULP PDF module. The domination of the low energy modes shown here is also apparent in the $D(r)$ shown in also Fig. 2.6.

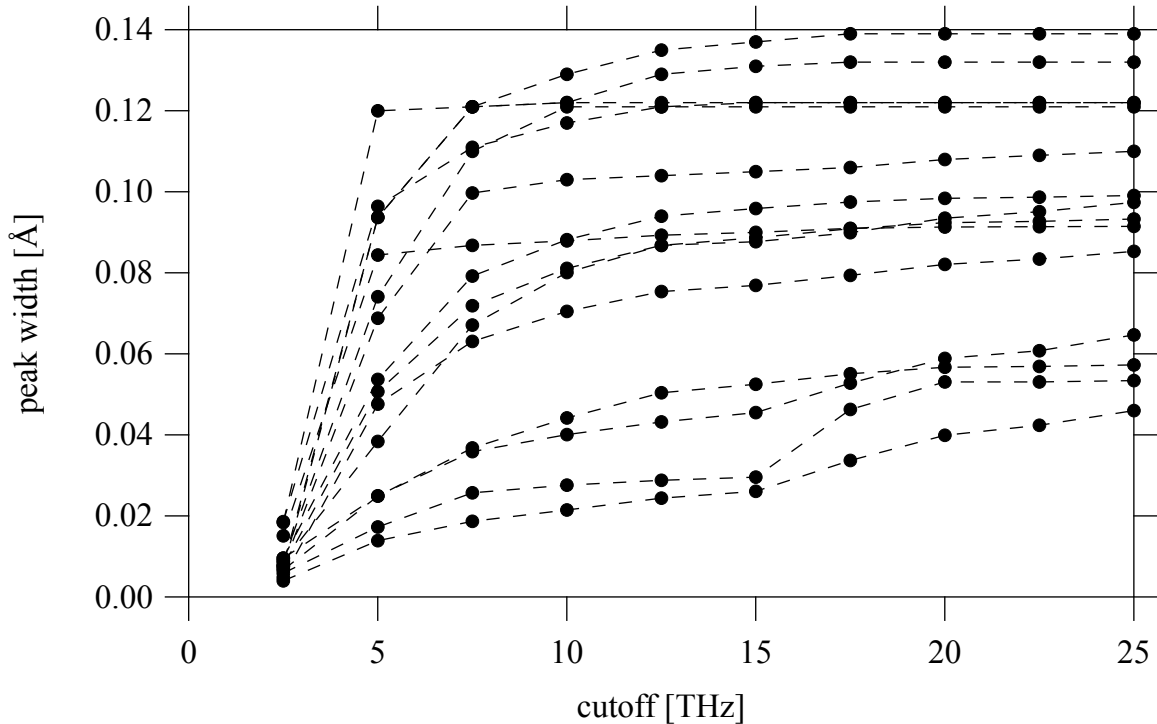


Figure 2.8: PDF peak widths for a selection of peaks for SrTiO_3 , against the maximum cut-off frequency used in the new GULP PDF module. It can clearly be seen that the low energy modes dominate the width of the PDF peaks, with the high energy modes making very little difference.

about the phonon contributions to the peak-widths for that specific pair. The trends shown here are independent of temperature.

The importance of these results lies in the implications for attempts to extract phonon dispersion curves from diffraction data (total scattering patterns). It is well understood that the contribution to the atomic displacements of any vibration of frequency (ω) is proportional to $1/\omega^2$, so it can be expected that low frequency modes are more likely to be accessible through this approach. These calculations quantify this: the point at which the majority of peak-widths stop changing with increasing ω_{max} corresponds to the maximum energy modes extracted from neutron total scattering by our group using RMC.

2.5.4 α -Cristobalite (SiO_2): interatomic models and the PDF

Silica is a hugely important mineral, found extensively in rock formations and of technological importance as a glass and in ceramics. It is made up of rigid units of SiO_4 tetrahedra: the different possibilities for the connectivity of these building blocks give it a highly varied phase

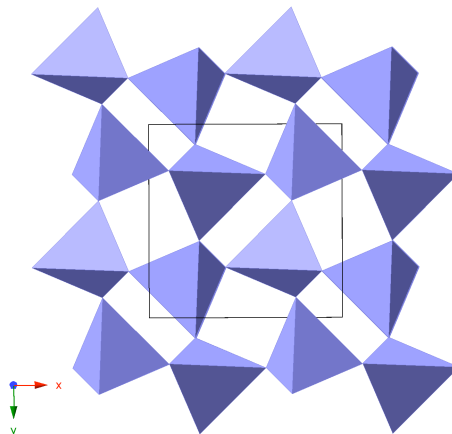


Figure 2.9: The unit cell of α -cristobalite, showing the interconnected SiO_4 tetrahedra.

diagram. This local ordering provides the common feature between the crystalline and amorphous counterparts (studies of amorphous silica are presented in Chapter 5). Cristobalite is the high-temperature crystalline phase of silica stable above 1743 K. It exists as the disordered β -cristobalite (see Chapter 3), metastable with respect to quartz, until cooled below 533 K. It then transforms to the tetragonal $P4_12_12$ structure (see Pluth *et al.*, 1985; Schmahl *et al.*, 1992) of α -cristobalite shown in Fig 2.9.

I have performed many computational studies of silicates in this thesis, so it is important to justify the choice of interatomic model. α -Cristobalite the appropriate polymorph for these initial investigations because the structure of α -cristobalite is well accepted, simulations on this polymorph are not overtly computationally expensive, and I am able to compare simulations to experimental total scattering and (in Chapter 5) INS powder spectra. I present a detailed PDF study for two widely used transferable silicate interatomic potential models; the polarisable shell empirical model of Sanders *et al.* (1984) and the rigid ion model based on *ab initio* calculations from Van Beest *et al.* (1990) (VB). In the light of this, I discuss the density of states for these and two other rigid ion interatomic models (Tsuneyuki *et al.* (1988) commonly referred to as TTAM, and a new refinement by Carré *et al.* (2008) based on the VB model), giving comprehensive justification for the choice of the Sanders model for all silicate studies performed in this thesis.

2.5.4.1 Experiment and simulated PDFs

Experimental total scattering data, published in Tucker *et al.* (2001c), were collected on a powdered sample of α -cristobalite using the (now decommissioned) ISIS LAD diffractometer (Howells & Hannon, 1999), the forerunner to the GEM diffractometer used in the other examples. Reverse Monte Carlo (RMC) analysis was used to generate PDFs from a configuration of

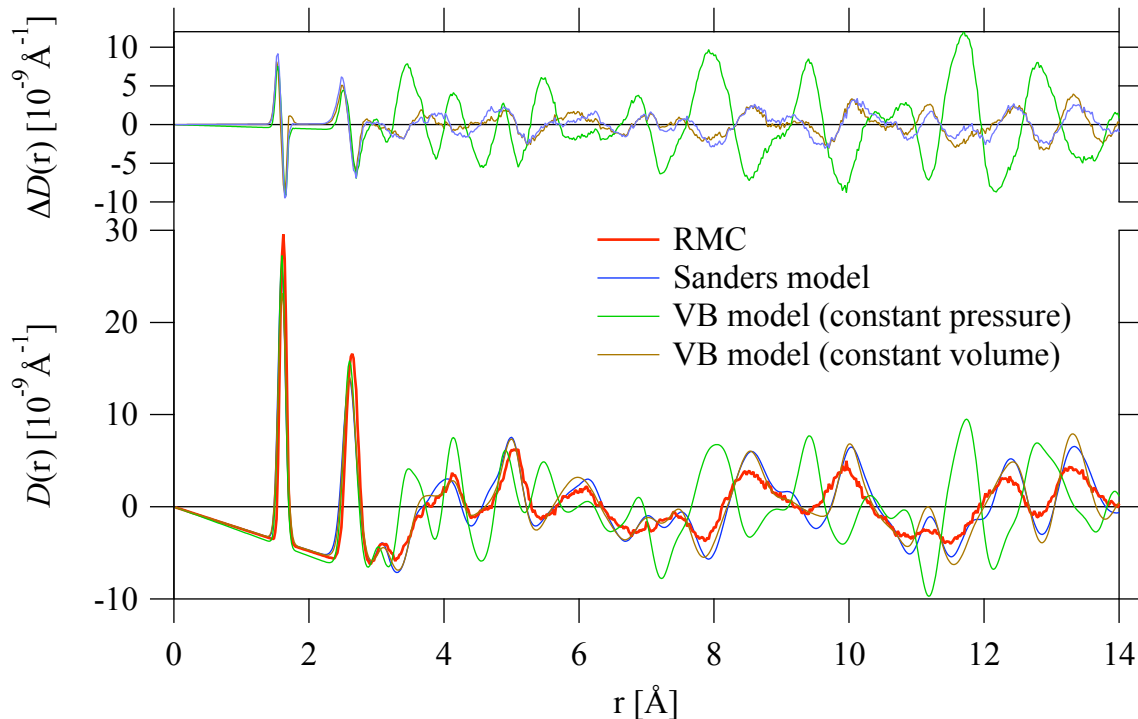


Figure 2.10: $D(r)$ for α -cristobalite at 475 K, showing the RMC data (red), Sanders model (blue, $A^2 = 0.073$, $A_r^2 = 0.510$), VB model optimised at constant pressure (green, $A^2 = 0.122$, $A_r^2 = 4.292$), and VB model optimised at constant volume (brown, $A^2 = 0.056$, $A_r^2 = 0.457$). The effect of the unit cell distortion in the constant-pressure VB model is clear.

12000 atoms. The excellent agreement between RMC and experimental PDFs demonstrates the benefit of this approach for avoiding Fourier ripples, as shown in Fig 2.1.

The Sanders and VB models were used with the new GULP PDF module to calculate PDFs for α -cristobalite at 475 K using 42875 \mathbf{k} -points. The Sanders model optimises to give a unit cell of $a = b = 5.01$ Å and $c = 7.06$ Å, matching experimental results, but the VB model optimised to have $a = b = 4.89$ Å and $c = 6.53$ Å. To allow the best comparison between the models, the VB model was also constrained to optimise at constant volume, fixing the unit cell to the experimental parameters.

Comparing models and RMC experimental data (Fig. 2.10), it can be seen that the choice of interatomic potential model is important. Both the Sanders model and the constant-volume VB model give a very good fit and similar results. The constant-pressure VB model shows very little correspondence to the data as the peaks are in completely the wrong positions. This is primarily due to the difference in unit cell – especially as the optimised unit cell is proportioned slightly differently, with a relatively shorter c axis. First principles models, such as those used in the development of the VB model, often fail to exactly reproduce the experimental unit cell

while still preserving accurate phonon information. What has been demonstrated is that this model provides excellent agreement to the experimental PDF *when the cell is correct*.

2.5.4.2 Energy cut-offs

Before studying the effects of energy cut-offs on the different models, it is helpful to be familiar with both density of states: these are shown in the bottom two plots in Fig. 2.11 together with those of the two other models discussed below. The low energy region shows strong similarities between the constant-volume VB model and the Sanders model, with a clear shift to higher energies occurring when the constant volume constraint is removed from the VB model. At the other extreme the two models place the high energy modes at different energies, although the relative intensities of the peaks are not hugely different. The VB model is expected to perform well here as these modes were included in its development.

There are also considerable differences around 60 meV. As will be seen in Chapter 5, it is important for the INS studies to be able to correctly reproduce the experimental drop in the density of states in this region, which has been observed across many silicate polymorphs through INS (e.g. Nakamura *et al.*, 2001; Price & Carpenter, 1987). In this respect, the Sanders model is better suited to my purpose than the VB model. The question is whether this is born out in the PDF?

Using the same ‘cut-off’ approach as for MgO and SrTiO₃, the effect of different regions from the two models can be seen in Fig. 2.12. The effect of the cut-off energy on peak widths (for the first three peaks and two other representative peaks) is shown in Fig. 2.13. For most peaks, the low energy modes dominate the peak width with the high energy modes (particularly about 100 meV) making very little difference. These high energy modes will correspond to the internal modes of the SiO₄ tetrahedra – the Si–O stretch. It is therefore not surprising that these modes *do* have a more significant role in the first Si–O peak. The Sanders model (as seen in Fig 2.11) places these modes at considerably lower energy than the VB model. The equivalent high energy modes from vitreous silica were included in the development of the VB model so are closer to experimental values. Indeed the constant-pressure VB PDF gives the best fit to the first peak. Constraining the unit cell made little difference to the high energy modes but a large difference to the first 10 meV, and had a detrimental value on the quality of the fit here, leaving the Sanders model to give the closer agreement. It is important to note that beyond the first nearest neighbour, the Si–O interactions no longer show a marked dependency on the high energy modes.

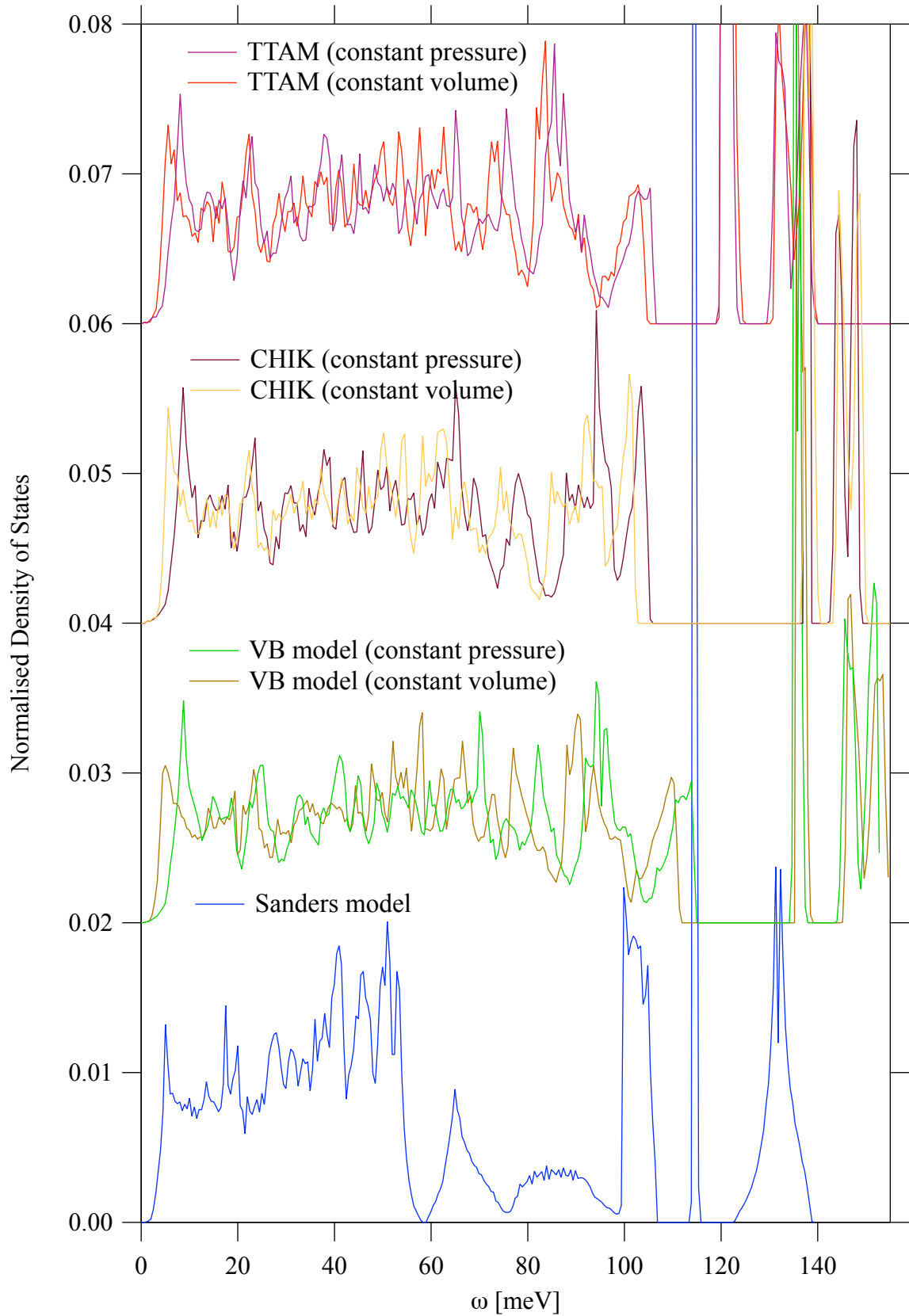


Figure 2.11: A comparison of the density of states for the models discussed in the text. The Sanders model optimised to have the same unit cell as seen experimentally. The other models have to be constrained to this volume. The CHIK model is a refinement of the VB model.

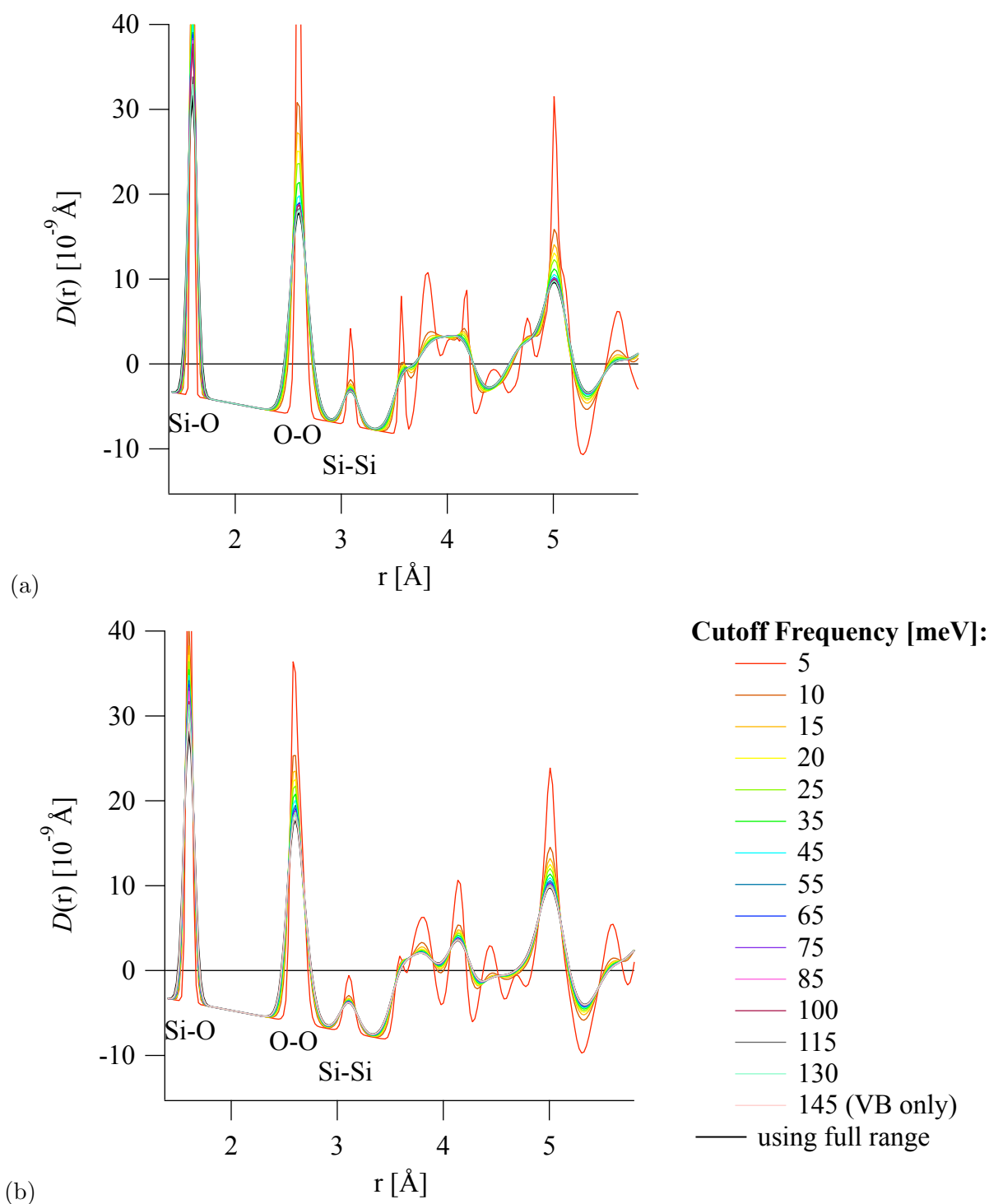


Figure 2.12: Simulated PDFs with a range of energy cut-offs for (a) the Sanders potential model and (b) the VB potential model optimised at constant volume. It can clearly be seen in both models that the low energy modes dominate the PDF, but the higher energy modes continue to make a visible difference, especially in the first Si-O peak. (The density of states in in Fig. 2.11 shows that the VB model at constant volume includes modes up to 155 meV, compared to 140 meV in the Sanders model.)

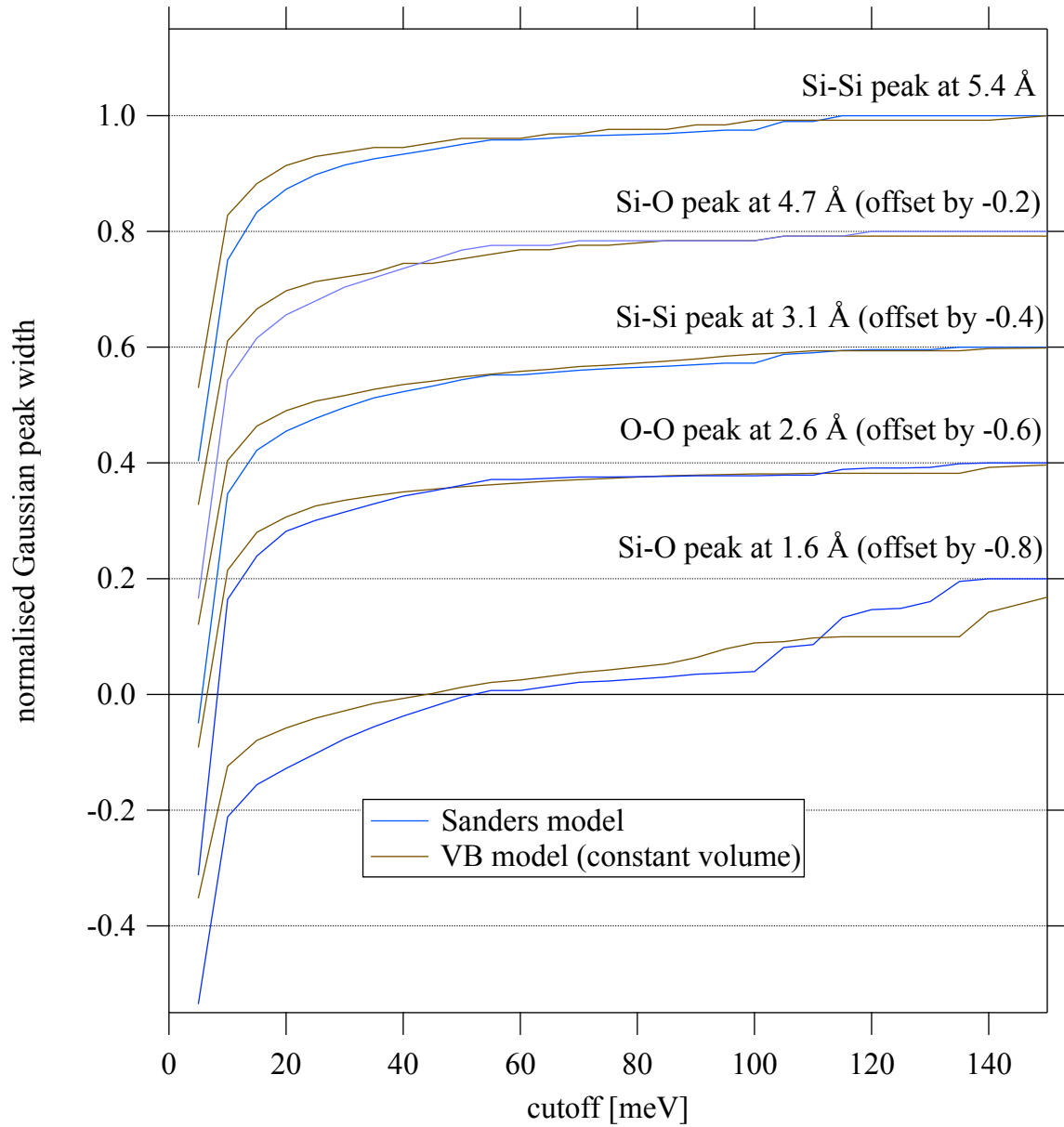


Figure 2.13: The effect of energy cut-offs on the width of PDF peaks from both the Sanders and VB model at constant volume can be seen to be dominated by the low energy modes, with the exception of the first Si–O peak which is very dependent on the high energy modes – note that the density of states in in Fig. 2.11 shows that the VB model at constant volume includes modes up to 155 meV, compared to 140 meV in the Sanders model. The other main difference between the two density of states is in the 55 to 100 meV region: there are small differences in the development of the peak widths through this region, but the overall relative contribution of these modes is not large.

2.5.4.3 Refinement using PDFs

In light of these findings, it is not surprising that the Sanders and VB (constant volume) models give very similar PDFs as the dominant low energy modes are very similar. The key question now is whether the PDF could be used for refinement of interatomic models? This is a subtly different question to whether full phonon dispersion curves can be extracted in a model-independent fashion from total scattering data, as it assumes a reasonable starting model. Recent work by Carré *et al.* (2008) has provided a new approach to potential refinements that does use the PDF, with considerable success. The so-called CHIK model, also shown in Fig 2.11, was based on the VB model and refined against Car-Parrinello molecular-dynamics (CPMD) simulations. As I would expect, the low energy region of the density of states, which was already reasonable, showed an improved fit to the CPMD density of states. The mid-range region (where the VB and Sanders models are so markedly different), also improved, with the desired decrease in the density of states occurring at the critical ~ 60 meV region. However, the refinement process was unable to fully enforce the large changes needed here. Finally, the high energy modes from the refinement were not such a close fit to the CPMD density of states as the starting VB model. In light of the results presented in this Chapter, I can confirm that, while there is some information in the PDF to loosely constrain the high energy modes, the low energy modes will be preferentially refined.

What these recent developments have shown is that there is scope for model refinement using the PDF, but it should be coupled to other experimental observables with appropriate weightings to ensure that the high energy phonon modes are not degraded. The inclusion of the new simulation module in GULP means that such a development could be implemented with relative ease: GULP already allows refinement of interatomic models against a range of phonon properties with adjustable weightings. It would also allow direct interaction with the experimental data, rather than a first principles simulation which is likely to misrepresent the experimental unit cell.

2.5.4.4 Choice of model

It has been seen that the popular silicate interatomic models have similar density of states in the low energy region yielding similar peak widths in the PDFs. Excellent agreement to the PDF was seen for both the Sanders and constant volume VB model. However, studies such as the first principles calculations by Benoit & Kob (2002), have confirmed that the VB model fails to reproduce the mid-to-high energy regions vibrational density of states and have also shown the eigenvectors to be poor. Crucially for the structural studies in the next chapter, only the Sanders model reproduces the experimental unit cell under normal conditions. The polarisable

oxygen shell in the Sanders model allows for realistic modelling of the electronic behaviour in the silicates. The other models are simpler rigid ion models, so it is perhaps not surprising that I find Sanders model is the one best suited to the current work.

I have included the density of states for another widely used interatomic model for silicates in Fig. 2.11: the so-called TTAM model (Tsuneyuki *et al.*, 1988). Like the VB model, this is a rigid ion model that was produced from first principles calculations. It can be seen that this shows many similarities to the two models examined in more detail, and also provides good fits to experimental data (not shown) although, like the VB model, it optimises to a unit cell that is slightly different from the experimental value unless constrained. I include it here as it is the model used in the generation of the silica supercells (as described by Trachenko *et al.*, 2000) for use in Chapter 5. The actual lattice dynamical calculations shown for these, and the other silicates in this thesis, were all performed using the Sanders model, although the robustness of the results was confirmed using the other potential models.

2.6 Conclusions

This new methodology is a powerful tool for performing PDF simulations, useful both for understanding experimental results, for example making it simple to label the partial (atom-specific) contributions, and for designing experiments, for example assessing the effects of incident neutron energy. The calculated PDFs are comparable to those found using RMC analysis of experimental data without the use of any adjustable parameters beyond the choice of interatomic potential model. The PDF has been shown to be sensitive to average structure while particularly suited to revealing short- to mid-range ordering, as seen in CaSrTiO_3 . These features will be relied upon in the rest of this thesis.

One advantage of adding this functionality to the GULP package is that the dynamical matrix used for the PDF can be calculated from any of the potential or force constant model-types currently available within GULP. GULP fitting routines can be used to refine these empirical potential models against other experimental observables prior to simulating the PDF, giving the best possible simulations. Moreover, the effects of temperature or pressure can be incorporated, making it appropriate for use with a wide range of crystalline systems under conditions both within the normal experimental range, and beyond it. Looking at the work of Carré *et al.* (2008), it is clear that there is a place for refinement of interatomic models against PDF spectra, but I feel that the high energy modes have been shown here to be so under-represented that it is almost dangerous to use the PDF without the addition of other experimental observables to provide better constraints on the high energy modes. GULP is ideally suited to such a development.

Another of advantage of these simulations is the ability to manipulate the input to the PDF, allowing experimenters further insight into the origins of the PDF. The partial PDF output gives the component parts of each peak as seen in the SrTiO_3 plot in Fig. 1.5, making identification easy. The excellent agreement of the simulation to experimental data in SrTiO_3 confirmed that the refined potential model was suitable for further ‘computational experiments’ on local ordering. The use of a mean-field atom in GULP – the ‘virtual crystal approximation’ – to give a simulation of a disordered material, together with the study of different cation ordering patterns, gave the same local ordering in CaSrTiO_3 as had been concluded from other simulation studies.

Perhaps one of the most important results has been the confirmation that low energy modes dominate the PDF to such an extent that the model-independent extraction of high energy phonon dispersion curves from total scattering data is never going to be possible: there is a point beyond which increasing energy contributions make very little difference to the PDF peaks. At the same time, the degree to which low energy modes effect the peaks implies that reliable dispersion curves should be attainable in this region, as has been found by our group in Cambridge. With the PDF simulation software, it is possible to predict the cut-off point for phonons-from-diffraction for each individual case. The simulation of α -cristobalite from the two different potential models with similar low energy density of states, but very different high energy modes, is a further example of this.

This chapter has introduced the formalism for simulation of PDFs, a set of quantitative agreement factors, and provided some illustrations of the power of the new GULP PDF module. This new code has now been incorporated into the beta-version of GULP 3.5, so it is hoped it will soon find use among a much wider audience. The RMC community are already making use of it: recent (unpublished) applications include separating the molecular and inter-molecular components to the PDF of organic crystals. It is used in the rest of this thesis to study local ordering and as a means of assessing the validity of different potential models (in their ability to reproduce low energy dynamics and stable structure), and has proved a useful tool alongside the simulation of inelastic neutron scattering patterns for many materials.

Chapter 3

Evaluation of domain models for β -cristobalite from the Pair Distribution Function

The new technique of phonon-based computer simulations of Pair Distribution Functions (PDFs) is used¹ to address the question of whether the structural disorder in the high temperature β -cristobalite phase of silica can be explained on the basis of domain models. None of the domain models give as good an agreement to experimental data as previously reported atomic configurations derived from a Reverse Monte Carlo analysis that are consistent with the Rigid Unit Mode model. This has immediate implications for the use of these models for simulation studies.

3.1 Introduction

The atomic structure of the high-temperature β -phase of cristobalite, SiO₂, has long elicited a controversy that remains unresolved. Whilst the average structure is undisputed – cubic $Fd\bar{3}m$ space group, Si atoms occupying sites that form a diamond lattice, and O atoms having average positions mid-way between Si atoms (Peacor, 1973; Schmahl *et al.*, 1992; Wright & Leadbetter, 1975) – and whilst it is also generally accepted that the structure must be disordered, there is no consensus as to the nature of the disorder.

The simple representation of the average structure described here is shown in Fig. 3.1. The main reason for believing that the structure of β -cristobalite is disordered is that this literal interpretation of the structure gives an unnaturally straight Si–O–Si bond angle of 180° and a

¹The majority of results presented here have recently been published as an IOP select paper (Cope & Dove, 2010).

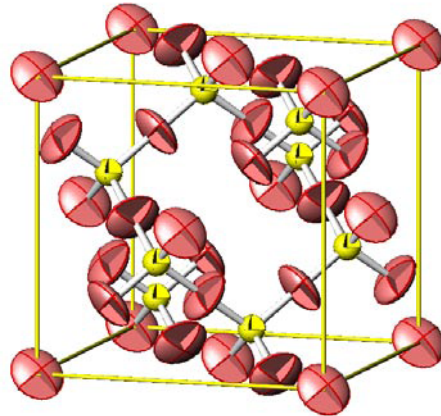


Figure 3.1: Crystal structure refinement of β -cristobalite with the single-site model for the oxygen atoms have unrealistically straight Si–O–Si bonds. The refinement yields large thermal displacement ellipsoids for the oxygen atoms elongated in the directions normal to the nearest-neighbour Si–Si vectors. (From Tucker *et al.* (2001c), used with permission.)

Si–O bond of length 1.55 Å, in contrast to typical values for silica and silicate structures of $\sim 145^\circ$ and ~ 1.61 Å respectively, as in the structure of low-temperature α -cristobalite (Pluth *et al.*, 1985; Schmahl *et al.*, 1992). The refined crystal structure of β -cristobalite based on this idealised structure presented in Fig. 3.1 shows a wide distribution of displacements of the oxygen atoms in directions normal to the Si–Si vector. This suggests either large thermal fluctuations or, more likely, some degree of disorder in the actual positions of the oxygen atoms (Dove *et al.*, 1997a; Peacor, 1973; Schmahl *et al.*, 1992; Tucker *et al.*, 2001c).

The rigidity of SiO_4 tetrahedra means that large-amplitude rotations of the Si–O bond can only occur by rotating the tetrahedra, and since neighbouring tetrahedra are linked into an infinite network a rotation of one tetrahedron will necessitate coupled rotations of surrounding tetrahedra. Thus the question that is often posed, even if only implicitly, is how to create disorder on a local scale whilst preserving the integrity of the tetrahedra? The importance of this question transcends the specific example of cristobalite; this issue is encountered, for example, in attempts to understand the relationship between structural fluctuations and physical properties, such as negative thermal expansion (Barrera *et al.*, 2005).

Within the literature there are two approaches for understanding this disorder, based either on the existence of domains or on Rigid Unit Modes (RUMs): work by our group in Cambridge has demonstrated that the dynamic disorder produced by RUMs can yield excellent agreement to experimental data. However, to date there has been no attempt to assess the relative merits of the domain models, and no means to compare them to the RUM model at the critical short- to

mid-range length scale. The key experimental probe required to assess the validity of the various models on an experimental basis is measurement of the PDF (Schmahl *et al.*, 1992) which can reveal fluctuations of the local structure that give rise to significant differences from the average structure.

Data for the PDF of the two phases of cristobalite were first reported by Dove *et al.* (1997a) and subsequently analysed using the Reverse Monte Carlo (RMC) method (Tucker *et al.*, 2001c). The experimental PDF showed that the average instantaneous Si–O bond lengths are indeed around 1.61 Å over a wide range of temperatures, and the PDF data for O–O and Si–Si distances can be best understood with an average Si–O–Si angle of 146° and ideal tetrahedral geometry of the SiO₄ units (Dove *et al.*, 1997a). This immediately confirmed that the local structure of β -cristobalite must arise through rotations of the SiO₄ tetrahedra.

What is needed to conclusively demonstrate which approach can best model the dynamical disorder in high temperature cristobalite is the new PDF simulation tool introduced in Chapter 2. The primary aim of this chapter is to use this new approach to resolve the controversy surrounding the local structure of β -cristobalite through the first quantitative analysis of the different models. I begin with a historical review of the various models followed by a detailed comparison of predictions from the different models.

3.2 Historical survey of models of disorder in β -cristobalite

3.2.1 Multi-site models

The first attempt to describe a disordered atomic structure of β -cristobalite, shown in Fig. 3.2, was to assume that the oxygen atoms occupy six positions in a ring around the mean position, each with a fractional mean occupancy of 1/6 (Nieuwenkamp, 1937; Peacor, 1973). This allows better agreement between the calculated and observed diffraction patterns than using the ideal cubic structure, giving bond lengths and angles that match the PDF analysis (Dove *et al.*, 1997a; Peacor, 1973; Schmahl *et al.*, 1992; Tucker *et al.*, 2001c). However, the model doesn't address the issue of how the disorder can be accommodated when it requires rotations of whole SiO₄ tetrahedra. Moreover, it is not easy to differentiate between a multi-site model and a continuous distribution of atomic positions because the distance between neighbouring oxygen sites in this model is comparable with the resolution of the diffraction experiment. The problem is amplified when thermal motion is included – as demonstrated by the way the thermal fluctuations shown in Fig. 3.2 smear the distribution of oxygen atoms when described using the six-site model. It should be appreciated that the maximum scattering vector Q obtainable

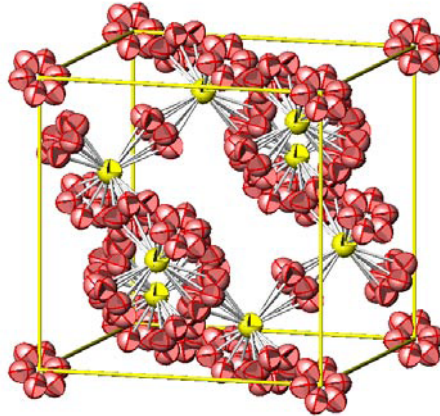


Figure 3.2: Crystal structure refinement of β -cristobalite with the six-site model, showing more reasonable bond angles than in the single-site model. Note the overlapping rings of oxygen thermal displacement ellipsoids, discussed in the text. (From Tucker *et al.* (2001c), used with permission.)

with conventional diffraction, $Q_{\max} = 2\pi/d_{\min}$, leads to a best resolution in any refined real-space structure of $\Delta r = 2\pi/Q_{\max} = d_{\min}$, where d_{\min} is the minimum d -spacing observed in the diffraction pattern. For X-ray diffraction experiments using standard Cu K_{α} radiation, the best real-space resolution possible is $\Delta r \sim 0.8 \text{ \AA}$. Using neutron diffraction from a spallation source as in Schmahl *et al.* (1992) can further improve this. Total scattering experiments extend the Q range so the resolution is even finer: the data used here have a resolution of 0.13 \AA .

3.2.2 Domain models

The most popular interpretation of the structural disorder has been to assume that the local structure consists of domains of a lower-symmetry phase, with the average cubic symmetry arising as an average over all possible orientations of these domains. The first domain model was proposed by Wright & Leadbetter (1975) (WL), followed by an alternative model proposed by Hatch & Ghose (1991) (HG). A search of the Science Citation Index at the time of submission highlights the fact that the WL model has gained more popularity than the HG model in the literature and is frequently being used in simulation papers as the starting point for static energy calculations (such as Arasa *et al.*, 2008; Jiang & Carter, 2005) although neither model has been subjected to detailed scrutiny.

3.2.2.1 The WL model

The WL model (Wright & Leadbetter, 1975) proposes that the disorder is accommodated by a local distortion of the crystal structure into the tetragonal form of space group $I\bar{4}2d$. The average cubic phase results from disorder over all possible orientations of small domains of this structure. In fact, WL suggested that a domain could be as small as one unit cell. The structure proposed by WL is shown in Fig. 3.3: it is derived from the ideal cubic structure (also shown) by a rotation of the tetrahedra about the $[0, 0, 1]$ axis. This distortion corresponds to a phonon mode of zero wave vector (the Γ point at the centre of the Brillouin zone). The lattice parameters for this model (after lattice energy minimisation, see Section 3.4) are $a = 5.028 \text{ \AA}$ and $c = 7.205 \text{ \AA}$, with a mean Si–O distance of 1.597 \AA .

3.2.2.2 The HG model

In the HG model (Hatch & Ghose, 1991) the disorder arises from all twelve orientations of domains of the tetragonal low-temperature α form of cristobalite. The structure can be compared with the ideal cubic and WL structures in Fig. 3.3. Here, tetrahedra are rotated about axes parallel to the horizontal and vertical directions in the plane of the diagram (orthogonal axes normal to the $[0, 0, 1]$ axis). This distortion arises from a phonon mode with wave vector $\mathbf{k} = (1, 0, 0)$, corresponding to the X -point on the face of the Brillouin zone. The lattice parameters for this model (after lattice energy minimisation) are $a = 5.010 \text{ \AA}$ and $c = 7.062 \text{ \AA}$, with a mean Si–O distance of 1.597 \AA .

3.2.3 The Rigid Unit Mode model and evidence from Reverse Monte Carlo simulations

Analysis of the rigidity of a model structure based on fixed SiO_4 tetrahedra with flexible linkages at the shared corners showed the existence of planes of wave vectors in which one or more phonons could propagate without deforming the tetrahedra (Hammonds *et al.*, 1996; Swainson & Dove, 1993). These phonons, called Rigid Unit Modes (RUMs), will have low frequency because they do not involve the larger force constants associated with deformations of the tetrahedra. The prediction of planes of low-frequency modes in β -cristobalite exactly matches the diffuse scattering seen in transmission electron diffraction (Hua *et al.*, 1988). Thus it was proposed that the disorder in the cubic β -cristobalite arises from the dynamic superposition of all RUMs across the planes of wave vectors, giving large contributions to the atomic motions because their amplitudes scale as $1/\omega$. This interpretation by our group in Cambridge has been supported by a number of independent simulation studies (Bourova & Richet, 1998) as well as model simulations (Gambhir *et al.*, 1999).

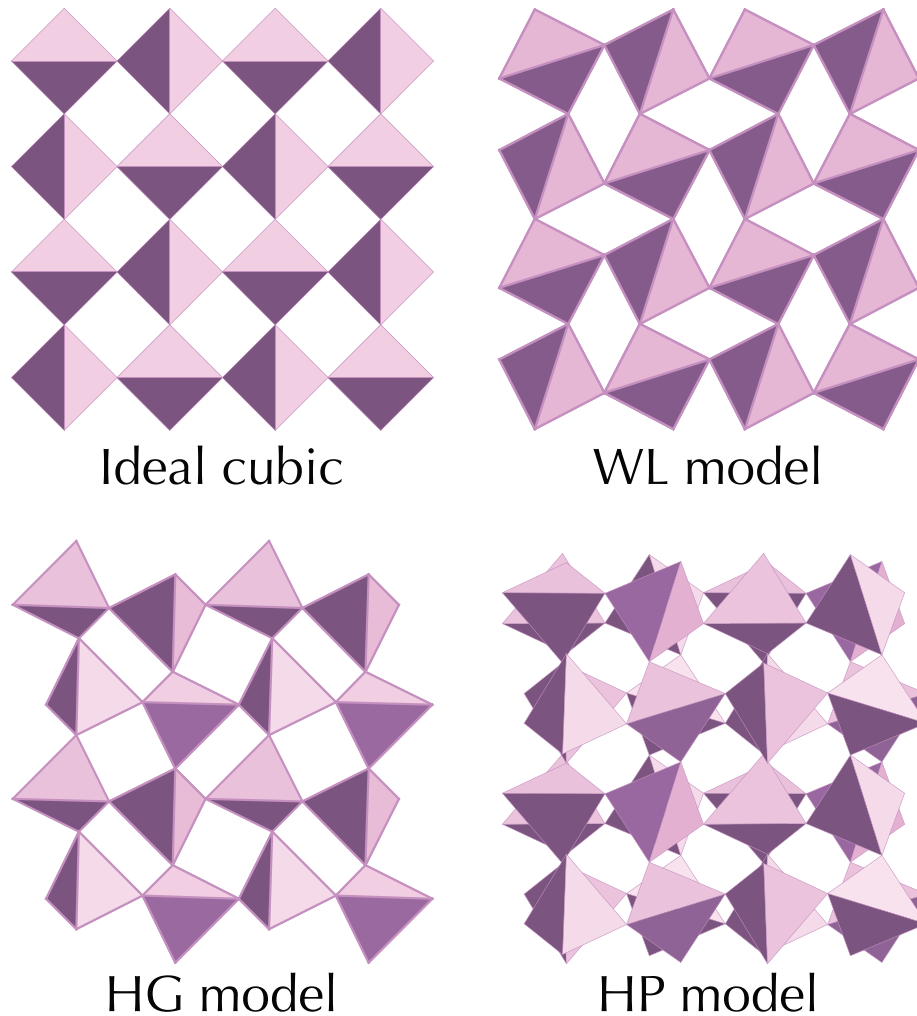


Figure 3.3: Comparison of the ideal cubic representation of the crystal structure of β -cristobalite with the crystal structures of the WL model (space group $I\bar{4}2d$, viewed down the tetragonal $[0,0,1]$ axis), the HG model (experimental α -phase, space group $P4_12_12$, viewed down the tetragonal $[0,0,1]$ axis), and the HP phase (experimental high-pressure phase, space group $P2_1/c$, viewed down the $[2,0,1]$ direction). These structures correspond to modulations having wave vectors located at different points on the surface of the Brillouin zone of the ideal cubic structure. SiO_4 tetrahedra are highlighted as shaded solid objects. Model structures were obtained using lattice energy minimisation as described in the text.

The suitability of the RUM model is demonstrated by its prediction of the existence of the soft mode for the β - α transition as seen in spectroscopic measurements in the α -phase (Swainson *et al.*, 2003; Zhang & Scott, 2007), as well as giving low-frequency phonons that can provide transition pathways between the different phases.

Reverse Monte Carlo (RMC, Tucker *et al.*, 2001a) simulations based on experimental total scattering data (Tucker *et al.*, 2001c) showed a number of features supporting the RUM model. These include reproducing three-dimensional diffuse scattering patterns predicted by the RUM model and as seen in electron diffraction, and that the oxygen atoms are continuously distributed on a broad annulus around the Si-Si vector rather than occupying specific sites. Analysis of the configurations showed that the most significant contributions to atomic motions arose from SiO_4 tetrahedra moving as rigid bodies (Wells *et al.*, 2002).

3.2.4 A new domain model: the HP model

Given that the popular domain models are formed by deformation of the ideal cubic structure by the eigenvectors of specific RUMs, it became apparent that it would be equally credible to construct a domain model based instead on the structure (Dove *et al.*, 2000a) of the high-pressure monoclinic phase. This structure is derived from the parent cubic structure by a more complex set of rotations involving unequal rotations of the SiO_4 tetrahedra about two orthogonal axes with wave vector $\mathbf{k} = (\frac{1}{2}, \frac{1}{2}, \frac{1}{2})$, corresponding to the L -point on the face of the Brillouin zone. This is compared with the other structures in Fig. 3.3. The lattice parameters for this model (after lattice energy minimisation) are $a = 8.739 \text{ \AA}$, $b = 5.017 \text{ \AA}$, $c = 10.067 \text{ \AA}$ and $\beta = 125.2^\circ$, with a mean Si-O distance of 1.597 \AA .

3.2.5 Is there a way to reconcile the models?

The three domains discussed above all represent distortions of the cubic structure via condensation of individual RUMs of β -cristobalite. Thus the RUM model of disorder will include fluctuations into each of the domain model phases considered here, but will also include a myriad of other fluctuations with a range of wave vectors. Whilst all three domain structures are symmetry subgroups of the parent cubic symmetry, they are not subgroups of each other but instead are orthogonal deformations of the structure. There is no *a priori* reason to suggest a preference of either the WL, HG or HP structures over the others as candidates for any domain model, but it is possible that one domain fluctuation might be particularly important. This has not yet been tested.

All models imply a length scale over which the local symmetry will be lower than the average symmetry, which might enable certain anomalies in the spectroscopy to be understood: both

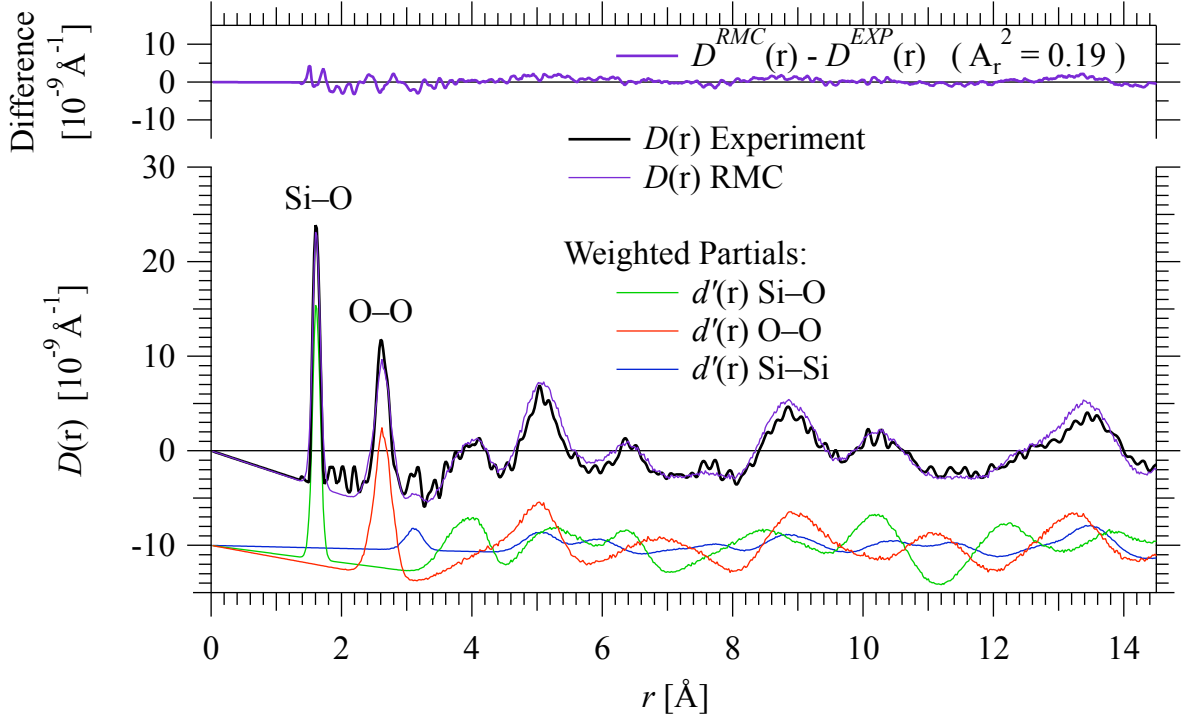


Figure 3.4: Experimental (thick black line) and RMC model (purple) $D(r)$ of β -cristobalite (SiO_2) at 700 K, showing how the weighted partial pair distributions (offset) for each atom-type contribute to the total $D(r)$. The difference plot shows the excellent agreement between the RMC model and the experimental data, giving an A_r^2 agreement factor of 0.19. The extra ripples in the experimental data are Fourier truncation ripples and should be ignored.

Infrared and Raman spectra contain an unexplained mode in the α phase that remains on heating above the α - β phase transition but that should be absent by symmetry in the β phase. In contrast, all other vibrations that are expected to disappear at the phase transition do in fact do so (Swainson *et al.*, 2003). In light of this Zhang & Scott (2007) proposed that the WL model should be reconsidered as the best approach to understanding the structure of β -cristobalite. Unusually, they also suggested that the structure of the α phase, about which there has been no controversy, should be assigned to a lower-symmetry structure. Coh & Vanderbilt (2008) found a possible explanation for the anomalous IR mode through an analysis of the phonons in the WL structure based on *ab initio* DFT methods, based on domains of the WL structure. Accepting this as further proof of the importance of disorder, the critical issue is to understand the structure in terms of its short-range order and fluctuations. The PDF is the ideal probe of the relevant length scales, so the new GULP PDF module is the appropriate tool to allow comparison of the domain models against experimental data.

3.3 Experiment

Previously published neutron scattering measurements for the PDF of cristobalite (Dove *et al.*, 1997a; Tucker *et al.*, 2001c) are used for comparison with the new simulations. The original data were collected on the (now decommissioned) ISIS LAD diffractometer (Howells & Hannon, 1999); details are given in the primary references (Dove *et al.*, 1997a; Tucker *et al.*, 2001c). This was the forerunner of GEM, and provided low Q -space resolution but high intensity over a large Q -range yielding excellent resolution in the real-space PDF. The machine was optimised for use with disordered materials, but for a crystal of cubic symmetry and modest size unit cell it has still adequate Q -space resolution. A Monte Carlo approach was used to obtain the PDF from the total scattering data – this method enforces the absence of Fourier ripples before the first peak (Tucker *et al.*, 2001b). Experimental data are available for both phases of cristobalite, collected at temperatures of 475 K (α) and 575 K, 700 K and 825 K (β). The measured PDFs of the two phases show significant differences for distances beyond the nearest-neighbour Si–O, O–O and Si–Si peaks, as noted in the original publication (Dove *et al.*, 1997a). On the other hand, there appears to be little difference in the measured PDFs of the β phase at different temperatures.

Published RMC analysis (Tucker *et al.*, 2001c) of total scattering is used for comparison with the domain models. The RMC method (Tucker *et al.*, 2001a) enables the total PDF to be interpreted in terms of partial PDFs, $d'_{m,n}(r)$. These are shown in Fig. 3.4 to facilitate interpretation of the individual peaks in the PDF. It is clear that beyond the first two peaks the various features in the experimental PDF correspond to contributions from more than one atom pair.

3.4 Simulation

Computer simulations were performed using the new GULP PDF module described in detail in Chapter 2. I use the popular and highly transferable empirical potential model of Sanders *et al.* (1984), which I have shown to give a good PDF for α -cristobalite in Chapter 2. Therefore I expect the Sanders model to reproduce the positions of the main features in $D(r)$ to within 2–3%. Larger differences would mean that the calculation and experiment are not in agreement. In this regard it can be noted that the main features in the experimental PDFs of both phases of cristobalite show considerable differences beyond the first Si–Si peak (peak three).

Each structure was relaxed to give the minimum lattice energy, and phonon calculations were performed using these relaxed structures. Convergence tests were performed to ensure accurate calculation of phonon properties – with emphasis on the PDF peak widths – and obtained using

a standard Monkhorst-Pack grid with 35 points along each reciprocal lattice vector and 42875 wave vectors within the first Brillouin zone. PDFs were computed for the same temperatures as in the experiments.

3.4.1 Agreement factors

Quantitative agreement factors as defined in Section 2.4 have been calculated across the full range of the graphs presented here. To aid interpretation of the agreement factors, it should be noted that comparing the experimental PDF data for α and β phases gives a value of $A_r^2 = 0.66$.

3.5 Results, discussion and conclusions

3.5.1 A benchmark from analysis of α -cristobalite

Benchmarks for both good and poor agreement are provided by comparing computed PDFs of each model with α -cristobalite experimental data, Fig. 3.5(a). The HG model is expected to give good agreement in this case, as this model is that of α -cristobalite. On the other hand, the WL and HP models should give poor agreement. Thus $A_r^2 = 0.49$ obtained for the HG model contrasts with $A_r^2 = 3.11$ and $A_r^2 = 1.38$ for the WL and HP structures. Fig. 3.5(a) shows how the difference plot and peak positions, widths and intensities reflect the level of agreement with experimental data.

3.5.2 Evaluation of domain models for β -cristobalite

The β -cristobalite experimental data and the three proposed domain models are compared in Fig. 3.5(b). A close match for nearest-neighbour Si–O, O–O and Si–Si peaks is seen in all structures, reflecting the fact that all models have nearly-perfect SiO₄ tetrahedra. There is reasonable agreement with the positions of the two features at around 4 and 5 Å in the overall PDF – from Fig. 3.4 it can be seen that these correspond to peaks in both the Si–O and O–O partial PDFs – but although the positions of these features match the data, the widths given by the WL and HP models are significantly different from experiment.

The WL model matches the positions of several features in the experimental PDF up to about 10 Å, and beyond the first five peaks gives a better fit to the position of peaks than the HG model. However, features in the WL model are significantly sharper than for experiment. This enhanced sharpening arises from the fact that the WL model crystal structure is simpler than the other models, so the peak broadening arises mostly from phonon broadening rather than the overlap of several atom-pair peaks with similar r . The WL model shows a notable difference from the experimental PDF at around 11 Å. The agreement factor has a value of

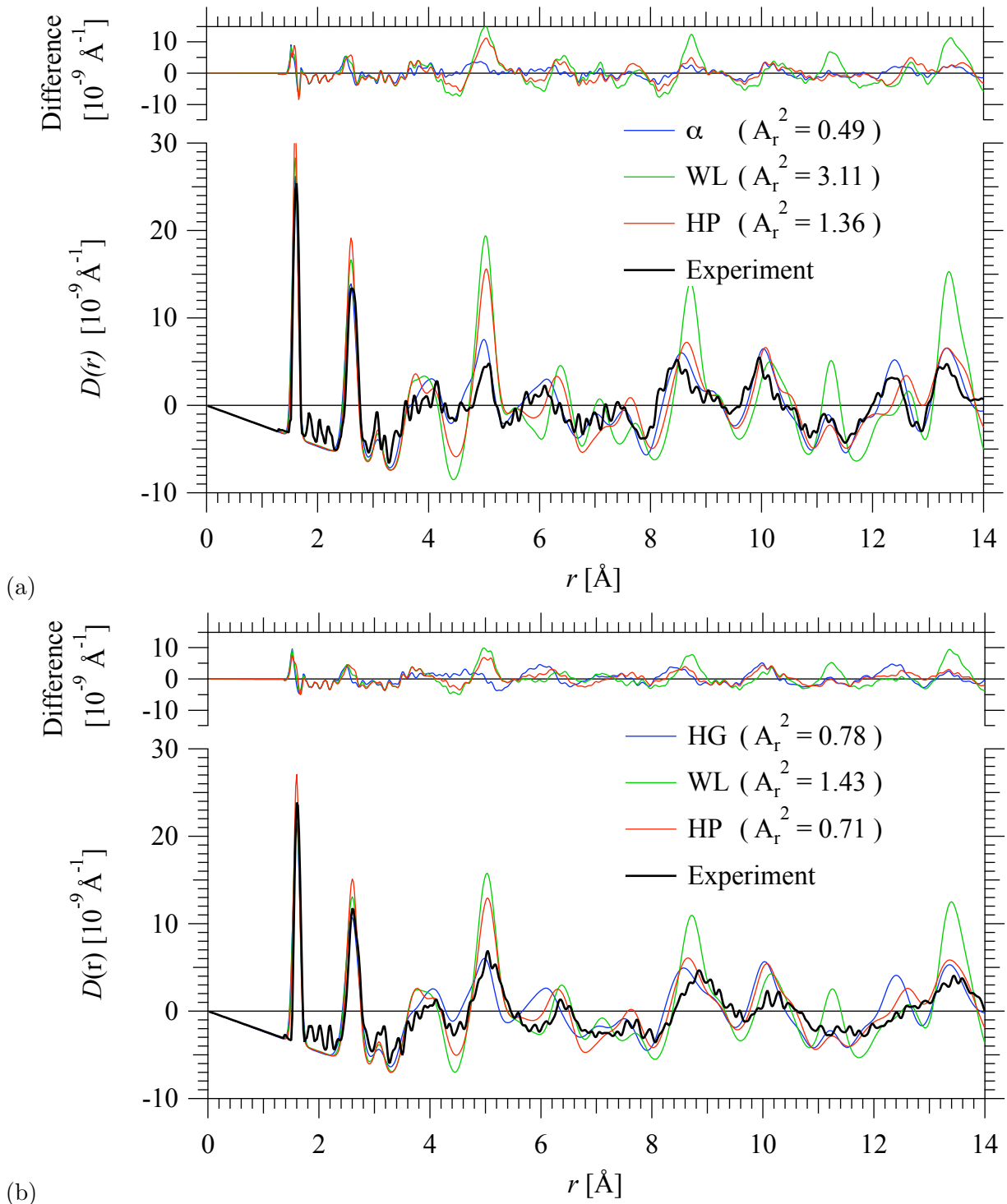


Figure 3.5: $D(r)$ of (a) α -cristobalite (SiO_2) at 475 K comparing experimental data (thick black line) with the three structural models discussed in the text. This shows how well the simulation can reproduce experimental data for a known structural model. Blue line: actual α -cristobalite structure. Green line: WL $I\bar{4}2d$ structure. Red line: HP $P2_1/c$ structure. The difference plot is shown above the main figure, using the same colours. (b) Shows the equivalent plot for β -cristobalite (SiO_2) at 700 K. The HG model is based on the α -cristobalite structure (blue line).

$A_r^2 = 1.43$, showing that the WL model no more corresponds to the β -cristobalite data than the HP model corresponds to the α -cristobalite phase. The WL model clearly gives a “poor fit” according to the benchmarks.

There is significant disagreement between the HG and experimental PDF beyond the first five peaks, starting clearly with the first feature at 6.4 Å. Subsequent features become out of register; for example, features at distances between 8–11 Å are at slightly lower r , and the predicted peak at 12.5 Å is not reflected in the experimental data. These discrepancies are consistent with differences between experimental PDFs for the two phases of cristobalite noted previously (Dove *et al.*, 1997a), and their effects are seen in the larger agreement factor of $A_r^2 = 0.78$ in the β -phase.

Finally, the HP domain model yields a similar level of agreement in its PDF to the HG domain model. It shows a reasonably good register of corresponding features between data and simulation, although the peak at 5 Å is too narrow. Like the WL model, the HP model gives a better fit than the HG model in the region of 6.4 Å and 12.2 Å due to having a more complex structure. This is reflected in the agreement factor, $A_r^2 = 0.71$, which is comparable to that obtained with the HG structures. Again, this falls outside the benchmark for a good agreement.

3.5.3 Discussion and conclusions

Having established the power of the PDF simulation software in the previous chapter, this study on β -cristobalite provided the opportunity to use these new methods of analysis to help resolve the controversy by assessing how far the popular structural models stand up to analysis on this key length-scale.

Our group in Cambridge have long argued (Gambhir *et al.*, 1999; Hammonds *et al.*, 1996; Schmahl *et al.*, 1992; Tucker *et al.*, 2001c; Wells *et al.*, 2002, amongst others), that a model of dynamic disorder is necessary to understand the structure of β -cristobalite, but showing that such a model can reproduce experimental data is not the same as proving that other, simpler methods, cannot. The results from my new phonon-based simulation tools makes it immediately obvious that none of the domain models have sufficient flexibility to accurately reproduce the experimental PDF. They all fail to give agreement factors in any way comparable to that of the α -cristobalite model to the α -cristobalite experimental data. However it is interesting to note that the HP domain model, which has not previously been considered as a possible domain structure, shows slightly closer agreement with experimental data than the WL and HG models at short length scales, while still breaking down on mid-range length scales (around 12.5 Å). This suggests that no one domain model can explain the disorder in β -cristobalite.

This first conclusion is of great importance as the WL model in particular is widely used as the starting point for simulations. The appeal is obvious: the domain models are simple, containing only a limited number of atoms. But it is important that workers in this area recognise that mid-range structural detail will not be accurately reproduced, making such simulations without merit.

It is clear that the best description of the PDF comes from the models generated by the RMC approach (Tucker *et al.*, 2001c), as is evident in the agreement factors. Given that the RMC method is driven by improving agreement to experimental data, this is not surprising. However, the degree to which this improves upon the domain models implies that the level of disorder in the RMC configuration realistically reproduces the experimental situation. While the agreement of the RMC results with data do not preclude other configurations with more constraints (e.g. a domain model) from giving similarly good agreement, none of these models actually do so. Moreover, the RMC fits are consistent with the absence of domains, as demonstrated through the calculation of the bond orientational distribution function (Tucker *et al.*, 2001c), and show a significant amount of RUM motion as seen in geometric algebra analysis (Wells *et al.*, 2002).

Much of the discussion about the disorder and local structure of β -cristobalite concerns the length scale over which structural fluctuations depart from the average structure. This is where comparison of models against experimentally-derived PDFs provides important quantitative information. Over length scales associated with Bragg diffraction, the space- and time-averaged structure has the ideal $Fd\bar{3}m$ structure, but over short length scales we expect fluctuations from this average structure. It has been interesting to see how the various domain models yield PDFs that have some similarities to the experimental PDF, but beyond distances of around 10 Å the similarities are lost, and even at lower distances the experimental PDF of the WL model appears to underestimate the degree of structural disorder. Since this length scale does not extend much beyond the unit cell, a considerable volume (more than half) of any structure that consists of domains of one unit cell size will actually be domain walls, and these will be formed by RUM deformations for a wide range of wave vectors.

Furthermore, whilst the various domains discussed here will exist as fluctuations of the structure over a local length scale, these results can preclude the possibility that the WL or HG domains will be dominant. By demonstrating that yet another RUM deformation can yield comparable or even closer agreement on the local scale, this favours the proposition of Swainson & Dove (1993) and Hammonds *et al.* (1996) – supported by the RMC analysis (Tucker *et al.*, 2001c) – that the local fluctuations will correspond to Fourier superpositions of the planes of RUM phonons. The WL, HG and HP RUMs (Γ , X and L points respectively) will be included but will not be the only contributions. It is anticipated that it will be possible to construct other

types of domains from the known RUMs, which, like the HG, WL and HP models, preserve the size and shape of the SiO₄ tetrahedra. Extending the recent simulations on transition pathways between different domains (Coh & Vanderbilt, 2008) has the potential to add significantly to our understanding of the disorder in β -cristobalite.

The approach used here has applications beyond the specific example of cristobalite. There are many situations where correctly reproducing the short- to mid-range structural detail is important, some of which will be discussed in the following chapters. This tool can incisively differentiate between models that can be hard to distinguish through other means. With the inclusion of this new software in the next release of GULP, it can be hoped that this approach can become routine. Moreover, there is no reason to be constrained to empirical potential models. Force constants extracted from *ab initio* models can equally be used, and it would not be difficult to adapt the routines in the new GULP module for use directly with *ab initio* software.

In conclusion, this chapter has further demonstrated the usefulness of this new analytical approach, giving rise to the recommendation that neither the WL nor HG domain models should be used as models for simulations involving β -cristobalite.

Chapter 4

New Methodologies for Inelastic Neutron Scattering: Simulation and Refinement

This chapter focuses in detail on simulations of single crystal and powder inelastic neutron scattering experiments using the new GULP SQW module, incorporating approximations for multiple scattering and multi-phonon events in powders. To apply experimental resolution functions to these simulations, and to allow refinement of underlying interatomic models, new cross section models have also been produced for TOBYFIT. A simple aluminium powder refinement is presented to demonstrate the new methodology.

4.1 Introduction

The new generation of inelastic neutron spectroscopy machines open up exciting opportunities for examining huge ranges of reciprocal space. The challenge is the software to handle, manipulate and simulate these datasets.

Inelastic neutron or X-ray spectroscopy (INS or IXS) is the best experimental probe of the full lattice dynamics of a crystal structure. However, it is important not just to see the effects of the phonon modes, but also to understand the origins of the atomic motion due to interatomic interactions. For this purpose, I have developed simulation software, in the form of new GULP modules, to give INS $S(\mathbf{Q}, \omega)$ spectra from any force constant or empirical potential model. I also use TOBYFIT to convolved the simulated spectra with experimental resolution functions, allowing direct comparison with experiment.

While extraction of phonon information has been shown in Chapter 1 to be highly computationally intensive, simulation of and indeed model refinement from magnetic neutron scattering is nothing new: TOBYFIT was designed for this purpose (Perring, 1989) and continues to be used by ISIS users (e.g. Christianson *et al.*, 2008). The challenge has been to adapt these approaches for *phonons*. With the advent of MERLIN, we have a machine capable of exploring large sections of reciprocal space simultaneously, providing the perfect dataset for simulation and model refinement. Recent advances in computing power have kept pace with developments in instrument design, and I am now able to produce INS spectra based on lattice dynamical calculations. The work contained in this chapter is the first step towards making full use of this huge sweep of data to produce highly accurate interatomic models.

In crystallography, structural powder refinement has become common place. For many systems, it is not possible to produce suitable single crystals for full extraction of phonon dispersion curves, so the inelastic scattering community is in need of a similar powder refinement approach for dynamical information. Phonons-from-diffraction can only go so far, as seen in earlier chapters. The question is now how much can be extracted from powder INS data?

In addition to convolving the INS spectra from my simulations with experimental resolution functions, working with TOBYFIT has allowed access to a Levenberg-Marquard least-squares refinement package which allows model refinement against powder INS data. Computing power has only recently reached a stage where it might be possible to perform these sorts of refinements. Other groups have been working (independently) on this problem: the first group to publish work in this area are based at the European Synchrotron Radiation Facility (ESRF) in France, working with IXS. Fischer *et al.* (2009) developed a new methodology for simulating the IXS powder spectra up to ~ 8 Å, and refining a force constant model against experimental data collected at ESRF using the Levenberg-Marquard algorithm, sampling the powder spectra and taking ten selected spectra (constant- Q cuts) for the refinement. They make the assumption that the one-phonon scattering dominates the collected IXS spectra (this is largely valid for both IXS and INS) and make a very simple approximation to two-phonon scattering, but otherwise include no other backgrounds (see Section 4.3.2.1). This approach successfully extracted full phonon dispersion curves compatible with single crystal data for simple test-cases of beryllium and graphite¹.

The same group reportedly ‘retrieved the full lattice dynamics of stishovite, SiO₂, by a combination of powder IXS and *ab initio* calculations’ (Bosak *et al.*, 2009). However, this was more a validation of the *ab initio* model against powder data, confirmed by comparison to single crystal data, than actual ‘retrieval’. Retrieval would suggest that the model was somehow

¹The refinements took of the order of 4 days on 2.5 GHz, 8GB RAM machines, although they also parallelised the program in line with the number of force constants.

improved in light of experimental data, for example by refining the underlying interactions to produce an empirical model based on the first principles interactions. Bosak *et al.* (2009) do adjust the energy scale by 1.05%, such a mismatch being normal for GGA DFT calculations, although simple energy scaling could just as well be performed against Raman or IR data. What they do achieve is validation of a first principles model against powder data. They sensibly advocate this method of model validation as being valuable for studying thermodynamics of materials where single crystals are unavailable. My work is able to mirror this for inelastic *neutron* spectroscopy through the new GULP and TOBYFIT developments, while also offering some important additional features, and a real possibility of retrieving lattice dynamics from powder INS spectra.

The challenge with powder refinement is that as the number of atoms in the unit cell increases, so do the number of modes. In embarking upon this project, the concern was always that it would be difficult to unambiguously decipher the different modes from the powder average alone. The work of Fischer *et al.* (2009) and Bosak *et al.* (2009) confirms this from IXS: they now believe ‘powder refinement’ is more accurately reduced to model validation and minor adjustments. They emphasize the need for a good starting model for any refinement, but still conclude that powder refinement is ‘impossible’ for complex materials with dense phonon branches. As will be demonstrated in this thesis, I disagree, believing there is good reason to expect that powder refinement, *with appropriate additional experimental data*, will be useful for a wide range of materials.

Where single crystals are available, it will soon be possible to perform full refinement of interatomic models against INS data. I have developed software to allow the simulation of single crystal INS spectra, fully convolved with experimental resolution functions for any crystal orientation. By combining many of these spectra, the four dimensional scattering can be built up and visualised using the purpose built HORACE package¹. Fitting is not yet possible as each simulation and convolution of the resulting spectra with experimental resolution functions takes several hours in the current implementation, leading to fitting cycles taking weeks or even months. However, there is no reason why refinement should not be possible once the computational barriers have been overcome through parallelisation.

At the same time, Russel Ewings at ISIS has been working on one-phonon coherent scattering simulations based on phonon information derived from *ab initio* calculations. His simulations are performed in HORACE, and are akin to the one-phonon single crystal data that the new GULP module produces albeit more readily visualised. Like the basic SQW GULP output, it ignores the resolution effects arising from the rotation of the crystal when an experimental dataset is

¹Further details are given below. Full documentation and the source code are available from URL - I.

produced. Recent (unpublished) work on MnSi showed excellent agreement between the *ab initio* model and experiment. The refinement capabilities within HORACE allowed small adjustments of the energy scale (as expected when working with *ab initio* phonons), but no attempts have been made to refine the underlying force constant models. Thus it is now possible to perform simulations for the validation of *ab initio* models using HORACE.

My work complements these developments as I am able to perform simulations producing spectra convolved with experimental resolution functions using both force constants (accessible from *ab initio* calculations or other models) and, uniquely, empirical potential models. Empirical models have the advantage of being transferable amongst polymorphs and experimental conditions. While the current trend is to build potential models, the non-linear contributions of the empirical potentials mean that they are not suited to automated refinement against such a huge bank of data except for very simple cases. Force constants are useful for giving a phenomenological understanding of atomic interaction and do not need optimising at every step. Thus a force constant model is well suited to refinement and can aid interpretation of the features seen experimentally. As the force constant model is related to an empirical potential as the first derivative, and as a good force constant model will encapsulate all the experimentally observable phonon properties such as phonon dispersion, elastic and dielectric constants, it would be possible to use such a model as the ‘observable’ in an empirical potential model refinement. This would be quicker and more accurate than refining the empirical model against the normal small subset of experimental observables, and simpler than attempting to refine the empirical model against the full INS single crystal spectra. However, in this chapter I focus on the general principle of refining interatomic models.

This chapter give details of these new computational methodologies: GULP INS simulations of powders and single crystals, additional powder backgrounds, use of TOBYFIT both for convolving with experimental resolution functions and finally for least squares refinement of interatomic models against powdered datasets. I conclude with a simple test case using aluminium powdered data, as proof of principle for both force constant and empirical model refinements. This gives the first indications of success for dynamics from powdered INS.

4.2 Existing software and file-types

I base my new simulation approach on two academic programs: GULP and TOBYFIT. GULP is used to produce the necessary phonon information from a wide variety of different empirical or force constant models, as discussed in Section 1.3. I have developed new modules to use this information to generate the inelastic neutron one-phonon scattering function, $S_1(\mathbf{Q}, \omega)$.

TOBYFIT (version 2)¹ is used to provide experimental resolution functions appropriate to the different chopper spectrometers. This package also allows fitting of user-defined models against experimental data using the MULTIFRILLS least squares refinement program (URL - H). I have produced several of these cross-section models for TOBYFIT making use of the new SQW GULP module.

TOBYFIT uses the ISIS `.spe` file-type. The ISIS data normalisation software, HOMER and ILIAD, which are part of the LibISIS suite², are used to create these files. INS time-of-flight data are converted into the phonon scattering function and normalised against the peak shape of a ‘white beam’ Vanadium standard, typically collected once each cycle. Use of a monochromatic vanadium run allows normalisation to absolute units (when combined with detailed sample information). Otherwise, data is self consistently normalised against one of the monitors. The monitors give a measure of the amount of beam seen by the sample, so allow the run-length to be assessed in terms of the number of counts, offsetting temporal variations in the beam. It should be noted that attempts to normalise to absolute units, even using a standard such as a vanadium sample (e.g. Verkerk & Well, 1985) can introduce significant errors (Benmore *et al.*, 1998), partly due to the inability to reproduce the sample geometry, as well as through multiple scattering, container effects and sample attenuation.

The ISIS `.spe` format files contain the scattering intensity (S) for each detector (by angle ϕ (P)) and energy bin (E). Every detector is interpreted individually for single crystals, but for powders, detectors are grouped into rings, to give a two dimensional dataset (which I denote Q, ω to distinguish it from the full four dimensional single crystal dataset of \mathbf{Q}, ω). A `.phx` file is used to interpret the detector information. The energy binning is set by the user during normalisation, and ranges from the negative (neutron energy gain in the collision with the crystal) through the elastic line to the positive (energy loss). The maximum energy available is typically a few meV below the incident energy, and appropriate binning is $\sim 10\%$ of the incident energy.

For visualising both experimental data and simulations, I use MSLICE³ together with the NIST MSLICE emulator in DAVE⁴. Powdered $S(Q, \omega)$ spectra are normally visualised as two-

¹TOBYFIT has recently had a major new release. Now based within MATLAB, TOBYFIT GRID has been parallelised and designed to run over a computational GRID of many remote machines. This release came too late for use in this work, but will provide interesting new opportunities for further developments of my work.

²LibISIS (URL - J) was primarily developed by Dickon Champion, Freddie Akeroyd, Pranav Amin, Toby Perring and Dean Whittaker, and runs within MATLAB.

³MSLICE is used for the visualisation and manipulation of data from `.spe` files. Source code and documentation are available from URL - K as both a MATLAB GUI (allowing further interaction with data through standard MATLAB commands) and standalone GUI (for windows). Originally developed by Radu Coldea, now maintained within the LibISIS suite of software.

⁴DAVE is available for download from URL - L, both as IDL source code and binaries for Windows, Linux and Mac OS X. The GUI for the MSLICE emulator is similar to the main ISIS version, although small differences exist as both versions have continued to develop independently.

dimensional slices with Q along the x -axis, ω along the y -axis, and $S(Q, \omega)$ reflected by the colour. Constant Q or ω cuts are also frequently used, with the scattering intensity on y -axis.

Single crystal data is more difficult to visualise due to the four-dimensional nature of $S(\mathbf{Q}, \omega)$. Individual INS spectra (from the `.spe` file) can be combined and visualised using the HORACE package introduced above. HORACE produces a finely binned grid of \mathbf{Q} and ω space – the generation of this overarching four dimensional dataset is slow, but once written to file can be reused and is in a format optimised to allow rapid access to the data – which can be sliced (two dimensions) or cut (one dimension), integrating over small regions in the other axes, to allow visualisation. HORACE also provides the ‘slice-o-matic’ to visualise multiple slices on a set of three dimensional axes, frequently two in Q and one in energy, with the colour representing the scattering intensity. The MSLICE emulator in DAVE is able to perform a similar function combining multiple `.spe` files. Without the generation of the intermediary files, each cut or slice can be slow, and the visualisation is less sophisticated than HORACE.

4.3 Program description for the new GULP SQW module

4.3.1 Main purpose

Working with standard GULP interatomic models, the phonon information (eigenvectors and frequencies) generated over a fine \mathbf{k} -grid covering the first Brillouin zone is used to produce the one phonon neutron scattering intensity for a given crystal, either as a single crystal or a powder average. Temperature dependence is introduced through the Debye-Waller temperature factor, calculated from a matrix of mean squared displacements (referred to as the *Bmatrix*) derived from the phonon information, together with the bose-occupation number.

For powdered samples, the GULP SQW module can function entirely within GULP. The INS spectra (which I denote $S(Q, \omega)$ with powders) are produced in a format suitable for visualisation with any plotting package. Additional backgrounds are available, with simple approximations for the multi-phonon and multiple scattering with powder averaged intensities. A *density of states* is already produced by GULP based on the phonon information alone, but the new SQW module also gives a density-of-states-weighted $G(Q, \omega)$ version of $S(Q, \omega)$ which is summed to give $G(\omega)$. In addition, with appropriate ISIS parameter files, the incident energy and detector range of ISIS chopper spectrometers can be used to define the appropriate coverage of reciprocal space, and an ISIS format `.spe` file can be produced for use with the MSLICE visualisation package.

For single crystals, the problem of visualising the four-dimensional INS spectra (which I denote $S(\mathbf{Q}, \omega)$ with single crystals) is reserved for specialist visualisation packages. Instead, a

machine-readable ASCII output file is produced for use with TOBYFIT to simulate the equivalent experimental runs at a given crystal orientation as `.spe` files. These can then be combined in DAVE or HORACE, allowing visualisation of the phonon features.

4.3.2 Implementation

Section 1.4 introduced the underlying equations governing neutron scattering, which have been implemented in a new module of GULP. GULP makes extensive use of symmetry, and the new code automatically picks up on this, working within a symmetry-reduced cell where possible¹.

A dense² Monkhorst-Pack grid is used to calculate the phonon information, as in normal GULP functionality. For the new module, the eigenvectors are rephased (see Section 1.2.1) to remove the dependence on the position of the atom with the cell, bringing them in line with the \mathbf{e} used in the formalism. Standard GULP usage overwrites the eigen-data for every \mathbf{k} -point to minimise memory requirements. The SQW module requires repeated access to this data, so here it is retained in memory.

The formalism of Section 1.2.6 has been implemented to yield the full anisotropic mean-squared-displacement matrix (*Bmatrix*) for each (core) atom in the primitive cell by summing over all \mathbf{k} -points in turn, as in Eqn. 1.24. The final *Bmatrix* is stored for subsequent use in INS simulations (or can be written to file). The number of \mathbf{k} -points required to achieve convergence of phonon properties, and thus suitable for producing the mean-squared-displacement matrix, may be considerably fewer than the number required to populate the INS simulations. Once a converged *Bmatrix* has been produced, manual parallelisation³ of the INS simulations is possible, performing the $S(\mathbf{Q}, \omega)$ calculation for each \mathbf{k} -point as a separate condor ‘job’. This allows many \mathbf{k} -points or huge supercells to be used efficiently.

The central code for the one phonon coherent scattering function (Eqn. 1.42) is the same for both powder and single crystal calculations. The main difference is in the binning of the output data, and the addition of powder averaging in the later case. Both use a simple grid approach, offering evenly spaced user-defined ‘bins’ in both energy and momentum transfer. Experimentally, detectors are evenly spaced in the angle ϕ , which gives rise to the characteristic curved shape of experimental data-ranges when viewed in the conventional \mathbf{Q} or Q . This `.spe` format can be mimicked by the new GULP module for powders. The interaction with TOBYFIT is through Cartesian \mathbf{Q} points, so the main internal storage of INS simulations is also on Cartesian axes. For powders, the momentum transfer is binned on a Cartesian array of Q with a specified

¹All atoms will be referred to as being in the *primitive cell*, although it should be understood that user-instructions to use the full cell are correctly implemented.

²It is essential that the user checks that convergence of phonon properties with density of \mathbf{k} -points has been achieved.

³Perl scripts for splitting and re-combining such jobs are included in Appendix C.2.

dQ . The step-size and range for each of the three axes in a single crystal simulation can be varied independently. Bins are centre anchored: the bin name refers to the centre point.

The new module uses an ‘extended zone scheme’ to map the contribution of each \mathbf{k} -point in the first Brillouin zone to an extended position¹. The required number of Brillouin zones along each of the Cartesian axes (to the user-defined limit) are calculated: each $\mathbf{Q} = \mathbf{k} + \mathbf{H}$, where \mathbf{H} is a vector to the origin of the specific Brillouin zone (Eqn. 1.21). Thus \mathbf{Q} -space is explored sequentially in \mathbf{H} . This method of summing over all reciprocal lattice vectors ensures the delta functions cancel the volume weighting term in Eqn. 1.42.

For each derived \mathbf{Q} -point, the `SQW_inner` subroutine is called, looping over all frequencies to generate the inner sum from $S(\mathbf{Q}, \omega)$ (Eqn. 1.42), while calling the `Fmode` function to perform structure factor calculations (Eqn. 1.43) and the `bose_eins` function to give the temperature dependent Bose factor $n(\omega)$ (Eqn. 1.9). Where both energy gain and loss are requested, the appropriate Bose weighting is applied for each case, and the results binned as negative or positive energies respectively. The difference between single crystal and powder output is that the resulting intensity is binned according to \mathbf{Q} or Q as appropriate. For powder samples, `SQW_inner` also applies the powder averaging, to ensure that the actual contributing Q is used as opposed to the bin-name ‘ Q ’. The powder averaging is:

$$P = \frac{V_{\text{BZ}}}{n_k V_Q d\omega} \quad (4.1)$$

where V_{BZ} is the volume of the Brillouin zone, n_k is the number of \mathbf{k} -points, V_Q is the volume of the bin in Q defined as $V_Q = 4\pi Q^2 dQ$ and dQ and $d\omega$ are the bin sizes of momentum transfer and energy respectively.

Similarly, the single crystals are corrected by a factor of S to account for the binning and \mathbf{k} -point density. This is performed in the calling routine (`SQW_single`) to optimise performance.

$$S = \frac{V_{\text{BZ}}}{n_k dQ_x dQ_y dQ_z d\omega} \quad (4.2)$$

In addition to recording the scattering intensity for each bin, a count is made of the number of ‘hits’ each bin received.

When generated experimentally at ISIS, the normalised output from HOMER has the units mbarn/meV. The `SQW` module output follows the same convention, although SI units are used internally. The user specifies desired units for energy, and chooses fractional or Cartesian units for single crystal momentum transfer.

¹By convention, I refer to positions in the first Brillouin zone as \mathbf{k} -points, and general points in reciprocal space as \mathbf{Q} -points.

The main purpose of the code is to produce the one phonon coherent neutron inelastic scattering function for both single crystal and powdered samples. Various additional functions have been produced to help with interpretation of the data, and with comparison with experiments.

4.3.2.1 Background: multi-phonon and multiple scattering

It is increasingly becoming obvious to the inelastic scattering community that there is a need for accurate determination of additional background scattering processes: this has been highlighted as topic for discussion at the next ISIS inelastic user group meeting. For visual extraction of dispersion curves from experimental data, or simple comparison of model and data, these ‘backgrounds’ are of little importance. But to allow model refinement it is essential to include at least an approximation to the key additional scattering process.

In addition to the one-phonon scattering, the new module contains two approximations to other significant background factors for use with the powder averaging: multiple scattering and multi-phonon scattering¹.

Multiple scattering (transmission factor) The most common form of multiple scattering is when an elastically scattered neutron is subsequently inelastically scattered before it leaves the sample. The effect of this is to introduce additional intensity at the energy of the inelastic event but with the ‘wrong’ momentum transfer. The amount of multiple scattering will depend on the transmission (T) of neutrons through the sample. T is typically of the order of 10% for the materials studied in this thesis.

The effect of multiple scattering in powder samples is most clearly seen at low Q and ω , where unexpected scattering can be observed under the lowest modes in a dispersion curve (this is clearly seen in the aluminium data presented below, Fig. 4.2). The more inelastic events occurring at a given energy at *any* Q (i.e. the greater the integral of the one phonon scattering function over all Q at that ω), the more intense the multiple scattering at all Q when combined with additional elastic scattering events. This gives a uniform addition to the one-phonon scattering intensity observed in a constant Q cut.

The multiple scattering at a given energy can be approximated from the integral of the scattering function over the entire Q -range, weighted by a transmission factor, T . Given that the scattering function in the new GULP module is binned in Q across n_Q **Qbins** of width dQ , and that $Q = \text{Qbin}(i_Q)$ for each bin indexed by i_Q , the multiple scattering component in each

¹The computational demands of similar backgrounds for single crystals have meant that these are currently not available.

bin is:

$$S_{\text{MS}}(Q, \omega) = \frac{T}{100 \cdot n_Q} \sum_{i_Q=1}^{n_Q} S(Q, \omega) dQ \quad (4.3)$$

Multi-phonon scattering One-phonon scattering processes occur with the creation or annihilation of a phonon of a given energy, subject to the conditions of conservation of energy and quasi-momentum. Multi-phonon scattering (two or more phonon events) has fewer constraints, as it is always possible to find two wavevectors that sum to meet the conservation of crystal momentum conditions (Section 1.2.5) as well as conservation of energy. Thus multi-phonon scattering does not show the characteristic Q -dependence of one phonon scattering but instead gives a smooth background to the inelastic scattering data, dominated by polynomial terms in Q . Importantly, the convolution of multiple inelastic events gives rise to additional scattering at higher energies, noticeably giving low intensity, Q -dependent intensity above the highest energy mode for the system.

While it is possible to calculate this explicitly (from Eqn. 1.41), this process is hugely computationally demanding for very little gain in accuracy over other quicker methods. Slightly more accessible is the incoherent approximation: the incoherent structure factor is multiplied by the coherent scattering length to give the many-phonon scattering (Placzek & Van Hove, 1955). The one-phonon incoherent scattering is then subtracted, leaving just the multi-phonon background. But this is still computationally demanding.

In order to balance the demand of a repeated iterative fitting process with a more advanced multi-phonon (up to 3-phonon) background, taking advantage of the powder averaging, I implement a different approach. First, recall that the multi-phonon scattering (Eqn. 1.41) contains a correlation function $\langle [\mathbf{Q} \cdot \mathbf{u}_i][\mathbf{Q} \cdot \mathbf{u}_j] \rangle^m$ which can be shown to be proportional to Q^{2m}/ω^m . This provides the relative weighting of one-, two- and three-phonon scattering.

As an approximation to two-phonon scattering, I assume equal likelihood of any one-phonon scattering event being followed by a second, from anywhere in the density of states. Without the need to satisfy the condition of conservation of crystal momentum, the Q -dependence in the one-phonon scattering is not preserved. Thus, I first remove the Q -dependent temperature factor (taking the average over all atoms in the unit cell) from the one-phonon scattering, and integrate over all Q to give $P_1(\omega)$. The Cartesian binning system in the new GULP module has n_Q equally sized `Qbins` such that $Q = \text{Qbin}(i_Q)$ for each bin indexed by i_Q , each bin having width dQ . Thus the unweighted one-phonon integral is:

$$P_1(\omega) = \frac{1}{n_Q} \sum_{i_Q=1}^{n_Q} \left(\frac{S(Q, \omega)}{\exp(-2W)} \right) dQ \quad (4.4)$$

This integral can be convolved with itself to give $P_2(\omega)$, introducing the necessary broadening of the energy ranges. When weighted by the appropriate $m = 2$, Q^{2m}/ω^m terms this forms the basis of the smoothly Q -dependent two-phonon scattering.

In the same way, the three-phonon ($m = 3$) contribution can be produced with a further convolution of $P_1(\omega)$ to give $P_3(\omega)$, which is weighted by the appropriate form of Q^{2m}/ω^m for $m = 3$.

The contributions from these two convolutions can be summed and the temperature factor ($\exp(-2W)$) reintroduced to give the final multiple scattering contribution:

$$S_{\text{MP}}(Q, \omega) = \exp(-2W) \left(\frac{Q^4}{2! \omega^2} P_2(\omega) + \frac{Q^6}{3! \omega^3} P_3(\omega) \right) \quad (4.5)$$

The overall effect of this is to broaden the density of states to higher energy: this is of particular importance when trying to fit high incident energy spectra. It should be noted that this approximation only holds for relatively heavy atoms, but has provided sufficient background to assist with the refinements performed in this thesis. This multi-phonon contribution is weighted by the ‘multi-phonon factor’, typically $\sim 10\%$: this weighting is a refineable parameter with TOBYFIT.

Fischer *et al.* (2009) were working on this problem independently, and instead model a simple two-phonon background as $1/2 Q_i U^{ij} Q_j$ where U^{ij} is thermal displacement (available from the literature) and Q is the momentum transfer. They find an integral two-phonon contribution of 9% for graphite and beryllium at 5 Å, giving a smooth and weakly modulated background. While this model is better than simply using the one-phonon scattering, I consider it to be too simplistic. I found that it was important to include the three-phonon terms as well as two-phonon terms, and that the energy-dependence of my approximation was crucial.

4.3.2.2 Density of states

Normal GULP usage allows an un-normalised phonon density of states to be calculated from a Monkhorst-Pack grid of \mathbf{k} -points. INS allows the experimental observation of the density of states, so the SQW module simulates the density of states for powdered samples. Each bin in the SQWarray is weighted as appropriate for the density of states, using the average mass, \bar{M} and the appropriate Bose weighting ($n(\omega)$ or $n(\omega) + 1$ depending on energy gain or loss):

$$G(Q, \omega) = \frac{2\bar{M}\omega S(Q, \omega)}{\hbar^2 Q^2 \exp(-2W) < n(\omega) + 1 >} \quad (4.6)$$

The sum over all Q is then used to give a density of states, $G(\omega)$, normalised to unity.

| | |
|------------------|--|
| SQWpowder | Calculate the powder averaged $S(Q, \omega)$ |
| SQWsingle | Calculate $S(\mathbf{Q}, \omega)$ for use with TOBYFIT |
| SPE | Calculate the powder averaged $S(\phi, E)$ |
| SQW1 | Calculate $S(\mathbf{Q}, \omega)$ for a given single point in \mathbf{Q}, ω space |
| SQWdispersion | Calculate $S(\mathbf{Q}, \omega)$ along a dispersion line |
| Outmodes | Output phonon information and $S(\mathbf{Q}, \omega)$ contribution of each \mathbf{k} |
| ShapeDos | Output any \mathbf{k} with a mode within the specified ω range |
| Debye or Bmatrix | Calculate the mean squared displacement matrix for each atom |
| Makeeigenarrays | Store all eigenvectors and frequencies after calculation |
| ArrayFrequencies | Output phonon details from internal arrays |
| Coreinfo | Output atomic information (for cores not shells) |
| Nosqwoutput | Suppress output of the SQW results to file |
| Nowarnings | Suppress warnings about imaginary eigenvectors |

Table 4.1: Summary of new SQW module keywords. These reflect the key functionality available within this module.

4.3.3 Input

The exact details of the nature of input and output files for the new GULP SQW module are not needed to understand the main functionality of the software, but are expanded upon in Appendix A. As with standard GULP, and the new PDF, a single ASCII file is used as input to the program, made up of *keywords* and *options*. New keywords are listed in Table 4.1; some of these, such as `SQWsingle`, change the behaviour of the program whereas others, such as `coreinfo` merely affect the output.

A GULP input file for a three dimensional crystal, producing *stable* lattice dynamics, is required, to which new SQW keywords can be added. The new SQW options are entered in a specific section of the input file which I have called the ‘neutron input block’. The new options for specific functionality are described in more detail in Appendix A, and include the addition of neutron scattering lengths and their modification (to allow mean field atoms, or to remove a specific atom from the scattering spectra), and the ability to set the energy and momentum transfer binning for the `SQWarray` and `SQWsingle` arrays together with weightings for the backgrounds.

4.3.4 Output

The new GULP module outputs are described in detail in Appendix A.6. Appropriate output is added to the normal GULP output file, and the Bose function, *Bmatrix* (for the Debye-Waller temperature factor), density of states, and inelastic scattering functions can all be written to separate files. For powders, the standard ISIS `.spe` output format can be adopted with appropriate detector parameter and incident energy settings, and an ASCII `.sqw` file is produced

containing the one-phonon scattering together with the approximations to multi-phonon and multiple scattering and the $G(Q, \omega)$ weighted output and number of ‘hits’ in each bin. The scattering intensity for a single crystal is written to a `.sqwt` output file which can be used as input to TOBYFIT and then HORACE to allow further manipulation and visualisation.

4.4 TOBYFIT: new developments

4.4.1 Main purpose

The interaction of the new GULP SQW module with TOBYFIT has allowed new methodologies for the preparation for and analysis of data from INS experiments on chopper spectrometers. There are four main reasons for combining the new GULP SQW module with TOBYFIT:

- convolving simulations with experimental resolution functions,
- producing suitable files to allow visualisation of single crystal simulations,
- fitting powder simulations against experimental `.spe` files,
- simultaneous simulation and fitting of multiple data sets at different incident energies.

GULP can be called either as a standalone program or directly by TOBYFIT, generating the one phonon scattering function (and appropriate backgrounds). One advantage of using GULP to generate the eigen-data for the initial simulation is that the standard GULP fitting procedures can be used to refine a model against other experimental observables, such as dielectric constants and IR or Raman spectroscopy, ensuring a reasonable starting model. More details on basic functionality of TOBYFIT, and specifically on the interaction with the new GULP SQW module, are given in Appendix B.

Tobyfit has been designed to allow a user to provide a ‘cross-section model’ to give the spectra weight for a given \mathbf{Q} and ω . With the addition of the new cross-section models, TOBYFIT not only convolves the spectra produced from the GULP simulation of the scattering function with experimental resolution functions, but can now be used to refine the underlying GULP model, calling GULP each time the interatomic potential or force constant parameters change. More simply, TOBYFIT can be used to refine the background (including multi-phonon and multiple scattering) and maximum intensity. Fig. 4.1 shows how the two codes interact.

In order to simulate and fit neutron scattering spectra generated with the new GULP modules against real experimental data, TOBYFIT has been modified slightly to allow it to call GULP as a subroutine. This combined code is executed using familiar GULP and TOBYFIT settings, with a few additional options. The source code for the new TOBYFIT models and the new GULP modules are stored in an electronic repository at DSpace@Cambridge (Cope, deposited 20.05.2010).

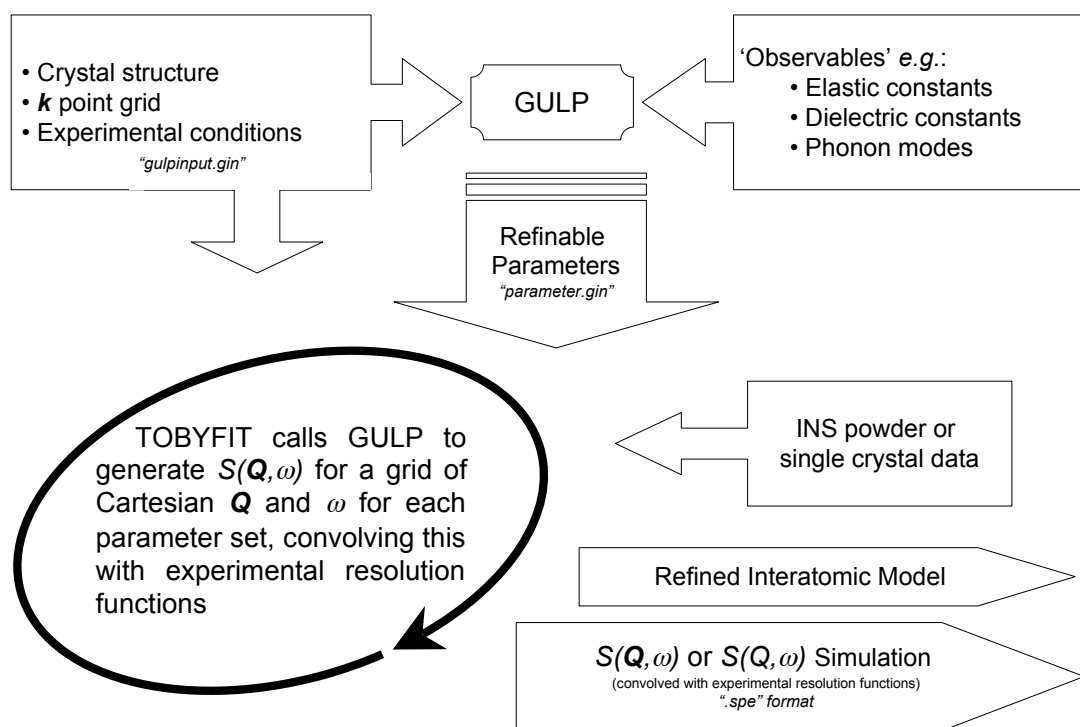


Figure 4.1: The fitting cycle for TOBYFIT and GULP. The crystal structure, experimental conditions and (converged) \mathbf{k} -point grid are contained in a standard GULP-style input file `gulpinput.gin`. GULP can be used to refine a reasonable starting model for the interatomic model against other experimental ‘observables’. These are then saved in the `parameter.gin` input file. TOBYFIT calls GULP using these two input files as a template to generate $S(\mathbf{Q}, \omega)$ or $S(\mathbf{Q}, \omega)$ for the current set of parameters, convolving with experimental resolution functions, and refining the interatomic model where a suitable experimental dataset is present.

4.4.2 Implementation and program design

In normal usage, TOBYFIT uses the experimental setup to define the range of momentum transfer and energy that should be explored, depending on the integration method selected (see Appendix B). For each required \mathbf{Q} and ω , the function `SQW.broad` is called. This user defined function returns the scattering function given by the specified cross section model. I have developed a range of models for use with both powders and single crystals to allow simulation and fitting against experimental data, which are listed in full in Appendix B.2. The details of each model are not necessary to understand the general principles.

TOBYFIT not only allows simulation of experimental data, but also fitting using the MULTIFRILLS least squares refinement routines (see Appendix B.5). When using GULP to generate

the lattice dynamical data, the most costly step is the diagonalisation of the dynamical matrices, so it is important to minimise the number of diagonalisation performed. χ^2 is calculated from a sweep of the entire dataset using the initial model parameters. For each free parameter, the calculation is repeated with a small positive and negative increment to the free parameter on *each datapoint in turn*. As with the stand-alone GULP SQW module, I use a dense Monkhorst-Pack grid of \mathbf{k} -points in the first Brillouin zone to seed an extended zone scheme of \mathbf{Q} -points, calling GULP once for a given set of parameters, and storing the resulting scattering function.

For powders, it is appropriate to store a binned full scattering spectra, as the powder averaging means that each datapoint in $S(Q, \omega)$ relates to many \mathbf{Q} . A copy of the resulting SQWarray is kept for each change in parameters, up to a user-defined maximum (at least $2p + 1$ where p is the number of free parameters). Thus as the fitting routine progresses, TOBYFIT need only consult an evenly binned search-table (giving rapid look-up times) to extract $S(Q, \omega)$ for each parameter set. By using a sufficiently-fine Monkhorst-Pack grid, there is no need to interpolate between \mathbf{k} -points, preserving accuracy and optimising the post-diagonalisation routines (although more \mathbf{k} -points come at the price of slower GULP calls).

The case of single crystals is more difficult. The most accurate results would be produced by reducing each \mathbf{Q} to a \mathbf{k} -point in the first Brillouin zone, generating and diagonalising the dynamical matrix, and calculating the scattering intensity. However, the fine Monkhorst-Pack grid and extended zone scheme is more efficient, as the same \mathbf{k} -point data can be used for many \mathbf{Q} . Initially, it seemed sensible to use GULP only to generate the eigen-data, and pass a stored `kgrid` giving the resulting eigenvectors and frequencies for each \mathbf{k} -point. Then it would be possible to interpolate the exact position of the required \mathbf{Q} , and use the SQW module subroutines to generate the scattering intensity. Unfortunately, a single experimental sweep of the calcite MERLIN data was projected to require 6 months to run on standard CamGrid machines, even after extensive optimisation. The calcite simulations require 200 of these runs to be repeated with one degree rotations in crystal alignment. Removing the interpolation and simply using a binning scheme improved the timings but still did not achieve realistic speeds.

In light of these problems, I decided to use a similar approach to the powder cross section models: the generation of the `SQWsingle` array containing the scattering function binned onto a grid of Cartesian \mathbf{Q} -points and energies. Again, I considered interpolation between the bins, but even without this additional time-cost, a simulations of a typical MERLIN experiment needs several hours to perform the TOBYFIT Monte Carlo integration for an individual crystal orientation, on top of the GULP calculation.

The big advantage of using the `SQWsingle` array approach is that the GULP run can be de-

volved from the TOBYFIT simulation. GULP simulations are normally¹ written to a `.sqwt` file which can be read back into TOBYFIT for convolution with experimental resolution functions. This allows manual parallelisation of the simulation process: if a `.sqwt` file is generated with sufficient Q range to cover all crystal orientations, this can be used as input for all remaining orientations and run in parallel on many machines. Using this approach, the generation of the entire calcite dataset at one incident energy could be achieved on the CamGrid within a week.

One of the aims of my current work was to investigate the possibility of refining interatomic models against single crystal data. It can be seen that this is not possible using TOBYFIT v2 due to time constraints. However, considerable improvements will be possible by parallelising the code as part of TOBYFIT GRID, although there will still be memory/file storage issues due to the size of the `SQWsingle` array. (The calcite `.sqwt` files are around 6Gb.) Consideration must be given to the storage of the $2p + 1$ sets of data needed for the fitting process – possibly with greater tuning of regions of reciprocal space based on the specified input files – as well as sensible allocation of jobs across processors. These issues are not insurmountable, but require further development of the software.

What has been achieved, as will be seen in the subsequent chapters showing the experimental results, is a means to produce excellent simulations of experimental data, that are fully compatible with the data visualisation and manipulation software at ISIS, and useful for both planning and analysing experiments.

4.4.2.1 Programming details: GULP-TOBYFIT interactions

The new modules in GULP have been designed to work both as subroutines of GULP and stand-alone routines called by TOBYFIT. The new GULP `SQW` module can produce `.sqw` or `.sqwt` files which the new TOBYFIT cross-section models can read. TOBYFIT then convolves them with experimental resolution functions. More powerfully, TOBYFIT can be used to call GULP, and to refine a model against experimental data interacting with the new GULP modules directly.

GULP is linked to the main TOBYFIT code through TOBYFIT's user-accessible `sqw_broad.F`. A few minor changes² had to be made to the release version of TOBYFIT v.2. The main change to GULP was to the input: normal GULP only reads a single input file, but when the appropriate flags are set both `gulpinput.gin` and then `neutron.gin` are read sequentially.

¹unless output is specifically switched off to save write-time and filespace.

²All 'pause' commands were changed to 'stop', the maximum number of datasets and related variables had to be adjusted to fit MERLIN datasets, the system-dependent date and time commands were set appropriately, and the energy parameters and output names were copied into `sample_parameters`, to allow access to these settings from within `sqw_broad.F`. All routines were encapsulated in a single Fortran module, to ensure that GULP and TOBYFIT variables do not interfere. GULP already had the potential to be called as a subroutine from another program, so only minor modifications were needed to allow TOBYFIT to control it.

4.4.3 Input

The standard input is an interactive or script based input file together with experimental parameter files and datasets (where appropriate). To minimise alterations to the main code, the new SQW input is restricted to the addition of two new GULP-style input files which together form a full GULP `.gin` file. Those settings which remain constant throughout a fit – lattice parameters, optimisation style, number of **k**-points etc. – are included in `gulpinput.gin`. The parameters for refinement and the `neutron` block settings are placed in `parameter.gin`. This data is read by TOBYFIT and used as the template for the `neutron.gin` file passed between TOBYFIT and GULP to update the fit parameters at each step in the refinement. More details and sample files are given in Appendix B.6, together with further information on the standard TOBYFIT setup including instrument and sample settings (Appendix B.1), but it is helpful to summarize the key points here.

Suprions in the experimental data can be masked by setting the errors to zero (this is best performed in MATLAB, functions for which are included in Appendix C.1), and the elastic line (which is not simulated) should be removed. High Q simulations are computationally demanding, so if no new information is contained in this region, it is advantageous to mask these regions from the experimental data prior to refinement. Entire detector banks can be removed using standard TOBYFIT commands¹.

The main point of interaction between the two codes is in handling the cross section parameters. The first five parameters control the interaction, setting scale, Q_{\min} and Q_{\max} (to override the normal `.phx` detector range), transmission (for multiple scattering) and the multi-phonon weighting. The remaining parameters map sequentially to the interatomic models read directly from `parameter.gin`. The ten new cross-section models are listed in full in Appendix B.2, giving the main functionality of the new code.

4.4.4 Output

TOBYFIT gives a standard output detailing progress and allowing interaction. Refinement against MERLIN data takes hours to days, so additional progress monitoring has been included². An iteration only progresses when a lower χ^2 is found, so five or six iterations performed with 15 free parameters can take well over a hundred GULP calls. Following successful refinement,

¹These cannot be removed directly from the `.spe` file as the number of detectors is linked to the instrument parameter file. When removing high- Q data, for example to prevent unnecessary calculation of non-dispersive high energy modes, the GULP `Qmax` setting should be set to reflect this upper limit in the `neutron` block in the `parameter.gin` file.

²For example, every (silent mode) GULP call is followed by a summary of the input parameters and timings. Optimum parameter shifts are written to the standard output, with reports of every calculated χ^2 .

simulations can be performed using the normal interactive TOBYFIT commands yielding the desired `.spe` files for visualisation with MSLICE.

4.5 Aluminium: a test-case for powder fitting

4.5.1 Experiment

Powder scattering data were collected from a powdered sample of aluminium on MARI by Steve Bennington in 1999. MARI (Taylor *et al.*, 1990) is another direct geometry chopper spectrometer at ISIS, but with a fraction of the number of detectors on MERLIN. This was used as a test case for the new simulation and fitting software before the commissioning of MERLIN.

Aluminium is a simple face centred cubic (FCC) structure, space group $Fm\bar{3}m$ with an experimental lattice parameter of $a = 4.03 \text{ \AA}$. Experimental data were collected at 20 K, with an incident energy of 54.14 meV. The data were normalised and binned with an energy step of 0.2 meV using HOMER: the resulting spectra is shown in Fig. 4.2(a). 144 powder-ring detector groupings are set with the `mari_powder_lowres_1171.par` file. MATLAB was used to remove the elastic line, to remove negative intensities arising from small inaccuracies in the data normalisation process (by masking them from the refinement and setting the displayed intensity to zero), and to mask out the door-edges.

4.5.2 Models

To test the efficacy of TOBYFIT powder $S(Q, \omega)$ refinement methodologies, two modelling approaches were taken. First, a force constant model was constructed and refined from various starting points against the experimental data. Second, a simple empirical potential model was used.

4.5.2.1 General TOBYFIT setup

To ensure that suitable experimental resolution effects are included in the simulations, the appropriate TOBYFIT settings for the instrument, moderator and chopper were selected for use with the full Monte Carlo integration method. Fitting was performed using the default MULTIFRILLS settings (see Appendix B.5) aiming for a χ^2 of unity through the Levenberg-Marquadt algorithm with convergence being reported when the change in χ^2 was less than 0.01.

It is clear that there is a significant amount of multiple scattering present in the experimental data from the smearing under the first dispersion curve, especially between 17 and 25 meV. Thus the initial value for transmission was chosen to be 15%. Similar proportions of multi-phonon contribution were added to the refinements and allowed to vary.

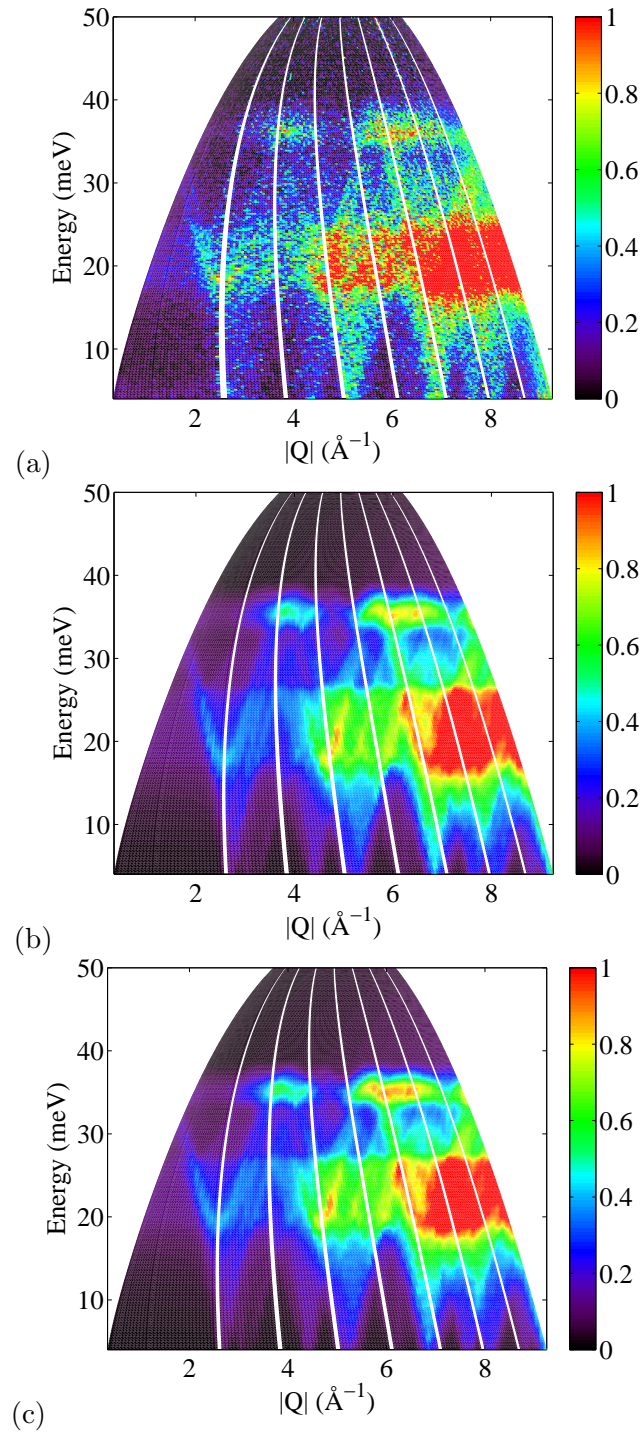


Figure 4.2: MARI INS spectra for aluminium powder experiments at 20 K, $E_i = 54.14$ meV. The elastic line has been removed, as this does not appear in the simulation. (a) Experimental data. No smoothing has been applied so the quality of the data can be assessed. (b) Simulation from the final force constant model. (c) Simulations from the final Lennard-Jones potential model. The energy dependence of the conversion from the even ϕ -step of the detectors to the displayed Q -range gives the characteristic shape of the $S(Q, \omega)$ image. The edges of the doors of detectors give rise to the white gaps in the data.

| Parameter | FC model | LJ model |
|----------------------------|----------|----------|
| χ^2 | 1.9921 | 1.5472 |
| Scale | 0.94 | 0.95 |
| Multiple Scatter (%) | 19 | 19 |
| Multi Phonon (%) | 21 | 18 |
| K_L (eVÅ ⁻²) | 1.1640 | |
| K_T (eVÅ ⁻²) | 0.00126 | |
| σ (Å) | | 2.9254 |
| ϵ (eV) | | 0.0865 |

Table 4.2: Final parameters for the FC and LJ potential models

4.5.2.2 Force constant (FC) model

The simplest way to model the structure is using two force constants (longitudinal and transverse) between nearest neighbour atoms. A maximum cutoff was set to ensure the interaction is restricted to nearest neighbours (set at 3.5 Å).

The initial starting model was produced by simply adjusting the transverse and longitudinal force constants manually, producing $S(Q, \omega)$ simulations until they came into rough agreement with the data: as long as the main band of scattering was within the experimental range the model refined successfully. Parameters were varied individually and collectively, gradually allowing more parameters to vary with no limits on their range. The final FC fit gave $\chi^2 = 1.99$, with the parameters given in Table 4.2.

4.5.2.3 Lennard-Jones (LJ) potential model

It is also possible to produce an empirical potential for use with aluminium. A standard Lennard-Jones model is suitable for use here:

$$V(r) = \epsilon \left(\left(\frac{\sigma}{r} \right)^{12} - 2 \left(\frac{\sigma}{r} \right)^6 \right) \quad (4.7)$$

A typical value for ϵ is around 0.1 eV. A suitable starting model was produced simply by adjusting ϵ and σ manually. Unlike force constant models, potential models need to be optimised at every step of the refinement to ensure that the energy has been properly minimised. In the case of the Lennard Jones potential, σ is largely responsible for the interatomic spacing, and thus the lattice parameter. Therefore, σ was initially held constant and the optimisation performed with constant volume to maintain $a = 4.03$ Å. As with the FC model, the parameters were increasingly allowed to vary until all parameters were freed, with no limits. The final fit was reported at $\chi^2 = 1.55$, with the parameters shown in Table 4.2.

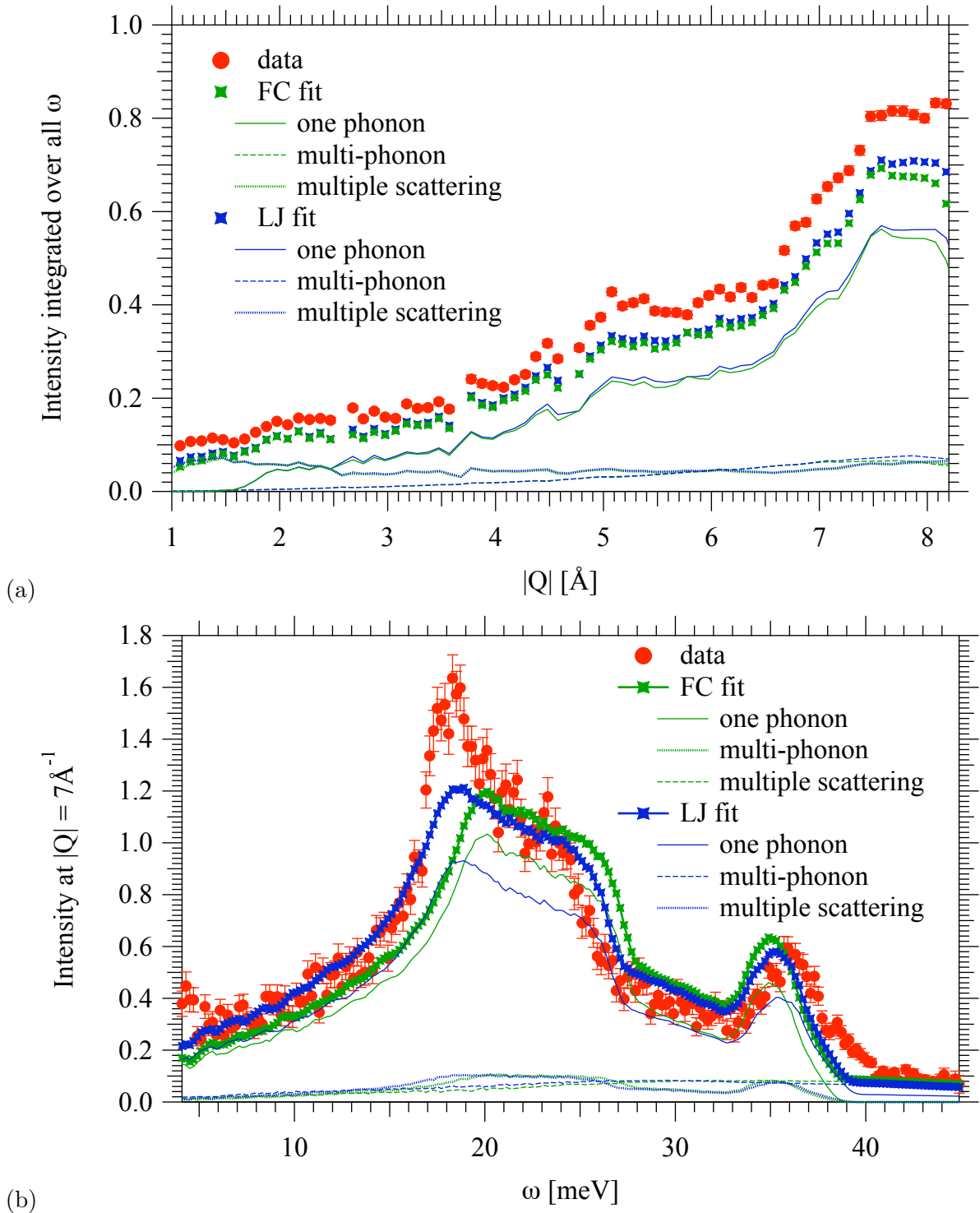


Figure 4.3: Cuts through the aluminium data and simulations showing the relative contributions of the different backgrounds (discussed in the text). Both models use almost identical backgrounds, and the LJ model is clearly a slightly better fit. (a) A cut along Q , summed over all modes. (b) A constant- Q cut at 7 \AA^{-1} .

4.5.2.4 Comparison to experiment

Both the LJ and FC model give similar χ^2 values confirming their good fit to the experimental data (Fig. 4.2). Constant Q (summed over the entire energy range) and constant-energy plots (through the most intense region at $Q = 7 \text{ \AA}^{-1}$, $\delta Q = 0.6 \text{ \AA}^{-1}$) reveal more detail (Fig. 4.3). It is clear that both models give a reasonable agreement to the experimental data in both dimensions. Notably, however, neither model accurately models the experimental peak at 18 to 20 meV. This could be due to incoherent scattering¹, which is not included in the model, or a failure to fully model the backgrounds, or most likely, additional components from next nearest neighbours. It should be noted that the error bars in this region in particular are significant, so the quality of the experimental data here may also be an issue.

Fig. 4.3(a) shows the excellent overall agreement between the line-shapes. As this cut is integrated over all energies, it gives an general assessment of the quality of the fit. However, the curved shape of experimental Q, ω space means that the extremes are dominated by the low energy fit. At low Q , there is only multiple scattering background. This shows no variance in Q in the model, although the curved shape of the plot, masking of the door edges, and binning effects combine to give a slight variance in this cut. There is Q -dependence in the multi-phonon scattering (from the approximation based on weighted contributions for two and three phonon scattering), which can be seen to be important.

The role of the additional scattering is clear in the constant Q cut in Fig. 4.3(b). The increasing effect of the multi-phonon scattering at higher energies can be seen, lifting the one-phonon scattering to the experimental level at 40 meV. In the same way, the multiple scattering, with its Q -independent increase on the observed peaks, is also crucial.

4.6 Conclusions

Using TOBYFIT to refine interatomic models against scattering data has proved successful. As with any fitting process, the quality of the background is important, and it should be noted that without simulation of the Bragg peaks an energy-dependent background, localised in Q will always be present. This suggests that further improvements to the methodology could be made by including the elastic scattering in the simulations, or else by sophisticated removal of the elastic scattering from the experimental dataset. I note that the recent work by Fischer *et al.*

¹Aluminium has an incoherent cross section of $0.81 \times 10^{-10} \text{ \AA}^2$, compared to $0.145 \times 10^{-7} \text{ \AA}^2$ coherent cross section. For comparison, the incoherent scattering for the silicates, which are successfully modelled in the next chapter, is much less: silicon has $0.32 \times 10^{-10} \text{ \AA}^2$ incoherent and $0.22 \times 10^{-7} \text{ \AA}^2$ coherent, and oxygen has $0.30 \times 10^{-11} \text{ \AA}^2$ incoherent and $0.42 \times 10^{-7} \text{ \AA}^2$ coherent scattering cross section.

(2009) uses a pseudo-voigt fit to account for the elastic scattering, while Bosak *et al.* (2009) simply ignore the elastic line and see a similar mismatch at low energy.

The aluminium test-case demonstrates that, for simple systems, even a poor model can be brought into agreement with experimental data using the new methodology. In the remainder of this thesis, both the simulations and refinement methodologies will be tested against several complex systems, allowing assessment of the viability of this approach, together with suggestion for further developments to the methodology.

In principle, when extending this work to more complex systems differentiating between different modes in dense regions will be challenging: in the current implementation there are no additional refinable parameters to ensure that certain modes are constrained in any way. Moreover, refinement of interatomic potential models without the elastic Bragg data is unlikely to be possible: the intense Bragg peaks will be needed to ensure the unit cell optimises correctly. For the Lennard-Jones model, holding constants σ until the final stages of the fit enabled successful refinement. Such appropriate stepwise variation of different parameters is part of the ‘art’ of model refinement, but elastic data would ensure better performance. Elastic data would also help to further constrain the phonon model through the temperature factor. Moreover, it has been seen that the elastic scattering provides a low-energy background around the Bragg peaks, which it would be helpful to either remove or simulate. In future work, it would also be advantageous to include the incoherent scattering: this was not relevant for the key earth materials initially investigated but the software has been designed to allow this improvement with minimal changes to the code.

It should also be noted that there is a mismatch between recently normalised ISIS data (using HOMER) and the error handling in TOBYFIT. While the old aluminium data reported excellent convergence with χ^2 approaching unity, any data normalised recently gives typical ‘converged’ $\chi^2 \sim 10^4$. In addition, the old aluminium data is not compatible with the latest version of HOMER. While investigations into this issue are taking place, all other refinements reported in this thesis have been set of achieve convergence when the change in χ^2 is at the same order of magnitude¹ as the reported error calculated for χ^2 .

In conclusion, the new TOBYFIT cross section models can be used to call the new GULP `SQW` modules both to produce INS powder simulations fully convolved with experimental resolution functions, accounting for one-phonon, multi-phonon and multiple scattering spectra, as well as refining the underlying interatomic model. In principle, any GULP potential model-type can be used to produce INS simulations, and any GULP parameters, such as Coulombic charges, can

¹If the convergence criteria is set too low, TOBYFIT continues to make smaller and smaller adjustments to the optimised parameters, resulting in changes too small to be passed between GULP and TOBYFIT through the `neutron.gin` input file.

be refined by TOBYFIT. Single crystals can also be simulated (as demonstrated in subsequent chapters), and the next challenge is making the refinement process sufficiently rapid to be achievable. In the rest of this thesis, these new approaches will be applied to a number of important mineralogical and technologically interesting systems.

Chapter 5

α -Cristobalite and v -SiO₂: a powder INS study of the Bose peak and related phonon modes

The lattice dynamics of the silica polymorphs have attracted considerable controversy, with suggestions of ‘fast sound’, the Bose peak and anomalous thermal features that appear to be universal to glasses. Using the new GULP SQW module it can be conclusively demonstrated that key features observed experimentally can be reproduced from a standard interatomic model. The Bose peak – the excess in the density of states compared to the Debye line seen at around 5 meV in silica – arises in simulations of both vitreous silica and the crystalline α -cristobalite. Moreover, the remarkably similar Q -variation for the crystal and glass, observed experimentally both in the Bose peak and at higher energies, is reproduced in the simulations. This study gives new insights to these features in glasses.

5.1 Introduction

The Bose peak (also known as the Boson peak) refers to a low energy excess peak in the Debye density of states, which is universally observed in glasses. It was first reported by Krishnan (1953) through Raman spectroscopy of vitreous silica (v -SiO₂), and subsequently reported for almost all glasses regardless of composition. It is so named as the peak scales with temperature according to Bose-Einstein statistics, and seen by many as “one of the universal features at the heart of the anomalous properties of glasses” (Ruocco, 2008). It has attracted considerable interest over the last 50 years, as it has been linked to several thermal anomalies. Understanding

the origins of these features could aid the design of glasses to have optimal thermal properties, with important technological implications.

The structure (Wright, 1994) of the prototypical network glass, v -SiO₂, is made up of corner-sharing SiO₄ tetrahedra in an infinite random network with local ordering existing up to ~ 10 Å. This has similar local structure to other silica polymorphs such as quartz, tridymite and cristobalite (Gaskell & Wallis, 1996; Keen & Dove, 2000): they all consist of these SiO₄ tetrahedra. Moreover, it displays the same degree of flexibility as the dynamically disordered crystalline phases (Trachenko *et al.*, 1998), undergoing large rotational rearrangements without deformation of the tetrahedra, and at little energetic cost. These similarities suggest that the study of the crystalline α -cristobalite may well have important consequences for the understanding of the key vibrational modes in v -SiO₂, and thus give important insights into glasses and amorphous materials in general.

The Bose peak has long been observed for glasses through Raman spectroscopy, but the density of states observed for the crystalline counterparts is very different. This poses the question, do the underlying modes responsible for the Bose peak exist in crystals, or only in glasses? Raman and IR selection rules mean only excitations at the zone centre are visible. For glasses, the lack of long range order makes the reciprocal unit cell vanishingly small: all modes are effectively at the Γ point and thus accessible. However, if the modes responsible for the Bose peak occur at higher \mathbf{k} they will not be seen in the crystalline counterpart. This has supported the widespread belief that the Bose peak is unique to glasses. Crucially, using INS to access these higher \mathbf{k} modes has revealed a very similar feature in *both* the glasses and crystalline counterparts (Harris *et al.*, 2000; Trachenko *et al.*, 2000).

Leadbetter (1969) suggested that the Bose peak in v -SiO₂ was due to the flattening of the dispersion of transverse acoustic modes (as occurs at the zone boundary in a crystalline material). Dove *et al.* (1997b) studied models of the dispersion curves in α -cristobalite and attribute the equivalent INS peak at ~ 5 meV to a combination of the two lowest phonon branches along [110] together with the flattening of the transverse acoustic modes along all directions. The [110] modes are important as these represent low energy rotations of rigid tetrahedra known as RUMs. Elliott (1996) and Taraskin & Elliott (1997a,b) had also demonstrated the role of RUMs (which they called ‘floppy modes’) in changing the low energy density of states. They showed that some fragile glasses (such as alkali silicates) have so many floppy modes that these mask the Bose peak completely. Dove *et al.* (2000b) unified the ‘floppy modes’ of network glasses with the concept of RUMs, which they had previously shown to be instrumental in the phase diagrams and behaviours of silicates (e.g. Hammonds *et al.*, 1996). RUM energies can be concentrated in a small energy region up to 5 meV and can spread even across the Bose peak in some materials

(Dove *et al.*, 1997b; Harris *et al.*, 2000). They are clearly visible in the experimental INS of v -SiO₂ as a distinct band at ~ 2 meV.

The first thermal anomaly observed in glasses was in the thermal conductivity of v -SiO₂ studied by Berman (1949) (and also Berman *et al.*, 1950) who observed that the thermal conductivities at low temperature displayed a plateau in the 1–10 K region. More strikingly, it has since been demonstrated (see, for example, Freeman & Anderson, 1986; Zeller & Pohl, 1971) that all glasses have remarkably similar thermal conductivity curves in this region. Not only this, but they all share a second thermal anomaly: a departure from the normal Debye behaviour of the specific heat capacity (C) with temperature. In normal crystals, $C \propto T^3$, but in glasses it is nearer $C \propto T$ in the 5 – 10 K region. This correlates to the excess of low energy phonon modes – the Bose peak – compared to Debye-conforming materials (see Buchenau *et al.*, 2007; Sokolov *et al.*, 1992). An association between this thermal anomaly and the Bose peak was first reported by Flubacher *et al.* (1959) through studies on v -SiO₂. It is interesting to note that as far back as 1975, Bilir & Phillips found no significant difference between α -cristobalite and v -SiO₂ specific heats around 10 K. In 1971, Zeller & Pohl reported a similar peak in the density of states of quartz (which is slightly denser than v -SiO₂), albeit of lower intensity and at a higher temperature, and in 1996, Liu & v. Lohneysen observed the thermal anomalies not just in many of the oft-reported amorphous systems, but also their crystalline counterparts. Pohl *et al.* (2002) recently reviewed the ‘universality’ of these features in glasses, and also noted that this behaviour is seen in a large number of disordered materials not just glasses. They reach the conclusion that the characteristic lack of long range order seen in amorphous solids is neither sufficient nor necessary for the thermal anomalies. Despite this history, the crystalline similarities are still often ignored, particularly by the glass community, as the crystalline Bose peak does not feature in conventional lab-based spectroscopy experiments.

Thermal anomalies in amorphous materials continue below 5 K, and are probably due to two-level tunnelling states. Trachenko *et al.* (2000) used molecular dynamics simulations with v -SiO₂ model structures containing up to 4096 SiO₄ tetrahedra to show that large co-operative (~ 30 tetrahedra) reorientations of rigid tetrahedra can occur with an energy barrier of only 0.06 eV, giving the required double well potentials.

The specific heat anomaly, and indeed the energy of the Bose peak, has been shown to be linked to the density of v -SiO₂ by Inamura *et al.* (1999), with densification giving a dramatic increase in the Bose peak energy. The most likely explanation is due to the void space in the glass shrinking while maintaining the tetrahedral structure (Inamura *et al.*, 1997), and is consistent with the observation that both the specific heat anomaly and the Bose peak are related to specific eigenvectors. Similar studies performed by Courtens *et al.* (2001), on both normal

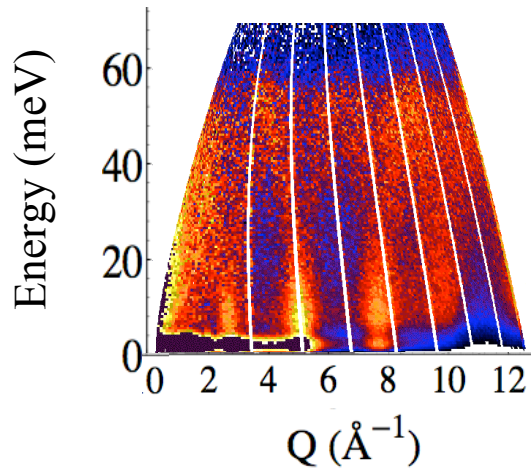


Figure 5.1: ‘Fast sound’: INS spectra in v -SiO₂, weighted by ω/Q , from the published data of Arai *et al.* (1999) (used by permission). The steep dispersive features gave a calculated sound velocity of 9400 m/s. The quasi-periodicity is notable given the amorphous nature of the material.

and densified v -SiO₂, conclude from Hyper-Raman spectroscopy that the crucial modes relate to the rocking of small groups of tetrahedra. The effect of density can also be seen through study of the INS spectra of quartz, which is denser than v -SiO₂. The Bose peak occurs at a higher energy (Harris *et al.*, 2000; Nakamura *et al.*, 2001). Changes are also observed with increasing temperature: Buchenau *et al.* (2007) report that the Bose peak in v -SiO₂ shifts to higher energy with increasing temperature.

Recently, Shintani & Tanaka (2008) have demonstrated that these ‘universal’ thermal anomalies in glasses and the related excess in phonon modes arises as a direct result of transverse modes – parallel planes of motion – and have been able to modify the position of the peak in lattice dynamical calculations by changing the force constants. The transverse nature of the modes responsible for the Bose peak in v -SiO₂ had previously been demonstrated numerically by Horbach *et al.* (2001) and Pilla *et al.* (2004).

The Bose peak, both in the glass and crystalline INS spectra, shows a characteristic Q -dependence, linked to the periodicity of the crystal in the case of α -cristobalite, and the underlying structure of the rigid tetrahedra in the glass. The same periodicity is also observed in step dispersive features extending to higher energy (~ 55 meV) first observed for v -SiO₂ by Arai *et al.* (1999), whose experimental data are reproduced in Fig. 5.1, and then also in α -cristobalite by Nakamura *et al.* (2001) (reproduced later in the Chapter, in Fig. 5.10). This has been dubbed ‘fast sound’ and is also observed in water (see, for example, Sette *et al.*, 1996, 1998). Arai *et al.* calculate an expected sound velocity from a fit to observed dispersive features in v -SiO₂ of

5.2 Model structures, pair distribution functions, and specific heat calculations

9400 m/s compared to the expected longitudinal value in glass of 6049 m/s (Hirao *et al.*, 1995). Arai *et al.* believe the coexistence of what they assume to be acoustic phonon dispersion above a strongly localised mode at the Bose peak agrees with the spectra they have observed in a range of silica polymorphs, and is an “absolutely unexpected property and is a really novel dynamics in network-forming glasses”. This conclusion mirrors independent conclusions drawn by Nakayama (1998); Nakayama & Sato (1998) from models of water and *v*-SiO₂.

What is needed is a comprehensive survey of how far all these experimental features can be reproduced using conventional lattice dynamics, which is something for which the new GULP SQW module is ideally suited. To achieve this, I make use of the polarisable-shell empirical potential model of Sanders *et al.* (1984). This shows good transferability between polymorphs, reproducing the experimental structural units, lattice dynamics and phonon properties. Lattice dynamical calculations for crystals are relatively straightforward, and a similar approach can be applied with glasses using a large model cell containing hundreds of tetrahedra to model the disorder in *v*-SiO₂. Performing these calculations in GULP, together with the two new PDF and SQW modules, allows the phonon properties, PDF and INS spectra to be calculated. TOBYFIT allows the inclusion of experimental resolution functions, together with a refinement of multiphonon and multiple scattering backgrounds. Therefore, comparative simulation studies for both α -cristobalite and *v*-SiO₂ against previously published INS spectra are presented. The dispersion curves can also be extracted from the model, and compared to experiment. Finally, computational experiments focussing on the scattering from individual species are presented. Together, these investigations allow conclusions on the origin of the Bose peak and ‘fast sound’ to be drawn.

5.2 Model structures, pair distribution functions, and specific heat calculations

The Sanders model was introduced and validated for α -cristobalite (space group $P4_12_12$) in Chapter 2.5.4, and is suitable for performing comparative lattice dynamical studies over a range of polymorphs by simply adjusting the unit cell (and, if necessary, the temperature and pressure) used in the model. To ensure the robustness of these results, all simulations were repeated using the TTAM and VB models (discussed in Chapter 2.5.4). The general trends observed are reproduced using these other models, but the failure to adequately reproduce the experimental unit cell leads to differences in the Bose peak energy. Therefore, only the Sanders results have been included in the figures shown in this Chapter.

To simulate *v*-SiO₂ I have used a primitive cell made up of 216 tetrahedra, previously derived by Trachenko *et al.* (2000). Details are given in the primary reference. A larger cell with

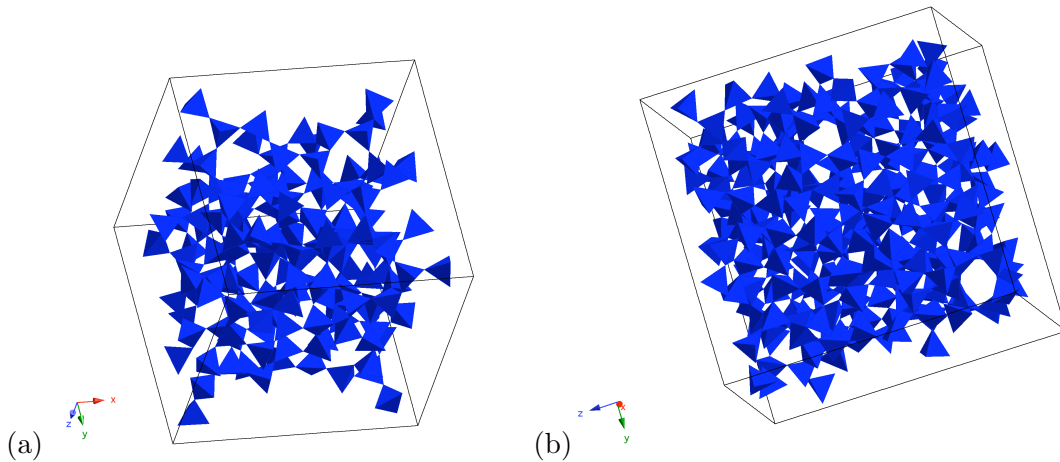


Figure 5.2: The two v -SiO₂ model structures, showing the coordination of the SiO₄ rigid units. (a) The model structure from Trachenko *et al.* with 216 tetrahedra, (b) the larger model structure with 384 tetrahedra. Only entire tetrahedra are depicted in the figures: the ‘empty space’ around the unit cell edges in fact contains tetrahedral fragments that continue the connectivity under periodic boundary conditions. Both cells show 5- and 6-fold rings, amongst other more disordered features.

384 tetrahedra was also produced in the same way by Martin Dove for use here. They are shown in Fig. 5.2 using a polyhedral model (the tetrahedral fragments at the edges of the unit cell are not shown). Both cells show the characteristic 5- and 6-fold tetrahedral rings of v -SiO₂, as well as more disordered chains.

The local and mid-range order in the model structures can be compared using PDF simulations performed using the new GULP PDF module. Pushing the computational possibilities to the limit with the current installation of GULP, the model structures were simulated with $4 \times 4 \times 4$ and $3 \times 3 \times 3$ \mathbf{k} -points for the 216 and 384 tetrahedra model structures respectively, which is appropriate given the size of cell.

The $D(r)$ form of the PDF (to emphasise the mid-range local ordering) is used in Fig. 5.3, which also includes α -cristobalite simulations as in Chapter 2.5.4. Both polymorphs show clear local ordering at low r . The first three peaks are well defined, corresponding to the rigid SiO₄ tetrahedra. The peaks are sharper in the glass simulations which suggests less variation in the tetrahedral units here. There are sharp peaks across the whole r -range for the PDF of α -cristobalite, and similar although much broader features in the vitreous counterpart with mid-range ordering in the simulated cells continuing up to 10 – 12 Å. The local ordering has been linked both to the intensity of the first sharp diffraction peak (Elliott, 1992) and also the frequency of the Bose peak maxima (Malinovsky *et al.*, 1988). Indeed, Sokolov *et al.* (1992) were able to use the first sharp diffraction peak and the Bose peak frequency to predict mid-range

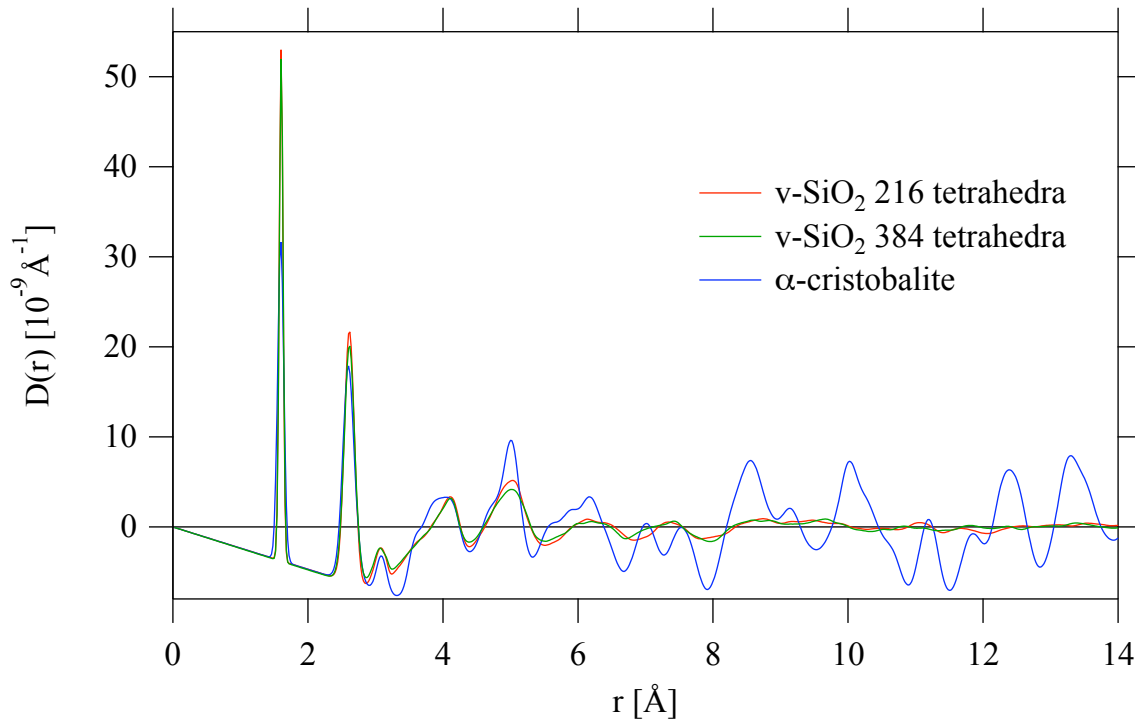


Figure 5.3: GULP simulations showing the PDF for v -SiO₂ from two different model structures, and α -cristobalite. The glass shows peaks up to ~ 10 Å indicating local ordering.

ordering in v -SiO₂ up to ~ 10 Å: this fits with the simulations produced here, where the vitreous plot shows the same degree of ordering as seen in experimental PDFs produced by Wright *et al.* (1991) from neutron scattering data.

The simulations show a high degree of similarity between the v -SiO₂ and α -cristobalite PDFs, as expected given the role of the rigid tetrahedra. Even closer agreement is seen experimentally between β -cristobalite and v -SiO₂ (Keen & Dove, 2000) because the dynamic disorder present in β -cristobalite (Chapter 3) is similar to the static disorder seen in the glass. The RUMs responsible for this dynamic disorder in β -cristobalite also correlate with the very low energy RUMs responsible for the low-temperature two-level-tunnelling effects seen in v -SiO₂ (Trachenko *et al.*, 2000).

There are small differences between the two silica samples, most notable in the flexibility of the ‘rigid units’ and also at ~ 5 Å. This latter spacing corresponds to the position of the 4th peak in the Si–Si partial, so is probably indicative of a slightly different average SiO₄ ring-size between the two model structures. The smaller model structure generally shows slightly more disorder with slightly broader peak-widths, both within the tetrahedral unit and at mid-range spacings.

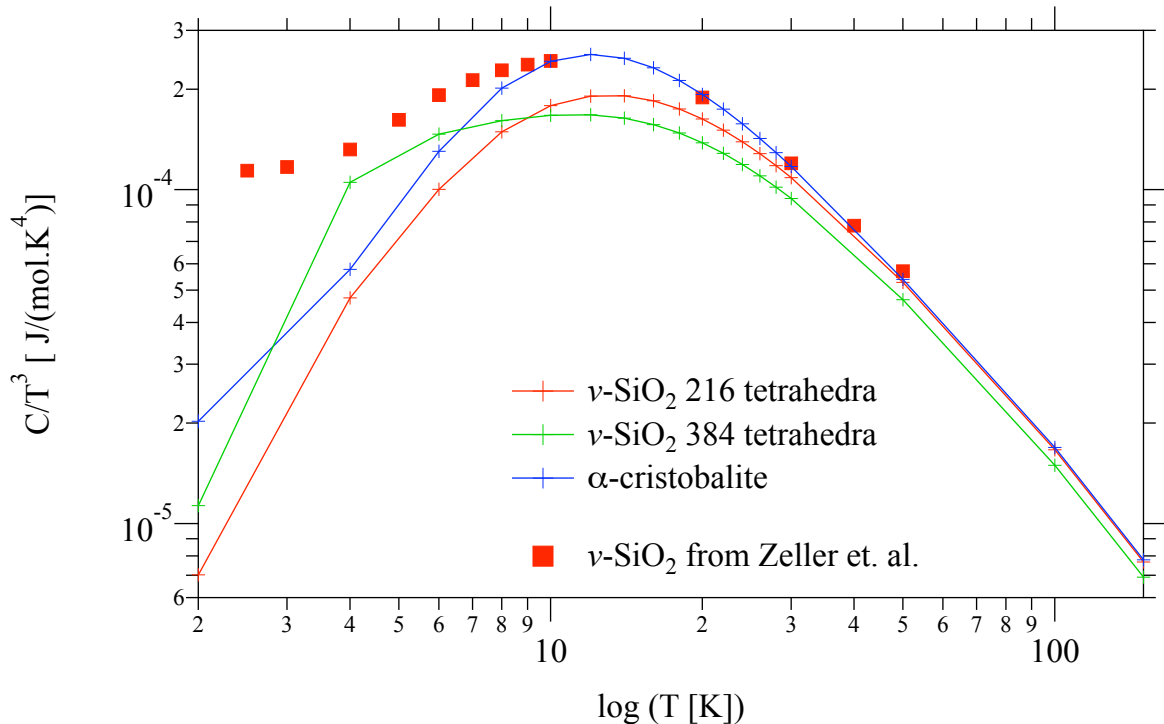


Figure 5.4: GULP models of the specific heat for both α -cristobalite and the v -SiO₂ models, together with a selection of datapoints taken from the published experimental work on v -SiO₂ from Zeller & Pohl (1971). The ‘thermal anomaly’ is the marked curvature of this line around 10 K: a Debye model would produce a flat line here. The two polymorphs both show similar deviation to the experimental result, suggesting a shared origin to this behaviour. It is not unique to the glass.

One of the ‘universal’ anomalies seen in glasses is a peak in the specific-heat capacity at around 10 K. Using the Sanders potential model, GULP simulations of both α -cristobalite and v -SiO₂ were used to produce a series of heat capacity data up to 300 K. The results are presented in Fig. 5.4, normalised per tetrahedral unit, together with a selection of data-points from the experimental work on v -SiO₂ by Zeller & Pohl (1971). It can clearly be seen that the model not only reproduces the observed behaviour for the amorphous material, but also that the same behaviour is seen in the crystalline counterpart. This is in agreement with the finding of Liu & v. Lohneysen (1996), who suggest a general correlation between the mechanisms leading to this peak in both amorphous and crystalline solids. Both v -SiO₂ models give reasonable agreement to experiment, with the larger model structure showing slightly closer agreement to the experimental data.

5.3 Experiment

Powder INS data for α -cristobalite and v -SiO₂ at room temperature were collected on the MARI spectrometer at ISIS by our group in Cambridge using an incident energy of 35 meV. Details are in the published reference (Trachenko *et al.*, 2000). The data were self-consistently normalised against the flux measured on the monitors and binned to give 600 energy bins between -30 and 30 meV. The experimental spectra (with a small amount of smoothing applied to guide the eye: MSLICE setting $s = 5$) are shown in the left column Fig 5.5.

5.4 Simulations

Simulations have been performed using the new GULP SQW module with TOBYFIT providing appropriate experimental resolution functions. The simulations incorporate temperature effects (303 K) though the Bose factor and Debye-Waller temperature factors. The α -cristobalite unit cell optimised to $a = b = 5.0$ Å, $c = 7.06$ Å using the Sanders model. This gives a density of 2.25 g/cm³. 42875 \mathbf{k} -points in the first Brillouin zone were used to populate an ideally spaced Monkhorst-Pack grid giving the one-phonon INS spectra as well as multi-phonon and multiple scattering contributions.

v -SiO₂ INS spectra were also produced using both structural models. The smaller cell, with 216 tetrahedra and lattice parameters of ~ 21 Å, optimised to have a cell volume of 9581 Å³, while the larger cell, with 384 tetrahedra and lattice parameters of ~ 25.5 Å, optimised to have a cell volume to 15181 Å³. The density of the two cells were 2.25 g/cm³ and 2.29 g/cm³ respectively.

Simulating the v -SiO₂, with over 1000 combined cores and shells even in the smaller model structure, provided a computational challenge. The computational demands meant that only one \mathbf{k} -point could be used in the SQW calculations at any one time, so Perl scripts were used to manually parallelise the code (see Appendix C.2), each \mathbf{k} -point producing an individual .sqw file. The Bmatrix for the Debye-Waller temperature factor cannot be calculated in this way, so was generated using the same number of \mathbf{k} -points (using the maximum memory available) as

| | v -SiO ₂ (216) | v -SiO ₂ (384) | α -cristobalite |
|-------------------------|-----------------------------|-----------------------------|------------------------|
| χ^2 | 70824 | 67231 | 42360 |
| Multi-phonon (%) | 16.6 | 16.9 | 13.7 |
| Multiple scattering (%) | 13.6 | 7.0 | 5.2 |

Table 5.1: Final χ^2 , multi-phonon and multiple scattering parameters for the three simulations shown in Fig. 5.5. The refined values for multi-phonon and multiple scattering are realistic. Clearly, the best agreement is between the α -cristobalite and experimental data, but the agreement is good in all case.

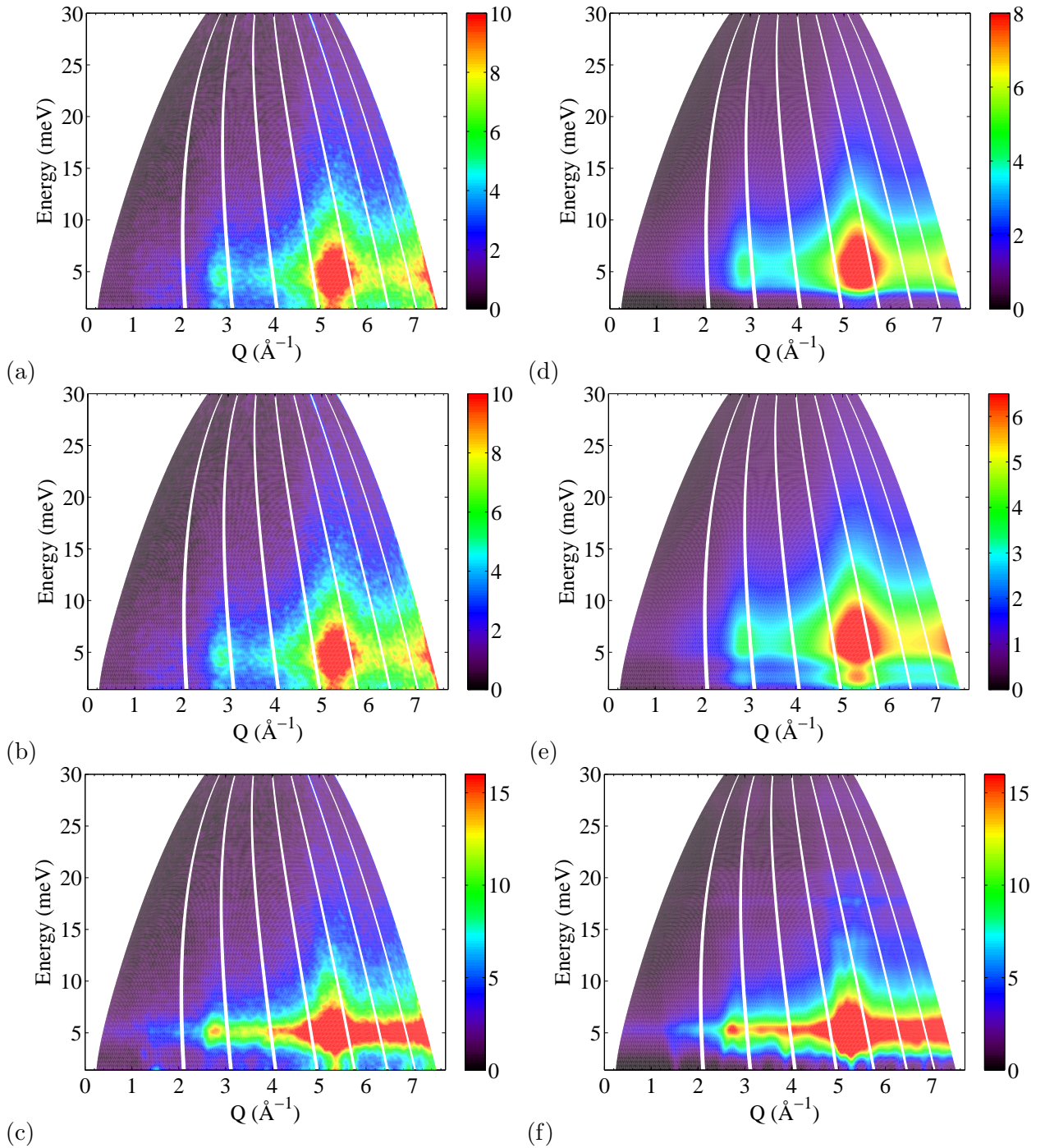


Figure 5.5: (Left) Experimental MARI datasets at room temperature: (a) v -SiO₂ (b) v -SiO₂ (reproduced for comparison with simulations) (c) α -cristobalite. (Right) Simulations (including backgrounds and experimental resolution functions) performed using TOBYFIT with the GULP SQW module: (d) v -SiO₂ with 216 tetrahedra, (e) v -SiO₂ with 384 tetrahedra (f) α -cristobalite. These are discussed in the text. It can be seen that all simulations and experimental INS spectra show a similar Bose peak at around 5 meV, as well as displaying characteristic variation in intensity along Q .

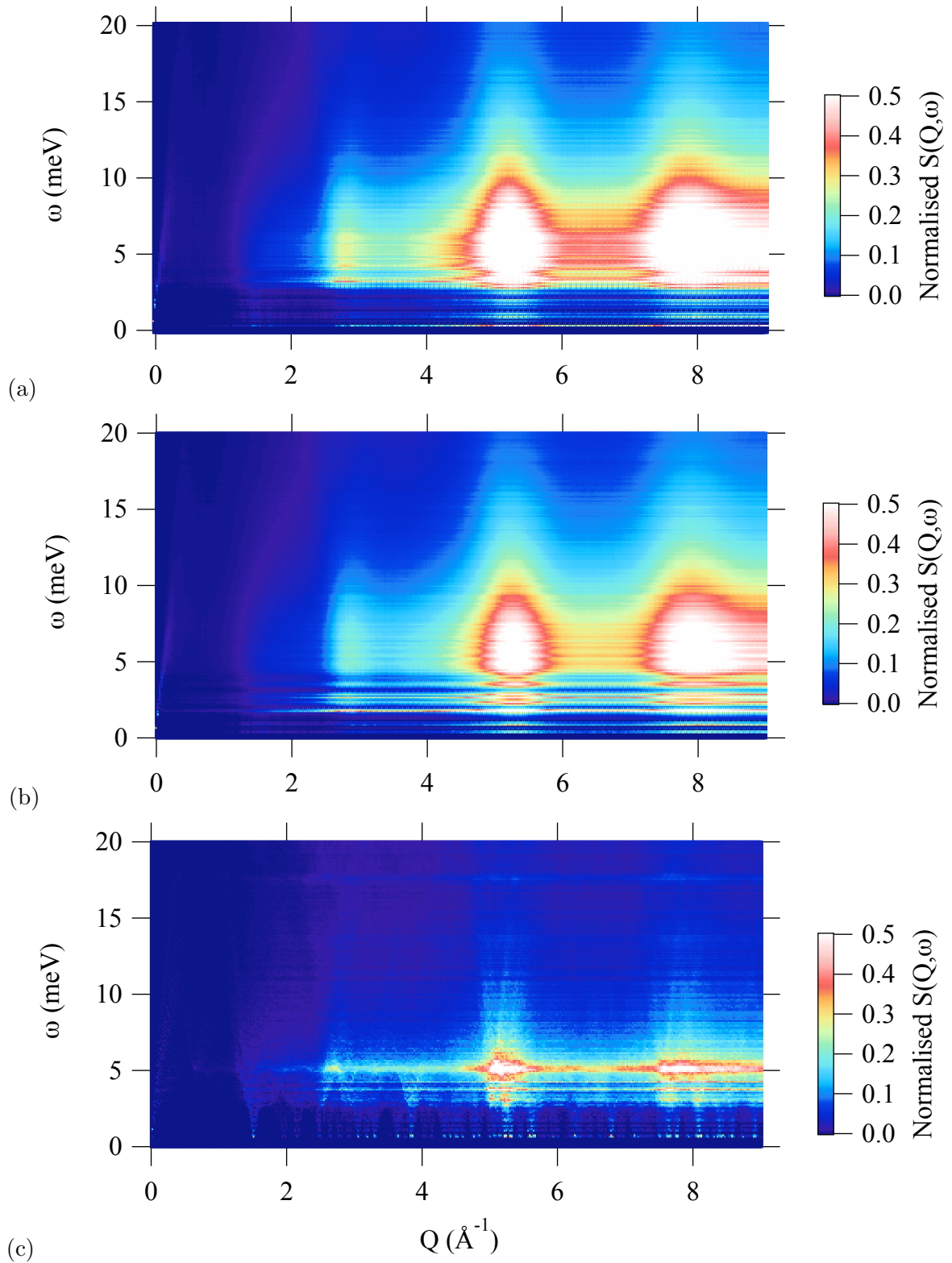


Figure 5.6: GULP simulations of the one phonon scatter in absolute units, without experimental resolution factors for (a) v -SiO₂ with 216 tetrahedra, (b) v -SiO₂ with 384 tetrahedra and (c) α -cristobalite. Without experimental resolution effects the details of the one phonon scattering function can be seen, particularly the bands of RUMs below the main Bose peak in all cases.

the PDF and specific heat calculations, and passed to each parallel SQW module calculation. The output from these simulations were then combined through another script, before being used as the input to TOBYFIT with one of the new powder cross-section models to convolve the spectra with the experimental resolution functions.

As the model structures are so large and contain so many atoms, relatively few \mathbf{k} -points are required to achieve convergence and adequately populate the SQWarray. Simulations for both cells were performed using 216 random¹ \mathbf{k} -points. Combining sub-selections of the resulting simulations confirmed that convergence had been achieved well before this point.

Approximations to multi-phonon and multiple scattering are calculated as part of the GULP simulation, and can be refined in TOBYFIT against our experimental data. The final parameters are shown in Table 5.1. While the output of the GULP simulation is in absolute units, the MARI data were self-consistently normalised against the flux recorded from the monitors so an experimental scaling factor is to be expected.

Simulations were performed in two ways to allow comparison with both low and high incident energy data. First, low energy features such as the Bose peak were revealed using a finely binned energy grid up to 35 meV. The one-phonon simulations are shown in Fig. 5.6. Together with refined multi-phonon and multiple scattering spectra, these were convolved with experimental resolution functions to enable direct comparison with our experimental data (collected with an incident energy of 35 meV) in Fig. 5.5.

The second set of simulations were designed to study the higher energy dispersive features seen by Arai *et al.* (1999) and Nakamura *et al.* (2001) with MARI data at $E_i = 100$ meV. Nakamura *et al.* weight the experimental INS spectra by ω/Q , which is directly comparable to a density of states weighting in the long wavelength limit. This highlights the controversial higher energy features. The higher energy simulations were performed with more coarse bins to reduce the extensive memory requirements. The weighted one-phonon spectra are shown Fig 5.11. Incorporating multi-phonon and multiple scattering effects with the same weightings as for the lower energy spectra, these were convolved with experimental resolution functions allowing comparison with the published data (at incident energy of 100 meV) of Arai *et al.* (1999) and Nakamura *et al.* (2001) in Fig. 5.10. The simulations also give access to the low- Q spectra, inaccessible by INS. An enlargement of this region, reflecting the 1st Brillouin zone, is shown together with dispersion curves for α -cristobalite in Fig. 5.9. Above the first few meV, there were negligible differences between the spectra from the two v -SiO₂, so the results from just the larger model structure are included for clarity.

¹Others in our group in Cambridge have found that using the Monkhorst-Pack grid with these large model structures can sometimes introduce grid artefacts, and recommend using *random* \mathbf{k} -points to reduce the number of \mathbf{k} -points needed to achieve convergence of phonon property calculations.

5.5 Results and discussion: $E_i = 35$ meV data

There is good general agreement between the simulated spectra and the 35 meV experimental data in Fig. 5.5. Considering the α -cristobalite first, visual comparison between the simulation and experiment is excellent with all the features being well reproduced. Cuts taken through the spectra at a representative constant- Q (integrating between $4 < Q < 4.2 \text{ \AA}^{-1}$) and a constant-energy cut along the Bose peak ($4 < \omega < 6$ meV) shown in Fig. 5.7 confirm that the model reproduces the experimental details very well. The simulations do not include the elastic line, but there are relatively few modes in the region affected by the elastic resolution in α -cristobalite so this is immaterial here. There is a marked periodicity in the intensity along Q in the α -cristobalite experimental data with peaks in the Bose peak intensity at 2.7 \AA^{-1} and 5.3 \AA^{-1} . This is perfectly reproduced by the simulations.

Comparison of the two model structures of v -SiO₂ with the experimental spectra shows that the key features have been reproduced. The agreement is not as close as for the α -cristobalite, which had the best χ^2 value of the three simulations¹ in Table 5.1. The larger model structure reports a more favourable χ^2 . Crucially, the Bose peak with its characteristic intensity-variation along Q is clearly present. Again there are peaks in the 5 meV constant-energy cut at 2.7 \AA^{-1} and 5.3 \AA^{-1} .

The intensity scale for the simulated v -SiO₂ spectra had to be adjusted to provide a good fit by eye, because the best mathematical scaling over the entire data-range resulted in the features at the Bose peak becoming indistinct. This is perhaps an indication that the multi-phonon scattering was underestimated: certainly the cut along Q appears to be lacking intensity at high Q (Fig. 5.7(b)).

There are small differences between v -SiO₂ simulations and experimental details below 5 meV (Fig. 5.7(a)). The resolution of the elastic line makes it difficult to extract accurate information here. No attempts have been made to fit this background in the $S(Q, \omega)$ simulations, but the shape of the elastic line can be extrapolated by eye, lifting the intensity of the lowest modes to agree with experiment. The presence of more modes around 2 meV than in the α -cristobalite make this region more relevant, and makes the refinement of the backgrounds and scaling parameters less reliable. Notwithstanding this, the two model structures, with slightly different degrees of mid-range order, do reproduce the general trends in the experimental INS spectra.

¹It has been noted in earlier chapters that the χ^2 values appear weighted to larger values with data self-consistently normalised against the moderators, so it is not expected that these values should achieve unity. Convergence was reported when the change in the χ^2 was less than the reported error in the calculation of the χ^2 .

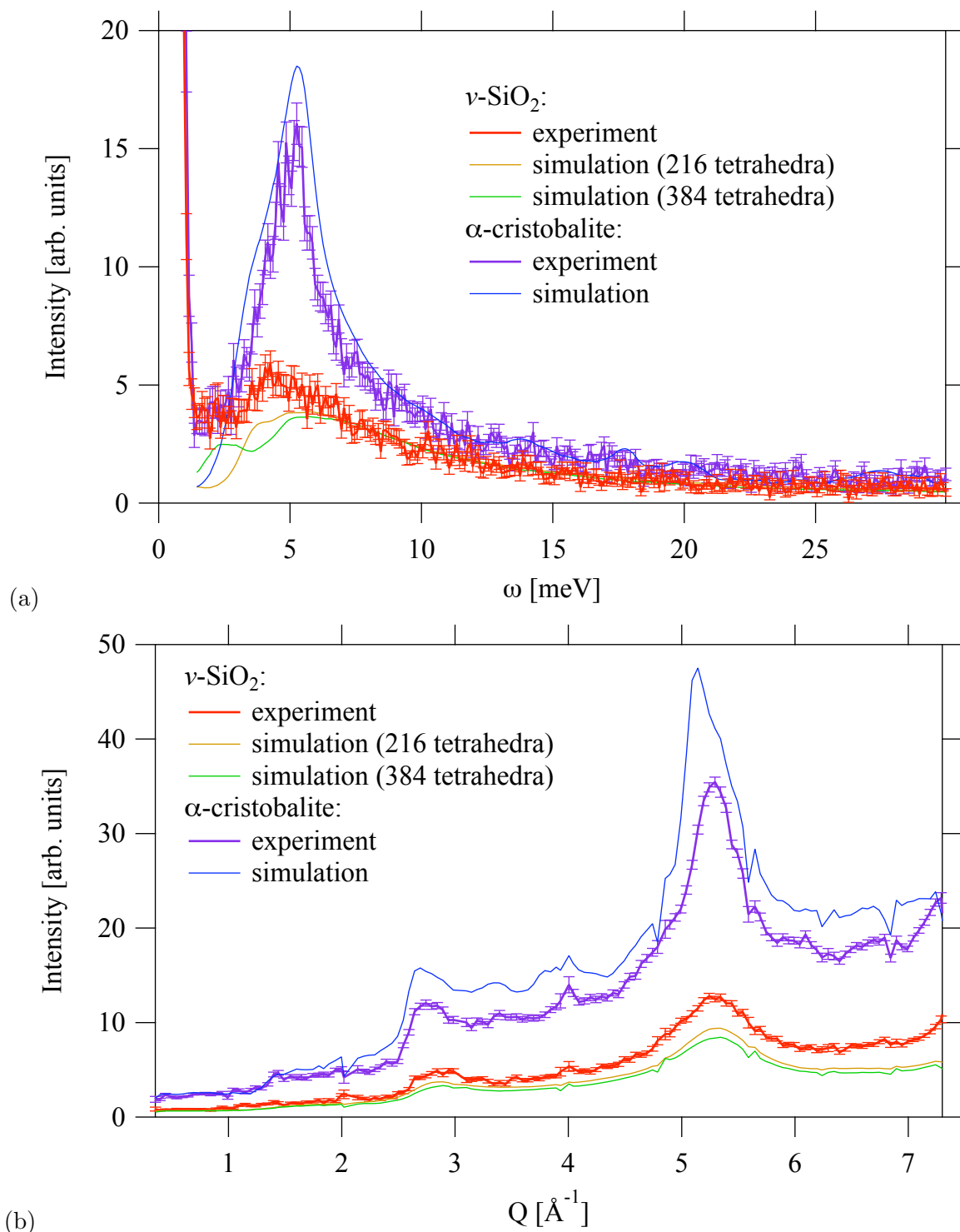


Figure 5.7: Cuts through both the experimental INS spectra at 35 meV, and the simulated spectra fully convolved with experimental resolution functions. (a) The cut at $4 < Q < 4.2 \text{ \AA}^{-1}$ shows the effect of the elastic line on the experimental data, as well as the quality of the simulations. (b) The constant-energy cut along the Bose peak ($4 < \omega < 6$ meV) shows the characteristic Q -variation even in the glass due to the tetrahedral unit. The sharp dips in the intensity of the data directly mimicked by the background components are due to the door-edges in the spectrometer.

The two model structures for v -SiO₂ give slightly different features below 5 meV: the larger cell elevated the energy of the main Bose peak, clearly separating into two component peaks. This cell also has a slightly higher density, confirming other studies that have linked densification to a shift in the Bose peak energy. The lowest modes are likely to be RUMs. These merge with the main Bose peak in the smaller silica cell. Neither simulation gives a perfect reproduction of experiment, but both are sufficiently close to be able to say that all the observed features can be simulated from standard lattice dynamical calculations.

It is now possible to make detailed comparison between the polymorphs, having established the ability of the models to reproduce the experimental data. The similarities are striking. Features are shaper in the crystal, but the same trends appear in both. This is emphasised by the constant- Q and constant-energy cuts in Fig. 5.7. The periodicity seen along Q must arise from the structural similarities between the polymorphs: the rigid SiO₄ tetrahedra.

The position of the Bose peak energy is the same for the smaller v -SiO₂ cell and α -cristobalite. Both have a density of 2.25 g/cm³, while the larger supercell has a slightly higher Bose peak energy and a slightly higher density. The level of agreement between the two polymorphs with the same density is important.

One difference between the lattice dynamics of v -SiO₂ and α -cristobalite is in the number of RUMs. α -cristobalite has only two branches of RUMs, whereas the glass has many RUMs, similar to the planes of RUMs found in β -cristobalite (studied in Chapter 3). This confirms the interpretation of the constant- Q data below 5 meV: if the additional peaks in the glass seen experimentally around 2 meV are due to these RUMs, the equivalent modes in the crystal merely put a shoulder on the main Bose peak. This line of discussion is expanded in the next section.

The most important observations here are the striking similarities between the vitreous and crystalline INS spectra, and that all the features in the 35 meV experimental spectra are closely reproduced from standard lattice dynamical calculations. The next stage is to look in more detail at the dispersion curves covering both the Bose peak and higher energies, before comparing the higher energy simulations with experiment.

5.6 Dispersion curves

The dispersion curves along four key directions for α -cristobalite have been calculated using the Sanders model and are shown in Fig. 5.8. The Bose peak region is dominated by branches that would be described as acoustic modes at the zone centre, although this description breaks down at higher \mathbf{k} . There is clearly an optic mode at ~ 4 meV at the Γ -point, which also crosses the relevant region, hybridising with the flattening acoustic modes. The two lowest energy branches in [110] are the RUMs for α -cristobalite: the v -SiO₂ of course has many more RUMs, but these

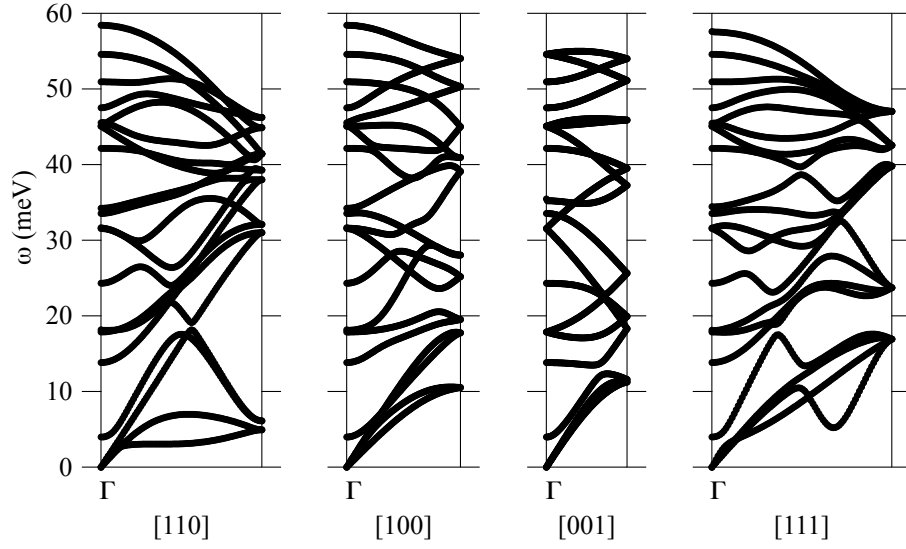


Figure 5.8: Dispersion curves calculated from the Sanders model for α -cristobalite. The Cartesian lengths for each direction are 0.887, 0.627, 0.445 and 0.992 \AA^{-1} respectively. These branches can clearly be seen when compared to the low- Q α -cristobalite one-phonon ω/Q weighted simulations in Fig. 5.9. The key feature here is that the steep curve linked experimentally to ‘fast sound’ is due to the hybridisation of many branches.

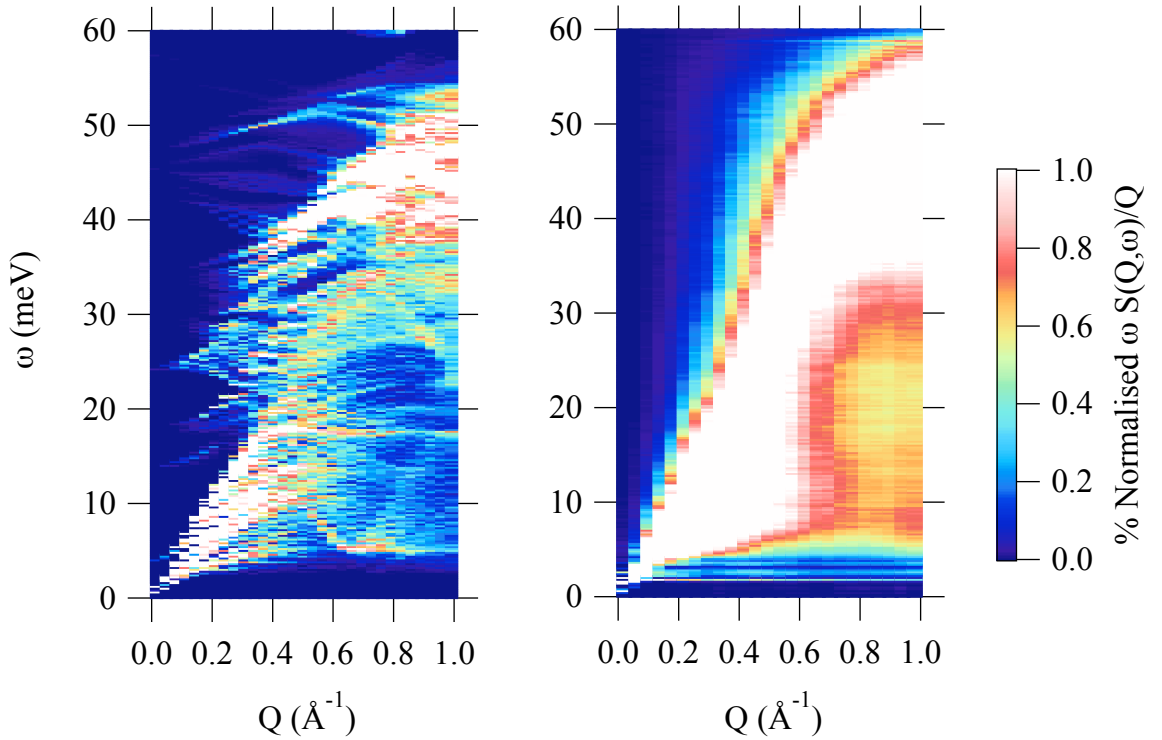


Figure 5.9: The one-phonon spectra weighted by ω/Q from the GULP simulations for (left) α -cristobalite and (right) v -SiO₂ with 384 tetrahedra, highlighting the crucial low Q region that is inaccessible by INS experiments. Higher Q simulations are shown in Fig. 5.11. The similarities between the two polymorphs can clearly be seen.

are the only RUMs in α -cristobalite. Looking at the one-phonon simulations in Fig. 5.6(c) at least the lowest of these RUMs forms a distinct feature at constant energy just below the main Bose peak. With experiment resolution, this detail merges into the ‘Bose peak’ and cannot be distinguished. In the constant- Q cut, the RUMs are the slight shoulder seen both experimentally and in the simulations at ~ 4 meV. By analogy, the continuum of modes seen below the Bose peak in the experimental spectra for the glass, the details of which can be seen in the one-phonon simulations in Fig. 5.6, will be the (many more) glass RUMs. The nature of these RUMs appears dependent on the different cells used to model the glass, implying a dependency on the tetrahedral-ordering in the model structure.

5.7 Results and discussion: higher energy features

The similarities seen in the Bose peak of v -SiO₂ and α -cristobalite extend to the higher energy region. The simulated spectra, convolved with experimental resolution functions, can be compared with the published INS spectra of Arai *et al.* (1999) (Fig. 5.1) and Nakamura *et al.* (2001) (reproduced in Fig. 5.10, together with the simulations). Higher Q features for v -SiO₂ were inaccessible due to the huge computational demands of such a simulation.

The effects of the experimental resolution functions can clearly be seen by comparison of the spectra in Fig. 5.10 with Fig. 5.11, which shows just the one-phonon INS spectra. The disorder in the glass leads to broadening of the high energy dispersive-features visible in the one-phonon simulation, but any fine detail in either polymorph is lost in experimental INS spectra due to experimental resolution functions. The smooth character and shape of this dispersive feature in both the full simulations and experimental data, makes it is hardly surprising that such experimental results have been interpreted as acoustic modes.

The higher energy dispersion curves in Fig. 5.8 are of great importance, as they provide the first real insight into the phenomenon sometimes referred to as ‘fast sound’ in the literature. The acoustic branches in α -cristobalite behave as expected, peaking below 20 meV. The higher energy branches would all be described as conventional optic modes at the zone centre. There is scope for confusion around ~ 19 meV where an optic branch continues to higher energies with a very similar slope to the lower energy acoustic branch, with anti-crossing indicating that they share the same symmetry. This mode hybridisation is repeated with other optic branches to higher energies. However, to describe these branches as optic at the zone boundary is not helpful, as the character of the atomic vibrations here are more acoustic-like. What is important is that there are many branches which hybridise to give the smooth dispersive features seen in the simulations.

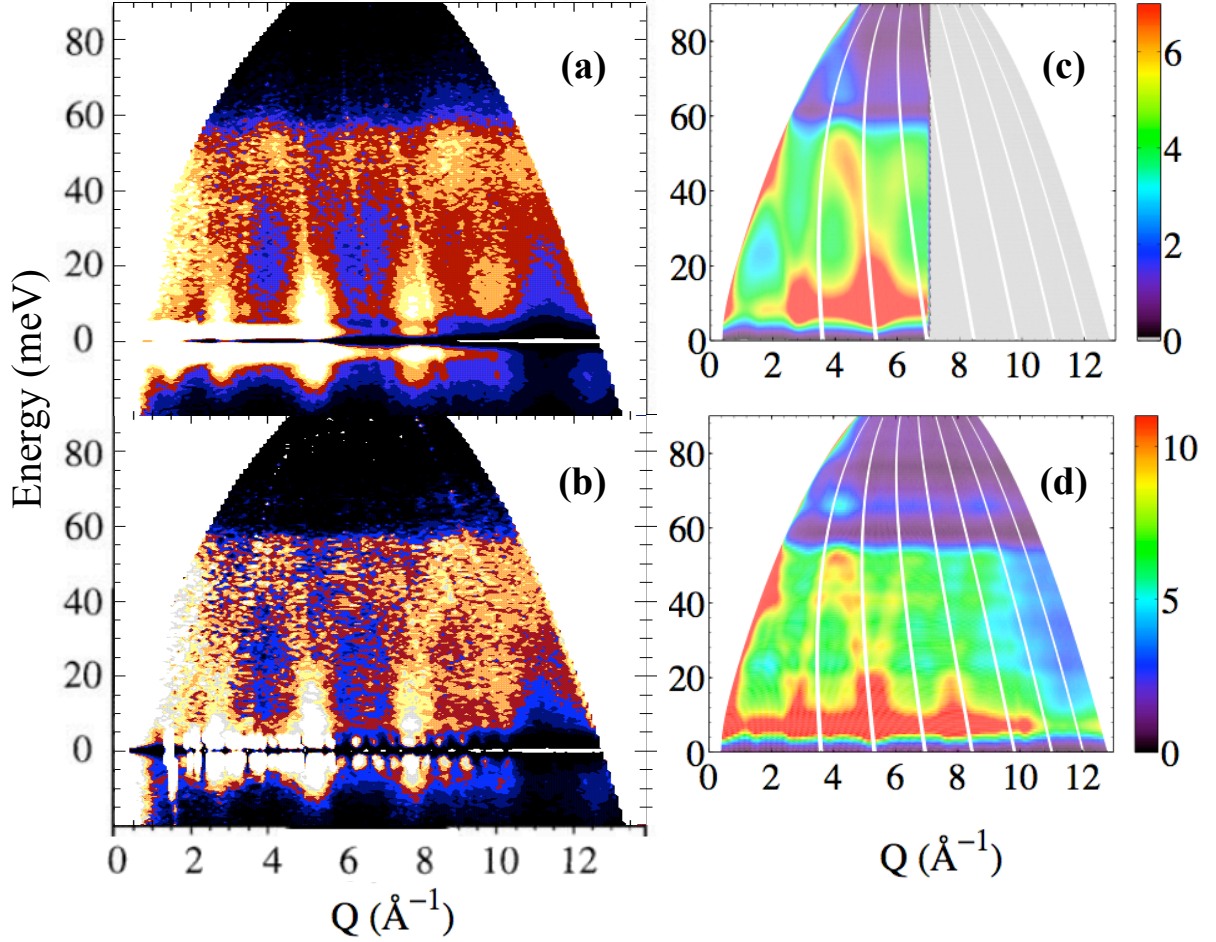


Figure 5.10: Comparison of the new simulations with previously published experimental INS spectra. (Left) A reproduction of the experimental data of Nakamura *et al.* (2001) (from Fig. 1 in the published paper, used with permission) showing experimental spectra collected on MARI at $E_i = 100$ meV and weighted by ω/Q to show the higher energy features for (a) v-SiO₂ and (b) α -cristobalite. (Right) Simulated spectra convolved with experimental resolution functions appropriate for MARI at $E_i = 100$ meV and weighted by ω/Q for (c) v-SiO₂ and (d) α -cristobalite. The key feature here is the similarity between the crystalline and amorphous behaviour. The effects of the resolution function masking the underlying detail in the broad high energy curves can be seen when compared to the one-phonon simulations in Fig. 5.11.

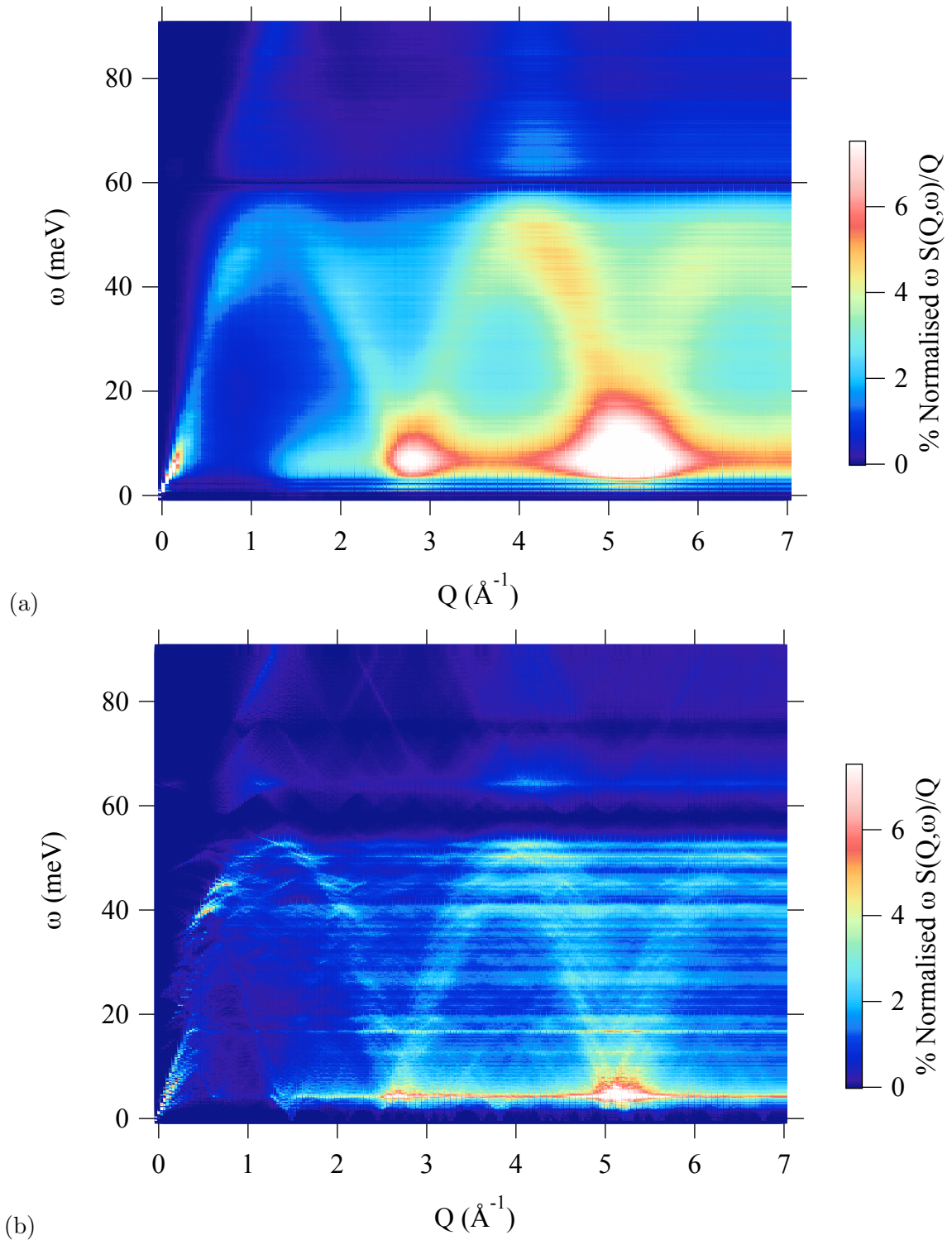


Figure 5.11: ω/Q weighted simulations for (a) $v\text{-SiO}_2$ and (b) $\alpha\text{-cristobalite}$ showing the ‘dispersive’ features seen by Arai *et al.* experimentally. The one phonon simulations here also show the very low Q range data inaccessible by INS, which was shown enlarged in Fig. 5.9. The agreement in the periodicity of the polymorphs is striking.

Fig. 5.9 highlights details of the one-phonon spectra within the first Brillouin zone, inaccessible by INS. The basic shapes of the dispersion curves can be seen, but now with the addition of the appropriate intensity. It is clear there is no one smooth acoustic mode ascending to high energy, but a superposition of many different modes.

It is interesting to calculate the velocity of sound from these simulations in two ways. First, the shape of the dispersive feature in the simulations gives a sound velocity of 9700 m/s, comparable with Arai *et al.*'s value of 9400 m/s. However, calculating the velocity of sound from the elastic constants returned by the GULP phonon property calculation, the P waves should travel at 6400 m/s and the sheer waves at 3800 m/s. These values compare well with the published values of Hirao *et al.* (1995). This still poses the question – now set in a self-consistent setting – of why the dispersion curves appear to have a higher velocity? This requires further investigation.

What is clear from these studies is that there is a shared origin for the Bose peak and the higher energy dispersive features. Moreover, the similarities between the crystalline and amorphous spectra (both experimentally and in the simulations) are remarkably close. There are still unanswered questions, but those questions have now been better defined.

5.8 Contributions from selected atoms

Study of the dispersion curves showed that flattening acoustic branches hybridising with the first optic branch giving rise the high intensity along the Bose peak. It has been argued in the literature (e.g. Buchenau *et al.*, 2007; Fabiani *et al.*, 2008) that the Bose peak arises from coupled rotations of tetrahedra – these must have some optic character. New insights into this can be gained by simulating the INS spectra for individual species in the α -cristobalite unit cell, as shown in Fig. 5.12.

Using the new GULP SQW module, the neutron scattering length for the two atomic species were each set to zero in turn, showing the contributions from each individual species. The Bose peak remains clearly visible in both, although the Si-only $S(Q, \omega)$ contributes only very lightly to the overall scattering function. Unsurprisingly, without the oxygens, the characteristic Q fluctuation is lost (Fig. 5.12(b)), leaving only the normal increase in Q from the scattering function. To confirm that the main features were maintained here, the two plots were summed, recombining to give all the features of the total $S(Q, \omega)$ although with some loss of intensity and detail due to cross-terms between the species. In the same way, each individual Si and O in the unit cell was taken in turn (not shown). Again, the Q -dependence was completely lost, but all maintained the Bose peak. Summing the individual contributions does not regain the periodicity as this is due to the cross-terms between spatially ordered atoms.

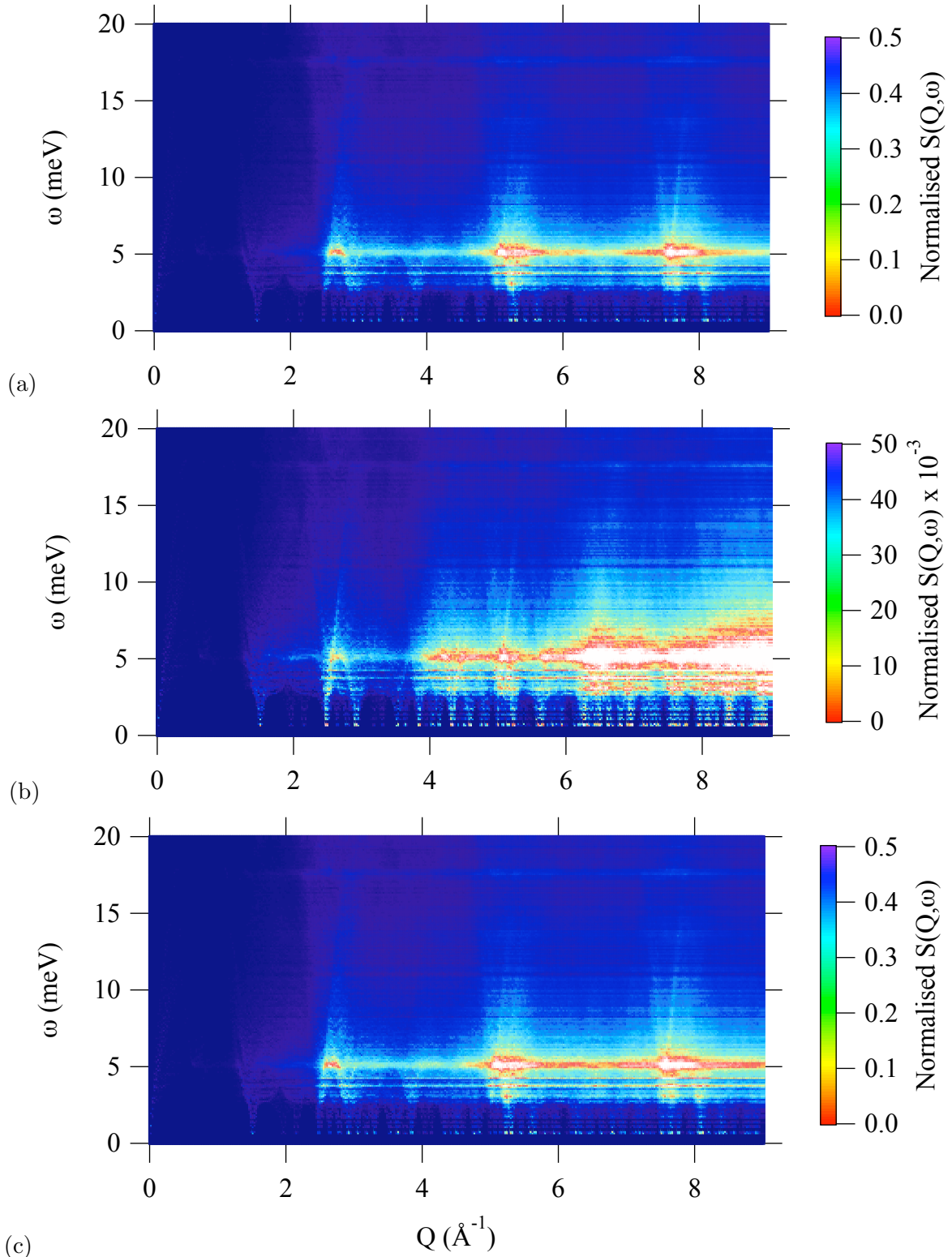


Figure 5.12: One-phonon scattering spectra with (a) scattering *only* from oxygen, and (b) scattering *only* from silicon. (c) The sum of the two partial scattering functions: this is less than the total scattering in Fig. 5.6(c) due to additional cross-terms, but the main features are still reproduced. All figures are normalised against the maximum scattering intensity of the full $S(Q, \omega)$. The scattering from Si only is small, but there is still a clear Bose peak.

This information is useful in understanding the origins of the Bose peak. If it were simply due to rotations of tetrahedra, the partial $S(Q, \omega)$ from Si should no longer show a peak. However, there is clearly a phonon mode corresponding to movement of the centre of the tetrahedra around ~ 5 meV. This implies that there is translation (probably as well as) rotation.

What is needed is a means of visualising the motions of the individual eigenvectors. This problem is currently being worked on by other members of our group, who are developing a means of creating video animations of the atomic motion encapsulated in the eigenvectors. This has shown great success with CASTEP eigenvectors, and is currently being implemented for GULP. Having demonstrated the validity of the current GULP models here, we should soon be able to confirm the nature of the modes in the Bose peak.

5.9 Conclusions

This chapter has demonstrated the power of the new methodology to probe the dynamics of powdered crystals and amorphous materials, gaining insights unavailable through experimental work. It has been shown that the ‘unique and universal’ features of glasses are also present in the crystalline networking-forming counterparts. This supports many (underrepresented) experimental reports in the literature and validates a comparative study of the crystal and glass. Such experiments have shed new light on both the Bose peak and the controversial ‘fast sound’, showing that these features have a shared origin in the lattice dynamics.

In light of the experimental and computational data presented here, it is clear that the Bose peak seen experimentally is often the superposition of two features. Low energy RUMs contribute to the scattering intensity near the elastic line and extend up to and in some systems (Dove *et al.*, 1997b), beyond the Bose peak itself. The position of these RUMs is well established in α -cristobalite, and due to the two lowest energy branches of the [110] dispersion curve. In the glass, there are many RUMs, whose energies depend on the mid-range ordering (as seen from the PDF).

The Bose peak is primarily made up of flattening acoustic branches, although there are also some low intensity optic modes that pass across the peak. However, this description is less useful further from the zone center, as the optic branches will show considerable acoustic character. The characteristic Q -variation arises from the tetrahedral unit (the crystalline unit cell is defined by four such tetrahedra, so has the same dependency). This is confirmed when the scattering from the Si atoms is ignored: it is the spatial distribution of the oxygens around the tetrahedra that dominates the Q -variance. More importantly, the Si atoms themselves show a peak in the density of states corresponding to the Bose peak. This demonstrates that the Bose peak cannot be due to coupled rotations alone, but must also involve displacements of the Si atoms at the

heart of the tetrahedra. As discussed, what is needed is direct visualisation of these modes, which will soon be possible. Finally, extending the analysis to higher energy modes has shown the role of mode hybridisation and the superposition of many branches in forming the smooth ‘dispersive’ feature seen experimentally. Animations of the eigenvectors will also help with the interpretation of these features.

In conclusion, the new methodology has shown that there are likely to be shared origins to the Bose peak and higher energy dispersive features, and that these features are not unique to glasses, but arise from the standard lattice dynamics of the network-forming crystalline counterparts. The common feature here is the SiO_4 tetrahedral unit, which dominates the periodicity of these features.

Chapter 6

Calcite: a powder and single crystal INS study

Inelastic neutron scattering spectra for CaCO_3 are simulated using the new TOBY-FIT cross section models and GULP SQW module. Experimental resolution factors are included in the simulation, giving results directly comparable to single crystal and powder data collected on the new MERLIN spectrometer at ISIS. The transferable carbonate empirical potential model developed by Archer et al. (2003) (making use of a polarisable core-shell model for the oxygens) is shown to give excellent agreement to experimental data, reproducing the general trends of dispersion curves and the soft mode that drives the $R\bar{3}c$ to $R\bar{3}m$ phase transition. With the assistance of this model, the dispersion curves are extracted from single crystal INS spectra, showing the \mathbf{a}^ dispersion for the first time. Refinement capabilities of the new software package are tested using a force constant model, revealing new possibilities for the inelastic equivalent of structural powder refinement.*

6.1 Introduction

The carbonate group of materials are highly prevalent, forming many sedimentary rocks and making up a sizeable proportion of the earth's crust. They show important geological and geochemical behaviour, and understanding the phase diagrams is important. A key example is calcite carbonate, CaCO_3 , known as calcite, which is found as a stable rhombohedral structure ($R\bar{3}c$, shown in Fig 6.1) at atmospheric pressure.

The phase diagram for calcite involves monoclinic calcite II (Singh & Kennedy, 1974) and calcite III (Merrill & Bassett, 1975), whose structure remains unclear, on increasing pressure. On the temperature spectrum, it undergoes an orientational order-disorder phase transition at

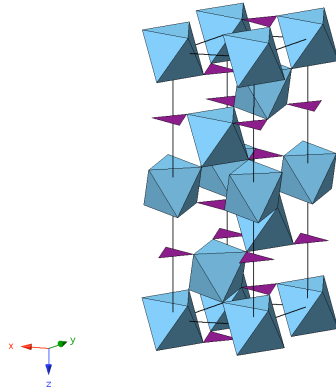


Figure 6.1: A polyhedral model of the calcite unit cell for the room temperature $R\bar{3}c$ structure. The carbonate group is shown as a purple triangle, the calcium octahedrally coordinated by oxygens is shown in blue.

1260 K (Dove & Powell, 1989) between the disordered high temperature $R\bar{3}m$ and ordered $R\bar{3}c$ structure. At higher pressures, MD simulations by Kawano *et al.* (2009) have shown a first-order isosymmetric phase transition occurring between two $R\bar{3}c$ phases prior to this transition. The high temperature transition is observed by the onset of super-lattice reflections in diffraction patterns at the Z point of the disordered high temperature Brillouin cell, and is driven by a soft transverse acoustic (TA) mode at the F point ($F = (\frac{1}{2}, 0, \bar{2})$ in the low temperature cell).

Experimentally, partial (low energy) dispersion curves for $R\bar{3}c$ calcite at room temperature have been published along the \mathbf{c}^* axis by Cowley & Pant (1973), and towards F by Dove *et al.* (1992). The latter direction is of particular importance as it reveals both the soft mode that drives the phase transition, and anomalous columns of soft phonons sharply localised at the F point. This continuum of excited states ranges from zero energy to the soft TA mode, with intensity scaling with temperature according to an Arrhenius relationship with $T^* = 1035$ K. The origin of this is thought to be thermal fluctuations into a different ordered structure. This column of scatter is observed in other materials, linked to coupling with electronic correlations, but this cannot explain how this behaviour arises in an insulator like calcite. Harris *et al.* (1998) suggest coupling between relaxational and phonon modes is responsibly here.

In order to fully understand the dynamics and phase diagram of this important mineral system it is essential to have an accurate computational model. Early force constant models (Cowley & Pant, 1973; Plihal & Schaack, 1970) showed the importance of a shell model in reproducing experimental data for calcite. Subsequently, Singh *et al.* (1987) produced an empirical potential model, although this failed to adequately reproduce phonon dispersion curves. This was followed by rigid ion empirical potentials developed for a number of polymorphs (Catti *et al.*,

1993; Pavese *et al.*, 1992), which accurately reproduced the individual structures although, like the force constant models, lacked transferability between the polymorphs. A transferable rigid ion model was successfully developed by Dove *et al.* (1992) which also reproduced experimental dispersion curves along [104] and the \mathbf{c}^* axis. However, to account for dielectric properties (as found with the early force constant models) and to study defect behaviour, a shell model is required. The first such a model was produced by Pavese *et al.* (1996) to reproduce the experimental structure for a number of carbonate polymorphs together with elastic properties. A very accurate structural fit was reported by Fisler *et al.* (2000), but this was achieved at the expense of the dynamics and indeed gave an unstable phonon model: the imaginary phonon frequencies in this model would lead to distortion. However, Archer *et al.* (2003) were able to use the shell model of Fisler *et al.* (2000) as a basis for a GULP refinement, producing a transferable carbonate empirical potential shell model by refining against experimental observables, including a few points from phonon dispersion curves along the \mathbf{c}^* axis. This model (which I refer to as the Archer model) achieves a good balance between transferability, accurate structural detail and (weighted slightly more heavily than in other empirical potential models) good phonon dispersion curves.

What is now needed for calcite is a more complete characterisation of the room-temperature lattice dynamics. MERLIN, with its huge sweep of detectors, is ideally suited to this purpose. I have collected single crystal INS experimental data, which I denote $S(\mathbf{Q}, \omega)$, as well as powder INS spectra, which I denote $S(Q, \omega)$.

This chapter has three inter-related aims. The first is to simulate powder and single crystal INS spectra, fully convolved with experimental resolution functions, using the well accepted Archer model. This will enable direct comparison of the spectra with experimental data allowing rigorous scrutiny of the dynamics in this model.

Second, calcite provides the perfect test-case for the new powder refinement approach in a more complex material, requiring information from densely overlapping modes to be extracted. I use a force constant model, which provides a simpler route to testing the refinement method than empirical potential models, without the need to minimise the energy at every stage and potentially changing the structure or pressure of the simulations. With the complete single crystal dataset, the results of this refinement can be assessed. The force constants presented here are not intended as an alternative model, but are indicative of the progress being made towards the goal of INS powder refinement, allowing a discussion of the limitations and successes, and the next stages in development for the powder refinement process.

The final aim is the extraction of dispersion curves in three key directions (along \mathbf{a}^* , \mathbf{c}^* and towards the F -point). Comparison with interatomic models is used in the extraction and

interpretation of experimental dispersion curves from the single crystal data.

6.2 The interatomic models

6.2.1 The Archer potential model

A transferable empirical potential model for carbonates was developed by Archer *et al.* (2003) with a polarisable core-shell model for the oxygen, to accurately model the calcite-aragonite phase transitions and to allow substitution of, and defects at, the calcium site: the charge on the Ca ion was fixed at 2+ for this purpose. Full details of the model and its development are available in the primary reference. The set of experimental phonon properties used as ‘observables’ when producing this model are shown in Table 6.5, together with the calculated properties. Elastic, static and high frequency dielectric constants for aragonite, selected calcite phonon modes for the F and Γ points, and spectroscopic data for the molecular carbonate modes (Table 6.3) were also used. Dispersion curves were not included in the fit, but the basic features of the dispersion curves towards F and along \mathbf{c}^* were reproduced, albeit with a small systematic error. The authors of the model state, ‘It is possible to refit the potentials and obtain better agreement with experimental parameters but for this potential structure such a refit results in degradation in the value of the soft mode’ – and correctly modelling this soft mode is crucial to accurate phase diagrams. The Archer model provides a good model for use with the new INS simulation software.

6.2.2 Developing the force constant (FC) model

I produced a new force constant (FC) model of calcite for refinement against the experimental data. Cowley & Pant (1973) (CP) had previously produced a polarisable-shell force constant model for calcite which had had some success in reproducing their experimental dispersion curves. However, the CP model was designed to illustrate the improvements seen when using a shell model over rigid ion models and to aid analysis of experimental triple axis neutron spectroscopy results. It was never intended as a definitive model. I consider their use of a shell model for *both* the oxygen and calcium to be unrealistic: certainly, the oxygen shell is required, but the electronic structure of the calcium gives little justification for the additional spring constant. Therefore, when making a new force constant model to refine against the new experimental data, I do not include a polarisable calcium.

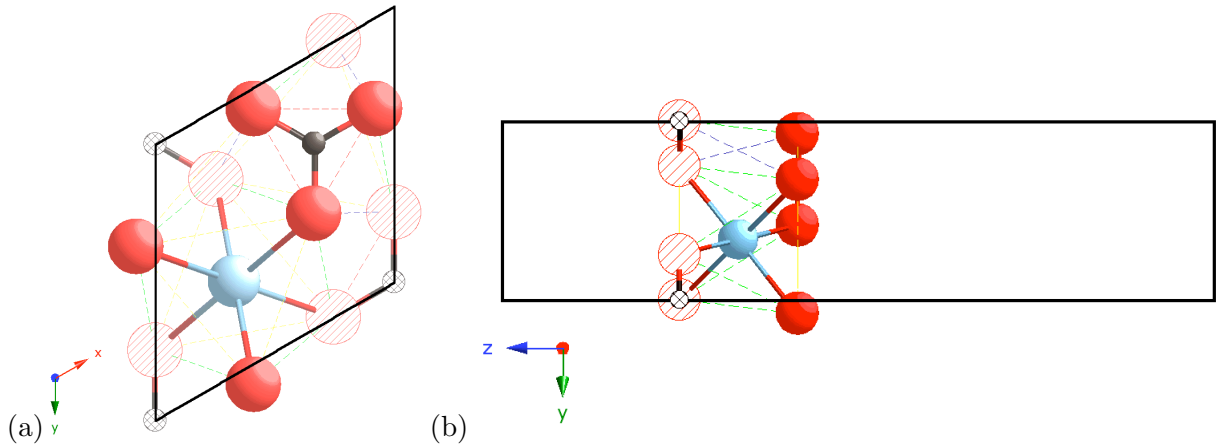


Figure 6.2: Cuts through the calcite unit cell showing only the atoms within two basal layers of oxygens, illustrating the force constant parameters used in the model. Atoms in the first layer are solid (oxygen = red, carbon = black, calcium = blue). The second oxygen and carbon layer atoms are shown hashed. True bonds are shown in as 3D multi-coloured bonds, and additional interatomic force constants are shown dashed, with the key to the colours in Table 6.2 below. (a) Projected down [001]. (b) Projected down [100].

| Atom Types | Cutoff [Å] Min : Max | Coordination | Depiction in Fig. 6.2 | L [eVÅ ⁻²] | T [eVÅ ⁻²] |
|------------------------|-------------------------|------------------------------|--------------------------|------------------------|------------------------|
| Intra-molecular | | | | | |
| C–O | 0 : 1.7 | Bonded [3] | Solid red/black | 114.77759 | 15.57098 |
| O–O | 0 : 2.2 | [2] | Dotted red | 8.74059 | -4.50410 |
| Interatomic | | | | | |
| Ca–O | 0 : 2.4 | Bonded [6] | Solid red/blue | 5.66330 | -0.89167 |
| O–O | 3.2 : 3.3 | In basal plane [4] | Dotted yellow | -0.32895 | -0.01715 |
| O–O | 3.0 : 3.2 | Out of plane [1up, 1down] | Dotted blue | 2.14140 | -0.22491 |
| O–O | 3.3 : 3.5 | Out of plane [2up, 2down] | Dotted green | 0.21800 | -0.00955 |

Table 6.1: The force constant model consists of longitudinal (L) and transverse (T) force constants acting between pairs of atoms with a separation falling between the range of cutoffs. For calcite, there are two types of interaction. First, the non-Coulombic *intra-molecular* force constants that act within the carbonate group (purple triangles in Fig. 6.1). These include the force constant between the bonded C and O, and that between the three O that make up the carbonate group. The second type are Coulombic *interatomic* interactions: the bonded Ca–O interaction and the three differently spaced O–O interactions outside the carbonate group (Fig. 6.2). The distinct average separation for each of these interactions is reflected by the minimum and maximum cutoff parameters for the interactions. All O force constants act from the modelled *shell*, other interactions are from the species cores.

| Atom | Charge | k_2 [eV/Å ²] | k_4 [eV/Å ²] |
|-----------|----------|----------------------------|----------------------------|
| Ca | 1.97120 | | |
| C | 1.42780 | | |
| O (core) | 0.22964 | | |
| O (shell) | -1.36264 | 67.641 | 3.4609 |

Table 6.2: Refined charges for the species used in the calcite FC model and refined spring constants for the polarisable oxygen.

GULP uses a longitudinal and transverse force constant to describe the interaction between any pair of atoms lying within the range specified by the cutoffs. When using a polarisable spring, additional spring constants (k_2 and k_4), together with the split of charges between the core and shell, model the polarisability. In my new FC model, both the charge-division between core and shell and the oxygen spring constants were taken from the polarisable oxygen shell in the Archer model and later refined using TOBYFIT.

I used the set of pair-wise interactions from the CP model. These are of two distinct types (and can be modelled as such within GULP). First, the non-Coulombic *intra-molecular* forces from the carbonate group (purple triangle in Fig. 6.1). Second, two body forces describing the interatomic interactions: Ca–O, and in- and out-of-plane O–O interactions. The nearest neighbour Ca–O interaction within the octahedral polyhedron have average separation of ~ 2.4 Å. There are six in-plane O–O interactions within the basal plane, but two are part of the same carbonate group and thus already modelled. This leaves two sets of interactions with separations of ~ 2.2 Å and ~ 3.3 Å as shown in Fig. 6.2. Finally, the out-of-plane interactions (as shown in Fig. 6.2), are of two characteristic lengths, ~ 3.19 Å and ~ 3.4 Å. These are encapsulated in this model as two distinct sets of force constants (distinct from the CP approach which used a single force constant for both interactions). Full details of the interactions, coordination and cutoffs for each force constant interaction are given in Table 6.2.

The actual force constants from the CP model are no longer helpful having allocated an additional set of force constants (when grouping the O–O interactions by average separation), and rejected the use of a polarisable shell for the calcium. Therefore a new ‘starting model’ for the TOBYFIT refinement was initially refined in GULP against the same set of published ‘observables’ as used in the development of the Archer model: the elastic and dielectric constants shown in Table 6.5, together with IR spectroscopy data for the high energy internal modes (White, 1974) in Table 6.3, and with a few selected modes from the experimental INS data of Cowley & Pant (1973) and Dove *et al.* (1992). The FC model was then refined against our MERLIN data using the new TOBYFIT cross section model for powders as described below.

6.3 Powder INS experiments, simulations and refinements

6.3.1 Experiment

INS spectra for powdered calcite (enclosed in an annulus of aluminium foil) were collected on MERLIN during the scientific commissioning of the new spectrometer in October 2008. Runs were performed at room temperature at three incident energies: high energy (250 meV) to show the full range of modes, mid-range energy (45 meV, where MERLIN has maximum flux) and low energy (15 meV) to focus on the acoustic modes to reveal the soft modes. Data was also collected for an empty foil wrapper for each energy and used for data correction, removing both aluminium scattering and other machine backgrounds. The data was self consistently normalised using the information from the monitors. The intensity between runs at different energies is not directly comparable, so the resulting spectra were re-scaled to give continuous intensities in constant- Q cuts.

6.3.2 Powder simulations and refinement

Both interatomic models were used with the new GULP SQW module to simulate the powder INS spectra, binned over an even Cartesian grid of 180 bins in Q , up to 9 \AA^{-1} , and 1000 bins in energy, up to 200 meV. TOBYFIT allowed the spectra to be convolved with the experimental resolution functions¹.

For the Archer model, the scale, multi-phonon and multiple scattering weightings were refined against the three sets of experimental data simultaneously to give the simulated spectra; for the FC model all parameters were allowed to vary. In the current implementation of TOBYFIT, parameters can either vary freely, or can be bound to another parameter to maintain a fixed ratio. It was not possible to freely vary the Coulombic charges as there is no means to ensure charge balance across the unit cell. Instead, the ratio of charges used in the Archer model was adopted, and the parameters allowed to vary with this ratio maintained.

It was important to include the high energy data in the refinement, but the energy resolution is worse than for the other two data sets. Moreover, the highly Q -dependent multi-phonon backgrounds mean that there is little discernible information below 50 meV. Therefore, this region was masked from the refinement to improve timings. The high energy spectra also extends to high Q , which is computationally expensive, and yields little experimental detail as the internal modes show little variation in Q . Therefore, only the scattering observed on the first 82 detector rings ($Q \approx 8 \text{ \AA}^{-1}$ at the elastic line) was used in the refinement.

¹This was performed using the new cross section model (15) for powders with a Cartesian grid of Q , allowing full calculation of multi-phonon and multiple scattering backgrounds as described in Appendix B.2.4.

A low-intensity constant background was applied to both models (to aid comparison, the same backgrounds were used in both cases). This was based upon the level of noise in the experimental data, and refined together with the FC model, giving final values of 0.0047 (arb. units) for $E_i = 15$ meV, 0.998 for $E_i = 45$ meV, and 0.074 for $E_i = 250$ meV.

A Monkhorst-Pack grid with 14 \mathbf{k} -points along each axis was used during refinement, and increased to $28 \times 28 \times 7$ (reflecting the relevant axis lengths) for the final stage of the fitting process and for the simulations shown here.

6.3.3 INS results and discussion

The room temperature powder experimental spectra are shown together with the results for the two calcite models in Figs. 6.3 & 6.6. Both models refined to give similar scale, multiple scatter and multi-phonon factors (Table 6.4). The overall χ^2 demonstrates that the Archer model gives the best fit to the experimental data¹.

Study of the experimental low incident energy dataset in Fig. 6.3(b) shows acoustic modes rising from the Bragg peaks, with some extra scatter from the elastic line even at 2.5 meV. Clear dispersive shapes can be seen, with a distinctive variation in intensity between the Brillouin zones.

The two models both give reasonable agreement to the low incident energy experimental data. The Archer model in Fig. 6.3 (a) has the main band of intensity slightly too high, falling between 8 and 11 meV, but the curves within this region can still clearly be seen, as in experiment. The lower energy band at $Q \sim 4.4 \text{ \AA}^{-1}$ lacks intensity, but the relative intensities of the different curves at low energy is close to experiment.

The FC model at first inspection appears to give a better fit to experiment. It reproduces the $Q \sim 4.4 \text{ \AA}^{-1}$ features well and correctly places the centre of the main band of intensity at ~ 8 meV, but extends to higher energy than seen experimentally. The relative intensity of the $Q \sim 2.7 \text{ \AA}^{-1}$ and $\sim 3.4 \text{ \AA}^{-1}$ curves at low energy appears switched, and the curves within the main intensity band are less clear.

Overall the details appear better reproduced in the Archer model, albeit with a slight energy offset. This is confirmed by the constant- Q cut at 3 \AA^{-1} in Fig. 6.4: the FC model peaks in the correct position but the actual (double) peak shape is better in the Archer model.

¹'Convergence' was reported when the change in χ^2 was less than the reported accuracy on χ^2 .

6.3 Powder INS experiments, simulations and refinements

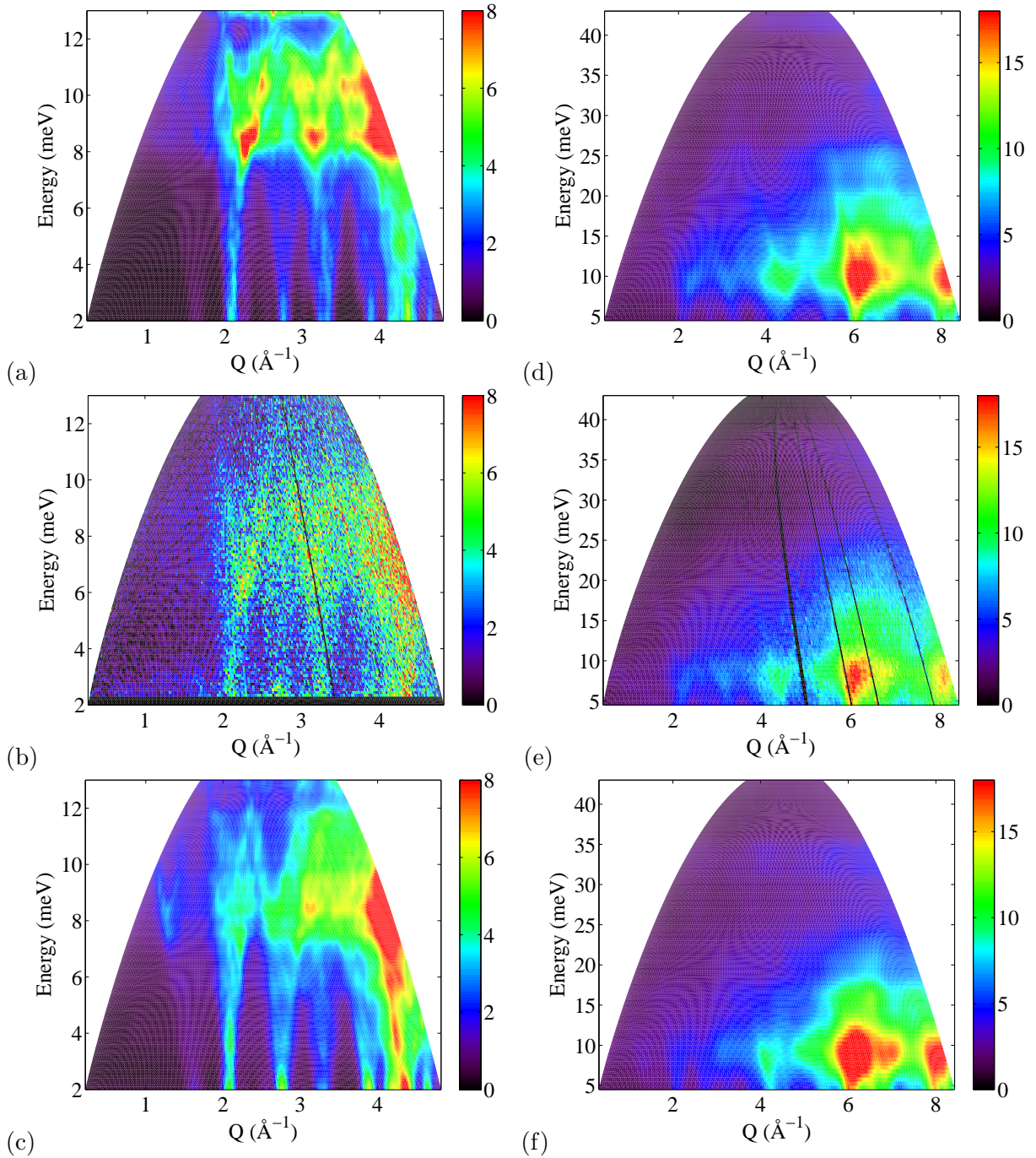


Figure 6.3: Powder MERLIN data and simulations with (left) $E_i = 15$ meV for (a) Archer model (b) experiment (c) FC model, and (right) $E_i = 45$ meV for (d) Archer model (e) experiment (f) FC model. The key features in the experimental data at both these incident energies appear well reproduced by the two models.

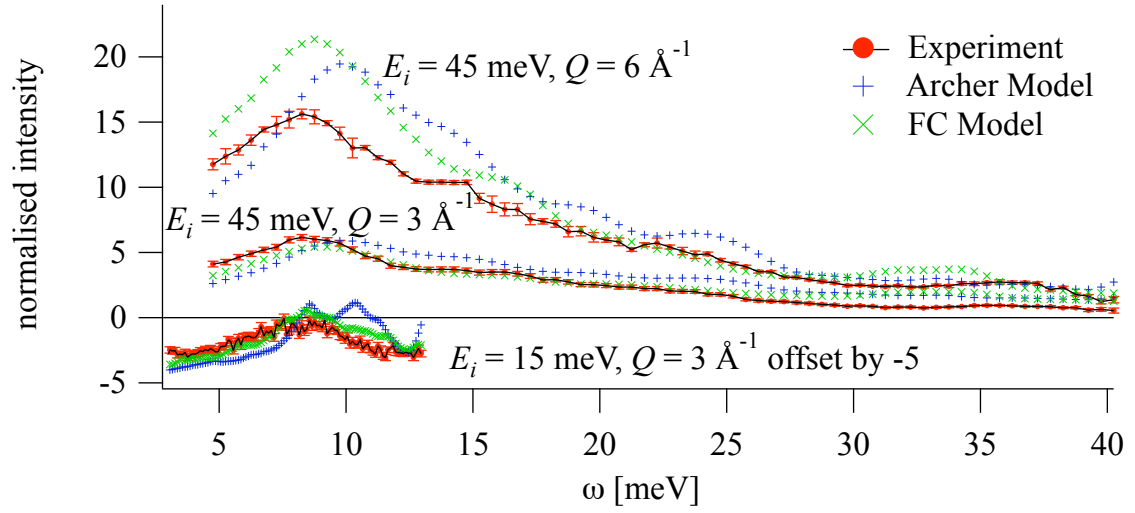


Figure 6.4: Constant- Q cuts at 3 \AA^{-1} and 6 \AA^{-1} ($\pm 0.2 \text{ \AA}^{-1}$) for incident energies of 45 meV and for $Q = 3 \text{ \AA}^{-1}$ at 15 meV (offset by -5 for clarity).

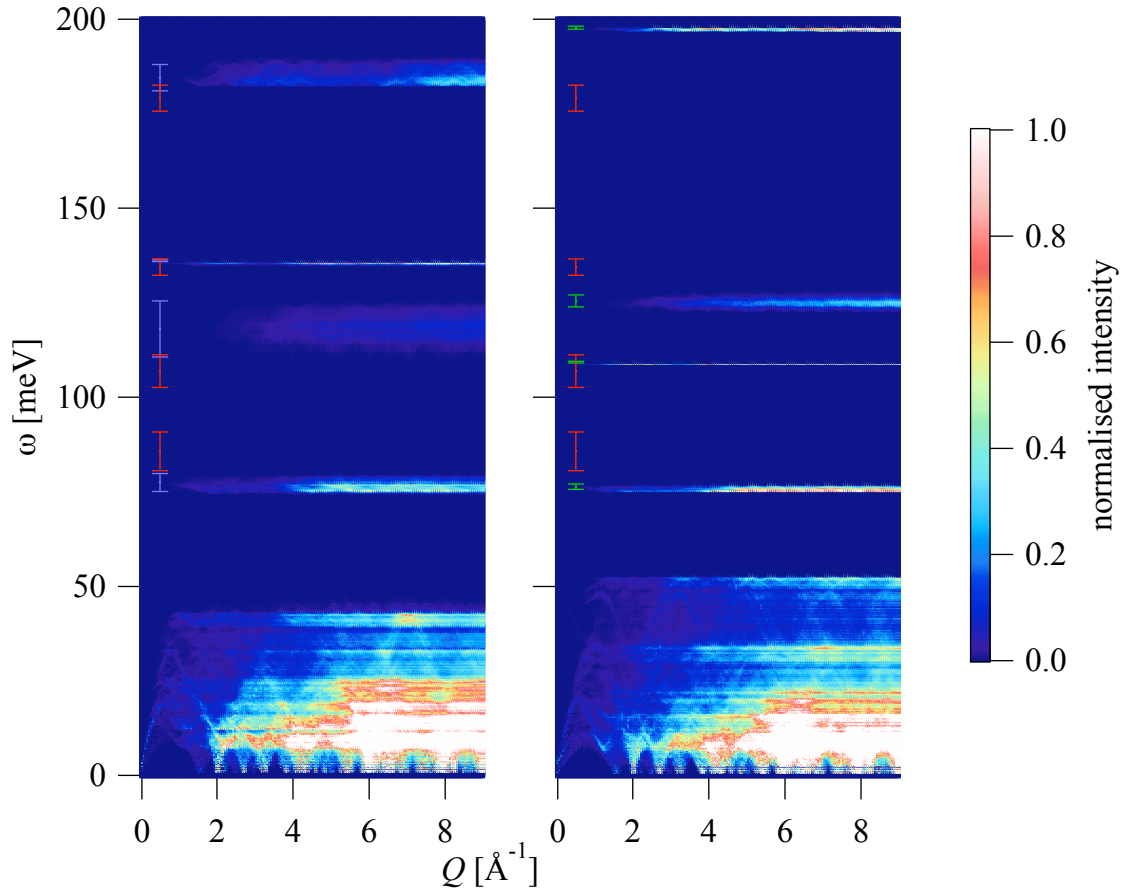


Figure 6.5: One-phonon simulations (left: Archer model, right: FC model) allowing comparison of the full range of modes and clearly showing internal modes. The mid-point and range of the internal modes has been marked (blue for Archer and green for FC model) together with the (red) experimental values from MERLIN data.

6.3 Powder INS experiments, simulations and refinements

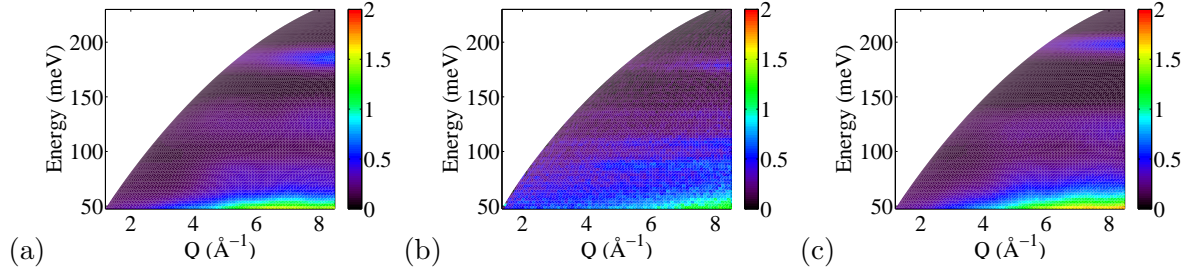


Figure 6.6: MERLIN data and simulations convolved with experimental resolution functions at $E_i = 250$ meV (a) Archer model (b) experiment (c) FC model.

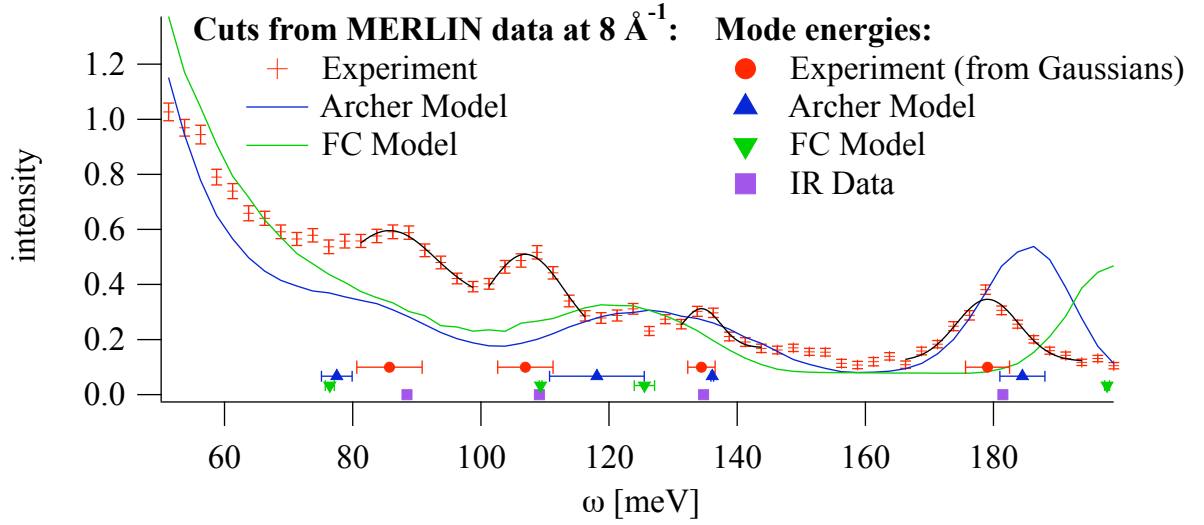


Figure 6.7: A cut at $Q = 8 \text{ \AA}^{-1}$ through the 250 meV incident energy experimental data and the simulations convolved with experimental resolution functions to show the positions of the internal modes. The published IR data is shown, together with the mean positions and spread from the one-phonon simulations.

| | IR data | Experiment | Archer model | FC model |
|---------------------|---------|-----------------|-----------------|-----------------|
| Asymmetric Stretch | 182 | 179.1 ± 3.4 | 184.5 ± 3.5 | 197.7 ± 0.4 |
| Symmetric Stretch | 135 | 134.4 ± 2.1 | 136.1 ± 0.2 | 125.5 ± 1.6 |
| Torsional Vibration | 109 | 106.9 ± 4.3 | 118.1 ± 7.4 | 109.3 ± 0.2 |
| Asymmetric Bend | 88 | 85.6 ± 5.1 | 77.5 ± 2.4 | 76.4 ± 0.7 |

Table 6.3: Comparison of CO_3 internal mode energies (meV) from experiment, model and published IR data (White, 1974).

| Parameter | Archer model | FC model |
|----------------------|-------------------|-------------------|
| χ^2 | 3.8×10^5 | 4.4×10^5 |
| Scale | 0.342 | 0.342 |
| Multiple Scatter (%) | 10.7 | 10.6 |
| Multi-phonon (%) | 14.5 | 15.0 |

Table 6.4: Final scaling parameters and χ^2 for the two interatomic models.

The 45 meV data (which corresponds to the single crystal study presented below) is shown in Fig. 6.3 (d-f). The effect of instrument resolution can be seen when comparing the 45 meV constant- Q cut (at $Q = 3 \text{ \AA}^{-1}$, Fig. 6.4) to the 15 meV cut, demonstrating the importance of including the low energy data in the refinements. The modes in this region are so dense that distinct peaks cannot be seen in the constant- Q cut, but both models appear to reproduce this mid-range data well in the INS spectra of Fig. 6.3.

The flaws in the FC refinement become obvious in the under-lying one-phonon $S(Q, \omega)$ simulations. Fig. 6.5 shows that, comparatively, the FC refinement has shifted several modes into the higher energy region. This is a weakness of the current refinement process: the band at ~ 50 meV is not at all well constrained by the data as this region is not covered in the mid-range datasets and the poor resolution and high multi-phonon backgrounds mask any detail in this region in the high energy data. As the low incident energy modes dataset cover a smaller Q -range over the same number of bins, the lower energy modes are effectively more highly weighted in the current refinement process. It is mathematically preferable, therefore, for the refinement package to push modes into higher energy region than have poorly fitting results. This has important implications for further developments of the software: it is necessary to have some means of limiting how high certain modes can be taken.

The high incident energy data and models (Fig. 6.6) show the level of agreement between the internal modes in the models and experiment. The one-phonon simulations for both models show a small amount of high-energy dispersion, giving fairly broad bands (Fig 6.5). Gaussian peak-shapes have been fitted to the experimental data in a constant- Q cut (Fig 6.7), confirming that the experimental data is in agreement with the earlier IR data. There are also additional features around 130 meV which are not drawn out by the IR data due to modes not at the Γ point. Comparison with the one-phonon Archer model confirms dispersion in the nearby modes.

The effects of the experimental resolution function are such that there is little observable difference between the Archer and FC models in the constant- Q cut with the exception of the highest mode (asymmetric stretch) which is notably too high in the FC model. In the Archer model, the asymmetric stretch and torsional (out-of-plane) modes are a little high, but the symmetric stretch is well reproduced. The asymmetric bend is a little low, as is the same band in the FC model. This model gives a discrete mode that corresponds well with the experimental values for the torsional mode, but the other modes show large discrepancies. These results confirm the validation of the Archer model, and the weakness of the refined FC model.

To conclude, the refinement process has allowed a new model to be produced showing good agreement to low and mid-range energy modes in the powder data. However, the high energy

| Parameter | Experiment | Archer model | FC model |
|---|------------|--------------|----------|
| Elastic Constants(GPa): | | | |
| C_{11} | 145.7 | 151.9 | 54.6 |
| C_{33} | 83.3 | 96.0 | 168.7 |
| C_{44} | 33.4 | 45.3 | 48.8 |
| C_{12} | 55.9 | 65.1 | 39.6 |
| C_{13} | 53.5 | 62.7 | 63.8 |
| C_{14} | -20.5 | 22.1 | 7.5 |
| Static Dielectric Constants: | | | |
| 11 | 8.5 | 6.5 | 4.84 |
| 33 | 8 | 6.2 | 6.0 |
| High frequency Dielectric Constants: | | | |
| 11 | 2.75 | 1.75 | 1.15 |
| 33 | 2.21 | 1.85 | 1.21 |

Table 6.5: Comparison of the experimental² and simulated elastic (Dandekar & Ruoff, 1968), static dielectric (Kaye & Laby, 1982) and high frequency dielectric (Deer *et al.*, 1966) constants in calcite.

(internal) modes are not well constrained, and there is an excess of modes in the poorly represented ~ 50 meV region. The Archer model, meanwhile, provides a good fit to the shapes of the dispersion curves seen in the experimental data with some slight energy mismatches. This is to be expected as the Archer model was produced to allow the study of the calcite-aragonite phase transition, and some loss of accuracy in reproducing the phonon properties of the individual polymorphs was allowed to improve transferability.

6.3.4 Comparison with experimental phonon properties

To assess the quality of the refined model it is helpful to look at other experimental phonon properties. GULP allows the calculation of various phonon properties from a dense Monkhorst-Pack grid: the same settings were used here as for the SQW module. Results are compared with the calcite experimental observables used in the production of both models (Table 6.3 & 6.5).

In the long wavelength limit, the acoustic modes correspond to shear crystal strains, and the slope of the acoustic modes can be used to determine the elastic constants¹. These provide important insights into structural stability and mechanical properties, and can give a numerical indication of the quality of a model. Clearly, the Archer model gives the best fit to the experimental elastic constants²: the authors of the model acknowledge the discrepancies from experimental results but are confident that these are not large enough to cause the crystal to

¹The elastic constants are the second derivatives of the energy surface with respect to strain.

²The sign difference for C_{14} is most likely to be due to a difference in alignment.

distort unrealistically when pressure is applied. The FC model gives reasonable agreement to C_{44} , C_{12} and C_{13} , but fails to reproduce the other elastic constants implying that this slope has not been properly reproduced in several key directions through the Brillouin zone.

Another good test of an interatomic potential model is through the dielectric constants: those from the Archer model are much better than the FC results. Given the discrepancies in the elastic constants and the inability to freely refine the Coulombic charges, it is not surprising that the FC model gives dielectric constants slightly further from experiment.

6.3.5 Conclusions

This chapter asked two questions of powder simulations: can powder INS simulations *validate* an interatomic model and can they be used to *refine* an interatomic model. To answer the first, powder $S(Q, \omega)$ simulations have been used to validate the Archer model more completely than previously possible. Good agreement had already been noted by the authors of the primary reference with previously published dispersion curves and other experimental observables. Correctly reproducing the intensities of the powder INS spectra provides the first confirmation that the eigenvectors are also correct. Thus powder INS allows a more complete validation of the lattice dynamics from the Archer model, but fine details, including the important soft modes, cannot be absolutely confirmed without single crystal data.

Powder refinement was tested through the FC model. Never intended as a definitive model, this also reproduces many features of the powder INS spectra. Indeed, on visual inspection some of the features appear better reproduced than the Archer model. However, close examination of the one-phonon spectra and study of the high energy spectra convolved with experimental resolution functions showed that the refinement process had produced excellent agreement for a few modes at the expense of other modes. However, this is still promising, as it shows that certain features are already possible to refine.

I have not yet managed to refine the Archer potential model against powder INS data, but there is no intrinsic reason why this should not be possible. Given the necessary geometric optimisation in refining a potential model (as opposed to a FC model), this would benefit from simulations of the elastic line. This would also help constrain the refinement process to ensure that modes are not ‘hidden’ under the resolution function of the elastic features.

In assessing the viability of powder refinement, it is important to differentiate between limitations with the current implementation, and inherent problems with the approach. In the first category, this study has shown that the inherent higher-weighting of low-energy data in the experimental INS needs to be overcome. Partially, it is due to the Bose-weighting of the experimental spectra: refinements could be performed using ω weighted spectra to counteract

that. The higher energy modes are also underrepresented as there are fewer Q -bins per \AA^{-1} , and computational considerations mean that the higher Q -bins are frequently removed from a refinement to enhance the timings. This could be corrected for by an additional weighting factor. I believe the inclusions of other experimental ‘observables’, such as IR or Raman modes, would also be highly beneficial.

The second category of limitations are less clear at the current time. There is a question of whether features such as the soft modes will be refinable. This will depend on how visible these features are in the powder spectra: the Archer simulation is notably different to the FC model in the 15 meV data so they are probably encapsulated in this information, but the statistics may not be sufficient. Simple least square refinement may not work to fit these weak features, since like the high energy modes they will not contribute much to the χ^2 . Additional weighting for the crucial areas may help here. It is also possible that the starting model for the refinement will need to be fairly close to allow refinement of the soft mode. This need for a good starting model can also be seen as an advantage. It means that, having validated the model, it will be possible to perform computational experiments, following the effects on the INS spectra as a functions of, for example, temperature, pressure or doping. However, it is unlikely that powder data is ever going to be able see longer range interactions or subtle electron-phonon coupling, so refinement against single crystal data is going to be necessary here.

In conclusion, this section has delivered proof-of-concept for powder refinement. The current position reflects that of early crystallographical powder refinement, and the initial studies here have suggested a number of important advances to the methodology. It is important to remember that this is the start of a new approach to extracting lattice dynamics, and the initial report is very promising.

6.4 Single crystal

Single crystal INS is the standard method for studying the lattice dynamics of materials. The new ability to perform simulations of INS spectra fully convolved with experimental resolution functions making them directly comparable to experiment provides an opportunity for further validation of the Archer model. Despite the flaws already noted in the FC model, such comparisons can yield important information on the strengths and weaknesses of the powder refinement approach, suggesting further improvements. The simulations are compared to slices of experimental data across many Brillouin zones, giving a robust test of the eigenvectors as well as the mode frequencies. Finally, dispersion curves are extracted, confirming previous results along \mathbf{c}^* and toward the F point, as well as expanding this latter dataset, and giving the first experimental results along \mathbf{a}^* .

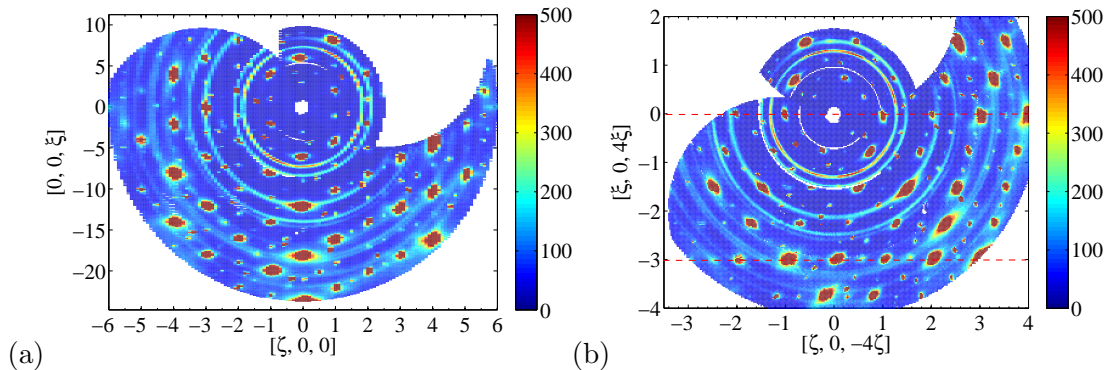


Figure 6.8: The sweep at the elastic line (integrated between -2 and 2 meV) for the 45 meV calcite single crystal in (a) the standard alignment allowing slices to be taken along both the \mathbf{a}^* and \mathbf{c}^* axes, and (b) the projection such that slices could be taken (shown in red) along $[10\bar{4}]$ (towards F).

6.4.1 Experiment

A single crystal of calcite was mounted on an aluminium stub in the cold cycle refrigerator (CCR) (to take advantage of the goniometer) in MERLIN, such that $[100]$ and $[001]$ were both in the scattering plane: alignment was based on crystal morphology¹. The crystal was rotated through 202° in one degree steps at room temperature with incident energy of 45 meV.

Following normalisation (against the flux observed by the monitors) the data were combined into a unified four dimensional dataset using HORACE, aligned along $\mathbf{x} = \mathbf{a}^*$ and $\mathbf{y} = \mathbf{c}^*$, the Bragg peaks from which are shown in Fig. 6.8(a). The pale rings are characteristic of the aluminium powder background, arising from the sample environment, which can also be seen as excess intensity crossing the elastic line in (\mathbf{Q}, ω) slices. To study the dispersion towards the F -point, the combined dataset was projected along $[10\bar{4}]$, as shown in Fig. 6.8(b).

6.4.2 Simulations

Single crystal simulations were performed for both models. An orthogonal supercell ($a' = 2a$, $b' = b$ and $c' = c$) was used with 60 (core) atoms in the unit cell to ensure correct alignment between TOBYFIT and GULP. A Monkhorst-Pack grid of $14 \times 28 \times 7$ \mathbf{k} -points achieved convergence of phonon properties and suitable `SQWsingle` array population. The Archer potential model optimised to a very slightly different unit cell than experiment, as reported in the primary reference. This has little implication for the comparison of data as results are given in reciprocal lattice units.

¹The faces are all of the form $[104]$ and the intersection of three faces with obtuse vertices gives the three-fold axis – the $[001]^*$.

TOBYFIT was used¹ to produce a GULP single crystal `.sqwt` output file, providing the simulated spectra for convolution² with experimental resolution function for each of the 214 crystal alignments to cover (and slightly exceed) the experimental datasweep. No other scaling or backgrounds were included in the simulation.

6.4.3 Results and discussion

One advantage of MERLIN’s many banks of detectors is that data from multiple Brillouin zones are collected simultaneously, and slices can be made along any direction in reciprocal space. The powder INS spectra allowed a certain degree of validation for the two models, but the true test is in how the single crystal data and simulations of these slices compare, both in mode energies and intensities. These slices also allow the extraction of dispersion curves along key directions, which can be compared directly with the dispersion curves from the two interatomic models and with previously published results.

6.4.3.1 INS spectra

The \mathbf{c}^* dispersion has previously been studied experimentally (Cowley & Pant, 1973), so representative slices from the new MERLIN data and simulations are shown in Fig. 6.9. The slices in Fig. 6.10 give the first experimental study of the \mathbf{a}^* direction, testing the Archer model against completely new ‘observables’. Finally, the agreement of the simulations to experiment towards the F point can be assessed in Fig. 6.11, which also reveals more experimental detail than seen in previously published results (Dove *et al.*, 1992).

The range of intensities for equivalent points in different Brillouin zones is immediately apparent from the results, showing how important it is to collect the experimental data over a wide range of momentum transfers. Each experimental slice is compared with the simulated spectra (convolved with the appropriate experimental resolution functions) from the Archer and refined FC models.

The Archer model gives reasonable agreement to the data in all the directions shown here, but, as implied in the original paper, there is often a systematic discrepancy in the energies of the dispersion curves. For the first time, the eigenvectors can also be assessed through their contribution to the dynamical structure factor seen in the scattering intensity. In general the agreement between the intensities in the Archer model and the experiment is very good, particularly where the mode energies are correct.

¹The single crystal cross section model 3 (see Appendix B.2.3) took almost 9 hours of CPU time on a CamGrid machine

²Using single crystal cross section model 4, with Monte Carlo integration, each of these simulations took between 4 and 7 CPU hours on the CamGrid machines.

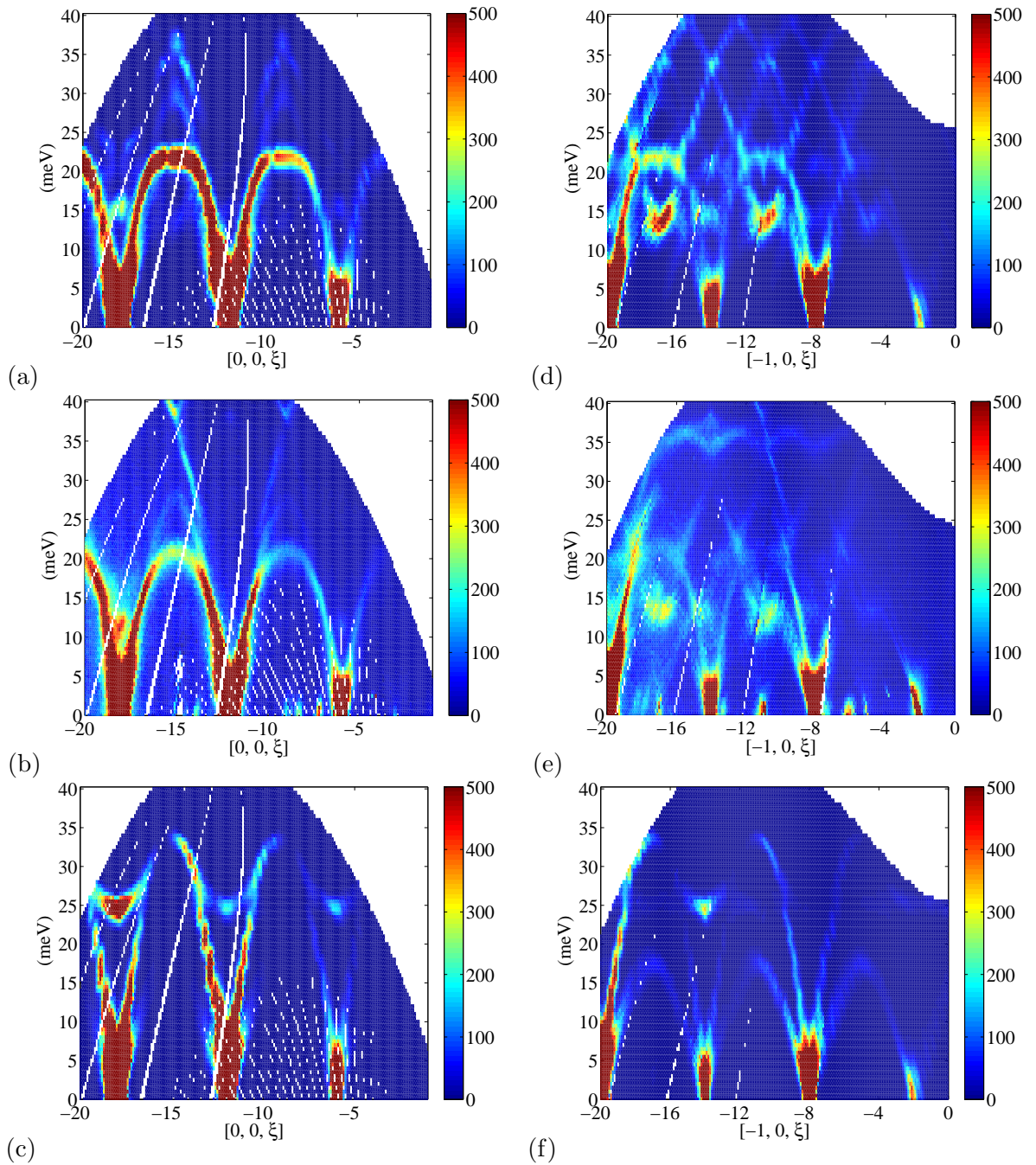


Figure 6.9: Slices along the \mathbf{c}^* axis integrated across 0.2 r.l.u centered at (left) $h = k = 0$ and (right) $h = -1, k = 0$. (a, d) Archer model (b, e) Experiment (including characteristic diagonal features across the elastic line due to powder aluminium scattering from the sample environment) (c, f) FC model. The Archer model gives close agreement to the general trends in the data. The FC model is poor, especially in (c): the wrong branch of the dispersion curve has clearly been used to fit the intense higher energy features. This is also true in (f) where the model lacks intensity for the first optic modes at ~ 15 meV.

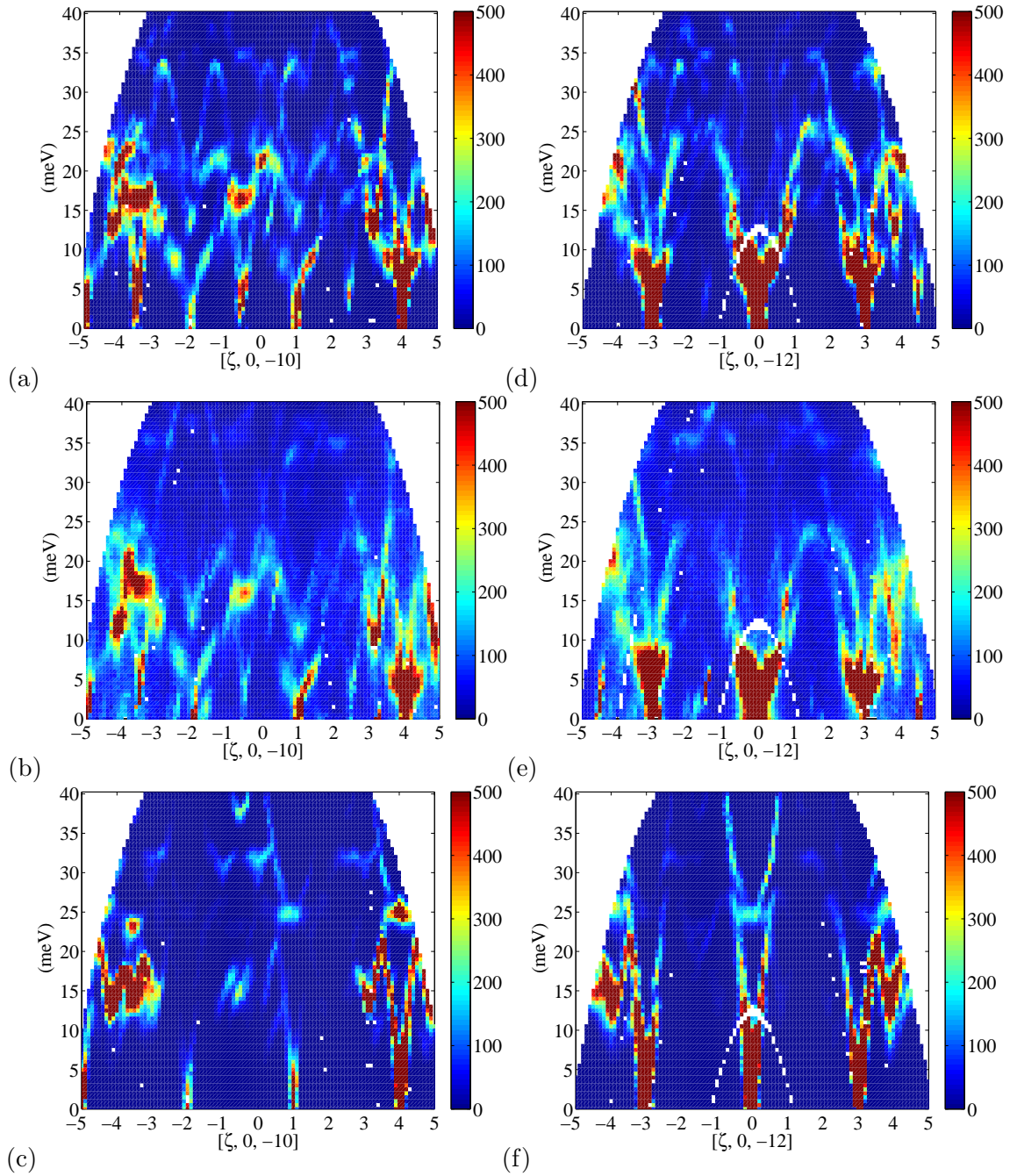


Figure 6.10: Slices along the \mathbf{a}^* axis, integrated across 0.2 r.l.u centered at (left) $k = 0$, $l = -10$ and (right) $k = 0$, $l = -12$. (a, d) Archer model (b, e) Experiment (including characteristic diagonal features across the elastic line due to powder aluminium scattering from the sample environment) (c, f) FC model. Both models reproduce the experimental higher intensity region around 15 meV, but the shape is more realistic in the Archer model. Notably, there is a clear zone boundary soft mode, reproduced by the Archer model, but not the FC model.

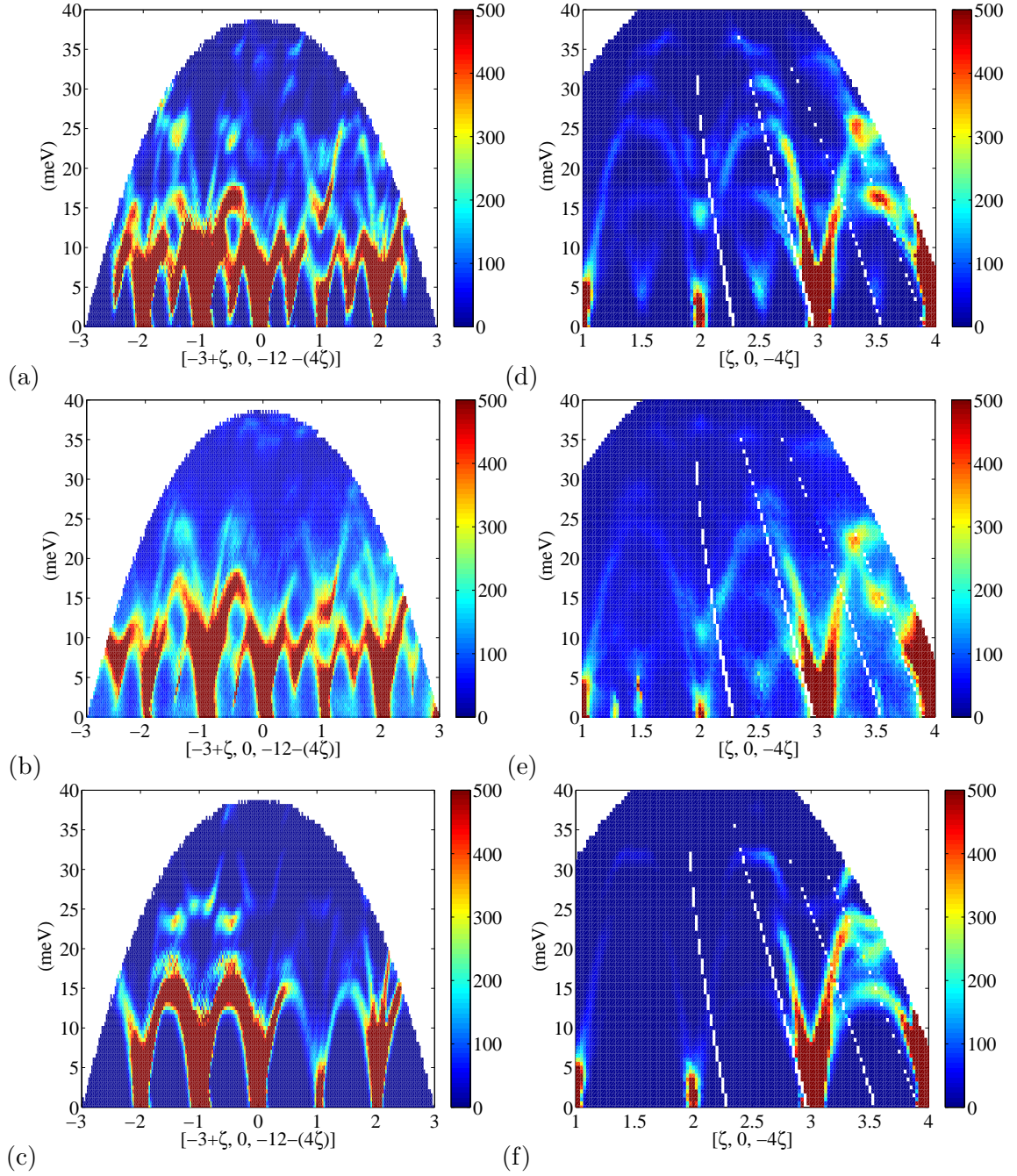


Figure 6.11: Slices along the $[10\bar{4}]$ axis, shown red dotted lines in Fig. 6.8(b). Slices were integrated across 0.2 r.l.u centered at (left) $\mathbf{v} = -3$ and (right) $\mathbf{v} = -0$ (a, d) Archer model (b, e) Experiment (including characteristic diagonal features across the elastic line due to powder aluminium scattering from the sample environment) (c, f) FC model. The Archer model reproduces the experimental detail, including soft modes. The FC refinement correctly models the intensity at ~ 15 meV and the curved features at ~ 25 meV, but missed the soft mode.

The FC model gives a marked difference to experiment in some areas, demonstrating that reasonable agreement of the powder INS spectra can mask crucial details. The refinement reproduces several of the key features in all the slices, usually the most intense features, but several other modes are clearly missing. This confirms the earlier conclusions (from the one-phonon powder INS simulations) that those modes which could not be made to fit the experimental data by the refinement were pushed to higher energy.

Neither model included any \mathbf{a}^* modes in the initial GULP refinements, yet both models show a comparative degree of agreement to the experimental data as seen in other slices. Indeed the FC model appears to reproduce more of the \mathbf{a}^* features than it does \mathbf{c}^* features. The key detail visible in Fig. 6.10 is the presence of a soft mode at the \mathbf{a}^* zone boundary in the experimental data, apparent in the Archer model, but not the FC model. The dispersion curves in this direction are clearly complex, with marked variation along the axis. Detailed comparison of the two models is best performed with the aid of the extracted dispersion curves (Section 6.4.3.2).

Perhaps the most interesting dispersion curve is that towards the F -point, given the anomalous columns of phonons seen by Dove *et al.* (1992) over a range of temperatures in the $[10\bar{4}]$ projection. All MERLIN experimental slices (representative examples of which are shown in Fig. 6.11) show the crucial soft mode at the zone boundary which drives the high temperature phase transition. The Archer model reproduces this, although with a slightly higher intensity than experiment in the softening branch. The FC model fails to reproduce the soft mode, but still reproduces many of the intense regions.

6.4.3.2 Dispersion curves

Reducing the INS spectra to the under-lying dispersion curves gives an overview of the phonon mode energies across different branches. These were extracted from the experimental single crystal spectra by taking constant- \mathbf{Q} cuts at regular intervals along the \mathbf{c}^* and \mathbf{a}^* axes, and towards the F point in the $[10\bar{4}]$ projection. By overlaying cuts from equivalent points in several Brillouin zones the mode positions for the dispersion curves could be obtained. These are shown, superimposed on a representative slice, in Figs. 6.12, 6.13 & 6.14 for slices along the \mathbf{c}^* and \mathbf{a}^* axes, and towards the F point in the $[10\bar{4}]$ projection, respectively. The final extracted dispersion curves are compared with the previous experimental data and the Archer model dispersion curves¹ in Fig. 6.15, and compared with the refined FC model dispersion curves in Fig. 6.16.

¹GULP allows the dispersion curves to be directly calculated for an interatomic model, without recourse to INS simulations

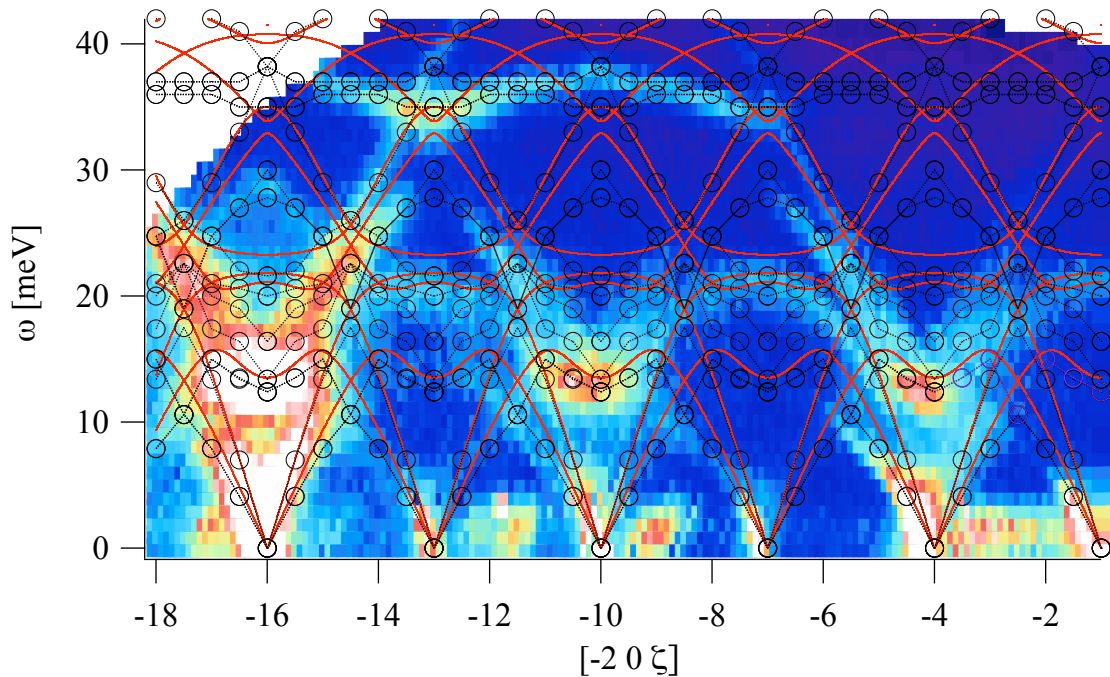


Figure 6.12: A representative experimental slice along the \mathbf{c}^* axis (Γ to $\Lambda = [0\ 0\ 0.5]$) with $h = 2$. The aluminium powder scatter present as a diagonal feature crossing the elastic line was ignored when extracting the dispersion curves. Derived modes are black circles. A dotted black line based on the branches of the Archer dispersion curves guides the eye through the derived datapoints. The Archer model dispersion curves are overlain in red. This highlights the excellent agreement of the Archer model to experiment, as well as the shape of the individual branches of the dispersion curves.

These data are important for two reasons: primarily, this is the first characterisation of the dispersion curves along the \mathbf{a}^* axis and at mid-range energies towards F as well as allowing confirmation of previous experimental results; and second, combining the INS spectra with the extracted dispersion curves helps comparisons to be made between the different models and experiment.

Historically, the \mathbf{c}^* axis dispersion curves were the first to be studied (Cowley & Pant, 1973, from TAS data). Fig. 6.15 (Γ to Λ) shows that there is good agreement between these and the experimental results from MERLIN. Comparison with the dispersion curves from the Archer model shows that all the key features are reproduced although not all branches have exactly the right energies. However, the agreement was sufficiently close that following the general trends of the Archer model could ensure appropriate degeneracies were maintained in the extracted dispersion curves. This is an important confirmation of the validity of the Archer model, especially as it reproduces the soft mode.

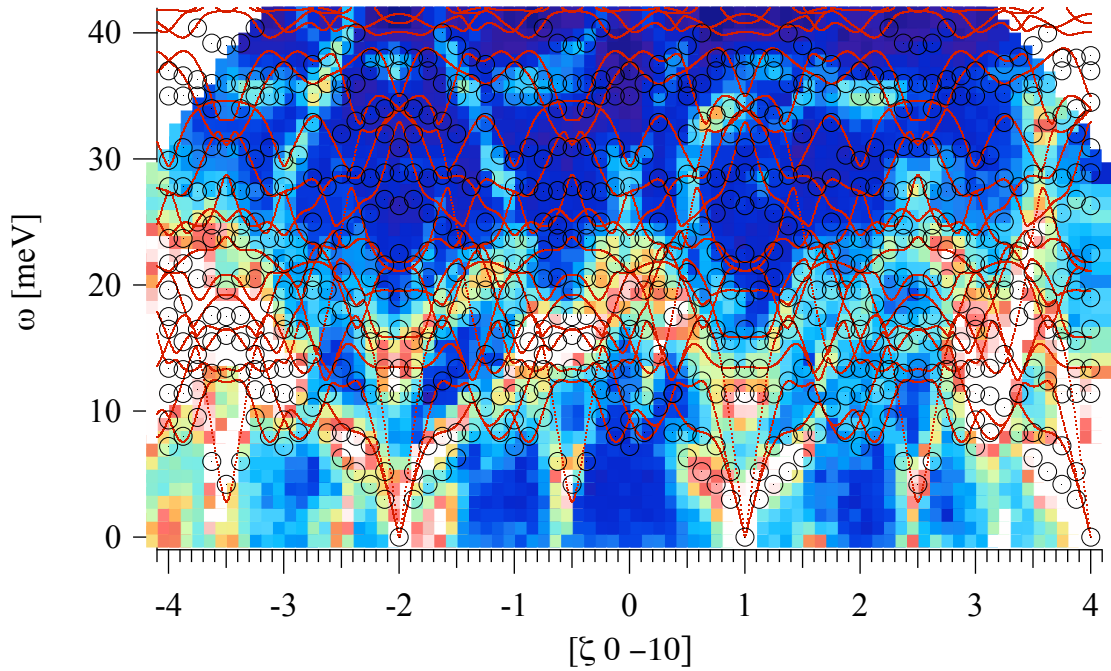


Figure 6.13: A representative experimental slice (with aluminium powder backgrounds crossing the elastic line) along \mathbf{a}^* (Γ to $L = [0.5 \ 0 \ 0]$) at $l = -10$. Derived phonon modes are shown as black circles. The Archer model dispersion curves are overlain in red.

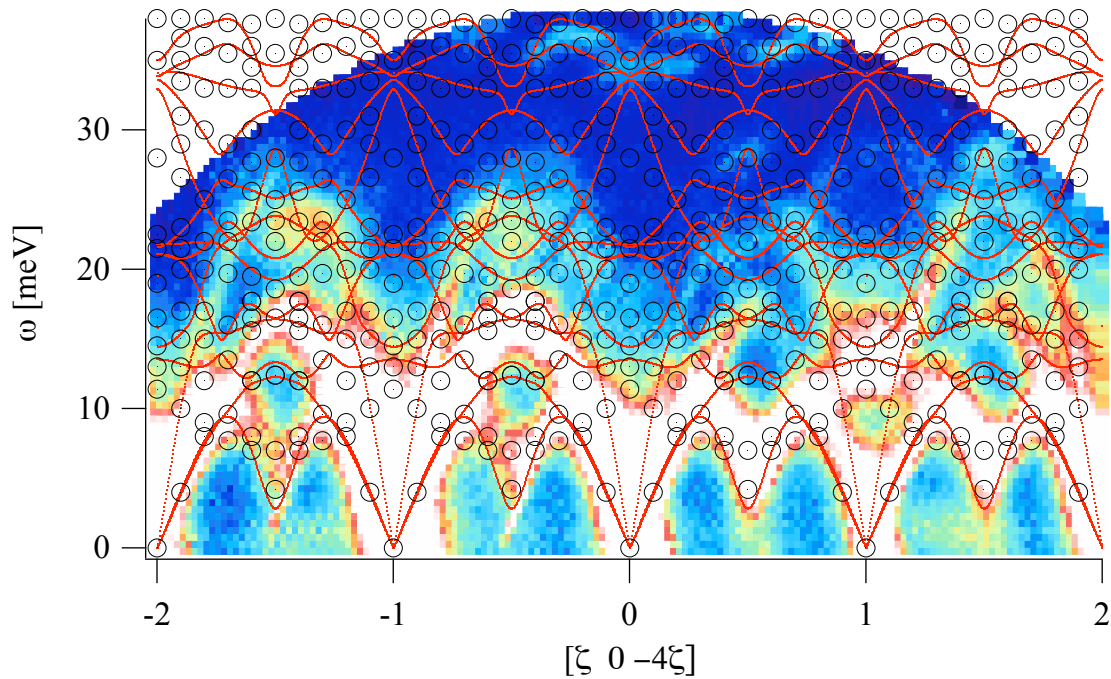


Figure 6.14: A representative experimental slice (with aluminium powder backgrounds crossing the elastic line) along $[\zeta \ 0 \ 4\bar{\zeta}]$ in the F direction, (Γ to $F = [0.5 \ 0 \ 2]$). Derived phonon modes are shown as black circles. The Archer model dispersion curves are overlain in red.

The equivalent FC model dispersion curves between Γ and Λ (Fig. 6.16) reproduce some experimental features. The lowest acoustic mode is very well reproduced, as are several zone boundary points such as the modes near 23 meV and 26 meV, as well as the fairly flat high energy region around 35 meV. However, it is clear that other features are completely missing. Without the intensity of the INS spectra, it is even more obvious that there are not enough modes present in the FC simulation below 45 meV. As discussed previously, this is because the refinement was able to ‘bury’ difficult modes in the poorly represented region at ~ 50 meV.

The dispersion along \mathbf{a}^* (Γ to L) is seen for the first time experimentally here, and presented here together with the Archer (Fig 6.15) and FC (Fig. 6.16) model dispersion curves. The dispersion is complex in this direction, but there is clearly a soft mode at the zone boundary. This is seen in the Archer model, providing important validation of the entire model as this was not included in its refinement. This soft mode is not present in the FC model. As seen in the previous direction, near-zone centre modes between 10 and 15 meV are missing from the model, having instead refined against the shape of the higher energy branches. That so many modes reproduce the experimental datapoints well is encouraging for the principle of powder refinement, but the failure to model *all* the branches shows that this particular model still needs further work. The missing soft mode is important: future developments of the powder refinement approach would benefit from being able to include some specific modes to help weight such key experimental features.

The dispersion curves (Γ to F) extracted from the experimental slices projected along $[10\bar{4}]$ are compared to previous experimental work (Dove *et al.*, 1992) and the Archer model in Fig 6.15. The FC model is shown with the MERLIN data in Fig. 6.16. The key soft mode is clearly visible, and the data suggest a splitting of the acoustic modes towards the zone boundary, which was not seen in the more limited Q -range data of Dove *et al.* (1992). At the same time, those modes which were identified in the previous study are closely reproduced here. The FC model, having been refined against the experimental data, also shows this splitting between the softening acoustic modes, but underestimates this softening. The Archer model accurately reproduces the softest mode, but not the softening of the second mode.

It has been shown that the new MERLIN data confirms and expands the range of experimental dispersion curves, as well as allowing direct comparison with dispersion curves from the two models. As expected from the INS spectra, the Archer model performs well. The dispersion curves are particularly informative in interpreting how and why the FC refinement has failed: it is clear from all three directions that those features that are well reproduced (usually intense features in the INS spectra) are very well reproduced, but sometimes with the wrong branches.

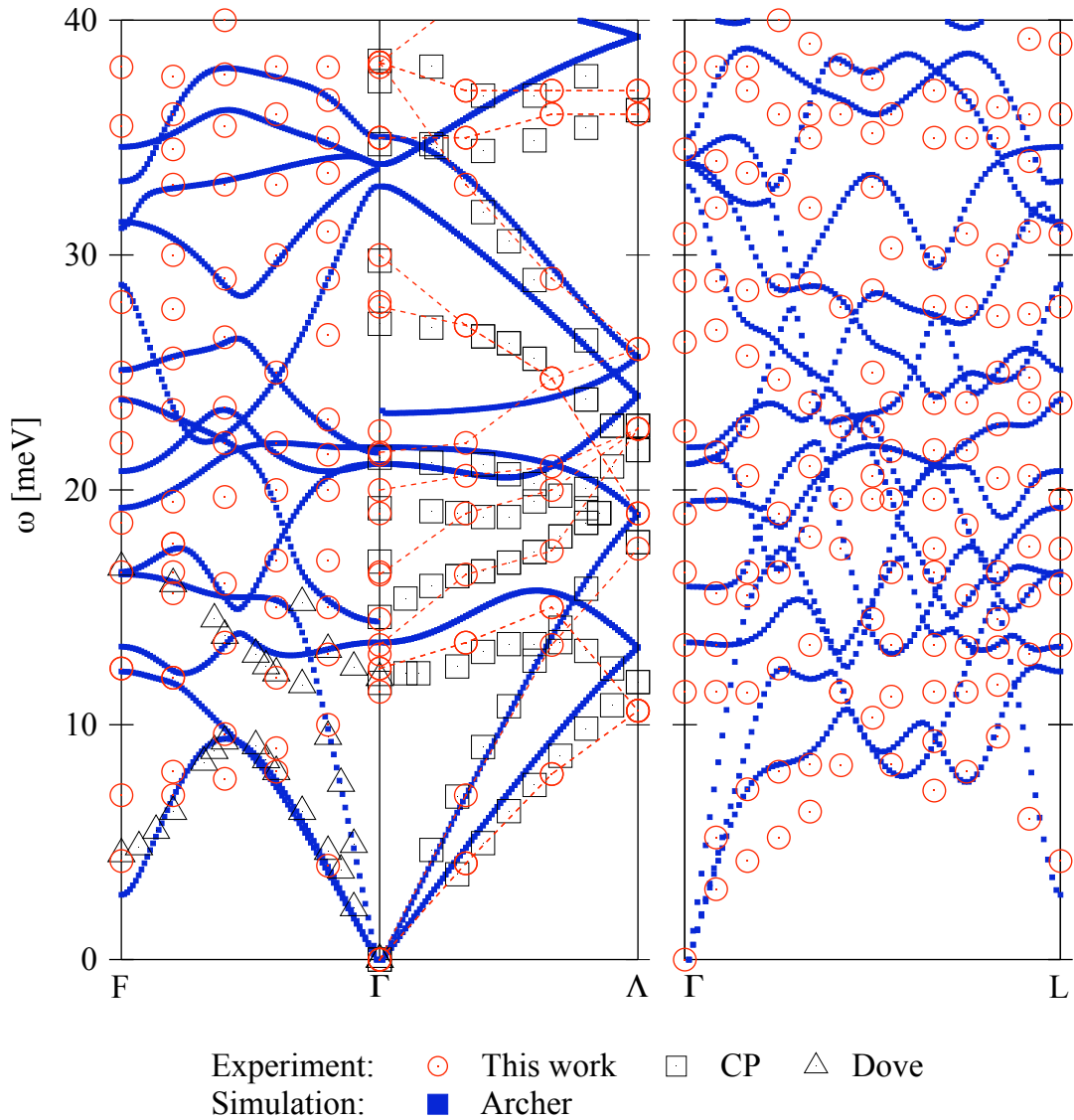


Figure 6.15: Calculated dispersion curves for the Archer model (blue), together with previously published experimental dispersion curves from Cowley & Pant (1973) and Dove *et al.* (1992) (black squares and triangles respectively) and the extracted modes found here (red circles). Along the \mathbf{c}^* axis, a dotted line guides the eye to the likely dispersion curve, based on comparison with the Archer model. The new MERLIN data agrees with previously published results, where available. The Archer model clearly reproduces the general trends in all three directions, although there is a systematic discrepancy in the energies of some branches.

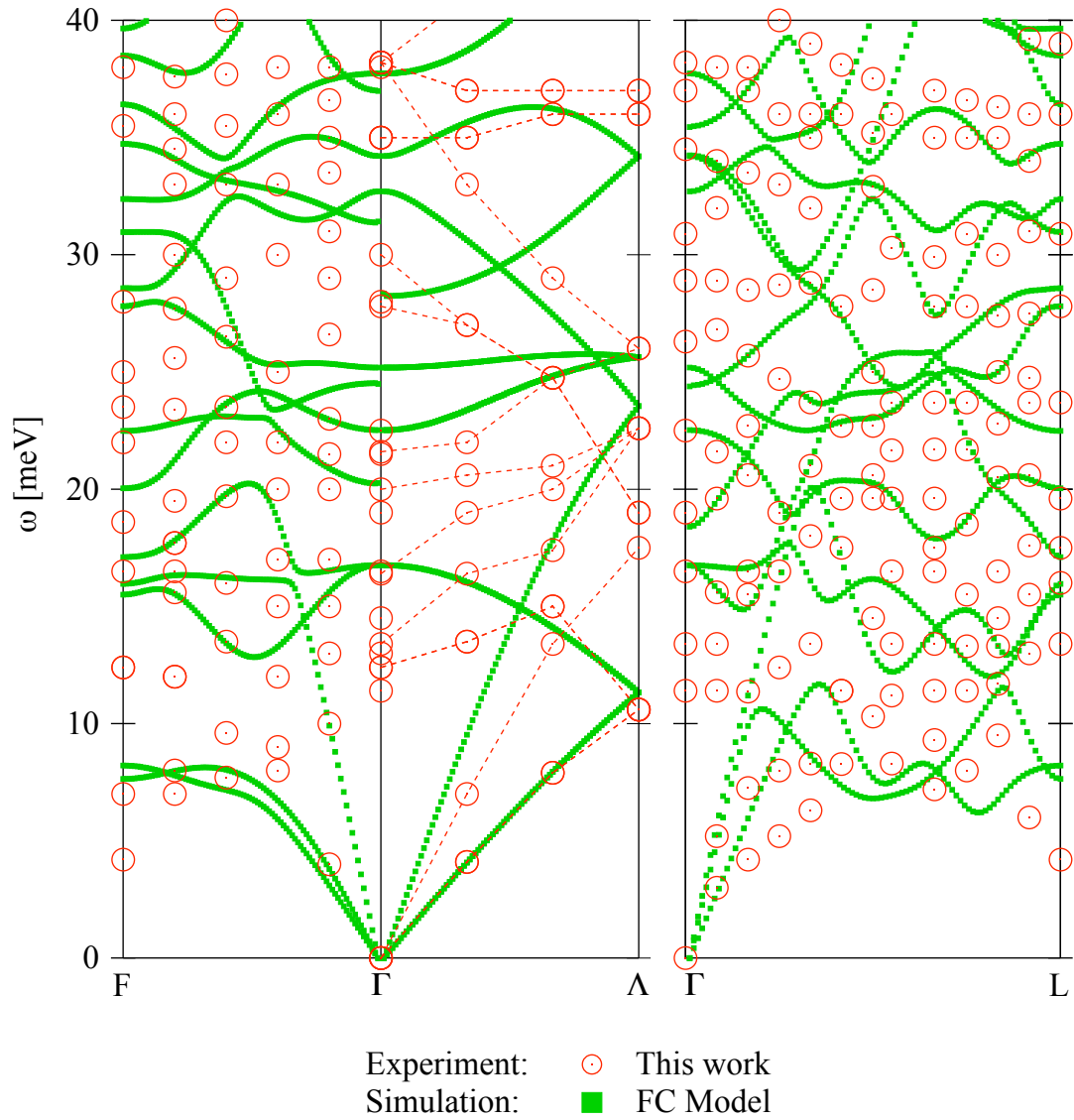


Figure 6.16: Calculated dispersion curves for the FC model (green), together with the extracted modes found here (red circles). Along the \mathbf{c}^* axis, a dotted line guides the eye to the likely dispersion curve, based on comparison with the Archer model. It is obvious that some features have been well reproduced by the refinement, but there are insufficient modes in this region of the model to reproduce all the experimental branches.

6.4.4 Conclusions

The single crystal data were used for two purposes: to further assess the validity of the two interatomic models; and to allow dispersion curves to be extracted along three key directions. The validity of an interatomic model is powerfully established by comparison to single crystal data. The powder simulations validated the general trends in the Archer model, but could not confirm whether specific features such as soft modes were reproduced. In all the directions studied, the single crystal data confirmed the excellent agreement of the Archer model to experiment, giving correct trends and relative intensities if not always the exact mode energy. Importantly, even the soft mode in the previously unpublished \mathbf{a}^* direction was reproduced.

Both models reproduced the low and mid energy powder INS spectra reasonably well, although the FC model had failed to correctly reproduce the higher energy spectra. The weakness of the FC model became absolutely clear from the single crystal simulations and comparison of dispersion curves. Those modes (usually intense modes) which were reproduced were well reproduced: this is good, and encouraging for the principle of powder INS refinement. Other modes were frequently missing, pushed ‘out of range’ in the refinement. This suggests further advances to the methodology to help constrain this through the use of additional ‘observables’ from other experimental techniques, as well as the ability to weight different regions of the INS spectra differently. Finally, the refinement failed to reproduce the soft modes. This is disappointing. Ensuring the appropriate branches of the dispersion curve are constrained to the correct energy regions so there are no ‘missing’ branches will help here, as will additional weightings or the key regions in the experimental spectra.

This confirms the conclusions from the previous section: powder INS refinement is in its infancy but shows great promise. Certainly, the degree to which the powder data has been successfully fitted using the new approach shows that single crystal refinement should provide excellent results. There is no theoretical reason to prevent this refinement process, and indeed the software has been designed to allow it, but required parallelisation to make the timings reasonable. Single crystal refinement will be very valuable, particularly when looking for weak magnetic features in the presence of phonons or broad soft features as in PMN (Chapter 7).

The calcite study was not just a test for refinement processes, but provided new experimental dispersion curves. The advantages of the simultaneous study of many Brillouin zones are clear from the relative ease with which these can be extracted. Important new features, such as a previously unseen zone boundary soft mode along \mathbf{a}^* , have been revealed.

In conclusion, the work presented in this Chapter has demonstrated the power of the new computational methodologies and how they can assist in the design, implementation and interpretation of experimental data.

Chapter 7

Further Applications

The main aim of this thesis was to produce analytical techniques to give new insights into phonon behaviour from neutron scattering experiments. Having successfully developed the basic tools, the new approaches are now being applied to complex technologically important materials. This chapter covers the analysis which has been performed combining experimental INS results with computer simulations for two such materials – the relaxor ferroelectric PMN ($\text{Pb}(\text{Mg}_{1/3}\text{Nb}_{2/3})\text{O}_3$) and a high-temperature superconductor ($\text{Ba}_{1-x}\text{K}_x\text{Fe}_2\text{As}_2$) from the newly discovered class of pnictides.

7.1 PMN: a single crystal INS study

7.1.1 Introduction

Lead magnesium niobate ($\text{Pb}(\text{Mg}_{1/3}\text{Nb}_{2/3})\text{O}_3$, PMN) is a mixed cubic perovskite of the ABO_3 type, and, together with the zircon-containing counterpart PZN, is considered a prototypical relaxor ferroelectric, with exceptional piezoelectric properties. Unlike normal ferroelectrics, these show an unusually broad and frequency-dependent dielectric susceptibility. Such materials are technologically important, for example as transducer devices, due to their large and anomalous electromechanical properties.

The average structure of PMN is cubic, space group is $Pm\bar{3}m$, over a wide range of temperatures (Fig. 7.1(a)). At room temperature, $a = 4.05 \text{ \AA}$ (Bonneau *et al.*, 1991). A substantial ‘skin’ has been observed (Conlon *et al.*, 2004), extending 10 to 50 μm into the bulk with a different lattice spacing resulting in strain between the bulk and skin.

In normal ABO_3 ferroelectrics, the dielectric behaviour is characterised by the Curie-Weiss law, with the *Curie temperature*, T_c , representing the dielectric peak: $\chi \propto 1/(T - T_c)$. However, Bokov & Mylnikova (1961) observed deviation from the Curie-Weiss law below what became

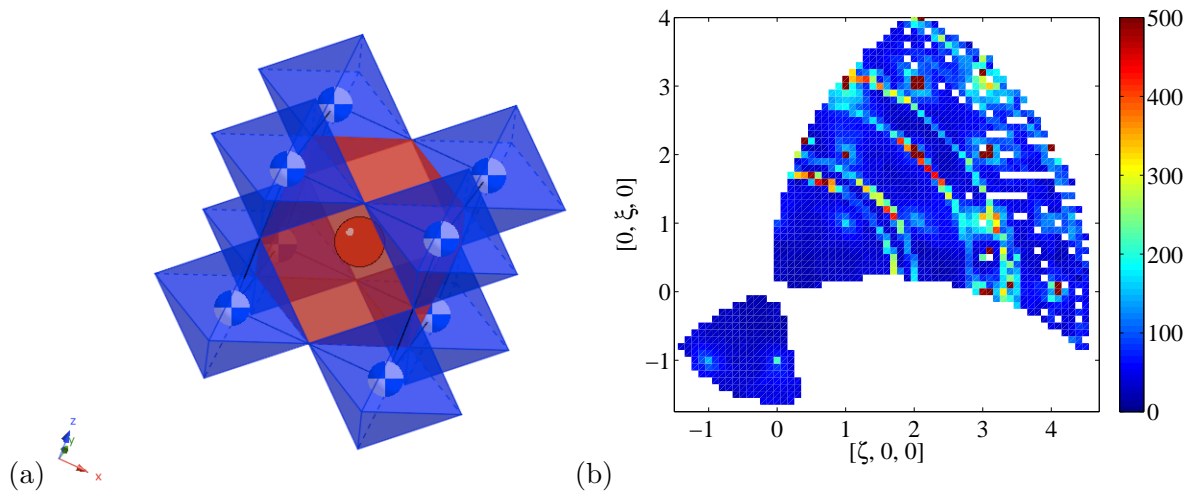


Figure 7.1: (a) A polyhedral model of the ideal $Pm\bar{3}m$ cubic perovskite PMN structure. Pb occupies the 12-coordinated (red) polyhedra, while, in the mean-field model, the random mix of Mg or Nb occupy the octahedrally coordinated (blue) polyhedra. (b) The experimental sweep at the elastic line for PMN. The Bragg peaks can clearly be seen, together with characteristic aluminium powder rings from the sample environment.

known as the *Burns temperature*, T_B , nominally given as ~ 620 K in PMN (as originally suggested by Burns & Dacol, 1983) but more recently found to be 420 ± 20 K (Gehring *et al.*, 2009).

The large dielectric constants seen in relaxor ferroelectrics are a result of the dipolar entities introduced through chemical substitutions: these materials typically have a random occupation of equivalent positions (the octahedrally coordinated B -site, Fig. 7.1(a)), in this case between Mg^{2+} and Nb^{5-} . There is significant difference in both size (ionic radii of 0.72 \AA vs 0.64 \AA) and Pauling electronegativity (1.2 vs 1.6). Below the Burns temperature the dipole moments are found in so-called Polar Nanoregions (PNRs), unique to relaxor ferroelectrics, giving rise to the large dielectric constants. The dipole moments are not observed at higher temperatures due to thermal fluctuations.

Recent work by Xu (2010) suggests the PNRs are ‘pancakes’ 10 to 20 nm diameter with a thickness 4 times smaller, aligned in six possible orientations ($\langle 1\bar{1}0 \rangle$ polarisations correlated in 110 planes). This gives rise to the observed diffuse scattering (Hiraka *et al.*, 2004; Hirota *et al.*, 2002; Xu *et al.*, 2004): a distinctive ‘butterfly’ pattern around the Bragg peak at $[1, 0, 0]$, and an ellipsoidal pattern extending in $[1\bar{1}0]$. The diffuse scattering begins at the Burns temperature and increases on cooling into the relaxor state. Similarly, Jeong *et al.* (2005) used RMC analysis of total scattering data to calculate the increase in volume fraction of PNRs from 0% at 650 K to $\sim 30\%$ at 15 K. Even in $PbTiO_3$ -doped samples, where a rhombohedral phase transition takes place on cooling, the PNRs persist into the low temperature phases as the local atomic displacements are *not* along the rhombohedral $\langle 111 \rangle$ as previously thought (e.g. Chen *et al.*,

1989; Siny & Smirnova, 1989).

The lattice dynamics of PMN are not well understood. The soft transverse optic (TO) mode that would drive the phase transition in a normal ferroelectric is still present, but Gehring *et al.* (2001) showed it to become anomalously broad for small \mathbf{k} across the entire temperature range between the Burns and Curie transition temperatures, although it subsequently recovers on further cooling. This was originally linked to coupling of the TO mode with the PNR, but subsequent studies (Stock *et al.*, 2006) showed the same over-damping in highly doped PMN-60%PT which is no longer a relaxor ferroelectric and does not display the characteristic PNR-related diffuse scattering. More recently, Swainson *et al.* (2009) used INS to reveal other unusual columns of phonon scattering, localised in momentum and extending across a wide section of energy, at high-symmetry points along the zone edge: $\mathbf{Q}_R = [0.5 \ 0.5 \ 0.5]$ and $\mathbf{Q}_M = [0.5 \ 0.5 \ 0]$. This also occurred around the onset temperature of the zone-centre diffuse scattering. They found that these columns are due to zone boundary optic modes associated with Pb and O displacement.

There are many challenges in understanding the lattice dynamics of this technologically important material. What is needed initially is a good model of the dynamical behaviour above the Burns temperature, which can then be used to aid understanding of the properties of the system as it is cooled.

7.1.2 Experiment

I have collaborated with Chris Stock¹ to look at the lattice dynamics of PMN. With the use of a simple interatomic model, I was able to use simulations of the INS spectra for PMN to aid with interpretation of experimental data during a MAPS (URL - M) experiment at ISIS. MAPS was the first direct geometry chopper spectrometer to have the large banks of detectors allowing simultaneous access to vast areas of reciprocal space. The crystal was comprised of three ~ 60 g samples of PMN which had been coaligned and characterised using the E3 spectrometer at Chalk River. The samples were grown using the modified-Bridgeman technique described by Luo *et al.* (2000). We collected data at 600 K using an incident energy of 100 meV. The crystal was rotated from $\psi = -5$ to 67.5 in 2.5° steps giving the coverage (at the elastic line) shown in Fig. 7.1(b).

7.1.3 Simulations

Martin Dove and I developed an interatomic model based on a stable polarisable-shell Buckingham potential model for PbTiO_3 . Assuming B -site ordering as seen in PNRs would be negligible at 600 K, a mean-field ‘MN’ cation was used, based on average properties of $1/3$ Mg

¹Chris Stock is now based at NIST but was, until recently, machine scientist on MERLIN at ISIS.

and 2/3 Nb. Experimental elastic constants (Ahart *et al.*, 2007, Table 7.1) and selected phonon modes were used in the refinement. The charges not refined, but kept constant at the original values: $MN = +4$, $Pb = +2$, $O_{\text{core}} = +0.84819$ and $O_{\text{shell}} = -2.84819$. During the experiment, this was used to produce simulations of the one-phonon INS intensity along specific directions in reciprocal space. It is now possible to simulate the full four dimensional spectra, convolved with experimental resolution functions. Selected regions of this simulation, generated using a Monkhorst-Pack grid of $20 \times 20 \times 20$ \mathbf{k} -points in the first Brillouin zone, are shown in Fig. 7.4. The GULP input file was modified for PDF simulation, allowing comparison with the published data of Jeong *et al.* (2005). It must be noted that this model (Table 7.2) was never intended as a definitive model, but has the potential for further refinements.

Gvasaliya *et al.* (2003) published ‘preliminary’ results of an interatomic polarisable-shell force constant model (GFC model) with a mean-field atom ($MN = 1/3$ Mg and $2/3$ Nb) in the B -site (Tables 7.3 & 7.4). Simulations of the INS spectra and PDFs were obtained from this model in the same way as described for the Buckingham potential model.

7.1.4 Results

7.1.4.1 PDF simulations

PDFs have been shown to provide an informative comparison between interatomic models. albeit with emphasis on the low-energy modes. They will also provide a key analytical tool for probing the PNRs in future work. Jeong *et al.* (2005) produced PDFs using total scattering data collected up to $Q_{\text{max}} = 25 \text{ \AA}^{-1}$, at 650 K (to avoid inclusion of PNRs). Datapoints from the published graph are reproduced in Fig. 7.2 together with the PDF simulations from the two models. It is immediately obvious that the low energy dynamics of our Buckingham potential model are closer to the published experimental work than the GFC model, with the majority of GFC peaks being too narrow. This is perhaps not surprising as the elastic constants are so much better in the Buckingham potential model. However, the relatively low Q_{max} means that the real space resolution is only of the order 0.2 \AA . The results presented here show some of the limitations of the published GFC model, but are principally intended as an indication of the starting points for future model refinements.

The partial PDFs for both models are shown in Fig. 7.3. The oxygen interactions in particular appear to be sharper in the GFC model than experiment or the other model. This type of analysis will be helpful in assessing the progress of refinement for the different interatomic models, especially to see how the different partials improve. Study of the partial PDFs can also help in selecting the order in which to include more distance interatomic interactions during the development of more advanced models.

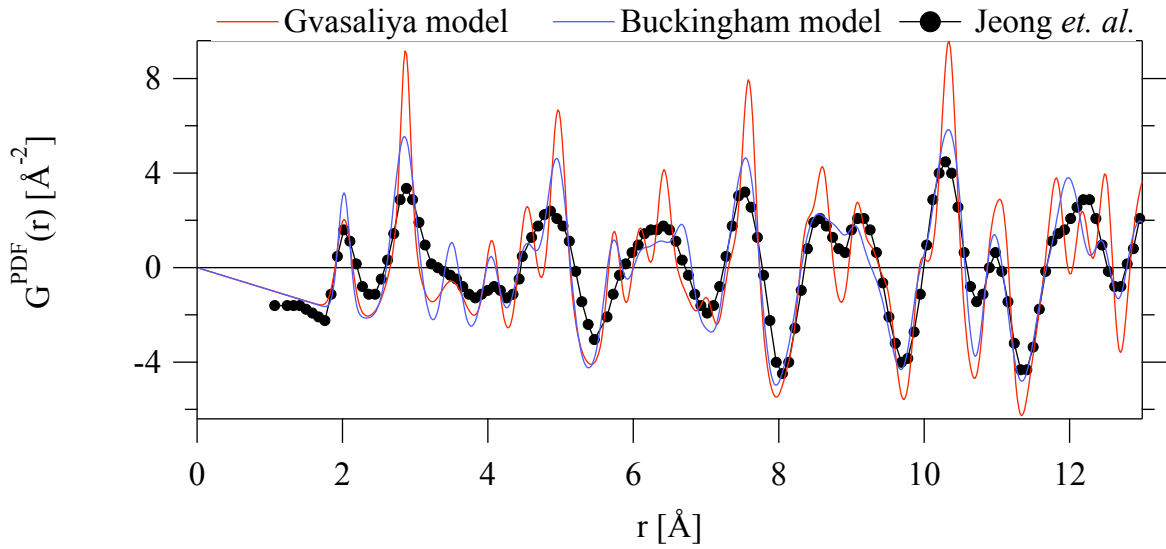


Figure 7.2: Comparison between the idealised $Pm\bar{3}m$ Buckingham potential model and GFC model, overlain with datapoints taken from the published PDF of Jeong *et al.* (2005) at 650 K. Jeong *et al.* use the $G^{\text{PDF}}(r)$ form of PDF to emphasise fit at higher r .

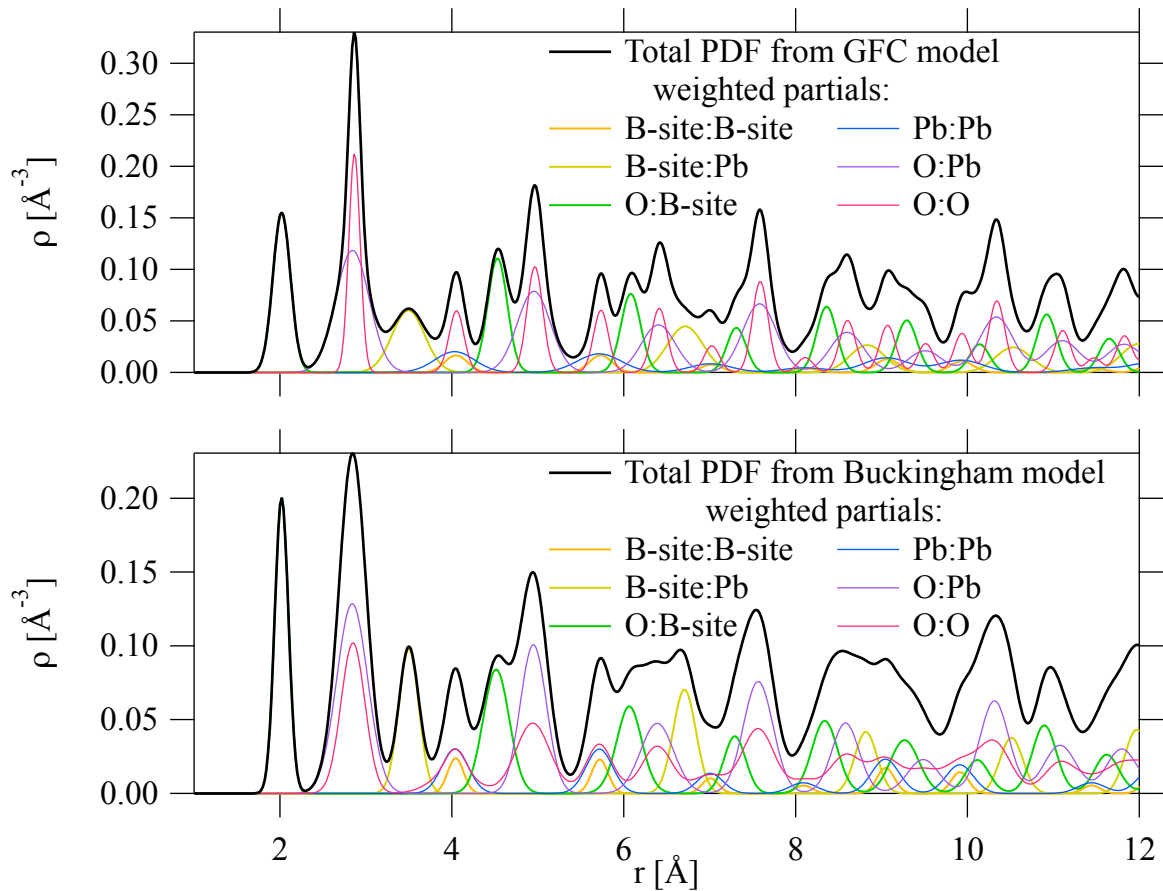


Figure 7.3: Partial $\rho(r)$ at 650 K. (Top) The GFC model and (bottom) our Buckingham potential model. The $\rho(r)$ format is used as it allows direct comparison of the partial peak widths at all r on a flat background.

| | Experimental | Buckingham model | GFC model |
|----------|-----------------|------------------|-----------|
| C_{11} | 156.2 ± 3.4 | 263 | 538 |
| C_{12} | 76.0 ± 3.9 | 135 | 244 |
| C_{44} | 68.5 ± 4.0 | 135 | 218 |

Table 7.1: Experimental elastic constants (GPa) at room temperature (Ahart *et al.*, 2007), compared to model elastic constants at 600 K.

| Pairs | Potential | A | B | C | Cutoffs [Å] | |
|-----------|--------------|---------------------|-------|------|-------------|--------|
| | | | | | Min | Max |
| Pb c O s | Buckingham | 0.137×10^4 | 0.351 | 19.5 | 0.000 | 20.000 |
| M-N c O s | Buckingham | 739.0 | 0.400 | 0.00 | 0.000 | 20.000 |
| O s O s | Buckingham | 0.228×10^5 | 0.149 | 27.9 | 0.000 | 20.000 |
| O c O s | Spring (c-s) | 164.0 | 0.00 | 0.00 | 0.000 | 0.600 |

Table 7.2: Refined Buckingham potentials for PMN.

| Pair | max cutoff [Å] | L [eV/Å ²] | T [eV/Å ²] |
|---------|----------------|--------------------------|--------------------------|
| Pb – O | 2.86 | 3.1208 | -0.062415 |
| MN – O | 2.02 | 10.299 | -0.15916 |
| O – O | 2.86 | 7.4274 | -0.24966 |
| Pb – MN | 3.50 | 0.49932 | -0.093629 |
| Pb – Pb | 4.04 | 0.87381 | -0.50244 |

Table 7.3: Ion pairs, their cut-off distance and longitudinal (L) and transverse (T) force constants as used in the GULP implementation of the GFC model.

| Ion | Core [e] | Shell [e] | k [eV/Å ²] |
|-----|----------|-----------|--------------------------|
| Pb | 1.6 | -0.70 | 4.82 |
| MN | 2.18 | -0.38 | 26.61 |
| O | -0.26 | -0.64 | 301.87 |

Table 7.4: Core charges, shell charges, and spring constants (k) for the GFC model.

7.1.4.2 INS simulations

Comparisons can be made between experimental data and models for $[h\xi 0]$ for $h = 1$ and 2 . It is immediately obvious that while both models produce simulations comparable to experimental data, there is very little information to be readily extracted from the experimental data in this format, making refinements challenging. Weighting experimental data by energy (Fig. 7.5) shows more detail. A cut has been taken (dotted line in energy), showing that neither model accurately reproduces the exact position of these modes, but both show curves that look close enough to form a good starting point for a refinement. The experimental cut has peaks at 27 meV and 34 meV, but are not well defined. New experimental data are required to supplement the current findings.

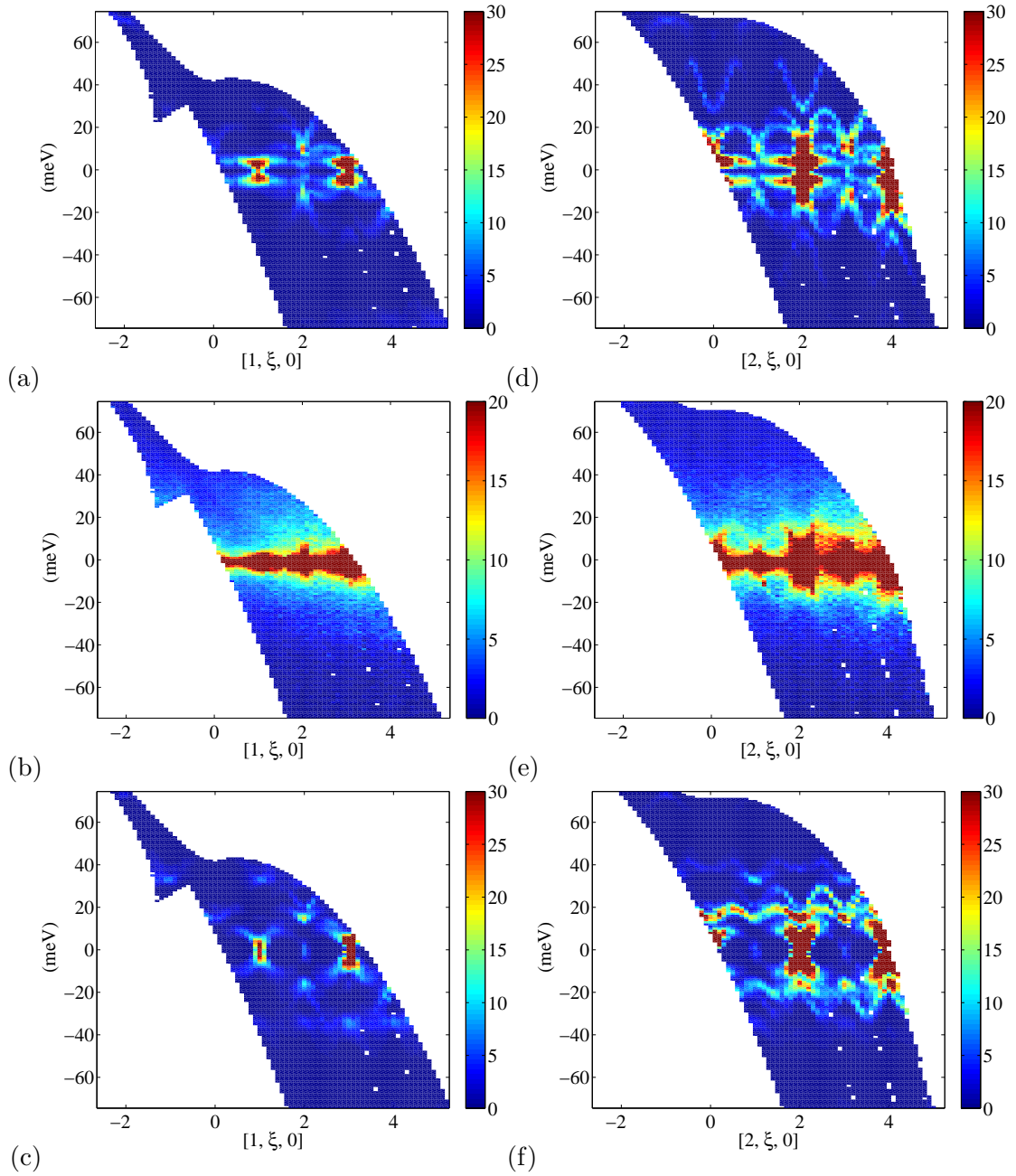


Figure 7.4: Two sets of MAPS INS spectra for PMN with $E_i = 100$ meV at 600 K: (Left) $[1\xi 0]$: (a) GFC model (b) Experiment (c) Buckingham potential model. (Right) $[2\xi 0]$: (d) GFC model (e) Experiment (f) Buckingham potential model. Data are presented for both neutron gain and loss: the experimental data includes the elastic line, although the simulations do not.

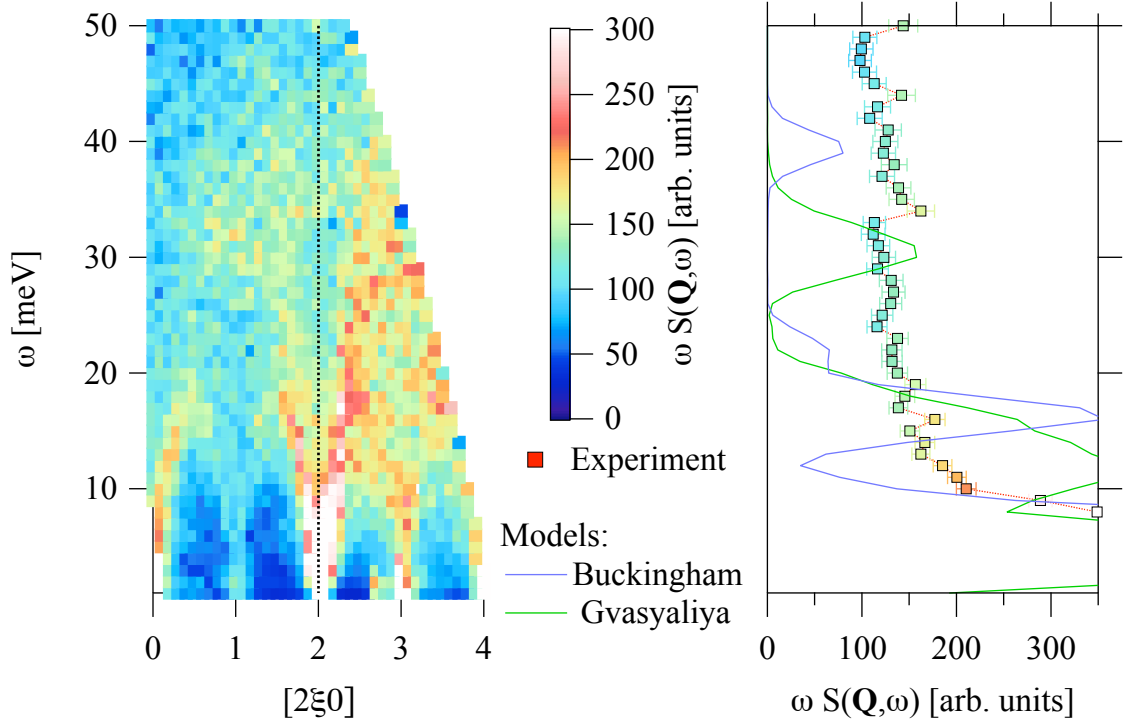


Figure 7.5: Scattering intensity weighted by the energy, highlighting higher energy modes along (left) a slice along the $[2\xi 0]$ axis and (right) a cut through the $[220]$ line shown (dotted), comparing the models with experiment. The models have been weighted by 50% to bring them into the same range as the data.

7.1.5 Conclusions

The new computational approach has been shown to aid in the design of INS experiments, directing appropriate regions of \mathbf{Q} and energy as well as helping with the interpretation of data as it is collected. It has also allowed proper testing of different interatomic models, both through PDF and INS simulations. There is now a need for more data which will allow better testing of the models.

7.2 $\text{Ba}_{1-x}\text{K}_x\text{Fe}_2\text{As}_2$: powder simulations and refinement

The second application of the new simulation techniques has been powder refinement with the recently discovered class of high temperature iron-based superconductors (Kamihara *et al.*, 2008). These possess a layer of face-sharing FeAs_4 tetrahedra, separated by ionic layers (Fig. 7.6), with doping occurring on the A -site. This causes partial oxidation (hole doping) or reduction (electron doping) of the (FeAs) -layers, and gives rise to superconductivity.

Superconductors have no electrical resistance, so unlike conventional conductors allow elec-

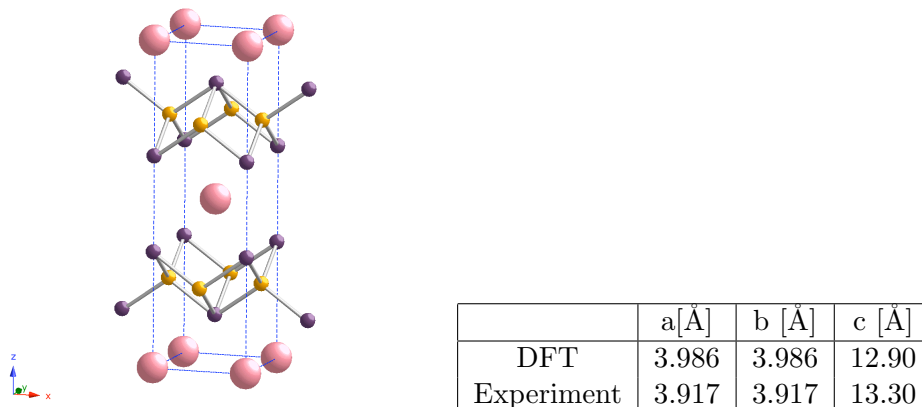


Figure 7.6: The structure of $\text{Ba}_{1-x}\text{K}_x\text{Fe}_2\text{As}_2$: Ba (or K when doped) occupies the pink A -site. The face-sharing FeAs_4 tetrahedra (yellow Fe and purple As) can be seen to form layers separated by the doped A -sites. The Table shows the experimental and DFT model lattice parameters for $x = 0.4$ at 10 K

tric current to flow without loss. This new class of materials superconducts at relatively high temperatures – the maximum is currently 56 K in samarium-doped SrFeAsF (Wu *et al.*, 2009) – and understanding how they work is one of the fundamental questions of condensed matter research today. Results here may also shed light on the still unsolved problem of high-temperature cuprate superconductivity.

I have performed computational modelling on the iron pnictide $\text{Ba}_{1-x}\text{K}_x\text{Fe}_2\text{As}_2$. This is a doped $A\text{-Fe}_2\text{As}_2$ -type pnictide. It exhibits superconducting behaviour when doped, ranging from $T_c = 3$ K with low doping to a maximum 38 K (Rotter *et al.*, 2008) when $x = 0.4$.

The undoped structure has orthorhombic symmetry ($Fmmm$) and antiferromagnetic spin (Su *et al.*, 2009) below 140 K, undergoing a structural and magnetic phase transition to tetragonal $I4/mmm$ on heating. Doping reduces this transition temperature exponentially, with structures doped above $x \approx 0.23$ being tetragonal at all temperatures: a phase diagram has been published by Rotter *et al.* (2008). Similar A -type pnictides with $A = \text{Ca}$, Sr and Ba have been shown to display superconducting behaviour up to 29 K without doping when under pressure (Alireza *et al.*, 2009; Kreyssig *et al.*, 2008).

Single crystals of these new materials were originally not available, so initial explorations of the phonon properties have come from calculations and powder INS or IXS studies. Reznik *et al.* (2009) have now published single crystal IXS results along some key directions, enabling a proper criticism of original *ab initio* Density Function Theory (DFT) results. They have now found it necessary to include magnetic moments in the DFT calculations, even for the non magnetically

ordered superconducting phase: non-magnetic calculations produce a poor agreement with experiment for phonons around 20 meV. The need for the addition of magnetism even in the phases without long range ordered magnetic structure implies strong fluctuations remain in these phases together with magneto-elastic coupling. However, in a field where so little is known, any insights into the phonon behaviour could lead to an improved understanding of the lattice dynamics and superconductivity.

7.2.1 Experiment

Collaborating with Frank Weber¹, who was involved in powdered BaFe₂As₂ neutron spectroscopy experiments on MERLIN in 2008 (Christianson *et al.*, 2008), I have performed initial investigations using the new powder refinement approach. Data were collected as described in the primary reference, over a range of different doping ratios and temperatures, to investigate the resonant magnetic excitations especially around $Q = 1.15 \text{ \AA}^{-1}$ (Fig. 2 of Christianson *et al.*, 2008). There was also considerable phonon information. The experimental spectra (Fig. 7.7(b)) used for the refinement of the force constant model was collected for Ba_{0.6}K_{0.4}Fe₂As₂ at 10 K using $E_i = 60 \text{ meV}$.

7.2.2 Simulations and refinement

Ba_{1-x}K_xFe₂As₂ is tetragonal (space group $I4/mmm$) at 10 K and $x = 0.4$: the experimental cell parameters are $a = b = 3.917 \text{ \AA}$ and $c = 13.30 \text{ \AA}$. INS simulations were performed using a force constant model extracted from the original non-magnetic DFT results described by Reznik *et al.* (2009), and used as the basis for refinement. The Coulombic charges are subsumed into the force constants in the DFT model, so nominal charges were set to zero in GULP. I produced a mean-field atom with the combined mass, bonding and neutron scattering properties of 0.6% Ba and 0.4% K. As the data contained a strong magnetic excitation at low Q which will not be reproduced using a phonon model, the first 18 ‘workspaces’, corresponding to $Q_{\max} = 1.7 \text{ \AA}^{-1}$ at the elastic line, were removed from the fit. The region around the vane crossing the elastic line near $Q = 7 \text{ \AA}^{-1}$ was also masked: the vanes, while helpful in removing some cross-sample scatter, have caused problems with local normalisation. The multi-phonon and multiple scattering were also included and the weightings allowed to vary freely.

As is usual with first principles calculations, the DTF cell has slightly different lattice parameters (Fig 7.6), but the force constant model used in GULP was built from the *ab initio* force constants with the cell parameter adjusted to match experimental data. A Monkhorst-Pack grid of $11 \times 11 \times 3$ was used, reflecting the shape of the unit cell. The first results are presented here.

¹Frank Weber was, until recently, part of Ray Osborne’s Neutron and X-ray Scattering Group at Argonne National Laboratory, and is now the group leader of the Scattering Group at the Karlsruhe Institute of Technology.

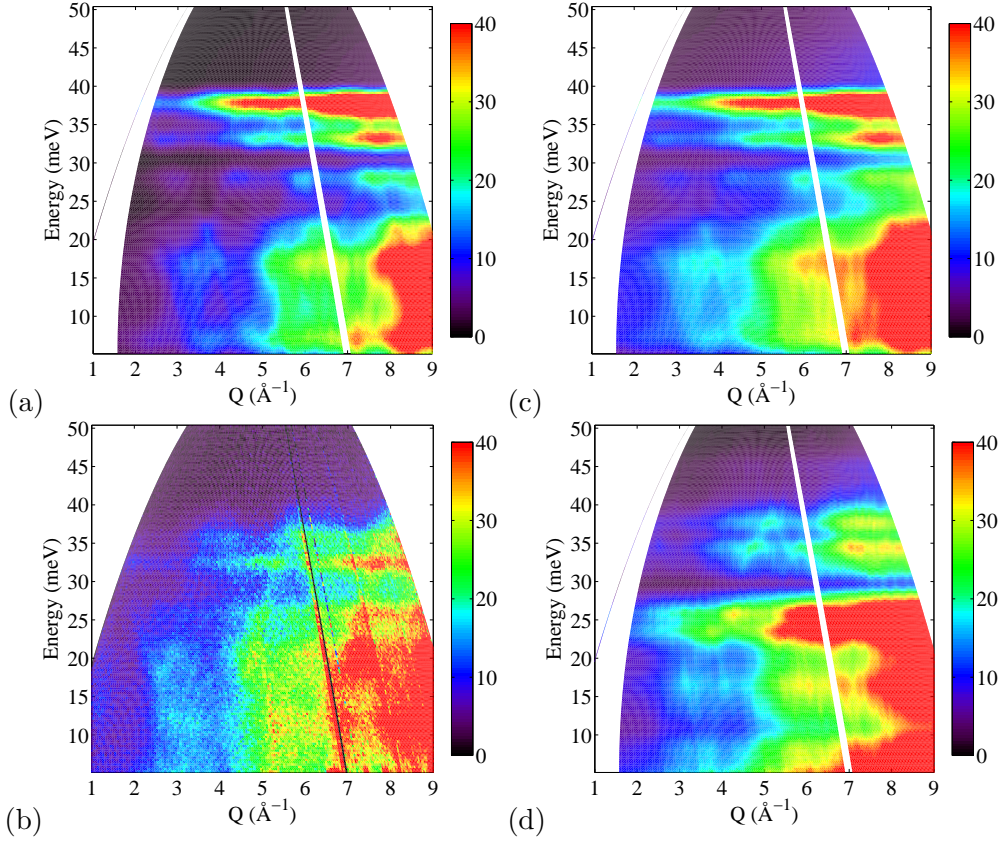


Figure 7.7: (a) The starting point of the fit from the mean-field implementation of the DFT model adjusted to have the experimental cell parameters, with backgrounds of 15% (b) Experimental data for $\text{Ba}_{0.6}\text{K}_{0.4}\text{Fe}_2\text{As}_2$ at 10 K. (c) The DFT model for which the backgrounds and scale have been allowed to vary freely. (d) The best optimised FC refinement. In all the simulations, the masked (white) regions cover the magnetic resonance in the experimental data, as well as the poorly normalised data around the 90 degree vane.

7.2.3 Preliminarily results

The DFT model is shown in Fig. 7.7. Multi-phonon and multiple scattering were limited to 15% in the first refinement, and the scale allowed to vary freely, while the second version had all three varying freely. The final values for the backgrounds together with relative improvement to χ^2 is shown in Table 7.6. Finally, the full force constant refinement which yielded the lowest χ^2 is presented. The force constants for the initial and final models are compared in Table 7.5, although it must be noted that this is by no means a definitive model.

Comparison of the DFT model to the experimental data shows that many of the features are reproduced (Fig. 7.7). This is the first time the DFT model has been seen through a simulation of INS fully convolved with experimental resolution functions, and it goes some way to validating it. However, it is immediately apparent that there is something missing from the

7.2 Ba_{1-x}K_xFe₂As₂: powder simulations and refinement

| | | DFT [eV Å ⁻²] | | Refined [eV Å ⁻²] | | cut off [Å] | | |
|------|------|---------------------------|------|-------------------------------|----------|-------------|-------|-----|
| | | L | T | L | T | min | max | |
| Fe | Fe | NN | 0.98 | 0.80 | 0.72261 | -0.10523 | 2.6 | 2.9 |
| | | NNN | 0.26 | -0.15 | -0.69234 | -0.18915 | 3.8 | 4.0 |
| As | As | NN | 0.78 | -0.17 | 3.0833 | -0.77242 | 3.8 | 3.9 |
| | | NNN | 0.37 | -0.03 | -0.35247 | 2.7927 | 3.901 | 4.0 |
| Ba-K | Ba-K | NN | 0.85 | -0.10 | -5.1864 | 0.79796 | 3.8 | 4.0 |
| Fe | As | NN | 5.90 | 0.968 | 5.3198 | 1.3968 | 2.3 | 2.5 |
| Ba-K | Fe | NN | 0.23 | 0.01 | 0.41481 | -0.26413 | 3.7 | 3.9 |
| Ba-K | As | NN | 0.01 | -0.03 | 0.41197 | -0.042441 | 3.3 | 3.5 |

Table 7.5: Nearest and next-nearest neighbour interactions used from the original DFT model and refined FC model giving the longitudinal (L) and transverse (T) force constants together with the cut-off distances for these interactions.

| | DFT (constrained) | DFT (free) | Refined FC |
|------------------------|--------------------|--------------------|--------------------|
| χ^2 | 11.8×10^5 | 5.55×10^5 | 3.40×10^5 |
| Multi-phonon (%) | 15 | 47 | 37 |
| Multiple scattering(%) | 15 | 54 | 6 |

Table 7.6: χ^2 , multi-phonon and multiple scattering weightings for the different models. When allowed to vary freely for either the DFT or refined FC model, the multi-phonon contribution is unrealistically high, indicative of a strong degree of incoherent scattering from the hydrogen recoil line (also Q^2 dependent). The multiple scattering, however, is reasonable for the refined model. When the backgrounds are limited to a sensible values (15%) for the DFT model, the χ^2 value is twice as big.

model. In both the DFT and refinement models, the multiple scattering background dominates when left to refine without limits. This suggests that there is something missing with a strong Q^2 dependence. The most likely explanation for this is incoherent scattering from hydrogen giving a Q^2 recoil line. As noted by Reznik *et al.* (2009), the non-magnetic DFT model fails to reproduce the phonon features around 20 meV.

The model refinement has been able to correctly push the high energy modes around 35 meV to have appropriate intensity weightings, and has elevated some modes to fill the gap between 20 and 25 meV. However, these improvements have been at the cost of pushing some modes too high (as can be seen in the one-phonon scattering spectra, without experimental resolution functions, in Fig. 7.8). At the same time, some modes have moved to unrealistically low energies, just above zero.

This is a fast moving field, and new first principles models and single crystals have recently become available. This new approach will allow the validity of this model to be assessed, and the use of single crystal data will make this even more rigorous.

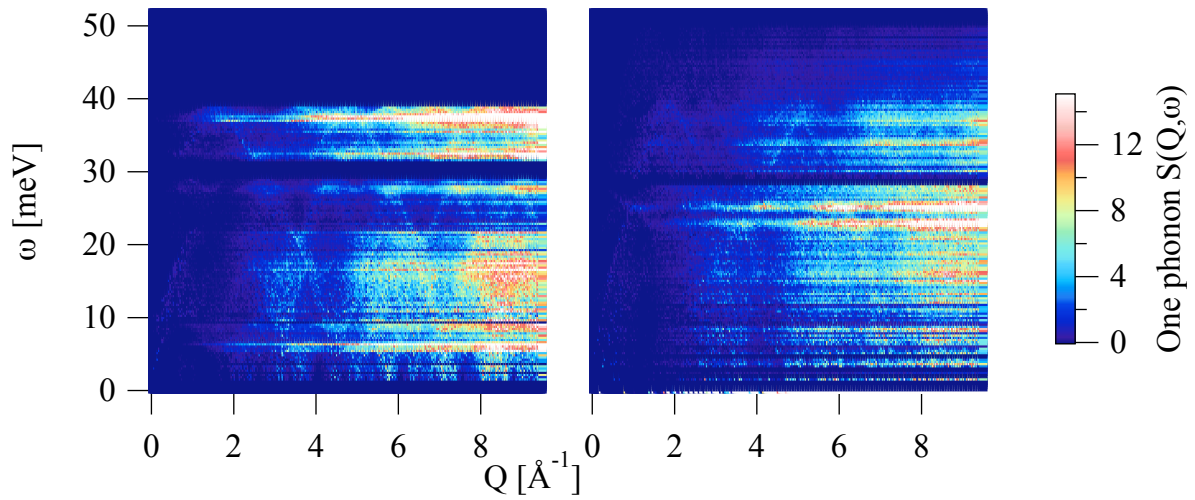


Figure 7.8: One phonon INS simulations, showing (left) the original DTF model and (right) the final refinement.

7.2.4 Conclusions

This study has shown that the validity of a DFT model can be assessed through powder INS simulations and that the refinement approach can identify unexpected additional scattering features: the possibility of hydrogen has been raised for the first time due to comparisons between the DFT simulations and the experimental data. It has demonstrated that the methodologies contained in this thesis can give new insights into technologically important materials, and are already being used beyond our group in Cambridge.

Chapter 8

Summary and Conclusions

The ability to investigate both the structure and dynamics of a material is essential to understanding the fundamental properties. Neutron scattering is a powerful experimental technique, revealing atomic scale motion from powders (or indeed amorphous materials) as well as single crystals. In order to aid the interpretation of this experimental data, there is a need for a computational modelling approach allowing direct access to the atomic vibrations giving rise to the observed neutron scattering. This is delivered by the new methodologies described in this thesis.

The first part of the thesis focussed on the spread of interatomic separations characterised by the pair distribution function (PDF) generated experimentally from neutron total scattering experiments. Implementation of phonon-based simulation techniques as part of the widely used GULP package now makes modelling the PDF a relatively straightforward process, giving new insights on a wide range of materials. The ability to reproduce experimental result with a good interatomic potential has been demonstrated, and the advantages and disadvantages of refining an interatomic model against the PDF have been discussed. It has been clearly shown (as is to be expected) that the low energy modes dominate the PDF. This has implications for the limitations of ‘phonons-from-diffraction’, as well as interatomic model refinement using PDFs.

The PDF is an excellent probe of short- to mid-range structural order. This was utilised in the β -cristobalite study, looking at simulations based on different structural models. For the first time, it was possible to accurately reproduce the effects of the different models on the short-range scale and provide a quantitative comparison to experiment. The combination of structure and dynamics here was crucial.

One of the most powerful aspects of the PDF simulation software is the ability to perform computational experiments, as demonstrated by the question of cation ordering in the calcium/strontium titanates. The PDF simulations clearly demonstrated the differences between

PDFs from the different ordering patterns that could be expected experimentally. This is important as it gives a general approach that could be used to look at other doping and ordering problems. It reveals the level of differences to be expected in experimental results, so the viability of extracting this information from total scattering data can be assessed. This could be using RMC approaches, or through the direct interpretation of the new simulations.

The new GULP PDF modules have been incorporated into the latest β -version of GULP, so will soon be widely available on academic licence. The RMC community have already had success applying the new techniques to molecular materials, and the software has been tested by various other international groups.

The effects of dynamics, while crucial to the proper understanding of total scattering data, have conventionally and most powerfully been studied through inelastic neutron spectroscopy. The main aim of the thesis was the development of a comprehensive new methodology incorporating computer modelling of INS spectra. Again, the flexibility of GULP for use with a wide range of interatomic models suitable for many different materials, and the advantages of the in-built symmetry operations to reduce calculations to the appropriate primitive cell, made it the perfect computational basis for this work.

The coherent one-phonon scattering function, together with full anisotropic Debye-Waller temperature factors, can now be calculated with the new SQW GULP module. This has the flexibility to produce scattering intensities for a single point or a line in reciprocal space, as well as taking a powder average or producing the information for the entire four-dimensional scattering function of a single crystal. For the materials studied in this thesis the coherent scattering dominated the INS spectra. However, the necessary flexibility has been built into the new modules to allow the inclusion of other processes such as incoherent scattering, which will become increasingly important as the approach is used more widely.

The original aim of this work was to produce one-phonon INS simulations, but comparison to experimental data soon revealed an important problem. The effects of multiple scattering and multi-phonon scattering, particularly at higher momentum transfers, cannot be ignored. Therefore, investigations were made into the most appropriate way to include such effects in the powder INS spectra. The approximations now included have been shown to be successful, without adding excessive processing time to the simulations.

The new approach includes the GULP SQW module in new TOBYFIT cross-section models, allowing the convolution of the simulated INS spectra with experimental resolution functions appropriate for the specific experimental set-up on the full range of ISIS direct geometry chopper spectrometers. This has allowed direct comparison with experiment, and introduced the possibility of refining the underlying interatomic models. Interest in these new approaches has been

List 1 Further developments for the power refinement methodology

The applications of the original software as shown in this thesis have prompted a number of proposed further developments, summarised here:

- simulation of elastic scattering,
 - use of appropriate resolution functions for the elastic line,
 - addition of incoherent scattering,
 - relative weighting of different regions of the experimental INS patterns,
 - addition of other (weighted) ‘observables’,
 - direct inclusion of the PDF in the refinement process,
 - greater flexibility in the refinement of Coulombic charges (while maintained a charge neutral unit cell),
 - ability to refine using ω or ω/Q^2 weighted data with appropriately weighted experimental resolution functions,
 - possible combination with (pre-existing) magnetic cross-section models.
-

expressed by several of the ISIS instrument scientists, and I hope to make these new techniques part of the standard suit of data-analysis software available to ISIS users during experiments.

Refinement of powder diffraction data is now a standard and important technique for crystallographers. With INS requiring relatively large single crystals, and with some materials simply not suited to producing well characterised single crystals, the ability to refine an interatomic model from powder data would have immediate and far-reaching implications. However, there were concerns that powder refinement would not be possible, especially for unambiguously deciphering individual phonon branches from densely populated areas of the density of states. For the first time, powder INS refinement has been made available in the new methodologies developed here, allowing the proper assessment of its long-term viability.

My work has shown that, for a simple system like aluminium, powder refinement is indeed possible. For more complex situations, like the calcite and pnictide, the new methodology has certainly allowed refinement, but there were a number of pitfalls as discussed in the individual studies. Future developments for the methodology in light of these are summarised in List 1.

I consider the current viability study to have delivered proof-of-concept. Powder refinement of INS is a real possibility, albeit requiring some further developments. There are analogies to be drawn here with the development of crystallographic refinement techniques: structures were originally derived from single crystal data, but Rietveld refinement from powders has now become routine. Powder refinement of phonon modes from INS is ahead of its time, but achievable.

The new methodology concerns more than refinement. Simulations allow the link between the underlying phonons and the observed spectra to be investigated. This is perhaps the most important feature of the new approach, and was powerfully demonstrated in Chapter 5 with the investigations into the origins of the strikingly similar phonon modes seen in the crystalline and amorphous silica INS spectra. It has been shown that a standard lattice dynamical model can reproduce the PDF, the 10 K thermal anomaly in the heat capacity and the Bose peak and ‘fast sound’ features of INS spectra. Having shown that the simulated spectra, with appropriate backgrounds and fully convolved with experimental resolution functions, could completely reproduce the observed scattering, the one-phonon spectra allowed a detailed study of the underlying behaviour. Not only did this reveal the nature of the scattering spectra beyond the experimentally accessible range of momentum transfers, but also allowed, for the first time, proper discussion of the nature of the different regions of the experimentally observed phonon modes.

This demonstrates the power of the new approach. As the refinement processes become more effective, improved empirical interatomic models will be possible for a huge range of materials. Accurate simulation of the observed INS spectra over many Brillouin zones is the most rigorous possible test of an interatomic model. The study of the underlying phonon modes will allow experimentally observed features to be explained. Combining this with the new approach being developed by our group to convert GULP eigenvectors into video animations of atomic motion will make this even more powerful.

The single crystal simulations of calcite provide another demonstration of the power of the new methodology. They provided a comprehensive validation of the Archer empirical model and the excellent reproduction of the general trends shown by this model aided interpretation of the experimental data and extracted dispersion curves. Such simulations are also valuable in planning further experiments. Allowing simulation of many Brillouin zones, this will be a powerful tool for those working with triple axis spectrometers, providing a bigger picture onto which their experimental results can be projected. Furthermore, there is no theoretical reason why single crystal model refinement should not soon be a possibility. The computational demands are large, but not insurmountable, and with appropriate parallelisation this will become an extremely powerful resource.

The software is currently linked to the ISIS in-house software, making it readily accessible to other ISIS users. There are plans to unify the current ISIS normalisation, visualisation and analysis software and for this package to be used at other facilities around the world. The incorporation of these new modules into that larger body of code would allow many more users to take advantage of its power and flexibly.

In conclusion, the work presented in this thesis has demonstrated that the new computer modelling approach, in conjunction with either the PDF (linked to neutron total scattering) or INS spectra, can reveal the link between the underlying structure and dynamics of a system and the observed experimental scattering. Unique insights are available from the different layers of the simulations – from the under-lying one-phonon scattering, from the multi-phonon and multiple scattering, and from the experimental resolution functions – as well as by performing more complex computational experiments such as removing the contribution to the INS from specific atoms or adjusting the ordering patterns. As more materials are studied, the interaction between the computational and experimental aspects are iteratively improving the overall methodology. Crucially, many important results have already been obtained. Moreover, these exciting developments will soon be made available to a much wider audience of ISIS users, as well as in my own ongoing research, making the study of the structure and dynamics of materials more accessible than ever before.

Appendix A

Additional Details for the new GULP SQW Module

The discussion on the new GULP SQW module in Section 4.3 introduced the main purpose and implementation of the new code. Details of the input and output formats were not necessary for interpreting the science performed with this new software, but it is helpful to document the available options in a little more detail here.

GULP uses an ASCII input file made up of keywords and options. The new SQW keywords (shown in Table 4.1) have appropriate dependencies set to trigger standard GULP keywords such as `eigen` and `phonon`, thus generating the phonon information. They also enable GULP to call the appropriate new routines, and to read the `neutron` options.

The main GULP input file provides the crystal structure, empirical potentials or force constant model, and other standard GULP input options. Of particular importance are `temperature` and `shrink` (used for adjusting the density of the Monkhorst-Pack grid of \mathbf{k} -points). When using `shrink`, it is essential that the user checks that convergence of phonon properties with number of \mathbf{k} -points has been achieved.

Most of the new SQW options are placed within a specific block in the GULP input file, headed with the word `neutron` and closed with `end`. This is known as the `neutron` input block, and behaves in a similar manner to other GULP input blocks.

A.1 Neutron scattering lengths

I have incorporated neutron scattering lengths into the main elemental data in GULP, which will be released with GULP from version 3.5. The most important addition here is the inclusion of the coherent scattering length, \bar{b} . As with other elemental properties in GULP, the default

setting can be changed using the GULP `element` block. Here, `at. no.` refers to the atomic number, but can also be replaced by the atomic symbol. The units are Å.

```
element [at.no.] [bbar] end
```

There is a further option, used within the `neutron` block, to switch off the scattering contribution from specific atoms. Here, each n refers to the incremental number of the atomic ‘core’ within the primitive cell as listed using the `coreinfo` keyword. These can be used here in any order and need not be sequential.

```
ignore [n1] [n2] ...
```

A.2 Setting the energy binning in the neutron block

Energy bins can be entered manually in two ways. The first defines the minimum (optional, default zero) and maximum energy together with the number of bins with the `wbins` option:

```
wbins [<wmin>] [wmax] [nw]
```

The second is to define the binning explicitly with the `Emin`, `Emax` and `dE` set of keywords (this follows the conventions of TOBYFIT). Where the binning does not divide exactly, `Emax` will be increased to a round number of dE .

```
Emin [Emin]
```

```
Emax [Emax]
```

```
dE [dE]
```

The default units are THz, but this can be changed by adding `unit freq [rad/THz/cm/wav/meV]` within the `neutron` block. The same units will be used for output.

A.3 Setting the Q binning for powders in the neutron block

To understand the input options for the powder momentum transfer, which I denote as Q , it is necessary to appreciate that there are two different internal storage formats. The standard internal setting is a nQ by $n\omega$ grid of $S(Q, \omega)$, and this is normally input using `qbins` option. The minimum is optional (default zero). The minimum and maximum values given here refer to the range limits, not the bin names (the centre-point of each bin).

```
qbins [<qmin>] [qmax] [nq]
```

This binning directly maps to that in the `.sqw` output file. However, when the `SPE` keyword has been specified, a second array is allocated to hold a Q, E range based on the experimental spread of detectors as described by the ISIS `.phx` file. This is specified using the `input phx` option (the `.phx` extension is assumed if not stated). A multiplier m can also be given, which

A.4 Setting the Q binning for single crystals in the neutron block

can be used simulate the effects of double or triple the number of detectors over the same range (often used in conjunction with TOBYFIT).

```
input phx [filename] [<m>]
```

The parameter file gives the angular spacing and number of detectors. To convert this to Q the experimental incident energy must also be specified using the `Ei` option (the units are THz unless set with the `unit freq` option):

```
Ei [Ei]
```

The conversion from ϕ to Q gives the characteristic curvature seen in plots of the powder inelastic scattering data. The internal `SPE` array therefore contains variable bin sizes, decreasing in width with increasing energy. The normal `SQW` array, however, mimics the `.spe` format range by performing the conversion to Q at the elastic line and then maintains a constant dQ with increasing energy. To speed the simulation, however, only data necessary for the desired `.spe` output is actually calculated, so the same curved shape is seen in the `.sqw` output.

Two further option exist for manipulating the input when a detector file has been used. It is possible to further restrict the range of calculations by setting cutoffs:

```
cutqmin [qmin]
cutqmax [qmax]
```

In this case, the `SQW` and `SPE` arrays will be set up according to the detector range, but calculations will only be performed within the range $qmin \leq Q \leq qmax$, leaving all other bins at zero. This function is of most use during fitting with TOBYFIT.

A.4 Setting the Q binning for single crystals in the neutron block

The single crystal $S(\mathbf{Q}, \omega)$ is stored internally on a four dimensional centre-anchored Cartesian $nQ_x \times nQ_y \times nQ_z \times n\omega$ `SQWSINGLE` array. Minimum values are optional (default zero). Limits (actual data range as opposed to bin names) are either input in Cartesian units:

```
Qxbins [<Qxmin>] [Qxmax] [nQx]
Qybins [<Qymin>] [Qymax] [nQy]
Qzbins [<Qzmin>] [Qzmax] [nQz]
```

or fractional reciprocal lattice units:

```
Qhbins [<Qhmin>] [Qhmax] [nQh]
```

etc.

A.5 Additional powder options set in the neutron block

Working with powders, it is also possible to directly calculate a density of states. This is performed (with the same binning as the momentum transfer at the elastic line) when a filename is given using `output dos`.

There are also two options for multi-phonon and multiple scattering, whose implementation are detailed in Section 4.3.2.1. The default option is to give only the one-phonon coherent scattering intensity. The multi-phonon option is activated by setting a non-zero M scaling factor (typically 10%):

```
multiphonon [M]
```

Similarly, the multiple scattering contribution is calculated based on the transmission properties of the sample set when T is given (typically 10%):

```
transmission [T]
```

Note that these backgrounds rely on sums over the entire data range, so ideally should be used with full datasets input using the `qbins` option, rather than the limited detector-based Q -range.

A.6 Output

GULP writes to the standard output, listing all the program settings and details of the calculations and calculated properties, the level of detail dependent on user settings. This output must always be checked for warnings, especially warnings concerning imaginary frequencies (energetically unstable structures). It is possible to produce `SQW` output for unstable systems using the `nowarnings` keyword, but such results should be handled with care!

A brief summary of the `SQW` output is given towards the end of the standard GULP output. For example, for powdered samples, ten reports are made of the number of \mathbf{k} -points used to seed the \mathbf{Q} -points and thus produce `SQW`, followed by a timing analysis (in seconds), the number of frequencies and \mathbf{k} points ignored, and the energy range in both SI and user-selected units. Equivalent data are also produced for single crystals.

In addition to the standard output, the key `SQW` information is written to separate files, discussed below.

A.6.1 .sqw files

The main output from a powder run is a `.sqw` file (see Output 1). The headers are extensive as they give both human-readable output, appropriate headers for the original PGPLOT plotting program (now depreciated in preference to using MATLAB with TOBYFIT) and TOBYFIT

headers to enable this data to be convolved with experimental resolution factors. The `neutron` block settings are reproduced, together with the number of \mathbf{k} -points, temperature, and final cell parameters.

The columns can be plotted in any standard package such as EXCEL or IGOR, or used to produce `.spe` files with TOBYFIT. The headers are fairly self explanatory:

```
Q w S(Q,w)c #hits #hits(powderav) multiscatter(Q,w) multiphonon G(Q,w)
```

`Q` and `w` give the centre-anchored bin names, `S(Q,w)` the one-phonon scatter in mbarn/meV. The number of hits refers to the number of times a calculation was performed using `Q` and `w` in that bin. This array also had the same powder averaging performed as the experimental data: this is the data given in `#hits(powderaveraged)`. The `multiscatter` column contains the multiple scattering approximation based on the transmission factor. The `multiphonon` column contains the multi-phonon approximation. (Both described in Section 4.3.2.1). The total scattering is not listed explicitly to improve both timings and space usage, but can be quickly produced by summing the three relevant columns. This also allows the three components to be refined independently in TOBYFIT. Finally, the total scattering is weighted appropriately for a density of states, and written as `G(Q,w)` (see Section 4.3.2.2)

A.6.2 .sqwt files

A single crystal simulation generates huge amounts of data, and it is unfeasible to give a human readable output file. The output is designed to be read into TOBYFIT, and used for the parallel generation of `.spe` files at multiple crystal orientations. These can later be recombined into a four dimensional HORACE file for visualisation. The `.sqwt` file for the calcite single crystal is 5.7Gb.

The headers in a typical `.sqwt` file contain the essential information to allow TOBYFIT to produce `.spe` files (see Output 2). Namely the Cartesian reciprocal lattice matrix ($\mathbf{k}\mathbf{v}$), the momentum transfer binning as specified by the user in the `neutron` block, and the energy range. The data are written following four nested `do loops`, for Q_1 , Q_2 , Q_3 and ω respectively.

A.6.3 .bose files

The population of phonon modes is dependent upon the temperature through the bose function, $n(\omega)$, (Eqn. 1.9). To show the effect of this, and for use in manipulating data, the `.bose` file gives $n(\omega)$ and $n(\omega) + 1$ for each energy bin, see Output 3. This output is available for any `SQW` simulation, and controlled by the `output bose` option.

Output 1 Headers from a typical powder run in .sqw format

```

#### S(Q,w) [mbarn/meV] output####
Output for configuration 1:
Number of kpoints:      1728
Temperature:            300.00K
Transmission:          10.00%
Multiphonon weighting: 10.00%
  Written at 11:01.36 13th January 2010
#####
Data from powder data
  Final Cartesian lattice vectors (Angstroms) :
      2.484341  1.434335  5.692304
     -2.484341  1.434335  5.692304
      0.000000 -2.868670  5.692304
  Final Cartesian reciprocal lattice vectors (1/Angstroms) :
      1.264558  0.730093  0.367935
     -1.264558  0.730093  0.367935
      0.000000 -1.460186  0.367935
# 1728 k points, of which 0 were rejected
# 0 frequencies were out of range
##### neutron block input #####
neutron
  qbins  0.0000  9.0000  90
  Emin  0.0000E+00
  Emax  0.2000E+03
  dE  0.200
  units freq meV
  transmission  10.00
  multiphonon  10.00
  end
#####headers for pgplot plotting program#####
# |Q|bin(1),|Q|bin(n),|Q|range,wbin(1),wbin(n),nq,nw,w_units
#####
  range 0.050000 8.950000 8.900000 0.100000E+00 0.199900E+03 90 1000 meV
|Q| w S(Q,w) #hits #hits(powderav) multiscatter(Q,w) multiphonon G(Q,w)
<data>

```

Output 2 Headers from a typical single crystal run in *.sqwt format

```

kv:
  0.73009555744351073      0.0000000000000000      0.0000000000000000
  0.0000000000000000      1.2645625910352389      0.0000000000000000
  0.0000000000000000      0.0000000000000000      0.36793343756991986
neutron
qxbin -8 8 160
qybin -3.5 3.5 70
qzbin -8 8 160
end
wmin = -.1000E+02 meV
wmax = 0.4000E+02 meV
nw = 125
S(Q,w) generated from nested loops of Qa, Qb, Qc and w:
<data>

```

Output 3 Typical headers for a .bose output in the .bose format

```
#### Bose-einstein n(w) output ####
Output for configuration 1:
Number of kpoints:      512
Temperature:            300.00\
  Written at 11:40.52 31st December 2009
#####
w/meV                   n(w)                   n(w)+1
<data>
```

A.6.4 .dos files

It is often useful to view the density of states generated by a powder simulation. When the output `dos` option is entered, the density of states is calculated as described in Section 4.3.2.2, and written out together with information on multi-phonon and multiple scattering, in a `.dos` file. The typical headers are shown in Output 4.

Output 4 Typical headers for the density of states output in the .dos format

```
####Density of States from S(|Q|,w) output####
Output for configuration 1:
Number of kpoints:      2744
Temperature:            300.00K
Delta w:                0.2000meV
Delta |Q|:              0.0500Angs-1
multiphonon weighting:  14 %
transmission:           5.16 %
  Written at 09:27.13 13th January 2010
#####
w, SUM_Q dQ
<Summed Scattering Data>
...
normalising densities of states with factor 1190.797
  w[meV ], 1-p G(w), total G(w)
<Density of States Data>
...
Multiple phonon scattering contribution
  w[meV ], multiphonon
<Multiple Phonon Density of States Data>
...
Multiple Scattering contribution
  w[meV ], multiplescattering
<Multiple Scattering Density of States Data>
...
```

Appendix B

Using TOBYFIT with the new GULP SQW Module

The new analysis methods produced in this thesis rely heavily on the TOBYFIT software package¹. It has the capacity for users to add their own FORTRAN code to produce the desired model for the scattering intensity: this is what I have done with the new GULP SQW module. It is helpful to summarise the key functionality of this code here with particular emphasis on the points of interaction with the new GULP module and the setup details for MERLIN.

B.1 The run menu

Tobyfit is designed to allow the simultaneous simulation or least-squares refinement of several datasets from multiple runs. Each ‘run’ relates to an experimental run, with certain experimental parameters such as temperature, chopper settings, moderator parameters, sample parameters etc. A dataset is defined as a single one-dimensional cut, two dimensional slice, or entire `.spe` file.

For MARI and MAPS experiments, the instrument parameters are built into the code, together with the available chopper settings. For MERLIN, however, these parameters need to be given explicitly as in Table B.1, together with suitably refined moderator line-shape parameters (more details in the TOBYFIT manual).

Having set up the instrument parameters, the crystal parameters must be set. Working with single crystals, it is essential to get the lattice parameters and alignment correct, although for powders any reasonable cell parameter (e.g. 2π) can be used. The alignment is defined with

¹Tobyfit version 2 is written in FORTRAN 77. Now generally replaced by the new GRID version (URL - F), the original code is still available direct from the author.

| | | |
|-------------------|------------------------------------|---------|
| x_0 | Moderator-chopper distance | 10 m |
| x_a | Collimation start-chopper distance | 1.7 m |
| x_1 | Chopper-sample distance | 1.83 m |
| w_a | Width of collimation at its start | 94 mm |
| h_a | Height of collimation at its start | 94 mm |
| p_{slit} | Chopper slit width | 2.28 mm |
| radi | Radius of chopper body | 49 mm |
| ρ | Radius of curvature of slits | 1300 mm |

Table B.1: Instrument parameters for MERLIN with the standard Fermi Chopper

respect to two vectors defining the horizontal scattering plane, \mathbf{u} and \mathbf{v} , where \mathbf{u} lies parallel to the incident beam. The sample shape and mosaic spread should also be taken into account.

Finally, temperature and the incident energy must be set. When performing a simulation without an input data file, the minimum and maximum energy range and energy step in meV should be given. However, TOBYFIT will overwrite these if experimental data is available. (While working with some of the GULP cross sections, these variables can also be used to control the energy range of the GULP output in place of the neutron block.)

B.2 Cross section models

The user must select a cross-section model (which may be user defined), the parameters of which are globally set in the `cross section` menu. There are a number of in-built models for magnetic fitting, but the phonon scattering models are reliant upon the new GULP models. Full details are given below.

There are two types of cross section model. ‘Sharp’ models return the energy of a dispersion relation and its spectral weight as a function of momentum transfer, \mathbf{Q} . These are not suited to phonon scattering, as there are $3N$ modes at any given \mathbf{Q} , so the interaction between TOBYFIT and GULP is performed using the `SQW_broad.F` routine, where the spectral weight for a given \mathbf{Q} and ω must be given.

When used with GULP, the parameters set in the cross section menu control the interaction between TOBYFIT and GULP.

B.2.1 ‘External parameters’ $P1-5$

The first five parameters are reserved in TOBYFIT for “external parameters” – those that are not part of the interatomic potential model. These are as follows:

1. Overall scale factor. Can be refined without re-calling GULP.
2. $|Q|_{\min}$. Ignores any $|Q| < P2$ when used in conjunction with the `rings_map.phx` models (icross 10,11,12), returning zero. With icross 15, duplicates changing the minimum Q bin set in `parameter.gin` (but effects MS and MP background correction).
3. $|Q|_{\max}$. (Used as $P2$.)
4. Transmission: Controls the relative intensity of the multiple scattering background – proportional to the transmission properties of the sample. $P4\%$ of the total sum-over- Q (including multi-phonon contributions) is used as the multiple scattering seed.
5. Multi-phonon: A weighting factor for the multi-phonon scattering approximation. Used when $P5 > 0$. Good starting values are around 10%.

B.2.2 Potential parameters

Subsequent parameters ($P6$ onwards) map to the entries in `parameter.gin` setting up the refinable parameters for the force constant model. These are not entered manually but read from `parameter.gin` where they are listed together with the interaction type. This occurs on the first GULP call of a simulation. To read them for fitting, the `@GULP` command should be entered at the Multifrills prompt.

B.2.3 Single crystals cross section models

- icross 1:** Full interpolation of the \mathbf{k} -grid, interpolating between the 8 \mathbf{k} -points forming a box around any desired point in reciprocal space. returning the appropriate polarisation vector and frequency. The scattering intensity is then calculated explicitly with the resulting eigen-data using GULP `SQW` module subroutines.
- icross 2:** Binning of the \mathbf{k} -grid, where the appropriate GULP bin for a \mathbf{Q} -point passed from TOBYFIT is used to provide the eigenvectors and frequencies for the explicit calculation of the scattering intensity using GULP `SQW` module subroutines.
- icross 3:** Binning of a GULP generated `SQWSINGLE` array (produced on the first function call with a given set of parameters).

icross 4: Binning of a `SQWSINGLE` array read from `gulpinput.sqwt` on the first function call with a given set of parameters¹.

icross 9: Data Mining: instead of calling GULP and returning scattering intensity, this simply tracks the momentum range TOBYFIT is using. Only suitable for use with the INT NULL integration method, this is used to check the maximum and minimum requirements prior to calling GULP. Especially useful when setting up a simulation of many orientations of the crystal before collecting data.

As discussed above, options 1 and 2 are too slow to use in the current implement. All single crystal simulations, therefore, are performed using icross 3 and 4, using icross 9 to set appropriate ranges.

B.2.4 Powder cross section models

The GULP `SQW` module allows binning of powder data based either on the instrument detectors or a Cartesian grid of Q . The first is useful for performing simulations to assist experiment design while varying incident energy. It is necessary to use the Cartesian binning for greater control of the binning of the GULP output, to allow one GULP simulation to be used with multiple incident energies, to get accurate edge effects, and to make proper use of multi-phonon and multiple scattering background approximations.

cross 10: Simulation of the one-phonon inelastic neutron scattering with the binning based on instrument detectors specified in the `.phx` file² using the GULP `SPE` keyword. The energy binning in the GULP run automatically mimics TOBYFIT's `elo`, `ehi`, `de`. The Q -binning maps 1:1 to the elastic line, converting from the detector number to Q with the incident energy set for that run in TOBYFIT (“Ei”)

icross 11: As for icross 10, but with a 2:1 mapping of Q bins at the elastic line

icross 12: As for icross 10, but with a 3:1 mapping of Q bins at the elastic line. (Usually too finely binned unless a very fine Monkhorst Pack grid is used.)

icross 15: Binning is controlled using the normal GULP neutron block, placed in the `parameter.gin` file instead of picking up on instrument settings³.

icross 50: Reads the contents of `gulpinput.sqw`⁴, instead of calling GULP. Used to repeat a simulation (for example, to produce a picture mid-way through a fit using the latest

¹This allows the scale parameter to be refined and additional crystal alignments to be simulated without recalling GULP.

²renamed (or linked as) `rings_map.phx`

³Either the `wbins` or `Emin` and `Emax` input form of energy binning can be used, but the energy must be in meV.

⁴This can be set up with a symbolic link to the original output file

GULP_call_n.sqw output file), or to fit external parameters $P1$, $P4$ and $P5$. All parameters greater than $P5$ are now ignored. The SQW and multi-phonon contributions are read in separately, with the multi-phonon being re-scaled to a weighting of 1.0 for storage in memory. Parameters $P1$, $P4$ and $P5$ are then used to scale the appropriate components.

B.3 Integration Methods

Tobyfit performs a simulation by sampling (\mathbf{Q}, E) space and collecting the spectral weight from the cross section model, and then convolving with the appropriate resolution functions. There are three integration methods available in TOBYFIT v 2 of which two are relevant here: NULL and MONTE-CARLO. NULL only takes account of the detector area (and optionally the mosaic spread of the sample). This is very quick, and suitable to planning experiments and simple visualisation. MONTE-CARLO, however, performs a full Monte Carlo integration over all contributions to the resolution function. Full details of this are available in Perring (1989). When using the MONTE-CARLO integration method, it is necessary to have a simulation that covers a slightly greater area of (\mathbf{Q}, E) space than the experimental detector spread. Failure to do this can lead to artefacts at the edges.

B.4 Background Models

Tobyfit contains a number of standard background models, for example, quadratic in energy and momentum transfer. These can be applied locally to any run (with the option to make them global across all datasets of that run). The parameters for the background models can be refined in the same way as the cross section parameters, although background are not convolved with experimental resolution functions.

B.5 Fitting in TOBYFIT: MULTIFRILLS

Least-squared refinement is performed using the MULTIFRILLS¹ v 1.2 subroutine library, embedded in TOBYFIT. This allows interactive fitting of several datasets simultaneously, with the ability to use both global parameters and those local to a single dataset. When used with TOBYFIT to fit .spe data, each position sensitive detector becomes a ‘workspace’, with energy bins along the x axis and the scattering intensity along y . The errors on the intensity are taken into account and anything with zero error is removed from the fit unless specifically cleared by the user. Subsequent datasets are given incremental workspace numbers. The least squares

¹Full details of MULTIFRILLS are given at URL - H. MULTIFRILLS is based on the original FRILLS code (Osborn (1991)) developed at ISIS by Ray Osbourn with additions by Toby Perring.

refinement can be performed using the Levenberg-Marquadt algorithm, a combination between a Gauss-Newton and Steepest Descents approach. This is often found to be more robust (more likely to find the true minimum from further away) than in a simple Gauss-Newton approach.

An optimum chi squared should be of the order of 1.0. When the numbers are much larger than this, either the model is a poor representation of the data, or the estimates on the errors are much too small. Similarly, a small value is likely to indicate an overestimate of the errors. However, it has been noted that there is a problem with the current interaction between current ISIS `.spe` files and TOBYFIT. The appears to be a problem with the interpretation of the errors. Thus, for all except the old aluminium data, the χ^2 did not approach unity but was pronounced ‘converged’ when the change in the χ^2 was reported to be less than the error calculated for χ^2 : the user can adjust the point of χ^2 convergence as appropriate. Errors on the parameters are estimated by the diagonal elements of the covariance matrix, assuming that they are uncorrelated.

The user is able to adjust the fitting parameters as follows :

- derivative step length
- accuracy¹ of χ^2
- maximum number of iterations
- the least-squares fitting algorithm (quasi-Newton or Levenberg-Marquadt)
- maximum number of times the parameter step is halved if χ^2 diverges (with quasi-Newton method)

MULTIFRILLS allows all or a selection of the cross section and background parameters to be ‘freed’ for fitting against experimental `.spe` files. Parameters can be bound to each other to ensure a constant ratio (although more complicated relationships cannot be defined). Limits can be imposed, although ideally fitting should be performed with free parameters.

¹the “accuracy” sets that point at which χ^2 is deemed to have converged if the χ^2 changes by less than the accuracy parameter between two iterations

Input 1 The `gulpinput.gin` file for a simple aluminium model.

```
#keywords (these are minimal, as TOBYFIT adds additions SQW keywords)
nokpoints
title
simple aluminium model
end
cell
  4.03  4.03  4.03  90.000000  90.000000  90.000000
fractional
Al core 0.000000 0.000000 0.000000
Space
225
species 1
Al core 0.000000
shrink 20
```

B.6 GULP input files for use with TOBYFIT

B.6.1 The `gulpinput.gin` file

The two additional input files constitute two halves of a normal GULP input file. The first, the `gulpinput.gin` file, contains the model setup and is used for each GULP call. During a fit, TOBYFIT uses the information in the second ‘half’, the `parameter.gin` file, combined with internal changes to parameters to produce a replacement `neutron.gin` file. GULP then reads `gulpinput.gin` followed by `neutron.gin`. At any stage, inspection of `neutron.gin` will reveal what TOBYFIT has asked GULP to do, and combining `gulpinput.gin` with `neutron.gin` will give a standalone GULP input-file.

An example of a `gulpinput.gin` file is given in Input B.6.1.

This file starts with normal GULP keywords. For empirical potentials, it is necessary to use the `optimise` flag (but this needs to be performed at constant volume (`conv`) to ensure the cell size does not depart from that set in TOBYFIT: this is meaningless with forceconstants. Appropriate keywords such as `C6` must be included, as they would for a normal GULP run. TOBYFIT will add the essential `SQWpowder`, `phonon`, `eigen` and `Bmat` keywords to the `neutron.gin` file. It is worthwhile setting `nokpoints` and `nophonon` to minimise output, although GULP is called in `silent` mode after the first function call, with only minimal output. It is advisable not to use additional output keywords such as `distance` or `property`, as these will still be calculated in `silent` mode, but not written, so only serve to slow a fit¹. In the same way, using the `SPE` keyword while fitting is not advisable, as this duplicates many of the calculations in order to fill the `SPE` array that matches the experimental setup as well as the standard `SQW` array, slowing

¹Re-running GULP combining `gulpinput.gin` and `neutron.gin`, and adding the temperature, will show the output of these keywords

progress considerably. It is better to use `icross 50` to re-read a `.sqw` output for monitoring the progress of a fit.

It is important *not* to include the temperature specification in the input file – this is picked up from the TOBYFIT run settings. However, the Monkhorst Pack grid of **k**-points must be defined in `gulpinput.gin` – in the example this has been set as `shrink 20` putting a $20 \times 20 \times 20$ grid into the first Brillouin zone. This value must be carefully chosen, to balance convergence of phonon properties (tested against normal GULP phonon properties) and population of the given SQW array (again, plot the GULP `.sqw` or `.spe` output to check – the `.spe` output from TOBYFIT is convolved with the resolution functions so should not be used for this check) with speed of calculations.

B.6.2 The `parameter.gin` file

The `parameter.gin` file contains the information that TOBYFIT will use to build up the `neutron.gin` input file. Specifically, all the force constant or potential model parameters, together with the names of the contributing atoms and their cutoffs, followed by the `neutron` block if using `icross 15` (powder) or 1, 2 or 3 (single crystal).

The `parameter.gin` file starts with a TOBYFIT header to specify the number of sets of potential models: `parameters N`. This is followed by N sets of standard GULP potential inputs. This consists of a line specifying the type of potential, e.g. `forceconstant`, `Buckingham` or `spring`. This line is simply copied and re-written into the `neutron.gin` file. Then the line with the actual parameters starts with the atoms involved (specifying core/shell if appropriate), followed by the parameters, followed by the cut-offs (where appropriate). It is essential that there are no fitting flags included (and that the GULP keyword `fit` does not appear in `gulpinput.gin`).

Many standard GULP models are supported. The parameter line into three sections, the atom description (e.g. `Al core Al core` or simply `Al Al`) is copied directly into `neutron.gin`, the parameters are read into cross section parameters sequentially – typically two or three terms will appear in a line, and then the cutoffs are copied directly into `neutron.gin`. More complicated GULP models, or those with an unusual number of terms, will need further ‘special cases’ adding to the code: `readpotentialparameters.F` currently contains several special cases.

In the version of the code, these parameters should only be entered through the `parameter.gin` file and not in the cross section menu. They are read into TOBYFIT automatically the first time a simulation is performed. To read them in for a fit, or to re-read the file, type `@GULP` in the MULTIFRILLS fitting menu. (This decision was made following consultation with users.)

Input 2 The `parameter.gin` file for the aluminium force constant model, also showing the alternative setting for the energy binning

```
parameters 1
forceconstant 1
al al 1.1668 0.15043E-01 0 3.2
neutron
qbins 0 10 250
Emin 4.0
Emax 50.0
de 0.2
end
```

or the alternative input format could be used:

```
neutron
qbins 0 10 250
wbins 4 50 230
end
```

The parameters used in any GULP call are copied to standard output, or can be inspected by opening `neutron.gin`.

When using `icross 15` (powders) or `icross 1, 2, or 3` (single crystals), it is then necessary to add a `neutron` block to the end of the file. This is exactly the same as a started `neutron` block from GULP, although the energy input is limited to be in meV, in agreement with the standard ISIS practice. Thus TOBYFIT automatically adds the `unit freq meV` line, and it should be omitted here.

As an example, the aluminium `parameter.gin` file used with `icross 15` is given in Input B.6.2. The force constant parameters will be listed as P6 and P7 when TOBYFIT runs. The energy binning could equally well have been entered as `wbins 4 50 230`. Note that when setting a minimum energy, this should not be higher than that used in TOBYFIT, or the minimum energy bin in the input `.spe` file. (Input `.spe` ranges overwrite TOBYFIT run menu settings)

Appendix C

Additional Scripts

C.1 MATLAB functions for tidying .spe files prior to a fit

Small discrepancies in the data normalisation procedures can lead to small negative numbers in the scattering intensities in .spe files. While this does not cause problems when visualising the data, it does effect the refinement process. Therefore, the .spe file should be loaded into MSLICE and the data extracted into MATLAB with the `data=fromwindow()` command. I have written the `seterrors` function (Program 1) to set the error to zero, masking the datapoint from TOBYFIT. The same routine can also be used to remove data at the elastic line by passing appropriate column numbers as variable `elastic`.

Having set the errors to zero, the `removenegatives` function (Program 2) should be used to set the same datapoints to have an intensity of zero (for visualisation purposes).

Program 1 MATLAB seterrors.m function

```
function B=seterrors(ERR, S, mask1, mask2,elastic)

% B=seterror(data).
% call as "data.ERR = seterrors(data.ERR, data.S, mask1, mask2, elastic)
% followed by "data.S = removenegatives(data.S, mask1, mask2, elastic)
%
% Run this BEFORE removenegative. Mimics removenegative, but sets
% everything that will be set to zero in that routine to have an
% error of zero -- thus marking it for removal from fits in TOBYFIT
% error column of data has element S, data is S
% mask1 and mask 2 are the detector to clear = 0
% also removes the elastic line: column "elastic". set to zero to ignore..

maxQ = size(S,1)
maxw = size(S,2)

for i=1:maxQ,
    for j=1:maxw,
        if (S(i,j)<0)
            S(i,j)
            B(i,j) = 0;
        else
            B(i,j) = ERR(i,j);
        end

        if (i == mask1)
            B(i,j) = 0;
        end
        if (i == mask2)
            B(i,j) = 0;
        end
        if (j == elastic)
            B(i,j) = 0;
        end
    end
end
end
```

Program 2 MATLAB removenegatives.m function

```
function B=removenegatives(S,mask1, mask2,elastic)

% B=removenegatives(data).
%
% Always precede by call to seterrors:
% call as "data.ERR = seterrors(data.ERR, data.S, mask1, mask2, elastic)
% followed by "data.S = removenegatives(data.S, mask1, mask2, elastic)
%
%
% data has element S
% mask1 and mask 2 are the detector to clear = 0
% also removes the elastic line: column "elastic"

maxQ = size(S,1)
maxw = size(S,2)

for i=1:maxQ,
    for j=1:maxw,
        if (S(i,j)<0)
            S(i,j)
            B(i,j) = 0;
        else
            B(i,j) = S(i,j);
        end

        if (i == mask1)
            B(i,j) = 0;
        end
        if (i == mask2)
            B(i,j) = 0;
        end
        if (j == elastic)
            B(i,j) = 0;
        end
    end
end
end
```

Program 3 splitkpoints.pl: Perl script to split SQW calculations by kpoint

```
#!/usr/bin/perl
# Read in a file and split the kpoints within it into
# chunks of $numOfKpointsPerFile, writing out a new gulp input file for
# each chunk
# Written by Richard Bruin and Beth Cope. June 2007
use strict;
my $templateInputFile = "silica.gin";
my $kpointFile = "kpoints.dat";
open(KPOINTFILE, $kpointFile) or
    die("Error: cannot open file '$kpointFile'\n");
my $lineCtr = 0;
my $line = "";
my $numOfKpointsPerFile = 1;
my $originalKpointsString = "kpoints $numOfKpointsPerFile\n";
my $outputKpoints = $originalKpointsString;
my $jobNum = 0;
while ($line = <KPOINTFILE> )
{
    if ( $lineCtr < $numOfKpointsPerFile )
    {
        my @tempLine = split(" ", $line);
        my $newLine = $tempLine[0] . " " . $tempLine[1] . " " . $tempLine[2];
        $outputKpoints = "$outputKpoints $newLine\n";
        $lineCtr++;
    }
    if ( $lineCtr == $numOfKpointsPerFile )
    {
        createNewFile($jobNum, $outputKpoints);
        $outputKpoints = $originalKpointsString;
        $lineCtr = 0;
        $jobNum++;
    }
    if ( $lineCtr < $numOfKpointsPerFile )
    {
        createNewFile($jobNum, $outputKpoints);
        print "warning. check number of k points in $jobNum\n";
    }
    print $jobNum ".jobs created";
    close(KPOINTFILE);
    # Create a new gulp input file with the passed variable as
    # part of the name with the kpoints that are also passed to it
    # Usage: createNewFile(job number, kpoints to put in);
    sub createNewFile()
    {
        my $outputFilename = "silica_rand216_job_" . $_[0] . ".gin";
        my $jobName = "silica_rand216_job_" . $_[0];
        'cp $templateInputFile $outputFilename';
        'perl -i -p -e 's/KPOINTS/$outputKpoints/' $outputFilename';
        'perl -i -p -e 's/JOB_OUTPUT/$jobName/g' $outputFilename';
    }
}
```

C.2 Perl scripts for the manual parallelisation of SQW simulations

When performing SQW simulations with many **k**-points, or, particularly, with many atoms in the unit cell, it is helpful to be able to perform the SQW simulations for individual or small groups of **k**-points, combining them retrospectively. To take full advantage of the many available computers within CamGrid, I have written the script in Program 3, to take a list of **k**-points and allocate a set number of them to each batch file. A gulp input file should be prepared with the words **KPOINTS** at the appropriate point, and **JOB_OUTPUT** for the appropriate output filenames.

Having run the batch job using Condor to submit each job to a suitable machine on CamGrid, the final results can be recombined using the scripts in Program 4 to recreate the **.sqw** and Program 5 for the **.dos**.

Program 4 newcombineqw.pl: Perl script to recombine multiple .sqw files

```
#!/usr/bin/perl
# Combines the .sqw files in jobs 1 to $jobNumber
# into one big .sqwfile called $outputFileName
# written by Elizabeth Cope 11th June 2007
use strict;
#variables to do with files
my $rootJobName = "silica_rand216_job_";
my $rootJobExtension = ".sqw";
my $thisJobFileName = " ";
my $outputFileName = "sanders_384_r216cv_combined.sqw";
my $lastJobNumber = 215;
my $firstJobNumber = 0; # this is to allow start at 0 or 1
my $count = $firstJobNumber; #loop variable for job loop
#variables to do with individual job
my $lineCtr = 0;
my $line = "";
my @tempLine = ""; #array containing line contents
my $numberHeaderLines = 47;
my $rangeDataLine = 43;
#variables to do with output, set on read of file
my $nq = 0;
my $nw = 0;
my $col = 0;
my $numCols = 8; # to match 8 columns in file
my $row = 0;
my $numRows = 0; # will be $nq*$nw once read
my @dataMatrix;
my @rowMatrix;
my $rowCounter = 0 ; #counting lines for the DataMatrix as filled
#body
JOBLOOP : while ($count<=$lastJobNumber){
    $thisJobFileName = $rootJobName . $count . $rootJobExtension;
    print "count : $thisJobFileName \n";
    #now open that file, and do things with it
    open(THISJOB, $thisJobFileName) or
        die("Error, cannot open file '$thisJobFileName'\n");
    #initialise line and lineCtr
    $lineCtr = 0;
    $line = "";
    $rowCounter = 0;
    LINELOOP : while($line = <THISJOB>){
        if (($count == $firstJobNumber) && ($lineCtr == $rangeDataLine)){
            print "ranges: |Q|min,|Q|max,|Q|range,wmin,wmax,nq,nw,w_units\n";
            print " $line\n";
            @tempLine = split(" ", $line); #read in line splitting at space
            $nq = @tempLine[6];
            $nw = @tempLine[7];
            $numRows = $nq * $nw;
            print "nq = $nq, nw = $nw \n";
            print "numCols = $numCols, numRows = $numRows \n";
            # now we know the size of the array we can make an empty one to fill
            # Two dimensional arrays are accessed by row-order, meaning that the row is listed first
            for ($col = 0; $col < $numCols ; $col++){
                push @rowMatrix, "0";
            }
            for ($row = 0; $row < $numRows; $row++){
                push @dataMatrix, [@rowMatrix];
            }
            $lineCtr ++;
            next LINELOOP;
        }
        if ($lineCtr<$numberHeaderLines){
            print "Header: $line\n";
            $lineCtr ++;
            next LINELOOP;
        }
        if ($rowCounter == $numRows){
            print "$rowCounter lines read : $line\n";
            next LINELOOP;
        }
        @tempLine = split(" ", $line); #read in line splitting at space
        # on first run though, the output file is the same as the input file so simply read it in
        if ($count == $firstJobNumber){
            my $i = 0;
            foreach my $value (@tempLine) {
                $dataMatrix[$rowCounter][$i] = $value;
                $i++;
            }
        } else {
            my $i = 0;
            foreach my $value (@tempLine) {
                if ($i>1){
                    $dataMatrix[$rowCounter][$i] = $dataMatrix[$rowCounter][$i]+$value;
                }
                $i++;
            }
        }
        $rowCounter ++ ;
        $lineCtr ++; #increment counter before finishing
    }#end of LINELOOP
    $count++; #increment outer while loop before finishing
    close(THISJOB);
} # end of JOBLOOP
open(NEWFILE, ">$outputFileName") || die("Cannot Open File"); #OPEN (and overwrite) NEWFILE
# print matrix
print NEWFILE " |Q| w S(Qw) #hits #hits(powav) MS MP GQW\n";
for($row = 0; $row < $numRows; $row++) {
    for($col = 0; $col < $numCols; $col++) {
        print NEWFILE "$dataMatrix[$row][$col] ";
    }
    print NEWFILE "\n";
} #end of matrix for loops
close(NEWFILE)
```

Program 5 combinedens.pl: Perl script to combine .dos files

```
#!/usr/bin/perl
# Combines the .dos files in jobs 1 to $jobNumber
# into one big .dos file called $outputFileName
# written by Elizabeth Cope 11th June 2007
use strict;
#variables to do with files
my $rootJobName = "silica_rand216_job_";
my $rootJobExtension = ".dos";
my $thisJobFileName = " ";
my $outputFileName = "sanders_384_r216cv_combined.dos";
my $lastJobNumber = 215;
my $firstJobNumber = 0; # this is to allow start at 0 or 1
my $count = $firstJobNumber; #loop variable for job loop
#variables to do with individual job
my $lineCtr = 0;
my $line = "";
my @tempLine = ""; #array containing line contents
my $numberHeaderLines = 648;
#variables to do with output, set on read of file
my $nw = 310;
my $col = 0;
my @w = 0;
my @dos=0;
my $rowCounter = 0 ; #counting lines for the DataMatrix as filled
my $i=0;
#body
JOBLOOP : while ($count<=$lastJobNumber){
    $thisJobFileName = $rootJobName . $count . $rootJobExtension;
    print "$count : $thisJobFileName \n";
    #now open that file, and do things with it
    open(THISJOB, $thisJobFileName) or
        die("Error, cannot open file '$thisJobFileName'\n");
    #initialise line and lineCtr
    $lineCtr = 0;
    $line = "";
    $rowCounter = 0;
    $i = 0;
    LINELOOP : while($line = <THISJOB>){
        if ($lineCtr<$numberHeaderLines){
            $lineCtr ++;
            next LINELOOP;
        }

        @tempLine = split(",",$line); #read in line splitting
        # on first run though, the output file is the same as the input file
        # so simply read it in
        if ($i<$nw){
            if ($count == $firstJobNumber){
                $w[$i]=$tempLine[0];
                print "$i $w[$i]\n";
                $dos[$i] = $tempLine[1];
                print "$i $dos[$i]\n";
                $i++;
            } else {
                $dos[$i] = $dos[$i]+$tempLine[1];
                $i++;
            }
        }

        $lineCtr ++; #increment counter before finishing
    }#end of LINELOOP
    #increment outer while loop before finishing
    $count++;
    close(THISJOB);
} # end of JOBLOOP

#OPEN (and overwrite) NEWFILE
open(NEWFILE,">$outputFileName") || die("Cannot Open File");
# print matrix
for($i = 0; $i < $nw; $i++) {
    print NEWFILE "$w[$i],$dos[$i] \n";
}
print NEWFILE "\n";
close(NEWFILE)
```

References

- AHART, M., ASTHAGIRI, A., YE, Z.G., DERA, P., MAO, H.K., COHEN, R.E. & HEMELU, R.J. (2007). Brillouin scattering and molecular dynamics study of the elastic properties of $\text{Pb}(\text{Mg}_{1/3}\text{Nb}_{2/3})\text{O}_3$. *Phys. Rev. B*, **75**, art. no. 144410.
- ALIREZA, P.L., KO, Y.T.C., GILLETT, J., PETRONE, C.M., COLE, J.M., LONZARICH, G.G. & SEBASTIAN, S.E. (2009). Superconductivity up to 29 K in SrFe_2As_2 and BaFe_2As_2 at high pressures. *J. Phys.-Condens. Mat.*, **21**, art. no. 012208.
- ARAI, M., INAMURA, Y., OTOMO, T., KITAMURA, N., BENNINGTON, S.M. & HANNON, A.C. (1999). Novel existence of collective propagating mode and strongly localized mode in vitreous silica. *Physica B: Condensed Matter*, **263-264**, 268–272.
- ARASA, C., BUSNENGO, H., SALIN, A. & SAYOS, R. (2008). Classical dynamics study of atomic oxygen sticking on the beta-cristobalite (100) surface. *Surf. Sci.*, **602**, 975–985.
- ARCHER, T., BIRSE, S., DOVE, M., REDFERN, S., GALE, J. & CYGAN, R. (2003). An interatomic potential model for carbonates allowing for polarization effects. *Phys. Chem. Miner.*, **30**, 416–424.
- BARAM, P.S. & PARKER, S.C. (1996). Atomistic simulation of hydroxide ions in inorganic solids. *Philos. Mag. B-Phys. Condens. Matter Stat. Mech. Electron. Opt. Magn. Prop.*, **73**, 49–58.
- BARRERA, G., BRUNO, J., BARRON, T. & ALLAN, N. (2005). Negative thermal expansion. *J. Phys.-Condens. Mat.*, **17**, R217–R252.
- BENMORE, C., MOS, B., EGELSTA, P. & VERKERK, P. (1998). Methane as normalisation standard for gases in thermal neutron experiments. *J. Neutron Res.*, **6**, 279–285.
- BENOIT, M. & KOB, W. (2002). The vibrational dynamics of vitreous silica: Classical force fields vs. first principles. *Europhys. Lett.*, **60**, 269–275.
- BERMAN, R. (1949). Thermal conductivity of glasses at low temperatures. *Phys. Rev.*, **76**, 315–315.
- BERMAN, R., KLEMENS, P.G., SIMON, F.E. & FRY, T.M. (1950). Effect of neutron irradiation on the thermal conductivity of a quartz crystal at low temperature. *Nature*, **166**, 864–866.

- BEWLEY, R. (2002). Preliminary design considerations for MERLIN. Tech. rep., ISIS Facility, RAL.
- BEWLEY, R., GUIDI, T. & BENNINGTON, S. (2009). MERLIN: a high count rate chopper spectrometer at ISIS. *Notiziario Neutroni e Luce di Sincrotrone*, **14**, 22–27.
- BILIR, N. & PHILLIPS, W.A. (1975). Phonons in SiO_2 - low-temperature heat-capacity of cristobalite. *Philos. Mag.*, **32**, 113–122.
- BILLINGE, S.J.L. & EGAMI, T. (1993). Short-range atomic-structure of $\text{Nd}_{(2-x)}\text{Ce}_x\text{CuO}_{(4-y)}$ determined by real-space refinement of neutron-powder-diffraction data. *Phys. Rev. B*, **47**, 14386–14406.
- BOKOV, V. & MYLNIKOVA, I. (1961). Electrical and optical properties of ferroelectrics with diffuse phase transition. *Sov. Phys. Solid State*, **3**, 613–623.
- BONNEAU, P., GARNIER, P., CALVARIN, G., HUSSON, E., GAVARRI, J.R., HEWAT, A.W. & MORELL, A. (1991). X-ray and neutron-diffraction studies of the diffuse phase-transition in $\text{Pb}(\text{Mg}_{1/3}\text{Nb}_{2/3})\text{O}_3$ ceramics. *J. Solid State Chem.*, **91**, 350–361.
- BOSAK, A., FISCHER, I., KRISCH, M., BRAZHKIN, V., DYUZHEVA, T., WINKLER, B., WILSON, D., WEIDNER, D., REFSON, K. & MILMAN, V. (2009). Lattice dynamics of stishovite from powder inelastic x-ray scattering. *Geophys. Res. Lett.*, **36**, art. no. L19309.
- BOUROVA, E. & RICHET, P. (1998). Quartz and cristobalite: High-temperature cell parameters and volumes of fusion. *Geophys. Res. Lett.*, **25**, 2333–2336.
- BUCHENAU, U., WISCHNEWSKI, A., OHL, M. & FABIANI, E. (2007). Neutron scattering evidence on the nature of the boson peak. *J. Phys.-Condens. Mat.*, **19**, art. no. 205106.
- BURNS, G. & DACOL, F.H. (1983). Glassy polarization behavior in ferroelectric compounds $\text{Pb}(\text{Mg}_{1/3}\text{Nb}_{2/3})\text{O}_3$ and $\text{Pb}(\text{Zn}_{1/3}\text{Nb}_{2/3})\text{O}_3$. *Solid State Commun.*, 853–856.
- CARRÉ, A., HORBACH, J., ISPAS, S. & KOB, W. (2008). New fitting scheme to obtain effective potential from Car-Parrinello molecular-dynamics simulations: Application to silica. *Europhys. Lett.*, **82**, art. no. 17001.
- CATTI, M., PAVESE, A. & PRICE, G.D. (1993). Thermodynamic properties of CaCO_3 calcite and aragonite: A quasi-harmonic calculation. *Phys. Chem. Miner.*, **19**, 472–479.
- CHEN, J., CHAN, H.M. & HARMER, M.P. (1989). Ordering structure and dielectric-properties of undoped and La/Na-doped $\text{Pb}(\text{Mg}_{1/3}\text{Nb}_{2/3})\text{O}_3$. *J. Am. Ceram. Soc.*, **72**, 593–598.
- CHRISTIANSON, A., GOREMYCHKIN, E., OSBORN, R., ROSENKRANZ, S., LUMSDEN, M., MALLIAKAS, C., TODOROV, I., CLAUS, H., CHUNG, D., KANATZIDIS, M., BEWLEY, R. & GUIDI, T. (2008). Unconventional superconductivity in $\text{Ba}_{0.6}\text{K}_{0.4}\text{Fe}_2\text{As}_2$ from inelastic neutron scattering. *Nature*, **456**, 930–932.

- CHUNG, J.S. & THORPE, M.F. (1997). Local atomic structure of semiconductor alloys using pair distribution functions. *Phys. Rev. B*, **55**, 1545–1553.
- CHUNG, J.S. & THORPE, M.F. (1999). Local atomic structure of semiconductor alloys using pair distribution functions. II. *Phys. Rev. B*, **59**, 4807–4812.
- COH, S. & VANDERBILT, D. (2008). Structural stability and lattice dynamics of SiO₂ cristobalite. *Phys. Rev. B*, **78**, art. no. 054117.
- CONLON, K.H., LUO, H., VIEHLAND, D., LI, J.F., WHAN, T., FOX, J.H., STOCK, C. & SHIRANE, G. (2004). Direct observation of the near-surface layer in Pb(Mg_{1/3}Nb_{2/3})O₃ using neutron diffraction. *Phys. Rev. B*, **70**, art. no. 172204.
- COPE, E.R. (deposited 20.05.2010). FORTRAN routines for the new SQW and PDF modules of GULP and TOBYFIT (<http://www.dspace.cam.ac.uk/handle/1810/225173>).
- COPE, E.R. & DOVE, M.T. (2007). Pair distribution functions calculated from interatomic potential models using the General Utility Lattice Program. *J. Appl. Crystallogr.*, **40**, 589–594.
- COPE, E.R. & DOVE, M.T. (2010). Evaluation of domain models for β -cristobalite from the pair distribution function. *J. Phys.-Condens. Mat.*, **22**, art. no. 125401.
- COURTENS, E., FORET, M., HEHLEN, B. & VACHER, R. (2001). The vibrational modes of glasses. *Solid State Commun.*, **117**, 187–200.
- COWLEY, E. & PANT, A. (1973). Lattice dynamics of calcite. *Phys. Rev. B*, **8**, 4795–4800.
- DANDEKAR, D.P. & RUOFF, A.L. (1968). Temperature dependence of the elastic constants of calcite between 160 and 300 K. *J. Appl. Phys.*, **39**, 6004–6009.
- DEER, W., HOWIE, R. & ZUSSMAN, J. (1966). *An introduction to the rock-forming minerals*. Longman.
- DIMITROV, D.A., LOUCA, D. & RÖDER, H. (1999). Phonons from neutron powder diffraction. *Phys. Rev. B*, **60**, 6204–6207.
- DOVE, M., KEEN, D., HANNON, A. & SWAINSON, I. (1997a). Direct measurement of the Si–O bond length and orientational disorder in the high-temperature phase of cristobalite. *Phys. Chem. Miner.*, **24**, 311–317.
- DOVE, M., CRAIG, M., KEEN, D., MARSHALL, W., REDFERN, S., TRACHENKO, K. & TUCKER, M. (2000a). Crystal structure of the high-pressure monoclinic phase-II of cristobalite, SiO₂. *Mineral Mag.*, **64**, 569–576.
- DOVE, M., ECCLESTON, R., HAYDEN, S. & K, M. (2002a). MERLIN: The case for support. Tech. rep., ISIS Facility, RAL.
- DOVE, M.T. (1993). *Introduction to Lattice Dynamics*. Cambridge Topics in Mineral Physics and Chemistry, Cambridge University Press, Cambridge.

- DOVE, M.T. (2002). An introduction to the use of neutron scattering methods in mineral sciences. *Eur. J. Mineral.*, **14**, 203–224.
- DOVE, M.T. & POWELL, B.M. (1989). Neutron diffraction study of the tricritical orientational order/disorder phase transition in calcite at 1260 k. *Phys. Chem. Miner.*, **16**, 503–507.
- DOVE, M.T., HAGEN, M.E., HARRIS, M.J., POWELL, B.M., STEIGENBERGER, U. & WINKLER, B. (1992). Anomalous inelastic neutron scattering from calcite. *J. Phys.-Condens. Mat.*, **4**, 2761–2774.
- DOVE, M.T., HARRIS, M.J., HANNON, A.C., PARKER, J.M., SWAINSON, I.P. & GAMBHIR, M. (1997b). Floppy modes in crystalline and amorphous silicates. *Phys. Rev. Lett.*, **78**, 1070–1073.
- DOVE, M.T., HAMMONDS, K.D., HARRIS, M.J., HEINE, V., KEEN, D.A., PRYDE, A.K.A., TRACHENKO, K. & WARREN, M.C. (2000b). Amorphous silica from the Rigid Unit Mode approach. *Mineral Mag.*, **64**, 377–388.
- DOVE, M.T., TUCKER, M.G. & KEEN, D.A. (2002b). Neutron total scattering method: simultaneous determination of long-range and short-range order in disordered materials. *Eur. J. Mineral.*, **14**, 331–348.
- ELLIOTT, S.R. (1992). A unified model for the low-energy vibrational behaviour of amorphous solids. *Europhys. Lett.*, **19**, 201–206.
- ELLIOTT, S.R. (1996). Comment on “Phonons in Glasses: Numerical Simulations and Phenomenological Theory”. *Phys. Rev. Lett.*, **77**, 4105.
- FABIANI, E., FONTANA, A. & BUCHENAU, U. (2008). Neutron scattering study of the vibrations in vitreous silica and germania. *J. Chem. Phys.*, **128**, art. no. 244507.
- FISCHER, I., BOSAK, A. & KRISCH, M. (2009). Single-crystal lattice dynamics derived from polycrystalline inelastic x-ray scattering spectra. *Phys. Rev. B*, **79**, art. no. 134302.
- FISLER, D.K., GALE, J.D. & CYGAN, R.T. (2000). A shell model for the simulation of rhombohedral carbonate minerals and their point defects. *Am. Mineral.*, **85**, 217–224.
- FLUBACHER, P., LEADBETTER, A., MORRISON, J. & STOICHEFF, B. (1959). The low-temperature heat capacity and the raman and brillouin spectra of vitreous silica. *J. Phys. Chem. Solids*, **12**, 53–65.
- FREEMAN, J.J. & ANDERSON, A.C. (1986). Thermal conductivity of amorphous solids. *Phys. Rev. B*, **34**, 5684–5690.
- GALE, J.D. & ROHL, A.L. (2003). The General Utility Lattice Program (GULP). *Mol. Simul.*, **29**, 291–341.
- GAMBHIR, M., DOVE, M. & HEINE, V. (1999). Rigid Unit Modes and dynamic disorder: SiO₂ cristobalite and quartz. *Phys. Chem. Miner.*, **26**, 484–495.

- GASKELL, P.H. & WALLIS, D.J. (1996). Medium-range order in silica, the canonical network glass. *Phys. Rev. Lett.*, **76**, 66–69.
- GEHRING, P., WAKIMOTO, S., YE, Z. & SHIRANE, G. (2001). Soft mode dynamics above and below the Burns temperature in the relaxor $\text{Pb}(\text{Mg}_{1/3}\text{Nb}_{2/3})\text{O}_3$. *Phys. Rev. Lett.*, **87**, art. no. 277601.
- GEHRING, P.M., HIRAKA, H., STOCK, C., LEE, S.H., CHEN, W., YE, Z.G., VAKHRUSHEV, S.B. & CHOWDHURI, Z. (2009). Reassessment of the Burns temperature and its relationship to the diffuse scattering, lattice dynamics, and thermal expansion in relaxor $\text{Pb}(\text{Mg}_{1/3}\text{Nb}_{2/3})\text{O}_3$. *Phys. Rev. B*, **79**, art. no. 224109.
- GOODWIN, A.L., TUCKER, M.G., DOVE, M.T. & KEEN, D.A. (2004). Phonons from powder diffraction: a quantitative model-independent evaluation. *Phys. Rev. Lett.*, **93**, art. no. 075502.
- GOODWIN, A.L., TUCKER, M.G., COPE, E.R., DOVE, M.T. & KEEN, D.A. (2005). Model-independent extraction of dynamical information from powder diffraction data. *Phys. Rev. B*, **72**, art. no. 214304.
- GOODWIN, A.L., TUCKER, M.G., COPE, E.R., DOVE, M.T. & KEEN, D.A. (2006). Dynamics from diffraction. *Physica B: Condensed Matter*, **385**, 285–287.
- GRAF, M.J., JEONG, I.K., STARR, D.L. & HEFFNER, R.H. (2003). Limits on phonon information extracted from neutron pair-density functions. *Phys. Rev. B*, **68**, art. no. 064305.
- GVASALIYA, S., STRAUCH, D., DORNER, B., LUSHNIKOV, S. & VAKHRUSHEV, S. (2003). Lattice dynamics of $\text{Pb}(\text{Mg}_{1/3}\text{Nb}_{2/3})\text{O}_3$ (PMN): Shell-model calculations. *Ferroelectrics*, **282**, 21–27.
- HAMMONDS, K., DOVE, M., GIDDY, A., HEINE, V. & WINKLER, B. (1996). Rigid-Unit phonon modes and structural phase transitions in framework silicates. *Am. Mineral.*, **81**, 1057–1079.
- HARRIS, M.J., DOVE, M.T., SWAINSON, I.P. & HAGEN, M.E. (1998). Anomalous dynamical effects in calcite. *J. Phys.-Condens. Mat.*, **10**, L423–L429.
- HARRIS, M.J., DOVE, M.T. & PARKER, J.M. (2000). Floppy modes and the Boson peak in crystalline and amorphous silicates: an inelastic neutron scattering study. *Mineral Mag.*, **64**, 435–440.
- HATCH, D. & GHOSE, S. (1991). The $\alpha - \beta$ phase transition in cristobalite, SiO_2 . *Phys. Chem. Miner.*, **17**, 554–562.
- HIRAKA, H., LEE, S.H., GEHRING, P.M., XU, G.Y. & SHIRANE, G. (2004). Cold neutron study on the diffuse scattering and phonon excitations in the relaxor $\text{Pb}(\text{Mg}_{1/3}\text{Nb}_{2/3})\text{O}_3$. *Phys. Rev. B*, **70**, art. no. 184105.

- HIRAO, K., TANAKA, K., FURUKAWA, S. & SOGA, N. (1995). Anomalous temperature dependence of the sound velocities of SiO₂-TiO₂ glasses. *J. Mater. Sci. Lett.*, **14**, 697–699.
- HIROTA, K., YE, Z.G., WAKIMOTO, S., GEHRING, P.M. & SHIRANE, G. (2002). Neutron diffuse scattering from polar nanoregions in the relaxor Pb(Mg_{1/3}Nb_{2/3})O₃. *Phys. Rev. B*, **65**, art. no. 104105.
- HORBACH, J., KOB, W. & BINDER, K. (2001). High frequency sound and the Boson peak in amorphous silica. *Eur. Phys. J. B*, **19**, 531–543.
- HOWE, M.A., MCGREEVY, R.L. & HOWELLS, W.S. (1989). The analysis of liquid structure data from time-of-flight neutron diffractometry. *J. Phys.-Condens. Mat.*, **1**, 3433–3451.
- HOWELLS, W.S. & HANNON, A.C. (1999). LAD, 1982-1998: the first ISIS diffractometer. *J. Phys.-Condens. Mat.*, **11**, 9127–9138.
- HUA, G., WELBERRY, T., WITHERS, R. & THOMPSON, J. (1988). An electron-diffraction and lattice-dynamical study of the diffuse-scattering in β -cristobalite, SiO₂. *J. Appl. Crystallogr.*, **21**, 458–465.
- HUI, Q., TUCKER, M.G., DOVE, M.T., WELLS, S.A. & KEEN, D.A. (2005). Total scattering and Reverse Monte Carlo study of the 105 K displacive phase transition in strontium titanate. *J. Phys.-Condens. Mat.*, **17**, S111–S124.
- HUI, Q., DOVE, M.T., TUCKER, M.G., REDFERN, S.A.T. & KEEN, D.A. (2007). Neutron total scattering and Reverse Monte Carlo study of cation ordering in Ca_xSr_{1-x}TiO₃. *J. Phys.-Condens. Mat.*, **19**, art. no. 335214.
- INAMURA, Y., ARAI, M., KITAMURA, N., BENNINGTON, S.M. & HANNON, A.C. (1997). Intermediate-range structure and low-energy dynamics of densified SiO₂ glass. *Physica B: Condensed Matter*, **241-243**, 903–905, proceedings of the International Conference on Neutron Scattering.
- INAMURA, Y., ARAI, M., YAMAMURO, O., INABA, A., KITAMURA, N., OTOMO, T., MATSUO, T., BENNINGTON, S.M. & HANNON, A.C. (1999). Peculiar suppression of the specific heat and Boson peak intensity of densified SiO₂ glass. *Physica B: Condensed Matter*, **263-264**, 299–302.
- JEONG, I.K., DARLING, T.W., LEE, J.K., PROFFEN, T., HEFFNER, R.H., PARK, J.S., HONG, K.S., DMOWSKI, W. & EGAMI, T. (2005). Direct observation of the formation of polar nanoregions in Pb(Mg_{1/3}Nb_{2/3})O₃ using neutron pair distribution function analysis. *Phys. Rev. Lett.*, **94**, art. no. 147602.
- JIANG, D. & CARTER, E. (2005). First-principles study of the interfacial adhesion between SiO₂ and MoSi₂. *Phys. Rev. B*, **72**, art. no. 165410.

- KAMIHARA, Y., WATANABE, T., HIRANO, M. & HOSONO, H. (2008). Iron-Based Layered Superconductor $\text{La}[\text{O}_{1-x}\text{F}_x]\text{FeAs}$ ($x = 0.050.12$) with $T_c = 26$ K. *J. Am. Chem. Soc.*, **130**, 3296–3297.
- KAPLOW, R., AVERBACH, B.L. & STRONG, S.L. (1964). Pair correlations in solid lead near the melting temperature. *J. Phys. Chem. Solids*, **25**, 1195–1204.
- KAPLOW, R., STRONG, S.L. & AVERBACH, B.L. (1965). Radial Density Functions for liquid mercury and lead. *Phys. Rev.*, **138**, A1336.
- KAWANO, J., MIYAKE, A., SHIMOBAYASHI, N. & KITAMURA, M. (2009). Molecular dynamics simulation of the rotational order–disorder phase transition in calcite. *J. Phys.-Condens. Mat.*, **21**, art. no. 095406.
- KAYE, G. & LABY, T. (1982). *Tables of physical and chemical constants*. Longman, London.
- KEEN, D. (2001). A comparison of various commonly used correlation functions for describing total scattering. *J. Appl. Crystallogr.*, **34**, 172–177.
- KEEN, D.A. & DOVE, M.T. (2000). Total scattering studies of silica polymorphs: similarities in glass and disordered crystalline local structure. *Mineral Mag.*, **64**, 447–457.
- KREYSSIG, A., GREEN, M.A., LEE, Y., SAMOLYUK, G.D., ZAJDEL, P., LYNN, J.W., BUD'KO, S.L., TORIKACHVILI, M.S., NI, N., NANDI, S., LEÃO, J.B., POULTON, S.J., ARGYRIOU, D.N., HARMON, B.N., MCQUEENEY, R.J., CANFIELD, P.C. & GOLDMAN, A.I. (2008). Pressure-induced volume-collapsed tetragonal phase of CaFe_2As_2 as seen via neutron scattering. *Phys. Rev. B*, **78**, art. no. 184517.
- KRISHNAN, R.S. (1953). The scattering of light in fused quartz and its Raman spectrum. *Proc. Indian Acad. Sci.*, **A 37**, 377–384.
- LEADBETTER, A.J. (1969). Inelastic cold neutron scattering from different forms of silica. *J. Chem. Phys.*, **51**, 779–786.
- LIU, X. & V. LOHNEYSSEN, H. (1996). Specific-heat anomaly of amorphous solids at intermediate temperatures (1 to 30 K). *Europhys. Lett.*, **33**, 617–622.
- LOVESEY, S.W. (1984). *Theory of Neutron Scattering from Condensed Matter. Volume 1: Nuclear Scattering*. The International Series of Monographs on Physics, Oxford University Press, 1st edn.
- LUO, H., XU, G., XU, H., WANG, P. & YIN, Z. (2000). Compositional homogeneity and electrical properties of lead magnesium niobate titanate single crystals grown by a modified Bridgman technique. *Jpn. J. Appl. Phys.*, **39**, 5581–5585.
- MALINOVSKY, V.K., NOVIKOV, V.N., SOKOLOV, A.P. & DODONOV, V.G. (1988). Low-frequency Raman-scattering on surface vibrational-modes of microcrystals. *Solid State Commun.*, **67**, 725–729.

- MERRILL, L. & BASSETT, W.A. (1975). The crystal structure of $\text{CaCO}_3(\text{II})$, a high-pressure metastable phase of calcium carbonate. *Acta Crystallogr. B*, **31**, 343–349.
- MONKHORST, H. & PACK, J. (1976). Special points for Brillouin-zone integrations. *Phys. Rev. B*, **13**, 5188–5192.
- NAKAMURA, M., ARAI, M., OTOMO, T., INAMURA, Y. & BENNINGTON, S.M. (2001). Dispersive excitation in different forms of SiO_2 . *J. Non-Cryst. Solids*, **293–295**, 377–382.
- NAKAYAMA, T. (1998). Low-energy excitations in water: A simple-model analysis. *Phys. Rev. Lett.*, **80**, 1244–1247.
- NAKAYAMA, T. & SATO, N. (1998). The origin of the Boson peak in network-forming glasses. *J. Phys.-Condens. Mat.*, **10**, L41–L47.
- NIEUWENKAMP, W. (1937). On the structure of β - cristobalite. *Z. Kristall.*, **96**, 454–458.
- OSBORN, R. (1991). FRILLS: An interactive least squares fitting package. *Rutherford Appleton Laboratory Report RAL 91-011*, **RAL 91-011**.
- PAVESE, A., CATTI, M., PRICE, G.D. & JACKSON, R.A. (1992). Interatomic potentials for CaCO_3 polymorphs (calcite and aragonite), fitted to elastic and vibrational data. *Phys. Chem. Miner.*, **19**, 80–87.
- PAVESE, A., CATTI, M., PARKER, S.C. & WALL, A. (1996). Modelling of the thermal dependence of structural and elastic properties of calcite, CaCO_3 . *Phys. Chem. Miner.*, **23**, 89–93.
- PEACOR, D. (1973). High-temperature single-crystal study of cristobalite inversion. *Z. Kristall.*, **138**, 274–298.
- PERRING, T. (1989). *High Energy Magnetic Excitations in Hexagonal Cobalt*. Ph.D. thesis, University of Cambridge.
- PILLA, O., CAPONI, S., FONTANA, A., GONCALVES, J.R., MONTAGNA, M., ROSSI, F., VILIANI, G., ANGELANI, L., RUOCCO, G., MONACO, G. & SETTE, F. (2004). The low energy excess of vibrational states in $v\text{-SiO}_2$: the role of transverse dynamics. *J. Phys.-Condens. Mat.*, **16**, 8519–8530.
- PLACZEK, G. & VAN HOVE, L. (1955). Interference effects in the total neutron scattering cross-section of crystals. *Il Nuovo Cimento*, **1**, 233–256.
- PLIHAL, M. & SCHAACK, G. (1970). Lattice dynamics of crystals of the calcite structure. I. Normal frequencies and normal modes at zero wave vector. *Phys. Status Solidi B*, **42**, 485–496.
- PLUTH, J., SMITH, J. & FABER, J. (1985). Crystal structure of low cristobalite at 10, 293, and 473K: Variation of framework geometry with temperature. *J. Appl. Phys.*, **57**, 1045–1049.

- POHL, R.O., LIU, X. & THOMPSON, E. (2002). Low-temperature thermal conductivity and acoustic attenuation in amorphous solids. *Rev. Mod. Phys.*, **74**, 991–1013.
- PRICE, D.L. & CARPENTER, J. (1987). Scattering function of vitreous silica. *J. Non-Cryst. Solids*, **92**, 153–174.
- PROFFEN, T. & BILLINGE, S.J.L. (1999). PDFFIT, a program for full profile structural refinement of the atomic Pair Distribution Function. *J. Appl. Crystallogr.*, **32**, 572–575.
- PROFFEN, T., BILLINGE, S.J.L., EGAMI, T. & LOUCA, D. (2003). Structural analysis of complex materials using the atomic pair distribution function - a practical guide. *Z. Kristall.*, **218**, 132–143.
- REICHARDT, W. & PINTSCHOVIVUS, L. (2001). Influence of phonons on the Pair Distribution Function deduced from neutron powder diffraction. *Phys. Rev. B*, **6317**, art. no. 174302.
- REZNIK, D., LOKSHIN, K., MITCHELL, D.C., PARSHALL, D., DMOWSKI, W., LAMAGO, D., HEID, R., BOHNEN, K.P., SEFAT, A.S., MCGUIRE, M.A., SALES, B.C., MANDRUS, D.G., SUBEDI, A., SINGH, D.J., ALATAS, A., UPTON, M.H., SAID, A.H., CUNSOLO, A., SHVYD'KO, Y. & EGAMI, T. (2009). Phonons in doped and undoped BaFe₂As₂ investigated by inelastic x-ray scattering. *Phys. Rev. B*, **80**, art. no. 214534.
- ROTTER, M., PANGERL, M., TEGEL, M. & JOHRENDT, D. (2008). Superconductivity and crystal structures of (ba_{1-x}k_x)fe₂as₂ ($x=0-1$). *Angew. Chem. Int. Edit.*, **47**, 7949–7952.
- RUOCCO, G. (2008). Glasses: when disorder helps. *Nat Mater*, **7**, 842–843.
- SANDERS, M., LESLIE, M. & CATLOW, C. (1984). Interatomic potentials for SiO₂. *J. Chem. Soc.-Chem. Commun.*, **19**, 1271–1273.
- SANGSTER, M.J., PECKHAM, G. & SAUNDERS, D.H. (1970). Lattice Dynamics of Magnesium Oxide. *J. Phys. C. Solid State*, **3**, 1026–1036.
- SCHMAHL, W., SWAINSON, I., DOVE, M. & GRAEME-BARBER, A. (1992). Landau free energy and order parameter behaviour of the α / β phase transition in cristobalite. *Z. Kristall.*, **201**, 125–145.
- SETTE, F., RUOCCO, G., KRISCH, M., MASCIOVECCHIO, C. & VERBENI, R. (1996). Collective dynamics in water by inelastic x-rays scattering. *Phys. Scripta*, **T66**, 48–56.
- SETTE, F., KRISCH, M.H., MASCIOVECCHIO, C., RUOCCO, G. & MONACO, G. (1998). Dynamics of glasses and glass-forming liquids studied by inelastic x-ray scattering. *Science*, **280**, 1550–1555.
- SHINTANI, H. & TANAKA, H. (2008). Universal link between the boson peak and transverse phonons in glass. *Nat Mater*, **7**, 870–877.
- SINGH, A.K. & KENNEDY, G.C. (1974). Compression of calcite to 40 kbar. *J. Geophys. Res.*, **79**, 2615–2622.

- SINGH, R.K., GAUR, N.K. & CHAPLOT, S.L. (1987). Lattice dynamics of molecular calcite crystals. *Phys. Rev. B*, **35**, 4462–4471.
- SINY, I.G. & SMIRNOVA, T.A. (1989). Preceding paraphases in diffuse transition ferroelectrics. *Ferroelectrics*, **90**, 191–194.
- SOKOLOV, A.P., KISLIUK, A., SOLTWISCH, M. & QUITMANN, D. (1992). Medium-range order in glasses: comparison of Raman and diffraction measurements. *Phys. Rev. Lett.*, **69**, 1540–1543.
- SOPER, A.K., HOWELLS, W.S. & HANNON, A.C. (1989). ATLAS - Analysis of Time-of-flight diffraction data from Liquid and Amorphous Samples.
- SQUIRES, G.L. (1978). *Introduction to the Theory of Thermal Neutron Scattering*. Cambridge University Press.
- STOCK, C., ELLIS, D., SWAINSON, I.P., XU, G.Y., HIRAKA, H., ZHONG, Z., LUO, H., ZHAO, X., VIEHLAND, D., BIRGENEAU, R.J. & SHIRANE, G. (2006). Damped soft phonons and diffuse scattering in 40%Pb(Mg_{1/3}Nb_{2/3})O₃-60%PbTiO₃. *Phys. Rev. B*, art. no. 064107.
- SU, Y., LINK, P., SCHNEIDEWIND, A., WOLF, T., ADELMANN, P., XIAO, Y., MEVEN, M., MITTAL, R., ROTTER, M., JOHRENDT, D., BRUECKEL, T. & LOEWENHAUPT, M. (2009). Antiferromagnetic ordering and structural phase transition in Ba₂Fe₂As₂ with Sn incorporated from the growth flux. *Phys. Rev. B*, **79**, art. no. 064504.
- SWAINSON, I. & DOVE, M. (1993). Low-frequency floppy modes in β -cristobalite. *Phys. Rev. Lett.*, **71**, 193–196.
- SWAINSON, I., DOVE, M. & PALMER, D. (2003). Infrared and Raman spectroscopy studies of the $\alpha - \beta$ phase transition in cristobalite. *Phys. Chem. Miner.*, **30**, 353–365.
- SWAINSON, I.P., STOCK, C., GEHRING, P.M., XU, G., HIROTA, K., QIU, Y., LUO, H., ZHAO, X., LI, J.F. & VIEHLAND, D. (2009). Soft phonon columns on the edge of the Brillouin zone in the relaxor Pb(Mg_{1/3}Nb_{2/3})O₃. *Phys. Rev. B*, **79**, art. no. 224301.
- TARASKIN, S.N. & ELLIOTT, S.R. (1997a). Nature of vibrational excitations in vitreous silica. *Phys. Rev. B*, **56**, 8605–8622.
- TARASKIN, S.N. & ELLIOTT, S.R. (1997b). Phonons in vitreous silica: Dispersion and localization. *Europhys. Lett.*, **39**, 37–42.
- TAYLOR, A., ARAI, M., BENNINGTON, S., BOWDEN, Z., OSBORN, R., ANDERSEN, K., STIRLING, W.G., NAKANE, T., YAMADA, K. & WELZ, D. (1990). First results from the UK-Japanese spectrometer MARI. *Proc 11th ICANS Meeting, KEK, Tsukuba*.
- TOBY, B. & EGAMI, T. (1992). Accuracy of Pair Distribution Function- analysis applied to crystalline and non crystalline materials. *Acta Crystallogr. A*, **48**, 336–346.

- TOBY, B.H., EGAMI, T., JORGENSEN, J.D. & SUBRAMANIAN, M.A. (1990). Observation of a local structural-change at T_c For $Ti_2Ba_2CaCu_2O_8$ by pulsed neutron-diffraction. *Phys. Rev. Lett.*, **64**, 2414–2417.
- TRACHENKO, K., DOVE, M.T., HAMMONDS, K.D., HARRIS, M.J. & HEINE, V. (1998). Low energy dynamics and tunneling states in silica glass. *Phys. Rev. Lett.*, **81**, 3431–3434.
- TRACHENKO, K.O., DOVE, M.T., HARRIS, M.J. & HEINE, V. (2000). Dynamics of silica glass: two-level tunnelling states and low-energy floppy modes. *J. Phys.-Condens. Mat.*, **12**, 8041–8064.
- TSUNEYUKI, S., TSUKADA, M., AOKI, H. & MATSUI, Y. (1988). First-principles interatomic potential of silica applied to molecular dynamics. *Phys. Rev. Lett.*, **61**, 869–872.
- TUCKER, M., DOVE, M. & KEEN, D. (2001a). Application of the reverse Monte Carlo method to crystalline materials. *J. Appl. Crystallogr.*, **34**, 630–638.
- TUCKER, M., DOVE, M. & KEEN, D. (2001b). MCGRtof: Monte Carlo G(r) with resolution corrections for time-of-flight neutron diffractometers. *J. Appl. Crystallogr.*, **34**, 780–782.
- TUCKER, M., SQUIRES, M., DOVE, M. & KEEN, D. (2001c). Dynamic structural disorder in cristobalite: neutron total scattering measurement and reverse Monte Carlo modelling. *J. Phys.-Condens. Mat.*, **13**, 403–423.
- TUCKER, M.G., KEEN, D.A., DOVE, M.T., GOODWIN, A.L. & HUI, Q. (2007). RMCProfile: Reverse Monte Carlo for polycrystalline materials. *J. Phys.-Condens. Mat.*, **19**, art. no. 335218.
- URL - A (accessed 08.04.2010). ESRF Web Pages: <http://www.esrf.eu/>.
- URL - B (accessed 08.04.2010). ISIS Web Pages: <http://www.isis.stfc.ac.uk/>.
- URL - C (accessed 08.04.2010). LET Web Pages: <http://www.isis.stfc.ac.uk/instruments/let/>.
- URL - D (accessed 08.04.2010). GULP Source Code: <http://www.ivec.org/GULP/downloads.html>.
- URL - E (accessed 08.04.2010). EISPACK Web Pages: <http://www.netlib.org/eispack/>.
- URL - F (accessed 08.04.2010). TOBYFIT Web Pages: http://tobyfit.isis.rl.ac.uk/Main_Page.
- URL - G (accessed 08.04.2010). Condor Web Pages: <http://www.escience.cam.ac.uk/projects/camgrid/>.
- URL - H (accessed 08.04.2010). MULTIFRILLS Web Pages: http://www.neutron.anl.gov/software/Multi-FRILLS/Multi_FRILLS.html.
- URL - I (accessed 08.04.2010). HORACE Web Pages: <http://horace.isis.rl.ac.uk/>.
- URL - J (accessed 08.04.2010). LibISIS Web Pages: <http://www.libisis.org/>.

- URL - K (accessed 08.04.2010). MSLICE Web Pages: <http://mslice.isis.rl.ac.uk>.
- URL - L (accessed 08.04.2010). DAVE Web Pages: <http://www.ncnr.nist.gov/dave/>.
- URL - M (accessed 08.04.2010). MAPS Web Pages: <http://www.isis.stfc.ac.uk/instruments/maps/maps4739.html>.
- VAN BEEST, B.W.H., KRAMER, G.J. & VAN SANTEN, R.A. (1990). Force-fields for silicas and aluminophosphates based on *ab initio* calculations. *Phys. Rev. Lett.*, **64**, 1955–1958.
- VERKERK, P. & WELL, A.A.V. (1985). Calculation of the dynamic structure factor from thermal neutron time-of-flight spectra. *Nucl. Instr. and Meth. A*, **228**, 438–464.
- WARREN, B.E. (1978). Calculation of powder-pattern intensity distributions. *J. Appl. Crystallogr.*, **11**, 695–698.
- WELLS, S., DOVE, M., TUCKER, M. & TRACHENKO, K. (2002). Real-space rigid-unit-mode analysis of dynamic disorder in quartz, cristobalite and amorphous silica. *J. Phys.-Condens. Mat.*, **14**, 4645–4657.
- WHITE, T.O.H., DOVE, M.T., BRUIN, R.P., AUSTEN, K.F., WALKER, A.M., ARTACHO, E., MURRAY-RUST, P., WALKINGSHAW, A.D., MARMIER, A., PARKER, S.C., COUCH, P.A., TYER, R.P., TODOROV, I.T. & WILSON, D.J. (2006). Information delivery in computational mineral science: the eMinerals Data Handling System. *Proceedings of the 2nd International IEEE Conference on e-Science and Grid Computing*, art. no. 59.
- WHITE, W. (1974). *The Infra-Red Spectra of Minerals*. Mineralogical Society Monographs, editor: VC Farmer, Longon.
- WILLIAMS, W.G., IBBERSON, R.M., DAY, P. & ENDERBY, J.E. (1997). GEM - General Materials Diffractometer at ISIS. *Physica B*, **241**, 234–236.
- WILLIS, B.T.M. & PRYOR, A.W. (1975). *Thermal Vibrations in Crystallography*. Cambridge University Press, Cambridge.
- WRIGHT, A. & LEADBETTER, A. (1975). Structures of beta-cristobalite phases of SiO₂ and AlPO₄. *Philos. Mag.*, **31**, 1391–1401.
- WRIGHT, A.C. (1994). Neutron scattering from vitreous silica. V. The structure of vitreous silica: What have we learned from 60 years of diffraction studies? *J. Non-Cryst. Solids*, **179**, 84–115.
- WRIGHT, A.C., HULME, R.A., GRIMLEY, D.I., SINCLAIR, R.N., MARTIN, S.W., PRICE, D.L. & GALEENER, F.L. (1991). The structure of some simple amorphous network solids revisited. *J. Non-Cryst. Solids*, **129**, 213–232.
- WU, G., XIE, Y.L., CHEN, H., ZHONG, M., LIU, R.H., SHI, B.C., LI, Q.J., WANG, X.F., WU, T., YAN, Y.J., YING, J.J. & CHEN, X.H. (2009). Superconductivity at 56 K in samarium-doped SrFeAsF. *J. Phys.-Condens. Mat.*, **21**, art. no. 142203.

- XU, G. (2010). Competing orders in PZN- x PT and PMN- x PT relaxor ferroelectrics. *J. Phys. Soc. Jpn.*, **79**, art. no. 011011.
- XU, G.Y., SHIRANE, G., COPLEY, J.R.D. & GEHRING, P.M. (2004). Neutron elastic diffuse scattering study of Pb(Mg_{1/3}Nb_{2/3})O₃. *Phys. Rev. B*, **69**, art. no. 064112.
- ZELLER, R.C. & POHL, R.O. (1971). Thermal conductivity and specific heat of noncrystalline solids. *Phys. Rev. B*, **4**, 2029–2041.
- ZERNIKE, F. & PRINS, J.A. (1927). Die Beugung von Röntgenstrahlen in Flüssigkeiten als Effekt der Molekülanordnung. *Zeits. f. Physik A*, **41**, 184–194.
- ZHANG, M. & SCOTT, J. (2007). Raman studies of oxide minerals: a retrospective on cristobalite phases. *J. Phys.-Condens. Mat.*, **19**, art. no. 275201.
- ZIMAN, J. (1979). *Principles of the Theory of Solids*. Cambridge University Press.